ACADEMICIAN ALEXEI V. SIMASHKEVICH – 85TH JUBILEE

June 27, 2014 is a special—85th jubilee—birthday in the life and activity of the Moldovan researcher Alexei V. Simashkevich. He is Full Member of the Academy of Sciences of Moldova, doctor habilitate in physics and mathematics, professor, researcher-consultant of the Institute of Applied Physics of the Academy of Sciences of Moldova (the IAP). Academician Simashkevich has contributed a lot in the development of the Faculty of Physics of Moldova State University (the MSU) and of the IAP, in the progress of semiconductor physics in Moldova, and in training of high-level specialists in physics.

He was born in Chisinau, into a family of intellectuals. In 1947–1952 was a student at the Faculty of Physics and Mathematics, Department of Physics, of the MSU. Then he continued his professional education as a candidate of science at the Chair of Experimental Physics of the same university. It was then that the future academician got interested in the most progressive ideas in semiconductor physics, becoming its loyal and active supporter and developer. Having a high standard of culture, great erudition, and intrinsic intuition, A. Simashkevich has always worked in the forefront directions of semiconductor physics research. He has developed and matured his interest in the study of AII-BVI semiconductors when they were just beginning to get a foothold in electronics.

As a physicist, Alexei V. Simashkevich made his first steps under the guidance of professor Mihail Kot, the founder of the Chair of Electrophysics (today the Chair of Applied Physics and Informatics) of the Faculty of Physics and Engineering at the MSU. First, as a disciple of professor Kot, later as the Head of the Chair at the MSU, A. V. Simashkevich actively participated in the initiation of the specialty ”semiconductor physics” at the MSU, in equipping specialized laboratories, and in developing and delivering standard and specialized courses for students for 40 years. For a long time, his scientific interests have been in the study of properties of thin semiconductor crystal layers, which later consolidated into the area of heterojunctions of group AII-BVI semiconductors.

Here are the steps of his scientific biography.

- In 1962 A. V. Simashkevich received his Candidate of Science degree from Vilnius University, Lithuania.
- In 1967-1969, as invited professor, he visited Algeria delivering a course of general physics at the Algerian Petroleum Institute, where he published three course books in French.
- From 1967, during 28 years, Alexei V. Simashkevich was the Head of the Chair of Semiconductor Physics and the Laboratory of Studies in Semiconductor Physics at the MSU.
- In 1979 A.V. Simashkevich received his higher—doctoral—scientific degree (now "doctor habilitate") in physics and mathematics from the Leningrad Polytechnic Institute (at present St. Petersburg).
- In 1981 he received the title of Full Professor.

Research outcomes of the Chair and Laboratory of Semiconductor Physics related to the properties of the group AIII-BV and AII-BVI semiconductors and heterojunctions based on them have been duly appreciated by the world scientific community. As a result, the USSR Academy of Sciences decided to organize the first All-Union Conference on properties of heterostructures in Chisinau in 1974. The Conference Chairs were Dr. A.V. Simashkevich from the MSU, Chisinau, Moldova and Prof. Zh.I. Alferov (the inventor of the heterotransistor and the 2000 Nobel laureate in physics) from the Ioffe Physicotechnical Institute of the USSR Academy of Sciences. During the years when academician Simashkevich was the Head of the Chair of Semiconductor Physics at the MSU, more than 600 students got their University Diplomas, many of them being citizens of Vietnam, Algeria, Syria, Cuba, Mexico, Germany, Mozambique, etc. Seven researchers from the Chair and the Laboratory received their Doctor Habilitate degrees and over 59 collaborators became Candidates of Science (in physics and mathematics and in engineering). Personally A.V. Simashkevich was the scientific adviser of 25 future doctors of science. The results of the research and teaching activities of A.V. Simashkevich are evidenced in over 300 communications at national and international conferences, 27 patents, around 600 scientific publications including chapters in 4 monographs and 6 course books.

Outcomes of his theoretical investigations can be summarized as follows:

The technology for obtaining crystals, thin films, and heterostructures based on group II-VI compounds has been developed; the mechanism of the charge carrier transport via these heterostructures has been established; the respective energy diagrams have been proposed; the energy spectrum of impurities in AII-BVI compounds and in solid solutions based on them, as well as the role of those impurities in the formation of the radiation spectra and of photo-conduction, have been determined; electroluminescence in the obtained heterostructures has been studied and a number of optoelectronic devices (luminescent diodes, efficient detectors of the electromagnetic and ionizing radiation have been designed etc.).

The scientific and managerial activities of academician Simashkevich have been duly appreciated. In 1983 he was decorated with the State Prize of the Republic of Moldova in Science and Technology. In 1989 a group of his colleagues and followers were decorated with the same prize, which means a high appreciation of the scientific school founded by academician Alexei Simashkevich. The same year he was elected Corresponding Member and in 1992 Full Member

of the Academy of Sciences of Moldova. As a continuation of his personal recognition, in 1995 academician Alexei Simashkevich was elected academician-coordinator of the Section for Mathematical, Physical, and Engineering Sciences of the Academy of Sciences of Moldova and a member of its Presidium.

Since then, academician Simashkevich has been working for the Academy of Sciences of Moldova, being the founder of a joint MSU-IAP Laboratory for Materials and Structures for Solar Energetics and remaining a prolific researcher of the IAP till nowadays. The entire period at the IAP, academician Alexei Simashkevich, first as the Laboratory Head and today as leading researcher-consultant of the IAP, pays special attention to the development of R&D of photovoltaic devices. He was Deputy Director in 2001 and Acting Director of the IAP in 2002–2005. Being a member of the administration of the Academy and then of the IAP in the hard periods for academic institutions, acad. A.V. Simashkevich made a significant contribution into the maintenance of the material and human assets of the institutes of Section headed by him and their integrity.

Research and teaching activities of academician Alexei Simashkevich have always been harmoniously combined with administrative and social work. Diversity of interests and areas of activity, amicability in the relationships with colleagues and students, high intellectual and cultural standards—all that makes it just to say that academician Alexei Simashkevich deserves to be of the highest rank on the scientific hierarchy scale, a hard and laborious but rewarding duty.

prof., dr. hab. Dormidont Serban
dr. Olga Iliasenco
Institute of Applied Physics

MICROSCOPY AND MOSSBAUER STUDIES OF IRON STATES IN DOPED GALIUM ANTIMONIDE

C. Turta[1,*], V. S. Teodorescu[2], A. Mihalache[3,*], E. Gheorghitsa[3], G.F. Volodina[4], and G. Filoti[2]

[1]*Institute of Chemistry, Academy of Sciences of Moldova, Academiei str. 3, Chisinau, MD 2028 Republic of Moldova, turtalcba@gmail.com*

[2]*National Institute of Materials Physics, 105 bis, Atomistilor str., Bucharest, Magurele, P.O. Box MG-7, Ro-077125 Romania, filoti@infim.ro*

[3]*Tiraspol State University, Moldova, Iablocichin str. 5, Chisinau, MD 2069 Republic of Moldova, alexei.mihalache@gmail.com*

[4]*Institute of Applied Physics, Academy of Sciences of Moldova, Academiei str. 5, Chisinau, MD 2028 Republic of Moldova*

(Received December 30, 2013)

Abstract

A single crystal of gallium antimonide doped with 3 at % ^{57}Fe was obtained via the Czochralski method. The Mössbauer investigations revealed four iron patterns: one diamagnetic and three Fe magnetically ordered sites, even at room temperature. The data suggested that iron-containing compounds are formed at grain boundaries, and the microscopy images revealed the presence of two types of boundaries and holes of different shape and size. The EDX spectrum provided different amounts of Fe in the crystal (GaSb) and, respectively, at the boundary area.

1. Introduction

Gallium antimonide (GaSb) is one of binary semiconductors with a narrow energy bandwidth, a low electron effective mass, and a high mobility. It is a material with crystal lattice and adequate parameters of semiconducting properties suitable for building optoelectronic devices in a range of 0.8–4.3 μm [1–3]. The influence of doping elements belonging to the 3d transitional metals Fe, Ni, Cr, and Mn in the binary semiconductors, for instance, gallium antimonide, on the new physical properties is of high relevance. Among other trends, of a special interest is the preparation of magnetic materials with polarized electrons in a high spin state, which are referred to as dilute magnetic semiconductors (DMSs) [4]. The most obvious advantage of these materials consists in the possibility to implement magnetic storage of information with electronic readout in a single semiconductor device. As was demonstrated in [5], the spin injection may be carried out when electrochemical potentials in the ferromagnets will be split and the resistance of the ferromagnet is of comparable magnitude to the contact resistance. Thorough studies of the Fe–Ga system function on the component ratios and temperature resulted in the publication of the state diagrams of alloys indicating stable intermetallic compounds and their compositions [6, 7]. The main intermetallic substances obtained are: the cubic α-Fe_3Ga, Pm3m space group, in a range of 20.6–26.3 at % Ga having the

solidification temperature of T_c = 588°C; the hexagonal β-Fe_3Ga, space group $P6_3/mm\bar{c}$, exists in the limits of 24.3–32.0 at % Ga and crystallizes between 590-700°C; the monoclinic or tetragonal Fe_3Ga_4 with composition in at % Ga between 56.5–58.0, the space group C2/m, has a peritectic formation temperature of 906 ± 2°C; the β-Fe_6Ga_5, R3m space group, containing ~45 at % Ga, exists in a narrower temperature range of 770–800°C; the α-Fe_6Ga_5, with the same composition, which is characterized by C2/m space group and is stable at temperatures below 770°C; and finally the tetragonal $FeGa_3$, space group P4n2.

According to [8, 9], the Fe-Sb phase diagram consists of two phases: stoichiometric $FeSb_2$ and $Fe_{1+x}Sb$. The $FeSb_2$ component is stable in the limits of 45–67 at % Sb at temperatures below 738°C. The space group of the monocrystal is Pnn2 (FeS_{2-m} type structure) [10]. Each Fe atom is situated in interstitial sites of Sb atoms and surrounded by six Sb atoms, while the Sb atom is surrounded by three nearer iron atoms and one antimony atom. The structure of $FeSb_2$ does not change at lower temperatures (4–80 K), but the quadrupole splitting is changed; FeSb is crystallized in a range of 42–48 at % Sb in the $B8_1$ structure type. The antimony atoms form a hexagonal close-packed lattice, and the iron atoms are situated either in octahedral or tetrahedral interstices [11]. The NiAs-type $B8_1$, the phase Fe_3Sb_2(ε), has a homogeneity range of 40–47 at % Sb with maximum liquid curve at 1025°C [12].

The role of doping atoms in semiconductors could be evidenced via indirect and direct experimental methods. The most ordinary (indirect) methods to investigate the role of doping atoms in a semiconductor host involve measurements of electrical conductivity, galvanomagnetic effects, photo conductibility, thermoelectric force, etc. These methods used in the investigation of semiconductor materials provide the biggest portion of information about the role and state of enclosed atoms in semiconductors. However, the interpretation of data concerning the location of these centers, which can be substitutional, interstitial, and located at the limit of the grain or on the vacancy places, requires great caution and finally is based on results obtained by direct methods, such as electronic paramagnetic resonance (EPR), nuclear magnetic resonance (NMR), nuclear quadrupole resonance (NQR), nuclear gamma resonance (Mössbauer spectroscopy, MS), X-ray photoelectron spectroscopy (XPS), perturbed angular correlations (PAC), etc. However, these methods are not universal, such as electrical conductivity or Hall Effect measurements; therefore, they are applicable to a limited number of semiconductors (containing accessible isotopes in the case of NMR and Mössbauer, valence and spin state for EPR) or to a restricted set of impurities, enclosed atom present in them. The role of electronic paramagnetic resonance spectroscopy method to justify the basics of the theory of doped centers in semiconductors is well known [13, 14].

During recent years, the specific literature has accumulated a significant amount of data on doped centers in Fe–Ga and Fe–Sb systems and III-V semiconductors obtained by Mössbauer spectroscopy [15-23]. In [24], the spin injection at room temperature by introducing of Fe_3Si epitaxial layer into GaAs matrix was successfully demonstrated. This result represents an example of ferromagnetic Heusler alloy (Fe_2FeSi) which is a case of favorable spin injection. Considering that the solubility of doping III-V semiconductors is effectively small, in order to surpass the difficulties, it was chosen to work far from equilibrium by using epitaxial molecular flow (EMF) at low temperatures. For the GaAs system, Curie temperature T_c values of 60 [25] and 159 K [26] were obtained. Upon switching to broadband semiconductors, GaN and ZnO, the T_c values were significantly increased. Thus, in [27] T_c above 740 K was obtained by 3% Mn doping in a GaN matrix on an Al_2O_3 support. A theoretical study [28] showed that Cr and Mn dopants in the cubic 3C-SiC polytype produce a ferromagnetic solid solution for both C and Si

position, exhibiting different magnetic moments. Implantation of Fe in SiC did not lead to magnetic phase, but the replacement of silicon (Si) by iron (Fe) (at low concentrations) in the hexagonal H_6SiC polytype changed the crystal into a ferromagnetic phase. The electrical and optical properties of specified devices are widely affected by the doping material, usually owing to the diffusion of the desired element into the semiconductor crystal [29]. The actual study reports on the growth of a p-type gallium antimonide doped with 3 wt % ^{57}Fe, the related optical and TEM images, and a large set of data obtained using ^{57}Fe Mossbauer spectroscopy performed at different temperatures (3–295 K).

2. Material and methods

Sample synthesis: Amounts of Ga, *m* = 0.6545 g; Sb, *m*= 1.4250 g; and ^{57}Fe, *m* = 0.0331 g were loaded into an optical quartz ampoule with thick walls (2–3 mm) and an internal diameter of ~12 mm. The evacuation of the atmosphere alternates with a few cycles of washing with argon. At the residual gas pressure of 10^{-5} mm Hg, the ampoule containing sample was sealed and tightly connected to an electromagnetic vibrator (50 Hz) to provide a homogeneous mixture. Both the ampoule and the vibrator were placed inside a tube type furnace. A constant temperature of 900°C was maintained for 24 h. After that, the electrical supply was switched off and the furnace was freely cooled via its thermal inertia. The obtained product was ground into a powder and then introduced into the zone melting facility to grow a single crystal via the Czochralski method. A mass of 0.040 g was separated from the grown single crystal, ground into a very fine powder and used as a sample (placed in a specific holder) for Mossbauer measurements.

Mössbauer measurements. The Mössbauer spectra were measured via Oxford Instruments Mössbauer-Spectromag 4000 Cryostat from Institute of Inorganic Chemistry, Karlsruhe University. The temperature was varied within 3.0–300 K. A ^{57}Co source (3.7 GBq) in a rhodium matrix was used. The spectrometer was of the electrodynamic type with a constant acceleration symmetrical waveform. Isomer shifts values are referred to Fe-metal at room temperature. The fits of the experimental data were performed using the wmoss and NORMOSS programs.

X-ray diffraction measurements (XRD) of powder were realized at the Institute of Applied Physics of the Academy of Sciences of Moldova via DPOH-УМ1 equipment. (FeK_α-radiation, Mn filter, $\theta/2\theta$ method.).

Transmission electron microscopy (TEM) images were recorded using a Jeol ARM 200F electron microscope. The ion thinning was performed using a Gatan PIPS model 691 device operating at 5 kV and 6 degrees incidence. Optical images were obtained using an AXIO-Zeiss-ObserverA1m microscope. For TEM specimen preparation, a slice with a thickness of about 500 μm was cut parallel to the basal plane from the cylindrical GaSb crystal sample, using diamond wire devices. In the second step, the slice was cut in nine smaller pieces. Finally, the 0.5 mm x 2 mm x 2 mm GaSb piece was mechanically polished on both faces until a thickness of about 30 μm and glued on a 3-mm copper TEM grid. This grid was then ion thinned to obtain a small hole in the middle. The edges of this hole are transparent to the electron beam in the microscope. The TEM specimen was oriented with the microscope axis parallel with the cylindrical axis of the initial cylindrical GaSb sample.

3. Results and discussion

Galium antimonide doped with Fe-57 isotope studied in this paper was obtained as described in "Materials and Methods." The Mössbauer spectra (MS) of GaSb-Fe sample (3 at % Fe-57) at different temperatures are presented in Fig. 1.

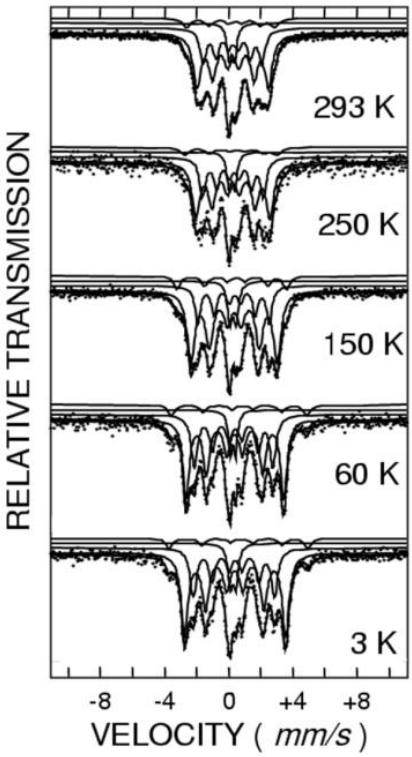

Fig. 1. Mössbauer spectra of GaSb-Fe sample (3 at % Fe-57) at different temperatures.

At a first glimpse, the most remarkable aspect of the spectra is the existence at a fairly high temperature of 298 K (RT = room temperature) of three six-line patterns, suggesting the magnetic species for three iron locations. These sextets, also the centrally placed doublet, appeared over the entire temperature range (3–295 K) of Mössbauer measurements. The Mössbauer spectra parameters of investigated sample are presented in Table 1.

It is remarkable that the values (last column in the table) of relative area (proportional to the amount of Fe ions on every of its location) remain in reasonable limits.

The presence of four different patterns in all exhibited Mössbauer spectra draw attention to a very important experimental feature. A homogeneous distribution of only 3 at % enriched ^{57}Fe inside the GaSb single crystal lattice (zinc blend cell), substituting either the Ga or Sb atoms, normally would provide two doublets corresponding to both tetrahedral surroundings of Ga and of Sb and showing identical distances to the nearest neighbors of different type and to the second sphere of 12 neighbors of the same type as the central ion of the coordination. In this case, both the IS and QS will show distinct figures due to a peculiar bond of Fe with Ga and, respectively Sb, with higher values for Fe location on Ga sites. Previous attempts of doping with Mn (for example, Mn in GaSb [30]) have failed to prove any substitution location. Therefore, the presence of Fe in four sites suggests the formation of potentially well crystallized (preparation route) of binary or ternary type compounds. These phases could exist mainly or only at dislocation or packing defects appearing during the growth of the single crystal. These dislocations are developed

preponderantly at the surface of the crystal and evolve inside the crystal, function of processing temperatures and the stress induced by growing.

Table 1. Mössbauer spectra parameters of the GaSb–Fe sample at different temperatures

T(K)	Compo-nents	B_{eff} (T*)	mm/s			A (%)
			QS	IS	W	
3	1	19.5	0.03	0.48	0.56	56
	2	15.7	-0.10	0.48	0.57	30
	3	0.0	0.34	0.39	0.36	8
	4	26.8	-0.22	0.51	0.27	6
60	1	18.8	0.03	0.48	0.47	52
	2	15.2	-0.10	0.47	0.47	34
	3	0.0	0.33	0.38	0.28	7
	4	26.2	-0.21	0.48	0.47	7
150	1	16.7	-0.02	0.45	0.57	59
	2	13.8	-0.07	0.44	0.41	22
	3	0.0	0.39	0.37	0.36	10
	4	21.1	-0.26	0.44	0.39	9
250	1	14.3	-0.03	0.39	0.57	53
	2	11.8	-0.07	0.41	0.46	30
	3	0.0	0.37	0.32	0.32	8
	4	17.9	-0.32	0.40	0.46	9
293	1	13.8	-0.04	0.38	0.58	54
	2	11.4	-0.04	0.37	0.48	29
	3	0.0	0.32	0.31	0.32	8
	4	17.0	-0.23	0.36	0.56	9

B_{int} is the internal magnetic field around the iron nucleus, error = ± 0.2 T; QS is the quadrupole splitting, IS is the isomer shift, W is the full line width, errors of QS, IS, W = ± 0.02 mm/s; A is the relative area, error = ± 1 %; T* is Tesla).

Another significant feature is the continuous decrease of the IS with temperature proving the effect of second order Doppler shift [31].

The assignation of the patterns was related to Mössbauer existing data from the literature and their analyses in terms of temperature and composition dependence of corroborated parameters.

According to the phase diagram (600°C) of ternary FeGaSb system presented in Fig. 1 of [12, 32] and phase diagrams of Fe–Ga and Fe–Sb [7, 8], at low iron concentrations, the FeGaSb system can contain the following phases: FeSb, $FeSb_2$, Fe_3Sb_2 (ε), Fe_3Ga, Fe_6Ga_5, Fe_3Ga_4, $FeGa_3$, and epitaxial iron particles at nanoscale [33, 34].

The most facile choice was for the doublet case. Comparing the experimental values of Mössbauer spectra parameters for doublet (component 3) of the sample at RT (IS = 0.31 mm/s, QS = 0.32 mm/s) (Table 1) with the literature data for MS doublets of Fe–Sb and Fe–Ga systems [15–17, 34–37] at the same temperature, one can see that they are closest to the diamagnetic $FeGa_3$ [38] (IS = 0.28, QS = 0.31 mm/s [37]). Checking the structures, the XRD diffractograms (Figs. 2a, 2b) confirm the presence of this compound.

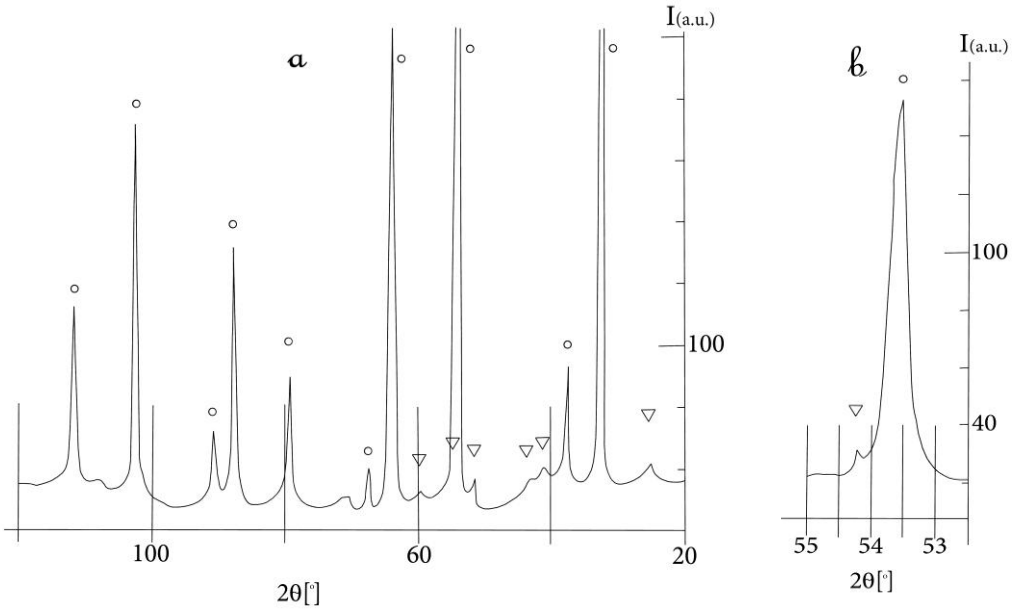

Fig. 2. (a) X-Ray powder diffraction spectra of investigated sample GaSb-Fe (3%): o—spectrum peaks for GaSb, ▽ —peaks for $FeGa_3$ substance and (b) line separation 220 GaSb (d = 2.156 Å) and 212 FeGa3 (d = 2.126 Å).

There have been as well other possibilities for a paramagnetic component; among the first of them, it was the presence of $FeSb_2$. However, in the actual case, it has to be completely excluded because the experimental values of QS (MS) are about 4 times lower (Table 1) than those reported in [15, 17, 18, 39] with values of QS = 1.26–1.29 mm/s and IS = 0.46–0.45 mm/s at RT.

Another alternative was amorphous a-$FeSb_2$ or more close in values of IS and QS the amorphous compound $Fe_{0.5}Sb_{0.5}$ [17] with QS = 0.44; 0.51 mm/s and IS = 0.43, 0.54 mm/s at RT and 4.2K, respectively, but these compounds are definitely out of any consideration, due to the process of growing single crystals. The data of $Fe_{1.3}Sb$ [40, 41] point to a doublet at RT but shows two sextets: one very pronounced, with B_{int} around 11–12 T, and the other one close to 16–17 T at 5 K; therefore, they are not suitable for our doublet assignation.

As specified above, the studied sample contains three sextet components (labelled 1, 2, 4) with different values of internal magnetic field B_{int} equal to 13.8 T (1), 11.4 T (2) and 17.0 T (4) at 293 K. Note that these values are much lower than that characteristic of α-Fe (B_{int}, 33 T), indicating the formation of systems with the composition $Fe_3(Ga_{1-x}Sb_x)_2$ [19, 20] or Fe_3Ga_4 [42], as well Fe_3Ga or $Fe_{1+x}Sb$ [40, 41], where x may cover a large range of values. It is worth noticing that, from the beginning, the formation of a Fe_3Ga_4 compound, where 4 sextets are observed and related IS values are close to zero, was excluded [42],. The $Fe_{1-x}Ga_x$ alloys were studied in [43],

with $0.15 \leq x \leq 0.30$. Those samples, obtained by ball milling, were studied by X-ray powder diffraction, magnetization, electroconductibility, and Mössbauer spectroscopy methods in a large temperature interval of 5–770 K. The XRD data demonstrated the presence of three crystallographic phases: α (Disorder (bcc)), stable within 15 to 20 at % Ga; α" (Order (bcc), $FeAl_3$-DO_3), stable within 20-30 at.% Ga; and β (Order (fcc), Cu_3Au=LI_2) stable within 25–30 at % Ga. Curie temperature T_c, magnetic moment μ (μB) /atom, B_{int}, IS, QS, and electroresistivity were determined. Later, close data were published in [44] for $Fe_{100-x}Ga_x$, where x = 15.7, 17.0, 19.0, 22.4, and 24.0, which was obtained by ball milling. In both cases, the values of B_{int}, IS, and QS differ from our data.

For all magnetic components of here investigated sample, the Curie temperatures T_c are higher than 293 K and in good agreement with the literature data. For example, in ternary systems $Fe_3(Ga_{1-x}Sb_x)_2$ and $Fe_3Ga_{2-y}As_y$, where $0.1 \leq x \leq 0.75$; $0.21 < y < 1.125$, it was demonstrated by various physical methods that the magnetic ordered state with T_C quite high up to 360–374°C is present and magnetic properties strongly depend on the proportion of Ga and Sb amount surrounding the Fe [19, 20, 35, 36]. In one attempt to assign the observed three magnetically ordered components of the investigated sample, we mainly used the results reported for $Fe_3Ga_{2-x}M_x$. According to [20, 35], the $Fe_3(Ga_{1-x}Sb_x)_2$ systems, as well as $Fe_3(Ga_{1-x}As_x)_2$, have the $B8_2$ hexagonal structure type belonging to the P63/mmc space group, which is characteristic of the Ni_2In type. In this structure, there are two positions of Ni ions: with octahedral (Oh, $NiIn_6$) environment and one asymmetrical $NiIn_5$ environment. It is obvious that the 1st and 2nd sextets should belong to the octahedral environment (lower values of QS parameter), while the 4th sextet to asymmetrical. As stated above, the most important approach in our analyses was the effect of presence of various elements from pnictide group on B_{int}, IS, and eventually QS parameters in Fe_3Ga_2 systems. From this point of view, the data from [20, 35] suggest a composition rather poor in Sb and richer in Ga in direct relation with reported data in [20]. In fact, Table 9 in [20] revealed that, with decreasing Sb content from x = 1 to x = 0.3, the B_{int} (at RT) augments by 1.5–1.7 T. Extrapolating the RT values found for the two octahedral surroundings in our study (Table 1), the observed patterns could stand for a composition with 0.10–0.15 Ga and 1.90 or 1.85 Sb. In the study of Smith et al. [20], a composition with x = 0.10 (T_C data with values around 375 K) was prepared; however, any Mössbauer spectrum or parameters were not provided.

The Mössbauer line widths W (Table 1) for the sextets of all three positions are fairly large compared to the line width measured with our source and a standard alpha-Fe absorber (W = 0.25 mm/s). The large line width may be assumed to be an effect of the tiny modified nonequivalent surroundings and to relaxation processes. It should be noted that the mentioned components of the GaSb–Fe system are not formed via substitutions of either Ga or Sb in the GaSb single crystal, but are formed at the boundary; hence, their influence on the magnetic, electrical, and other properties will be peculiar. Starting to elucidate the above statements, the optical and electron microscopy measurements were envisaged.

The reflection optical image of the "as prepared" TEM specimen is shown in Fig. 3. Two types of crystal domains are observed (transparent and grey) exhibiting large boundaries between them. The optical contrast is due to the ion beam etching for the different crystallographic orientations of the two types of the domains. The areas near the edges of the black hole situated in the middle of the image in Fig. 3 are transparent areas for the electrons in the microscope. Figure 4 shows a TEM image obtained in these transparent areas representing the GaSb mono crystal structure in the <111> orientation demonstrated by the electron pattern inserted in the

figure. The arrows in Fig. 4 show the presence of Ga precipitates on the surface of the GaSb TEM specimen after several minutes of observations under the electron beam irradiation being formed by diffusion of this element from the bulk.

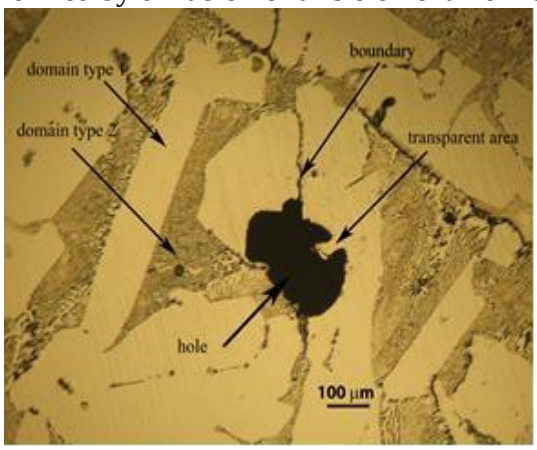

Fig. 3. Optical image (in reflection) of the axis the GaSb-Fe TEM specimen.

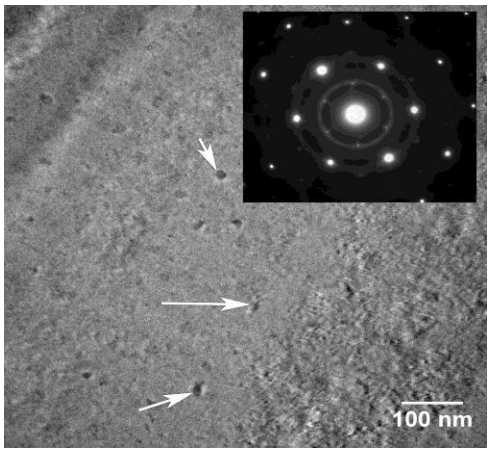

Fig. 4. Domain oriented in the <111> zone of the cubic GaSb structure.

As shown (Fig. 5) in the energy dispersive X-ray spectra (EDX), the Fe amount in the crystal bulk areas is less than 0.3 at %, while in the thick area (Fig. 6) of the specimen obtained from the location on the boundaries, about 2.5% Fe is present. The excess Ga concentration observed in the thin areas of the TEM specimens has two causes. The first one is the ion thinning process, which changes the sample concentration near the exposed surface, and the second one is the electron irradiation in the microscope, which enhances the Ga diffusion on the TEM specimen surface. After several minutes of observations, nanometric precipitates of Ga appear on the specimen surface, (see Fig. 4). In the thick areas of the TEM specimen, the Ga and Sb concentration resulted from EDX spectra are almost equal, because the amount of the Ga on the surface is less important, comparing to the total amount of the Ga present in the bulk.

As can be observed optically, the boundary regions between the crystal domains are large (about 1 μm) and, as described above, have a larger concentration of Fe (2.5%) than in the bulk (less than 0.3%). This large boundary region, which also shows some polycrystalline structures, can be attributed to the presence of the FeGa3 structure observed by X-ray diffraction.

Due to the complex structure of the boundary region, it was impossible to obtain real transparent areas for TEM in these regions; however, EDX spectra (shown in Fig. 6) could be recorded.

These results considerably confirm and support the Mössbauer data and the related location of iron containing phases at grain boundaries. This presence indeed could not substantially influence the physical properties of the GaSb single crystal doped with a fairly small amount of Fe.

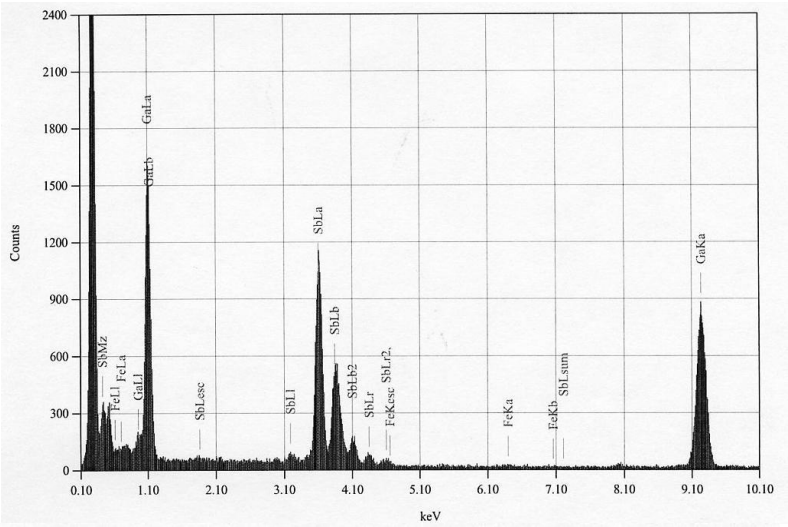

Thin Film Standardless Standard Quantitative Analysis
Fitting Coefficient : 0.5009

Element	(keV)	Mass%	Counts	Error%	Atom%	Compound	Mass%	Cation	K
Fe K	6.398	0.18	128.63	6.73	0.28				0.3986
Ga L	1.098	53.13	12874.93	0.05	66.34				1.1869
Sb L (Ref.)	3.604	46.69	13427.26	0.06	33.38				1.0000
Total		100.00			100.00				

Fig. 5. EDX spectrum from the thin transparent area of a bulk crystal after TEM observations. Ga is largely present on the specimen surface, probably due to the ion thinning process.

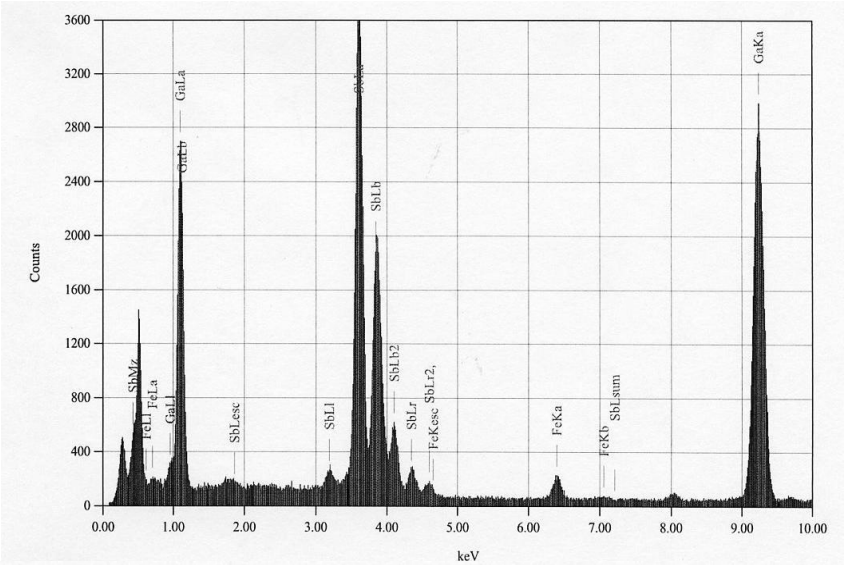

Thin Film Standardless Standard Quantitative Analysis
Fitting Coefficient : 0.2309

Element	(keV)	Mass%	Counts	Error%	Atom%	Compound	Mass%	Cation	K
Fe K	6.398	1.44	2529.94	0.13	2.46				0.3986
Ga L	1.098	34.58	20456.37	0.01	47.36				1.1869
Sb L (Ref.)	3.604	63.98	44918.98	0.01	50.18				1.0000
Total		100.00			100.00				

Fig. 6. EDX spectrum on the thick area of the specimen obtained from an area located on the boundaries between the crystal domains.

These results considerably confirm and support the Mössbauer data and the related location of iron containing phases at grain boundaries. This presence indeed could not substantially influence the physical properties of the GaSb single crystal doped with a fairly small amount of Fe.

4. Conclusions

A single crystal of GaSb doped with 3 at % Fe was prepared by the Czochralski method in order to be investigated using Mössbauer spectroscopy. The microscopy data, imperiously requested by MS results, revealed the formation of large monocrystalline domains (GaSb) with optically visible boundaries (of a few microns) and holes between them. The EDX spectrum of the boundary area granted the presence of 2.5 at % Fe concentration, while the Fe amount in the large domains of the crystal was less than 0.3 at %.

The first output from Mössbauer data was that Fe does not substitute any of the elements constituting the GaSb single crystal. The Fe is present as binary ($FeGa_3$) and ternary $Fe_3(Ga_{1-x}Sb_x)_2$ phases on the boundary sites between crystallites. Some Mössbauer parameters, such as isomer shift, line width, and fields at nucleus, are specifically influenced by the ratio between Ga and Sb in the investigated Fe-containing compounds.

References

[1] Physics of Compounds of Group IV Elements and III-V Compounds. Ed by Madelung O., Landolt-Bornstein New Series, Group 3. Mir.Moscow, 1967.
[2] A. G. Milnes and A. Y. Polyakov, Gallium antimonide device related properties, Solid-State Electron. 36, 803 (1993).
[3] P. S. Dutta, H. L. Bhat and V. Kumar, The physics and technology of gallium antimonide: An emerging optoelectronic material, J. Appl. Phys. 81, 9, 5821 (1997).
[4] H. Ohno, Making, Nonmagnetic Semiconductors Ferromagnetic, Science, 281, 5379, 951 (1998).
[5] G. Schmidt, D. Ferrand, M. Molenkamp, A. T. Filip, and van B. J. Wees, Phys. Rev. B, 62, R4790 (2000).
[6] H. Okamoto, The Fe-Ga (Iron-Gallium) system. ASM Int. Bull. Alloy Phase Diagrams, 11, 6, 576 (1990).
[7] H. Okamoto. Fe-Ga (Iron-Gallium) Section III: Suppl. Lit. Rev. J. Phase Equil. Diff. 25, 1, 100 (2004).
[8] H. Okamoto: "Fe-Sb(Iron-Antimony)" Phase Diagrams of Ternary Iron Alloys, ed., ASM International, Materials Park, OH, 366-370 (1993).
[9] K. W. Richter and H. Ioser, J.Alloys Comp., 247, 247 (1997).
[10] H. Holseth and A. Kjekshus, Acta Chimica Scand. 23, 9, 3043 (1969).
[11] M. Sladecek, M. Miglierini, B. Sepiol, H. Ipser, H. Schicketanz, and G.Vogl, Defect Diffus. Forum, 194-199, 369-374 (2001).
[12] V. Raghavan. JPEDA 25, 85 (2004) DOI:10.1361/10549710417740.1547-7037/ASMInternational.
[13] E. E. Vogel, O. Mualin, M. A. de Orue, and J. Rivera-Iratchet, Phys. Rev. B, 44, 4, 1579 (1991-II).
[14] J. E. Wertz and J. R. Bolton, Electron Spin Resonance: Elementary Theory and Practical

Applications, New York: McGraw-Hill, 1972.
[15] Ch.S. Birkel, G. Kieslich, D. Bessas, T. Claudio, R. Branscheid, U. Kolb, M. Panthofer, R.P. Hermann, and W. Tremel, Inorg. Chem.50, 11807 (2011) dx.doi.org/10.1021/ic201940r.
[16] J.M. Borrego, J.S. Blazqueza, C.F. Conde, A. Conde, and S. Rothet, Intermetallics. 15, 193 (2007).
[17] C.L. Chien, Gang Xiao, and K.M. Unruh, Phys.Rev. B, 32, 9 5582 (1985).
[18] A. Farhan, M. Reissner, A. Leithe-Jasper, and W. Steiner, J. Phys.: Conf. Ser. 217, 012142 (2010) doi:10.1088/1742-6596/217/1/012142.
[19] M. Monciardini, L. Pareti, G. Turilli, R. Fomari, A. Paoluzia, F. Albertini,O. Moze, and G. Calestani, J. Magn. Magn. Mater. 140-144, 145 (1995).
[20] N.A. Smith, P.J. Hill, E. Devlin, H. Forsyth, I.R. Harris, B. Cockayne, and W.R. MacEwan, J. Alloys Comp. 179, 111 (1992).
[21] G. Weyer, Hyperfine Interact, 177, 1 (2007). DOI10.1007/s10751-008-9607-y.
[22] R. Hu, R.P. Hermann, F. Grandjean, Y. Lee, J.B.Warren, V.F. Mitrović, and C. Petrovic, Phys. Rev. B, 76, 224422-1 (2007). doi: 10.1103/PhysRevB.76.224422.
[23] R.A. Pruitt, W. Marshall, and C.M. O'Donnell, Phys. Rev. B, 2, 7, 2383 (1970).
[24] A. Ionescu, C.A.F. Vaz, T. Trypiniotis, G.M. Gurtler, H. Garcia-Miquel, J.A.C. Bland, M.E. Vickers, R.M. Dalgliesh, S. Lanridge, Y. Bugoslavsky, Y. Miyoshi, L.F. Cohen, and K. R.A. Ziebeck, Phys. Rev. B, 71, 094401 (2005).
[25] H. Ohno, A. Shen, F. Matsukura, A. Oiwa, A. Endo, S. Katsumoto, and Y.Iye, Appl. Phys. Lett. 69, 363 (1996). http://dx.doi.org/10.1063/1.118061.
[26] C.T. Foxon, R.P. Campion, K.W. Edmonds, L.Zhao,K. Wang, N.R.S. Farley, C.R. Staddon, and B. Gallagher, J. Mater. Sci.: Mater. Electron., 15, 11, 727 (2005). doi:10.1023/BJMSE.0000043420.48864.072004.
[27] T. Sasaki, S. Sonoda, Y. Yamamoto, K. Suga, S. Shimizu, K. Kindo, and H. Hori, J. Appl. Phys. 91, 7911 (2002). dx.doi.org/10.1063/1.1451879.
[28] V.I. Shaposhnikov and N.A. Sobolev, J. Phys. Condens. Matter, 16, 1761 (2004).
[29] S.Dr. Derek, In the book: Springer Handbook of Electronic and Photonic Materials, Ed. by Safa Kasap Prof., Peter Capper Dr. 2007, Chapter 6. Diffusion in Semiconductors, pp.121-135. Doi:10.1088/0953-8984/16/10/008.
[30] A. Wolska, K. Lawniczak-Jablonska, M.T. Klepka, A. Barcz, A. Hallen, and D. Arvanitis, Acta Phys. Pol. A, 117 2, 286 (2010).
[31] R.V. Pound and G.A. Rebka, Phys. Rev. Lett. 3, 439 (1959), doi:10.1103/PhysRevLett.3.439.
[32] S. Deputier, N. Barrier, R. Guerin, and A. Guivarch, J. Alloys Comp., 340, 132 (2002.
[33] D.R.S. Somauajulu, M. Sarkar, N.V. Ptel, K.C. Sebastian, and M. Chandra, Hyperfine Interactions 136/137, 424-431 (2001).
[34] T.Yu. Kiseleva, E.E. Levin, A.A. Novakova, S.A. Kovaleva, T.F. Grigoreva, A.P. Barinova, and N.Z. Lyakhov, Proc. Tenth Israeli-Russian Bi-National Workshop 2011 "The Optimization of Composition, Structure and Properties of Metals, Oxides, Composites, Nano- and Amorphous Materials," Jerusalem, Israel, June 20-23, 2011, p.1–9.
[35] C. Greaves, E.J. Devlin, N.A. Smith, I.R. Harris, B. Cockayne, and W.R. MacEwan, J. Less Common Met. 157, 315 (1990).
[36] R. Harris, N.A. Smith, E. Devlin, B. Cockayne, W.R. MacEwan, and G. Longworth, J. Less Common Met. 146, 103 (1989).
[37] G.L. Whittle, P.E. Clark, and R. Cywinski, J. Phys. F :Metal Phys.10, 2093 (1980).

[38] K. Umeo, Y. Hadano, S. Narazu, T. Onimaru, M.A. Avila, and T. Takabatake, Phys. Rev. B, 86, 144421 (2012).
[39] J. Steger and E. Kostiner, J. Solid State Chem. 5, 131 (1972).
[40] P.J. Picone and P.E. Clark, J..Magn. Magn. Mater. 12, 233 (1979).
[41] P.J. Picone and P.E. Clark, J. Magn. Magn. Mater. 25 140 (1981).
[42] N. Kawamiya, K. Adachi, J. Phys. Soc. Jpn. 55, 2, 634 (1986).
[43] N. Kawamiya, K. Adachi, and Y. Nakamura, J. Phys. Soc. Jpn, 33, 5, 1318 (1972).
[44] J.M. Gaudet, T.D. Hatchard, S.P. Farrell, and R.A. Dunlap, J. Magn. Magn. Mater. 320, 821 (2008).

EXPERIMENTAL AND THEORETICAL TEMPERATURE DEPENDENCES OF THE THERMOPOWER OF $Pb_{0.82}Sn_{0.18}Te$

D. Meglei and S. Alekseeva

Gitsu Institute of Electronic Engineering and Nanotechnologies,
Academy of Sciences of Moldova

(Received April 03, 2014)

Abstract

In this study, the temperature dependences of the thermopower of five samples of $Pb_{0.82}Sn_{0.18}Te$ at different carrier concentrations ($0.52 \cdot 10^{17}$ to $15 \cdot 10^{17}$ cm^{-3}) were analyzed. The results showed that the thermopower heavily depends on charge carrier concentration. At low concentrations of charge carriers, the temperature dependences of thermopower exhibit a nonmonotonic behavior and have a maximum. A two-band Gottwick model with a linear temperature term was used to interpret the experimental data. In this approximation, it is assumed that a Lorentz resonance takes place near the Fermi surface. This model makes it possible to determine the Fermi energy, as well as the position and width of the resonance, from experimental data.

Significant interest in studying the properties of narrow-gap semiconductors, particularly lead telluride–tin telluride single crystals, is attributed to wide possibilities of their practical use as detectors and radiation sources in the infrared spectrum, thermocouples, strain gauges, etc. At the same time, scientific interest in these materials is primarily associated with their unusual galvanomagnetic, thermomagnetic, and magneto-optical properties.

The quality requirements for the samples under study are very high in order to obtain reliable experimental results: the volume distribution of the components must be uniform, and mechanical defects must be reduced to minimum. The most effective technique for preparing homogeneous $Pb_{1-x}Sn_xTe$ single crystals is the gas-phase growth method. We have developed a special technology for gas-phase growth of single crystals using high-purity Pb, Sn, and Te of the OSCh-0000 grade as initial materials (Te was purified by multiple zone recrystallization). Microstructural and spectral studies and Hall-effect measurements have confirmed the high quality of the prepared $Pb_{1-x}Sn_xTe$ ($x = 0.18$) single crystals.

In this study, the temperature dependences of the thermopower of five $Pb_{0.82}Sn_{0.18}Te$ samples at different carrier concentrations ($0.52 \cdot 10^{17}$ to $15 \cdot 10^{17}$ cm^{-3}) have been examined. The results have shown that the thermopower heavily depends on charge carrier concentration. For low concentrations of charge carriers, the temperature dependences of the thermopower are nonmonotonic and exhibit a maximum.

Figure 1 shows the derived typical temperature dependences of the thermopower of $Pb_{1-x}Sn_xTe$ ($x = 0.18$) at different concentrations of charge carriers. Samples with a low carrier concentration exhibit the thermopower sign reversal, which is indicative of the transition to the intrinsic conduction region (curves *4* and *5* in Fig. 1). The thermopower sign reversal for samples with a lower concentration of charge carriers is observed at lower temperatures.

Generally, it is fairly difficult to calculate the kinetic coefficients in semimetals and narrow-gap semiconductors because it is impossible to strictly take into account all the factors associated with the charge transfer in the crystal owing to strong nonparabolicity of the bands and

the complex mechanism of carrier scattering. Nevertheless, experimental studies of transport phenomena in these semiconductors provide the most complete information on the kinetics of charge carriers and their energy spectrum under a wide variation in temperature and concentrations of charge carriers and impurities.

The derived experimental data were interpreted using a two-band model with a linear temperature term proposed by Gottwick [1-4]. This approach assumes that Lorentzian resonance occurs in the vicinity of the Fermi surface. This model makes it possible to determine the Fermi energy and the position and the width of the resonance from experimental data.

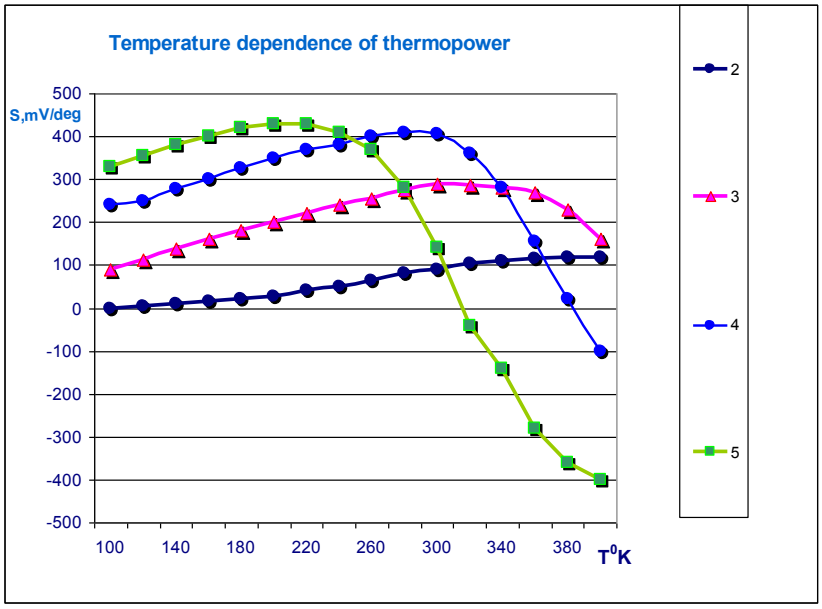

Fig. 1. Temperature dependence of the thermopower of $Pb_{0.82}Sn_{0.18}Te$ at different carrier concentrations: hole concentration, 10^{17} cm^{-3}, 77 K.

2	3	4	5
15	5.2	2.6	0.52

For theoretical analysis in terms of this model, we use the following formulas:

$$S(T) = \frac{AT}{B^2 + T^2} \tag{1}$$

$$A = \frac{2(E_0 - E_F)}{e} \tag{2}$$

$$B^2 = 3\frac{(E_0 - E_F)^2 + \Gamma^2}{\pi^2 k_B^2}, \tag{3}$$

where S(T) is the thermopower, T is the temperature, and A, B are constant coefficients.

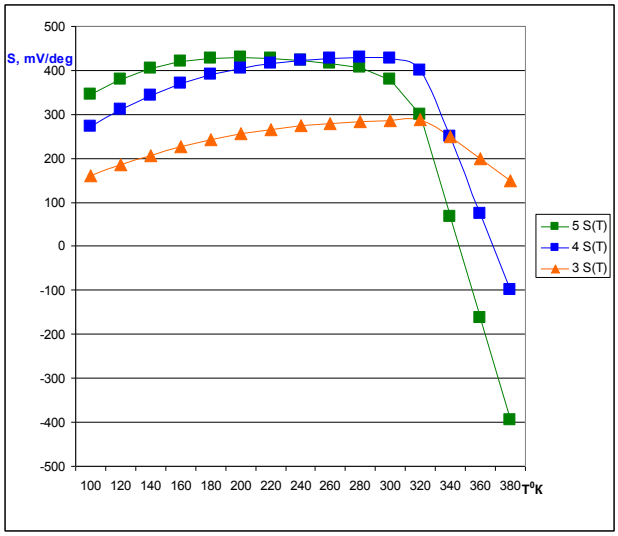

Fig. 2. Calculated temperature dependences of the thermopower of $Pb_{0.82}Sn_{0.18}Te$ at different carrier concentrations:

hole concentration,	10^{17} cm^{-3}, 77 K	
3	4	5
5.2	2.6	0.52

The table 1 lists parameters A, B, E_0, and Γ calculated by formulas (1)–(3).

Table 1. Parameters A, B, E_0, and Γ calculated by formulas (1)–(3)

	$S(T)_{max}$	B, K (B=T)	A, eV/C	E_F, eV	E_0, eV	Γ, eV
5	430	200	$5.38 \cdot 10^{17}$	0.066	0.043	0.021
4	410	280	$7.18 \cdot 10^{17}$	0.017	0.057	0.016
3	288	300	$5.40 \cdot 10^{17}$	0.03	0.043	0.0449

where C is coulomb.

The E_0 and Γ (gamma) are determined by the position of the center and the width of the resonance on the energy axis, respectively.

The resonance peak defined by formula (1) adequately describes the temperature dependence S(T). The thermopower passes through a maximum at the T = B point. Thus, we can determine B and calculate A, E_0, and Γ. The calculated temperature dependences of the thermopower of $Pb_{0.82}Sn_{0.18}Te$ at different carrier concentrations are shown in Fig. 2.

References

[1] U. Gottwick, K. Gloss, S. Horn, E. Stegiich, A. Grewe. J. Magn. Magn. Mater. 47-48, 536 (1985).
[2] Sh. R. Ghorbani. Stockholm Doctoral Dissertation, Royal Institute of Technology Solid State Physics, Department of Physics, IMIT, 2002.
[3] S. S. Ragimov and I. N. Askerzade, Zh. Tekh. Fiz. 80, 10, 150 (2010).
[4] O. S. Komarova and V. E. Gasumyants, Fiz. Tverd. Tela, 52, 4, 625 (2010).

CONDUCTIBILITY AND IRRADIATION STABILITY OF SINGLE CRYSTALS $ZnIn_2S_4$

V. Pintea[1], E. Arama[2], E. Gheorghitsa[3], A. Maciuga[1] and V. Zhitar[4]

[1] Technical University of Moldova, 168, Stefan cel Mare Blvd., MD-2004, Chisinau, Republic of Moldova
[2]State University of Medicine and Pharmacy „Nicolae Testemițeanu", 165, Stefan cel Mare, Blvd. MD-2004, Chisinau, Republic of Moldova
[3]Tiraspol State University, 5, Iablocikin str., MD-2069, Chisinau, Republic of Moldova
[4]Institute Applied of Physics ASM, 5, Academiei str., MD-2028 Chisinau, Republic of Moldova
E-mail: aramaefim@yahoo.com

(Received June 03, 2014)

Abstract

This study presents the results of investigations on the conductivity and irradiation stability of single crystals $ZnIn_2S_4$ in a wide range of incident electron energies (30–75 keV) and respective doses (10^{14}–10^{20} cm^{-2}). The possibilities of manufacturing accelerated electron detectors are explored, and their parameters are estimated. Considering that the energy values on the order of 10^2 keV are near the threshold of structural defects of intensive formation, the influence of this phenomenon on the detector parameters is subject to the analysis.

1. Introduction

The materials having semiconductor properties are quite sensitive and change their essential physical properties under the action of external radiation and elementary particles bombarding them at a high energy. Usually, under the action of external radiation or different high-energy particles in crystals, following the ionization, additional scattering centers of charge carriers appear.

Experimental and theoretical study of these processes is up-to-date in terms of characteristic stability of microelectronic devices and prevention of degradation processes in different devices made of different materials with semiconductor properties. Therefore, it is quite important to perform researches related to the influence of electron beams with energies up to 100keV on the physical properties of semiconductors. To highlight the changes occurring in optical, photoelectric and irradiation properties, optical absorption spectra and photoconductibility for nonirradiated samples and for samples irradiated with different doses of electrons at certain energies were examined. Depending on the doping element, the impurity concentration is in a range of $1.2 \cdot 10^{19}$ to $2 \cdot 10^{20}$ cm^{-3}. The growth technology for $ZnIn_2S_4$ is described in detail in [1, 2].

2. Experimental results on irradiation conductivity

This paper describes the experimental results regarding the change in photoelectric

properties and irradiation under the influence of an electron beam accelerated in ternary compounds of type $A^{II}B_2^{III}C_4^{VI}$, based on the example of typical ternary compound $ZnIn_2S_4$. For research, we chose perfect slabs in terms of defect density, with an outer surface that had a quality optical thickness of 0.20–1.0 mm, obtained from the gas phase using iodine as a carrier agent.

Irradiation conductivity was measured in vacuum at the temperature of 296 K, both under stationary and modulated conditions according to the method described in [3]. The current density of the electron beam was provided by the flow of 10^{16} $cm^{-2}s^{-1}$ particles; the bombardment energy was 30, 40, and 75 keV.

Based on the dependence of the relative resistance change R/R_0 and the current density of the electron beam for three samples of $ZnIn_2S_4$ at 40 keV (Fig. 1), one may observe that this dependence for all the samples is basically a linear function throughout the study period. The dependence between relative resistance (R/R_0) and irradiation dose at different levels of excitation of electron beam energy was also investigated. According to this dependence, it is observed that at 75 keV (curve *1*, Fig. 2), the resistance slightly decreases in a narrow range of variation of the irradiation dose. At an electron beam energy of 40 keV (curve *2)*, this transition is observed to be very slow and approximately linear; at an energy of 30 keV, the dependence on the dose is a linear function in the studied range.

For all the measurements described above, a constant conductivity of the samples in the dark was observed: 10^7–10^9 Ω. At high doses of radiation $(10^{18} \div 10^{20})$ cm^{-2}, irreversible changes of the resistance in the dark were observed, which indicates a sudden increase in the concentration of balanced charge carriers, in the volume of the single crystal (at least to the depth of penetration of the electrons of ≈ 5 μm).

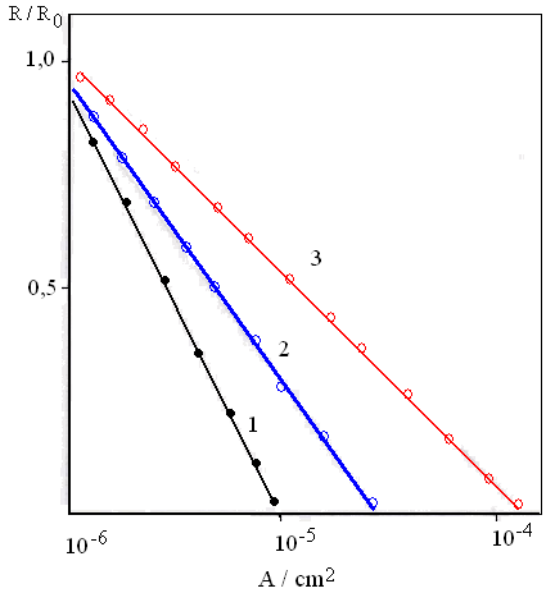

Fig. 1. Dependence of relative resistance $\Delta R/R_0$ on electron beam current for the $ZnIn_2S_4$ samples with a thickness of (*1*) 0.20, (*2*) 0.5, and (*3*) 1.0 mm.

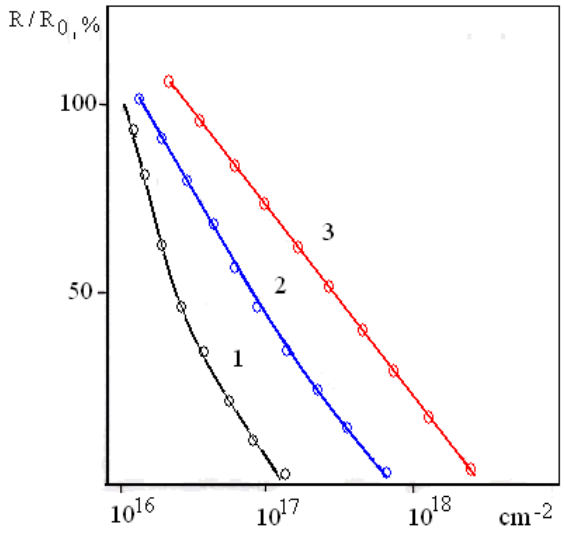

Fig. 2. Dependence of relative resistance $\Delta R/R_0$ and radiation dose at different values of the electron beam energy: (*1*) 75, (*2*) 40, and (*3*) 30 keV.

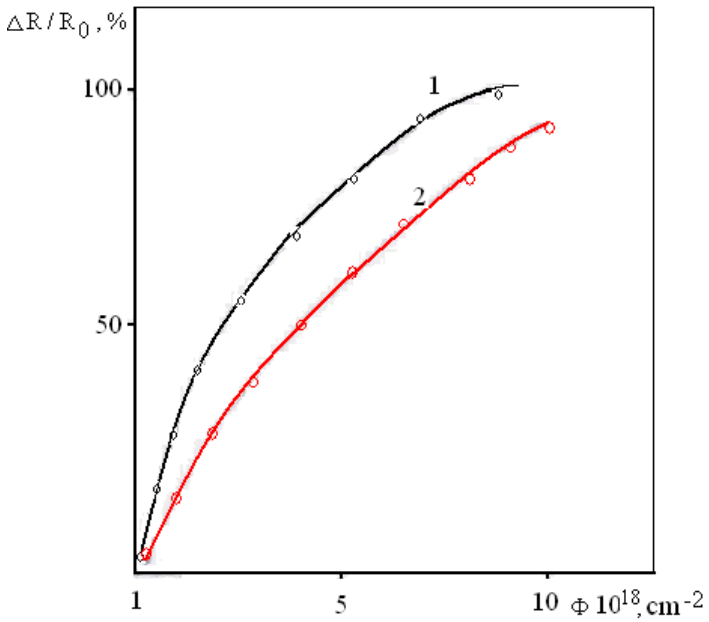

Fig. 3. Dependence $\Delta R/R_0$ of the $ZnIn_2S_4$ single crystals on the dose of irradiation, T = 296 K: (1) 50 and (2) 100 keV.

Figure 3 shows the dependence of $\Delta R/R_0$ on the dose of irradiation, where $\Delta R = R_0 - R$, R is the dark resistance of the sample after irradiation dose of $(10^{18} \div 10^{20})\ cm^{-2}$. This dependence suggests that, at a radiation dose of $10^{20}\ cm^{-2}$, the resistance in the dark becomes very small, it is approximately $10^2\ \Omega$.

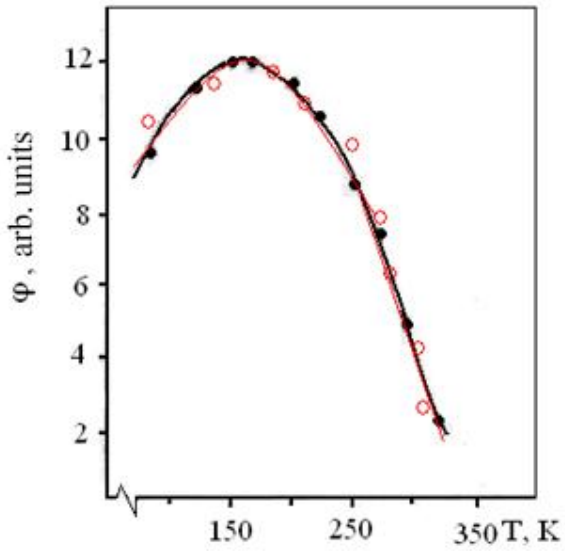

Fig. 4. Temperature dependence of the parameter φ for accelerated electrons:
1 - 50 keV; 2 - 100 keV; $5 \cdot 10^{18}$ cm^{-2}

Figure 4 represents the temperature dependence of the parameter φ for accelerated electrons with an energy of (*1*) 50 and (*2*) 100 keV at a radiation dose of $5 \cdot 10^{18}$ cm^{-2}, where $[\varphi] = \frac{\Delta R}{R_0 \Phi} =$ cm^{-2}. Following the above, it can be mentioned that the activation energy of the conductivity decreases with decreasing sample resistance.

The experimental results concerning the cathode conductivity of $ZnIn_2S_4$ single crystals suggest that, in this case, the conductivity type of the single crystals does not change. We assume that the concentration excess of balanced carriers occurs due to the activation of small donors, which are probably formed at an intensive irradiation. It was experimentally established that an increase in the dose leads to a decrease in the activation energy. For example, for a dose of $5 \cdot 10^{18}$ cm^{-2}, the activation energy was 0.006 eV, which is comparable to the ionization energy of Zn atoms between nodes Zn_i for the network ZnO according to the data 4 . Therefore, we could say that following the interaction of medium-energy electrons in $ZnIn_2S_4$, the zinc occurs between the nodes of crystalline network.

Based on previous results, we will examine some operation parameters of electron detectors with energies up to 50 keV made on the basis of $ZnIn_2S_4$. For electrons with energies of 50 keV having the number of excited electrons per second $\approx 10^{15}\ s^{-1}$, the lifetime of free carriers is approximately $\tau \approx 10^{-3}\ s$ and the interior propagation coefficient of carriers, at a calculated contact voltage of 5–20 V, achieves a value of $\approx 10^3$ [5, 6], which is obviously lower than 10^8 for the binary compounds. Being experimentally determined, the detector's power is up to 4 W · cm^{-2}, while for the detectors based on CdS and Cd Se, it is 10^{-3} W cm^{-2} 7 .

To develop detectors of high-energy particle and X-ray irradiation, it is necessary to take into account other advantages: simple manufacturing of detectors and their operation in steady-state and modulated conditions; high stability to the action of high energy electron beams and X-rays. Investigations on the development of new-type detectors or of their new modifications allow

obtaining some performances of exploitation parameters compared to the existing ones.

Having high stability at irradiation, the investigated compounds have many practical applications including for the construction of Roentgen radiation detector. In this way, the optimum parameters make it possible to use X-ray detector in medicine, ecology as well as in agriculture.

3. Experimental results on irradiation stability

As a result of experimental investigations, there have been determined photo-conductibility spectra (FC) of layered compounds $ZnIn_2S_4$ for the initial sample (Fig. 5, curve 1) and irradiated with different doses of accelerated electrons of 10^{18} cm^{-2}, 10^{20} cm^{-2} with an energy of 60 keV (curves *2* and *3*, Fig. 5). Comparison of these curves shows that, after irradiation with a dose of 10^{18} cm^{-2}, the highest spectrum moves towards the area of low energies located at 2.68 eV (curve 2, Fig. 5). On the high-energy wing of the spectrum, it is clearly perceived a platform feature at 2.85 eV. It should be noted that at a radiation dose of 10^{18} cm^{-2}, signal intensity FC in the maximum located at 2.85 eV increases, which corresponds to the fundamental absorption.

In the research, it was found that the spectrum FC of single crystals $ZnIn_2S_4$ undergoes radical changes with increasing dose of irradiation (curve 3, Fig. 5). During the irradiation of $ZnIn_2S_4$ with accelerated electrons of a 10^{20} cm^{-2} dose, the maximum value of sensitivity is shifted even further to the area of low energies and is set at 2.34 eV. On the high-energy wing of the spectrum, an additional maximum to the energy 2.63 eV is highlighted, giving way, in terms of intensity, to initial spectrum (curve 1). At high doses of radiation of 10^{20} cm^{-2}, the samples' resistance to the dark decreases irreversibly up to 10^2Ωcm and photosensitivity accordingly decreases. Similar studies were carried out on $CdGa_2S_4$ crystals and showed that, during their irradiation with a $D \approx 10^{20} cm^{-2}$ dose, significant changes in optical and radiation properties occur.

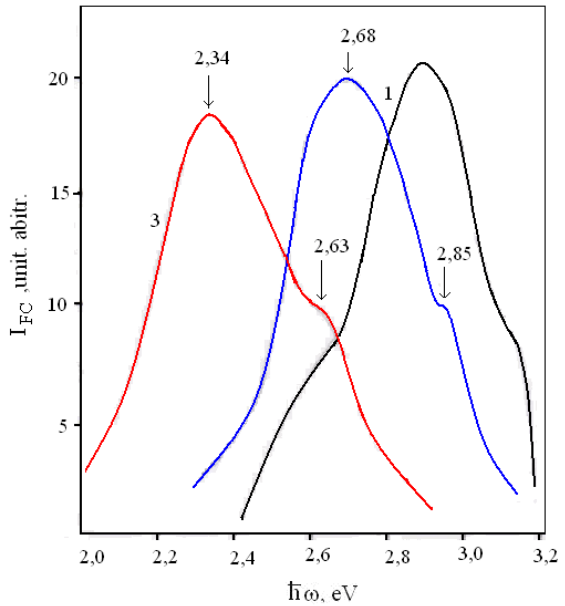

Fig. 5. Photoconductivity spectra of ternary compounds $ZnIn_2S_4$: original sample (curve 1) and samples irradiated with different doses of accelerated electrons $D \approx 10^{18} cm^{-2}$, $D \approx 10^{20} cm^{-2}$ (curves 2 and 3), with an energy of 60 keV.

4. Analysis of results

To summarize, based on these results, we could notice about high stability of optical and radiation properties of semiconductor compounds $CdGa_2S_4$ and $ZnIn_2S_4$, which is also demonstrated by the results of investigations of the optical absorption spectrum of $ZnIn_2S_4$ samples irradiated with accelerated electrons with an energy of 50 and 100 keV, respectively, at a density of electron beam of $1.5 \cdot 10^{-2}$ A $\cdot$ cm^{-2} and at a temperature of 296 K (Fig. 6). The exponential sector of the absorption spectrum can be attributed to the presence of "tails" of state densities of the conduction band conditioned by the disorder of cationic subnet. This fact is described in detail in the case of $(ZnIn_2S_4)$ 2 .

Based on the study of the bibliographic data, it can be noticed that significant changes in the properties of elementary or binary semiconductors [8] during their irradiation with electrons with energies of up to 100 keV occur starting with doses of $10^{14} \div 10^{16}$ cm^{-2}; in the case of $ZnIn_2S_4$ and $CdGa_2S_4$ compounds, essential changes in optical properties occur starting with doses higher than 10^{19} cm^{-2}. In the case of ternary semiconductor compounds, which have a energy band gap higher than 3 eV, while irradiating them with a dose of $\approx 10^{14}$ cm^{-2}, optical absorption in the ultraviolet spectrum decreases; this effect is referred to as the effect of low doses. These results correlate with the data presented in [9].

An increase in absorption is recorded at doses higher than 10^{15} cm^{-2}. The results described in this study concerning the nature of clear structure of the spectrum FC of single crystals $ZnIn_2S_4$ irradiated at a dose of 10^{18} cm^{-2}are consequences of the improvement of the state of crystal surface at the initial stage of irradiation, which is assumed to affect the recombination of free charge carriers at the sample surface.

At the same time, we find that the formation mechanism for threshold defects in layer compounds $ZnIn_2S_4$ is initiated at doses higher than 10^{18} cm^{-2}.

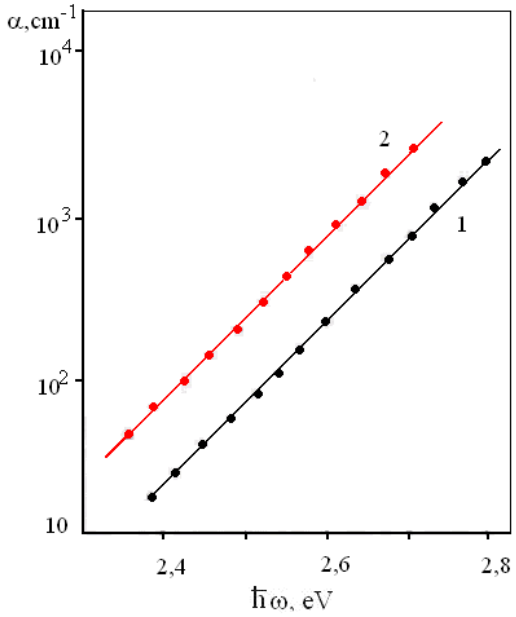

Fig. 6. Optical absorption for single crystals $ZnIn_2S_4$ irradiated with accelerated electrons: (1) 50 and (2) 200 keV, j = $1.5 \cdot 10^{-2}$ A $\cdot$ cm^{-2}; T = 296K.

5. Conclusions

1. The experimental liniar dependence of the relative rezistence of zinc thioindate on electron beam as the stimulant has shown that manganese thioindate can be used as an active element in electron X-ray detectors. A model of an X-ray and accelerated particle detector capable of operating under both steady and modular conditions has been proposed. The coefficient of internal amplification of charge carriers at a voltage of $\approx 10^3$ has been estimated. The amplification coefficient is $\approx 10^3$.

2. The conductibility and irradiation stability of $ZnIn_2S_4$ and $CdGa_2S_4$ single crystals have been studied. The study has shown that the optical and photoelectrical properties incur significant changes only for dozes higher than 10^{19} cm^{-2}. The results suggest that the studied ternary compounds have highly stable properties.

References

[1] V. F. Zhitar', E. D. Arama, A. I. Machuga, et al., Vliyanie spetsifiki i kristallicheskoi struktury na opticheskoe pogloshchenie, Voronezh, 1989, p. 8.

[2] V. F. Zhitar', E. D. Arama, S. I. Radautsan, et al., proc. VIII All-Union Conf. on crystal growth, Kharkov, 1992, vol. 1, p. 275.

[3] A. Maciuga, R. Radu, V. Pîntea, I. Stratan, Chişinău, ICMCS-2005. September 15-17, vol.1, p.204-207.

[4] V. F. Zhitar, V. I. Pavlenko, T. D. Shemyakova. Surf. Eng. and Appl. Electroch. V. 46, 6, 628 (2010).

[5] R. R. Atabekyan, V. L. Vipetskii, V. A. Gevorkyan, et al., Pis'ma ZhETF, 9, 23, 1448 (1983).

[6] Shengjie Peng, Linlin Li, Yongzhi Wu, Lin Jia, et.al., Cryst. Eng. Comm. 15, 1922 (2013).

[7] V. N. Komashenko, N. F. Mamok, G. A. Fedorus, et al., Poluprovodn. Tekh. Mikroelektron. 13, 33 (1973).

[8] V. S. Vavilov, A. E. Kiv, and O. R. Niyazov. Mehanizmy obrazovaniya i migratsii defektov v poluprovodnikakh, Nauka, Moscoe, 1981, p. 40.

[9] M. M. Mikailov, Izv. Vyssh. Uchebn. Zaved., Fiz. 7, 94 (1984).

A COMPARATIVE STUDY OF PLASMONIC EFFECTS IN ELECTROCHEMICALLY NANOSTRUCTURED $CuInS_2$ And $CuGaS_2$ CRYSTALS

V. V. Ursaki

Institute of Applied Physics of the Academy of Sciences of Moldova, Academiei str. 5, Chisinau MD-2028,
Republic of Moldova

(Received October 22, 2013)

Abstract

We investigate the differences in electrochemical nanostructuring of $CuInS_2$ and $CuGaS_2$ crystals. It is shown that thermal treatment of $CuInS_2$ crystals either in vacuum or in Zn vapors is a procedure providing necessary electrical conductivity to the as-grown high-resistivity crystals for a consequent electrochemical nanostructuring, while in $CuGaS_2$ crystals treatment in Zn vapors at temperatures higher than 700 ^oC is needed to make them suitable for electrochemical nanostructuring. Porous $CuInS_2$ structures with a uniform porosity and the pore diameter controlled by the crystal conductivity are demonstrated, while the porosity of $CuGaS_2$ structures is inhomogeneous. Possibilities of luminescence enhancement via thin Au and Cu film deposition onto nanostructured $CuGaS_2$ surfaces or ITO films onto $CuInS_2$ surfaces are also investigated.

1. Introduction

It has been demonstrated in previous works [1-3] that the surfaces of I-III-VI_2 ternary chalcopyrite materials can be nanostructured by electrochemical etching in aqueous electrolytes similarly to III-V [4–6] and II-VI [7–9] binary materials. However, there is an essential difference between electrochemical treatment of ternary and binary compounds. In contrast to binary compounds, anodization of ternary materials can be carried out only at low applied voltages of less than 1 V, since electrochemical treatment at higher voltages leads to the decomposition of these materials. The approach of electrochemical nanostructuring of semiconductors proves to be a strategy for a variety of applications. Particularly, the advent of methods for controlling inorganic materials on the nanometer scale opens new opportunities for the development of future generations of solar cells [10]. Solar cell technologies, using I–III–VI_2 direct band-gap chalcopyrite semiconductors as the absorber layer, have attracted great interest [11]. Solar cell technologies using I–III–VI_2 chalcopyrite semiconductors have made rapid progress in recent years. A conversion efficiency of around 20% has been reached with $Cu(In,Ga)Se_2$ thin-film solar cells [12, 13]. However, these solar cells contain a toxic component of Se. On the other hand, $CuInS_2$ does not contain toxic elements in comparison with $CuInSe_2$, while its band gap energy of about 1.5 eV matches well the solar spectrum for energy conversion, and it demonstrates a large absorption coefficient of 10^5 cm^{-1}. The advantages of nanostructured absorber layers in solar cells consist in trapping of light inside the cell instead of reflecting back out. Further boosting the performance of solar cells can be realized by combining nanostructuring with plasmonic effects by deposition of metallic nanostructures.

The goal of this paper is to perform a comparison of the effects of electrochemical

treatment upon $CuInS_2$ and $CuGaS_2$ crystals and to study the plasmonic effects in nanostructured layers of these materials covered with thin metallic films.

2. Sample preparation and experimental details

$CuInS_2$ and $CuGaS_2$ single crystals were grown by chemical vapor transport (CVT) in a closed system using iodine as a transport agent. The polycrystalline material, preliminary synthesized in iodine atmosphere from a stoichiometric mixture of the elemental constituents, was used as the raw charge in the CVT. The iodine concentration was approximately 5 mg cm^{-3}. The system was cooled down slowly at a rate of 10 °C/h to avoid straining of the crystals after crystal growth.

Electrochemical treatment for nanostructuring was performed in an electrochemical cell as described elsewhere [6]. A four Pt electrode configuration was used: a reference electrode in the electrolyte, a reference electrode on the sample, a counter electrode, and a working electrode. The area of the sample exposed to the electrolyte solution was 0.1 cm^2. The anodic etching was carried out in a 5% $HCl:H_2O$ electrolyte in the potentiostatic regime at room temperature. The resulting morphology of the etched samples was studied using a TESCAN scanning electron microscope (SEM). The photoluminescence (PL) was excited by a LD Pumped all-solid state MLL-III-532 laser, or by the 476.5 nm line of an Ar laser, and analyzed through a double spectrometer. The spectra were measured with a FEU 106 photomultiplier in a spectral range of 1.6–2.6 eV, with a FEU 62 photomultiplier in a spectral range of 1.1–1.6 eV, and with a PDA10DT InGaAs photodetector in a spectral range of 0.5–1.1 eV. The resolution was better than 1 meV. The samples were mounted on the cold station of a LTS-22-C-330 cryogenic system.

3. Results and discussions

The as-grown $CuInS_2$ and $CuGaS_2$ crystals are n-type with resistivity on the order of 10^6-10^7 Ω·cm and $>10^7$ Ω·cm, respectively. It is known that low resistivity crystals are required for nanostructuring by electrochemical treatment. For decreasing the resistivity of the as-grown $CuInS_2$ and $CuGaS_2$ crystals, a few types of thermal treatment have been applied. $CuInS_2$ crystals with the resistivity down to 0.3 Ω·cm were produced by annealing of crystals in vacuum. A similar treatment of $CuGaS_2$ crystals reduced their resistivity only to 10^4–10^5 Ω·cm. For a further decrease of resistivity, the samples were subjected to annealing in Zn vapors. The samples were subjected to annealing during 30 h. The parameters of samples as a function of the technological conditions are presented in Tables 1 and 2.

The PL spectrum of the as-grown grown $CuInS_2$ (sample #1) is presented by curve *1* in Fig. 1a. The spectrum consists of a few near-band-edge lines and a deeper PL band at 1.4 eV followed by unresolved phonon replicas. Among the near-band-edge lines, two most intensive lines at 1.52 and 1.53 eV are attributed to the recombination of bound excitons [14, 15], while the band at higher photon energies (1.537 eV) is due to the recombination of free excitons [14, 15]. The band at 1.4 eV was previously attributed to a free-to-bound optical transition with In interstitial (In_i) as a donor center involved in this transition.

Annealing of $CuInS_2$ crystals in vacuum at 700°C leads to the quenching of the exciton lines and the emergence of a new broad and asymmetric PL band in the near-band-edge region (at 1.55 eV). This PL band is attributed to the band-to-band transitions, since the shift of the

maximum and its broadening correlates with the shift of the equilibrium Fermi level [1–3]. A similar behavior was observed for the near-band-edge PL band in $CuInSe_2$ crystals subjected to a similar thermal treatment [2] and in ZnSe single crystals annealed in a Zn melt containing an Al impurity [16]. Note that the near-band-edge PL band is shifted to lower photon energies in samples annealed in Zn vapors as compared to samples annealed in vacuum [1, 2]. This behavior is explained in terms of the theory of heavily doped semiconductors [17, 18]. According to this theory, the asymmetric shape of PL bands is caused by potential fluctuations in the material due to the high concentrations of charged defects.

Table 1. Electrical parameters of $CuInS_2$ crystals subjected to different thermal treatment

$CuInS_2$	As grown, #1	Annealed in vacuum at 500°C, #2	Annealed in vacuum at 600°C, #3	Annealed in vacuum at 700°C, #4	Annealed in Zn vapors at 600°C, #5	Annealed in Zn vapors at 700°C, #6
ρ ($\Omega \cdot$ cm)	$10^6 \div 10^7$	20	1	0.3	0.1	0.05
n (cm^{-3})	-	$1 \cdot 10^{15}$	$3 \cdot 10^{16}$	$1.4 \cdot 10^{17}$	$6 \cdot 10^{17}$	$3 \cdot 10^{18}$
μ ($cm^2/V \cdot s$)	-	310	190	140	100	40

Table 2. Electrical parameters of $CuGaS_2$ crystals subjected to different thermal treatment

$CuGaS_2$	As grown, #1	Annealed in vacuum at 500°C, #2	Annealed in vacuum at 600°C, #3	Annealed in vacuum at 700°C, #4	Annealed in Zn vapors at 600°C, #5	Annealed in Zn vapors at 700°C, #6
ρ, ($\Omega \cdot$ cm)	$> 10^7$	$> 10^7$	$> 10^6$	$10^4 \div 10^5$	8	0.2
N, (cm^{-3})	-	-	-	-	$5.8 \cdot 10^{15}$	$3.3 \cdot 10^{17}$
μ, ($cm^2/V \cdot s$)	-	-	-	-	130	90

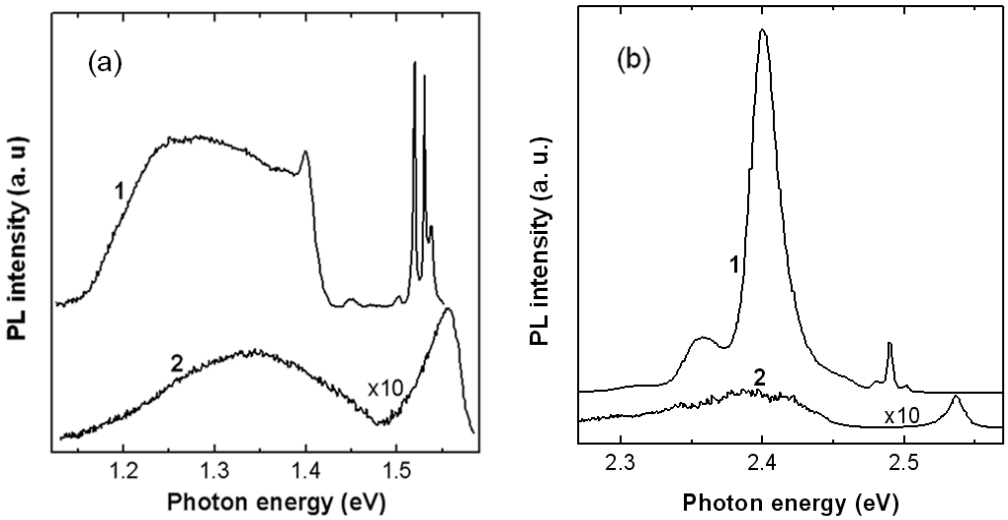

Fig. 1. (a) PL spectra of $CuInS_2$ crystals with numbers #1 (curve *1*) and #4 (curve *2*); (b) PL spectra of $CuGaS_2$ crystals with numbers #1 (curve *1*) and #6 (curve *2*). The spectra were measured at $T = 10$ K.

The PL spectrum of the as grown $CuGaS_2$ (sample #1) is presented by curve *1* in Fig. 1b. This spectrum is dominated by a strong PL band at 2.4 eV which has been previously attributed to donor acceptor pair (DAP) recombination [19, 20]. The weaker band at 2.357 eV is most probably a phonon replica of this DAP recombination. A series of three lines observed at higher photon energies is due to recombination of excitons. The line at 2.501 eV is due to recombination of free excitons [21]. The line at 2.490 eV is in the region of neutral donor bound exciton recombination [19, 22], while the band at 2.481 eV is in the region of excitons bound to neutral acceptors [21].

Unlike $CuInS_2$, annealing of $CuGaS_2$ crystals in vacuum at 700^{o}C or in Zn vapours at 600^{o}C leads only to a decrease in the luminescence intensity and broadening of the lines related to the recombination of bound excitons and to the disappearance of the band associated with the recombination of free excitons. At the same time, the spectrum of $CuGaS_2$ crystals annealed in Zn vapours at 700^{o}C (curve *2* in Fig 1b) resembles the spectrum of $CuInS_2$ crystals annealed in vacuum at 700^{o}C (curve *2* in Fig 1a). It consists of a PL band at 2.537 eV in addition to the PL band at 2.4 eV associated with the DAP recombination. That means that the high energy PL band (at 2.537 eV) in these samples is caused by potential fluctuations in the material due to the high doping.

The conductivity of $CuInS_2$ samples directly influences the processes of electrochemical etching. Porous layers with uniform porosity are produced under anodization with an applied voltage of 0.8 V in aqueous HCl electrolytes. The higher is the conductivity of the sample, the smaller is the pore diameter, which varies from 50 nm to 1 μm for porous layers produced on the basis of samples from Table 1. The morphology of a layer produced on $CuInS_2$ sample #4 is shown in Fig. 2.

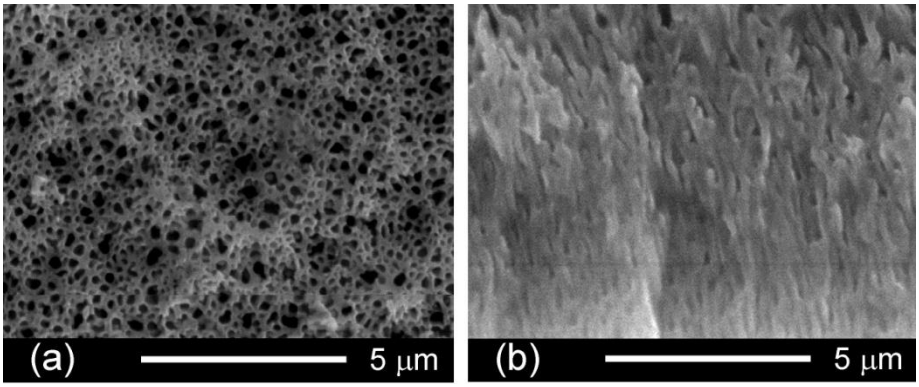

Fig. 2. Morphology of a porous layer produced on $CuInS_2$ sample #4 under anodization with an applied voltage of 0.8 V: (a) surface and (b) cross section.

Unlike $CuInS_2$, in $CuGaS_2$ crystals porosity can be introduced only in sample #6 from Table 2, since the conductivity of other samples is too low for the anodization. The morphology of the produced porous structure in this sample is non-uniform in comparison with $CuInS_2$ samples. One can see from Fig. 3a that the pore growth starts from separate regions *1* and *2*, and the pores propagate in radial directions as illustrated in Fig. 3b. When the pores propagating from regions *1* and *2* meet in region *4*, they further grow in the direction perpendicular to the initial sample surface, and a porosity illustrated in Fig. 3d is produced. At the same time, in isolated regions *3* the pores grow in a direction parallel to the sample surface, as illustrated in Fig. 3c.

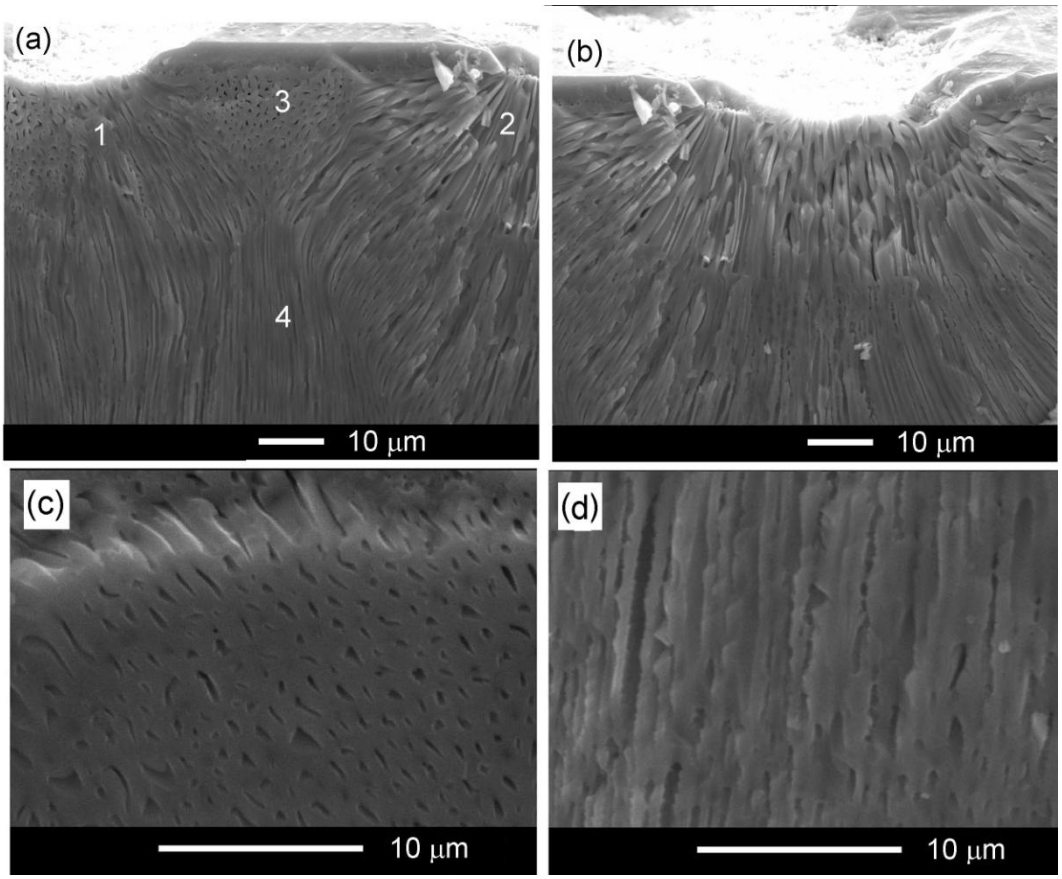

Fig. 3. (a) Morphology of a porous structure produced on $CuGaS_2$ sample #6 under anodization with an applied voltage of 0.7 V; (b) view of region *2*; (c) view of region *3*; and (d) view of region *4*.

Thin Au and Cu coatings were deposited onto nanostructured $CuGaS_2$ surfaces by means of a Cressington magnetron sputtering coater in order to investigate the plasmonic effects in metalized nanostructured ternary chalcogenides. Figure 4 illustrates the effect of deposition of thin Au and Cu films onto the surface of anodized $CuGaS_2$ sample #6. One can see that the integral PL spectrum of the as-anodized sample exhibits a PL band at 1.8 eV in addition to the above mentioned bands at 2.4 and 2.537 eV. A similar PL band was previously observed in Ga-rich $CuGaS_2$ layers [20].

One can see that deposition of thin Au films enhances the PL band at 2.4 eV and decreases the intensity of the 1.8 eV PL band. One can suggest that the enhancement of luminescence at 2.4 eV is due to surface plasmons, since the energy position of this PL band is close to the resonance energy of the surface plasmons at the $Au/CuGaS_2$ interface. On the other hand, the decrease of the intensity of the PL band at 1.8 eV is due to the absorption of the light in the metal film or due to the overall decrease of the PL intensity caused by the metal film deposition. The deposition of Cu films on the surface of the anodized $CuGaS_2$ sample, on the contrary, enhances the PL band at 1.8 eV and attenuates the PL band at 2.4 eV (Fig. 4b). That means that the resonance energy of the surface plasmons at the $Cu/CuGaS_2$ interface is closer to the position of the 1.8-eV PL band.

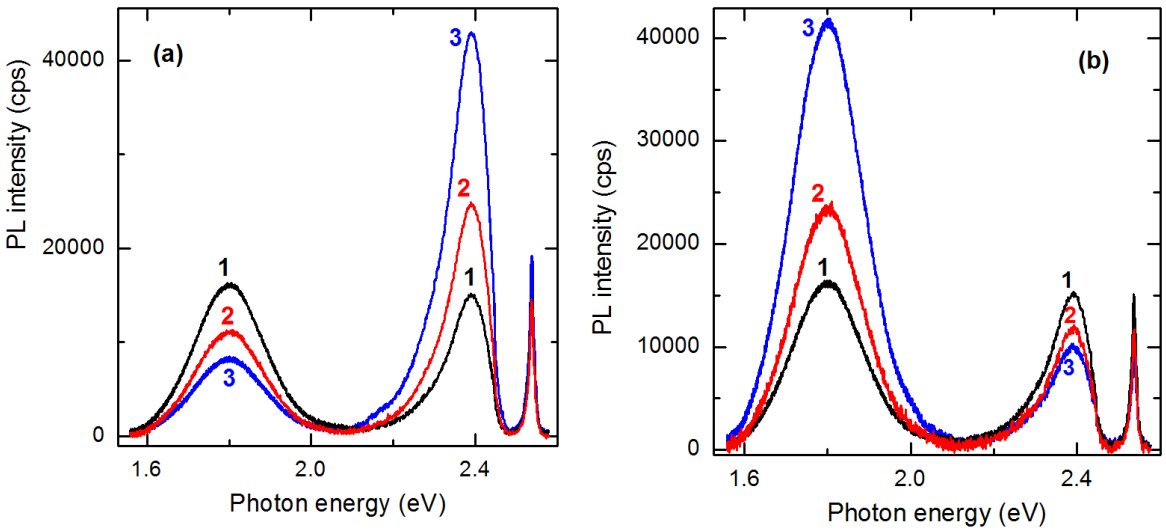

Fig. 4. (a) Low temperature (10 K) PL spectra of $CuGaS_2$ sample #6 after anodization (curve *1*), and after covering with Au films with a thickness of 5 (curve *2*) and 10 nm (curve *3*). (b) Low temperature (10 K) PL spectra of $CuGaS_2$ sample #6 after anodization (curve *1*) and after covering with Cu films with thickness of 5 (curve *2*) and 10 nm (curve *3*).

The influence of deposition of a conducting layer on the luminescence spectra was also investigated in porous $CuInS_2$ layers. No PL enhancement was observed after the deposition of Cu or Au films. On the contrary, the luminescence intensity decreased after the deposition of a metal film. An opposite effect was observed after the deposition of ITO films by a spray pyrolysis method described elsewhere [23]. Figure 5 shows the integral PL spectrum of nanostructured $CuInS_2$ sample #4. Several PL bands are observed in the low photon energy spectral interval in addition to the above mentioned bands at 1.3–1.4 and 1.55 eV.

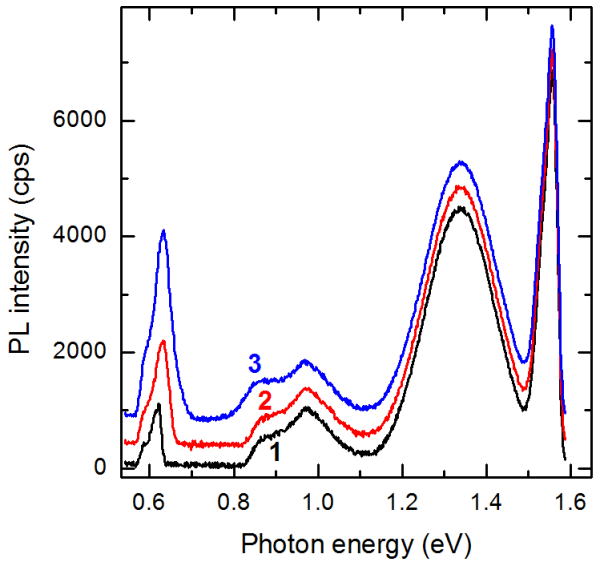

Fig. 5. Low temperature (10 K) PL spectra of $CuInS_2$ sample #4 after anodization (curve *1*) and after covering with ITO films with thickness of 5 (curve *2*) and 10 nm (curve *3*).

The PL bands at 0.87 and 0.97 eV have been previously assigned to the recombination within a deep-donor–deep-acceptor DD-DA complex. The underlying model was that these two bands are formed via a donor-acceptor pair recombination between pairs of the closest neighbors and between pairs of the next-closest neighbors, respectively [24]. The most long-wavelength band at 0.63 eV has been associated with a deep exciton bound to isoelectronic deep-donor–deep-acceptor pairs [24].

One can see from Fig. 5 that the infrared luminescence of the nanostructured $CuInS_2$ sample is enhanced by the thin ITO film deposition, and the luminescence intensity increases with an increase in the film thickness from 5 to 10 nm. The longer the wavelength of the PL band, the more prominent the luminescence enhancement. This effect suggests that the PL enhancement is again due to surface plasmons which exhibit a wide resonance at the ITO/$CuInS_2$ interface.

4. Conclusions

The results of this study demonstrate that porous $CuInS_2$ structures with a uniform porosity and the pore diameter controlled by the crystal conductivity can be produced by electrochemical treatment in an aqueous HCl containing electrolyte. The production of these structures is possible due to the control of the electrical resistivity in a range of 10^6–10^7 to 0.05 $\Omega \cdot$ cm by treatment either in vacuum or in Zn vapors at different temperatures. In contrast to this, only treatment in Zn vapors at temperatures above 700^{o}C provides a desired conductivity for $CuGaS_2$ crystals for the application of electrochemical nanostructuring, and the porosity of the structures produced in these crystals is non-uniform. A correlation exists between the material conductivity controlled by technological procedures and the photoluminescence spectra in both $CuInS_2$ and $CuGaS_2$ compounds. The luminescence of as-grown high-resistivity crystals is dominated by emission bands due to recombination of excitons and donor–acceptor pairs, while the near-bandgap PL spectra of highly doped crystals produced by annealing in Zn vapors at high temperatures consist of an emission band caused by potential fluctuations in the material due to the high concentrations of charged defects. The deposition of thin Cu films on nanostructured $CuGaS_2$ surfaces enhances the photoluminescence in a region of 1.8 eV, while Au films lead to the enhancement of luminescence in a region of 2.4 eV. Metallic coatings of Cu or Au have no positive effects on the photoluminescence of $CuInS_2$; on the contrary, the luminescence intensity is decreased by coatings. At the same time, the infrared luminescence of nanostructured $CuInS_2$ samples is enhanced by the deposition of a thin ITO film. These effects are attributed to the excitation of surface plasmons at the Cu/$CuGaS_2$, Au/$CuGaS_2$, or ITO/$CuInS_2$ interfaces.

Acknowledgments. This work was supported by the Academy of Sciences of Moldova, project 11.817.05.03A. The author would like to thank D. Sherban for the deposition of ITO coatings and M. Enachi for the deposition of metallic coatings on surfaces of the investigated samples.

References

[1] E. Monaico, V. Ursaki, V. Zalamai, A. Masnik, N. Syrbu, and A. Bullacu, Proc. 7th Int. Conf. Microelectron. Computer Sci., Chisinau, 2011, p. 139.
[2] V. V. Ursaki, Mold. J. Phys. Sci. 11, 312 (2012).
[3] V. V. Ursaki, Mold. J. Phys. Sci. to be published.
[4] H. Föll, S. Langa, J. Carstensen, M. Christophersen, and I. M. Tiginyanu, AdvanceMaterials, 15, 183 (2003).
[5] S. Langa, J. Carstensen, M. Christophersen, K. Steen, S. Frey, I. M. Tiginyanu, and H. Föll, J. Electrochem. Soc, 152 _8_ C525-C531 _2005.
[6] S. Langa, I. M. Tiginyanu, J. Carstensen, M. Christophrsen, and H. Föll, Appl. Phys. Lett., 82, 278 (2003).
[7] E. Monaico, V. V. Ursaki, A. Urbieta, P. Fernández, J. Piqueras, R. W. Boyd and I. M. Tiginyanu, Porosity induced gain of luminescence in CdSe. Semicond. Sci. and Technol. 19, L121-L123 (2004).
[8] I. M. Tiginyanu, E. Monaico, V. V. Ursaki, V. E. Tezlevan, and Robert W. Boyd, Appl. Phys. Lett. 86, 063115 (2005).
[9] E. Monaico, V. V. Ursaki, I. M. Tiginyanu, Z. Dashevsky, V. Kasiyan, and R. W. Boyd, J. Appl. Phys. 100, 053517 (2006).
[10] W. U. Hyunh, J. J. Dittmer, and A. P. Alivisatos, Science, 295, 2425 (2002).
[11] M. A. Green, K. Emery, D. L. King, S. Igari, and W. Warta, Prog. Photovoltaics 10, 355 (2003).
[12] M. Contreras, B. Egaas, K. Ramanathan, J. Hiltner, A. Swartzlander, F. Hasoon, and R. Noufi, Prog. Photovolt. 7, 311 (1999).
[13] I. Repins, M. A. Contreras, B. Egaas, C. DeHart, J. Scharf, C. L. Perkins, B. To, and R. Noufi, Prog. Photovoltaics 16, 235 (2008).
[14] I. H. Choi and D. H. Lee, Journal of the Korean Physical Society. 44, 1542 (2004).
[15] M. V. Yakushev, A. V. Mudryi, I. V. Victorov, J. Krustok, and E. Mellikov, Appl. Phys. Lett. 88, 011922 (2006).
[16] G. N. Ivanova, D. D. Nedeoglo, N. D. Nedeoglo, V. P. Sirkeli, I. M. Tiginyanu, and V. V. Ursaki. J. Appl. Phys. 101, 063543 (2007).
[17] A. P. Levanyuk and V. V. Osipov, Sov. Phys. Usp. 133, 427 (1981).
[18] B. I. Shklovskij and A. L. Efros, Electronic Properties of Doped Semiconductors, Springer, Berlin, 1984.
[19] S. Shirakata and S. Chichibu, J. Appl. Phys. 87, 3793 (2000).
[20] J. R. Botha, M. S. Branch, P. R. Berndt, A.W.R. Leitch, and J. Weber, Thin Solid Films, 6246 (2007).
[21] S. Levcenco, S. Doka, V. Tezlevan, D. Fuertes Marron, L Kulyuk, T. Schedel-Niedrig, M. Ch. Lux-Steiner, and E. Arushanov, Physica B 495, 3547 (2010).
[22] S. Shirakata, K. Saiki, and S. Isomura, J. Appl. Phys. 68, 291 (1990).
[23] A. Simashkevich, D. Serban, L. Bruc, A. Coval1, V. Fedorov, E. Bobeico, and Iu. Usatii, Mold. J. Phys. Sci. 3, 334 (2004).
[24] J. Krustok, J. Raudoja, and R. Jaaniso, Appl. Phys. Lett. 89, 051905 (2006).

ON THE DETERMINATION OF QUANTUM DOT SIZES BY SPECTROSCOPIC METHODS

I. I. Dobinda, V. I. Pavlenko, and I. V. Beloussov

Institute of Applied Physics, Academy of Sciences of Moldova,
Academiei str. 5, Chisinau, MD-2028 Republic of Moldova

(Received December 27, 2013)

Abstract

The dependences of the fundamental transition on the quantum dot size obtained experimentally at various temperatures using different measuring methods are analyzed and compared. A simple analytical relationship for approximation of these dependences is proposed. The possibility to extrapolate the results for the case of arbitrary temperature is discussed.

Semiconductor low-dimensional systems, in particular semiconductor quantum dots, attract a considerable interest due to the substantial size dependence of the energy of quantum transitions in them. This feature is promising for development of absorption and luminescent materials necessary for solving a wide range of applied problems from optoelectronic imaging and data transfer devices to biological fluorescence labels [1, 2].

Owing to the size quantization of the electron and hole states in quantum dots, the location of optical transitions depends on the nanocrystal radius. This phenomenon was observed experimentally in studies of the absorption spectra of semiconductor microcrystals dispersed in transparent dielectric matrices [3–5]. With the aim to explain the experimental results, a theory has been developed to describe the phenomena observed in semiconductors in the framework of a model of two simple direct zones of electrons and holes (with the effective masses m_e and m_h, respectively) with a parabolic dispersion dependence [6–8]. The proposed theory was constructed in terms of the effective mass approximation; that is, it was assumed that all essential lengths are large relative to the lattice constant. It was also assumed that the potential well confining the motion of electrons and holes in the quantum dot possesses spherical symmetry and infinitely high walls. Moreover, it was shown that, in the case of a strong dimensional quantization, where quantum dot radius a is considerably greater than Bohr radii a_e and a_h of the electron and hole, respectively, the electron and hole energy levels are defined by the expression $E_{l,n}^{e,h} = \hbar^2 k_{l,n}^2 / 2m_{e,h}$, where $k_{l,n} = \varphi_{l,n} / a$, and $\varphi_{l,n}$ is a universal set of numbers that do not depend on a. In the special case $l = 0$, we obtain $\varphi_{0n} = n\pi$ ($n = 1, 2, 3, \ldots$) and, hence, $E_{0,n}^{e,h} = \hbar^2 \pi^2 n^2 / 2m_{e,h} a^2 \propto a^{-2}$. Since for small a the distance between the energy levels is large, the electron - hole Coulomb interaction in the first order approximation was neglected.

It was shown that, due to the dimensional quantization of the electron and hole levels, a series of discrete lines should be observed in the interband light absorption where $\hbar\omega_{0,1} = E_g + \hbar^2 \pi^2 / 2\mu a^2$ is the absorption threshold value. Here, E_g is the forbidden gap of the bulk semiconductor and $\mu = m_e m_h / \left(m_e + m_h\right)$ is the reduced mass. The complex structure of the valence band and nonparabolicity of the conduction band in semiconductor quantum dots were taken into account in [9-15] where the effective mass approximation was also used. It was

demonstrated that, in this case, the transitions forbidden in the framework of a simple parabolic model appear.

The electron–hole Coulomb interaction for $a_h < a < a_e$ ($a_{e,h} = \hbar^2 \varepsilon / \mathrm{m}_{e,h} e^2$ are the Bohr radii of the electron and hole, respectively; ε is the dielectric constant, and e is the electron charge) was taken into account in the adiabatic approximation [6]. It was assumed that the energy of the electron motion considerably exceeds the energy of motion of the heavy hole; therefore, the electronic potential acting on the hole can be considered as averaged over the electron motion. It was shown that, if the Coulomb interaction is taken into account, each line in the absorption spectrum transforms into a series of close lines. In this case, the frequency of the fundamental transition $\omega_{0,1}$ acquires negative correction $\propto a^{-1}$ and positive correction $\propto a^{-3/2}$. Therefore, the Coulomb interaction becomes notable for quantum dots with small radii. The endeavors were made in [16-23] and other works to take into account the Coulomb interaction of the electron and hole in detail.

In some of the aforementioned papers (for example, [9, 21]), the finiteness of the potential barrier that confines the motion of the electron and hole in the quantum dot was taken into account. Here the barrier height served as an adjustable parameter for a better compliance of the theoretical dependences and experimental data. Since real quantum dots are always surrounded by a dielectric medium, the polarization boundary effects were also taken into consideration [24, 25].

Despite the fact that many experimental results related to the optical properties of semiconductor quantum dots were qualitatively explained, the theory for small-size dots is in general developed worse than for dots with greater dimensions. In particular, the dependence of the fundamental optical transition frequency on dot radius a, which is an important theoretical result, does not sufficiently well coincide with the experimentally obtained dependence and is usually fitted to it. This is mainly associated with the fact that, in the case of small a, it is necessary to use concepts and methods of solid state physics, molecular physics, and quantum chemistry simultaneously (see, for example, [26] and references therein). Therefore, hereinafter, while discussing this dependence, we will use only the experimental data obtained in various works.

Figure 1 shows the dependences of energy $E_0\,[\mathrm{eV}]$ of the fundamental optical transition (the energy of the first excited state $1S_{3/2}1S_e$) on parameter $x = 10^4 / a^2$ [Å^{-2}] for CdSe quantum dots plotted on the basis of the experimental data published in [11, 23, 26–33].

At a first glance, it seems that various experimental results suggest us substantially different values of the quantum dot radius for the same quantum transition and, therefore, the universal dependence of the fundamental transition energy on the radius does not exist! However, one should take into consideration that the results reported in [11, 28, 30] are based on experiments performed at a temperature of 10 K, though in [23, 26, 29, 32] on the studies [27, 31, 32] performed at 300 K. The forbidden gap width and other parameters of bulk CdSe are different for various temperature values. The radii of quantum dots could be determined with insufficient accuracy. Moreover, quantum dots in various works were studied in different surrounding. Respectively, both the potential barrier height, which confines the motion of the electron and hole, and the polarization phenomena at the quantum dot surface could be different.

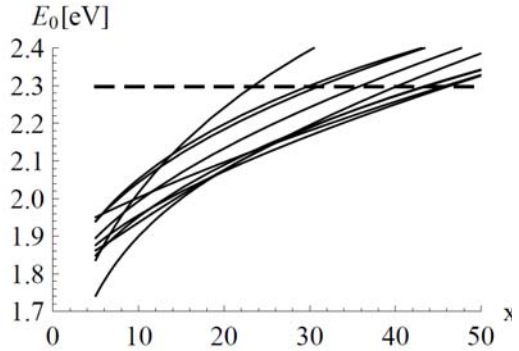

Fig. 1. Dependences of the main transition energy $E_0(x)$ vs. the CdSe quantum dot radius a taken from [11, 23, 26–33]. The horizontal dotted line corresponds to the frequency of second harmonic of YAP-laser.

Another reason the mismatch of the curves is that the graphical presentation of the experimental results is not sufficiently accurate. Actually, for example, the same experimental data are discussed in [30] and [28]. However, the data of these two papers presented at the same plot as $E_0(x)$ dependence provide two different curves!

To be sure that the universal $E_0(x)$ dependence actually exists, we will do the following. First, among all the curves presented in Fig. 1, we will choose one curve denoted as a reference one. We will approximate this dependence by a certain not very complicated analytical expression $E_0(x)$. Each of the remaining curves will be also approximated by its own $E_0(x)$ function. Then we will introduce additional parameters, which correspond to the shift of the entire curve, its extension or compression, into the resulting expressions. These parameters will be chosen so as to maximally approach all the curves to the reference one. If we succeed to do so, the universal dependence obviously exists; moreover, the pattern of deformation of the curves will probably help us to understand, why the curves initially did not coincide.

Let us discuss separately the experimental data for CdSe quantum dots, which refer to temperatures of 10 [11, 28] and 300 K [27, 31–33]. The dependences at 10 K, which are of interest for us, are presented in Fig. 2.

The $E_0^{(1)}(x)$ dependence is obtained according the experimental data [11]. Initially, we tried to draw two curves in one plot. The first curve was taken from Fig. 6 of [11], the second was drawn from Figs. 1–3 of the same paper for the strongly limited quantity of data. It was found that the energy mismatch of the curves amounted to $\sim 10 \div 80$ meV. This difference defines the accuracy of graphical presentation of the experimental data in the plots in [11].

It is evident from Fig. 2 that, though CdSe quantum dots were synthesized and characterized by the same research team [11, 28], the $E_0^{(1)}(x)$, $E_0^{(2)}(x)$, and $E_0^{(3)}(x)$ dependences are substantially different. It is easy to understand the difference between $E_0^{(1)}(x)$ and $E_0^{(2)}(x)$ if we take into consideration that different measurement techniques were used in [11] and [28]. In [11], the data were obtained using photoluminescence excitation (PLE) spectroscopy, and they were used to draw the $E_0^{(1)}(x)$ dependence. The $E_0^{(2)}(x)$ curve was obtained using the absorption spectra (Fig. 1 in [28] or Fig. 8 in [34]).

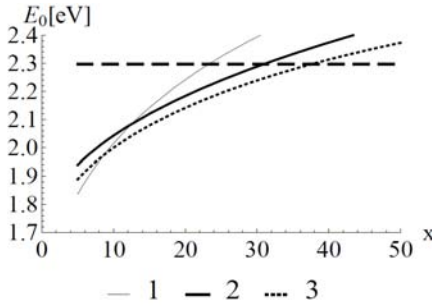

Fig. 2. Thin solid line *1* is the result fitted from [11]. It depicts the dependence of energy $E_0^{(1)}(x)$ of the main transition vs. the CdSe quantum dot radius a. Thick solid line *2* is the $E_0^{(2)}(x)$ dependence of the first maxima of the absorption spectra vs. the radius presented in Fig. 1 of [28]. Thick dashed line *3* shows the dependence $E_0^{(3)}(x)$ of the pump energies vs. the radius derived from Fig. 2 of [28].

The $E_0^{(3)}(x)$ dependence is plotted versus the laser pump energy (pump-probe experiment), as noted in [28] (Fig. 2 caption). Each mean dot radius a value corresponds to an energy value for which a "hole" is bleached at the absorption edge of a weak signal.

It is easy to see that the $E_0^{(1)}(x/4)$ curve coincides with the $E_0^{(3)}(x)$ curve with high accuracy if it is vertically shifted for a certain distance. This unexpected coincidence suggests that, though the concept of quantum dot radius a is used everywhere in [11], the dot's diameter $d = 2a$ is actually assumed there. If this is the case, the $E_0^{(1)}(x)$ dependence versus the radius in [11] should be represented as the curve shown as a dotted line in Fig. 2.

With the aim to determine the dependence of the fundamental transition energy versus the mean radius, one should use the curve $E_0^{(2)}(x)$ obtained using the absorption spectra in [28, 34]. It is shifted upwards form the curve $E_0^{(3)}(x)$ by the value of $\sim 30\,\text{meV}$. Note that, although though the author of [30] cites the data from [28], he fits his theoretical dependence to the $E_0^{(3)}(x)$ curve, but actually he should compare it with the $E_0^{(2)}(x)$ curve.

The dependences of the fundamental transition energy on the dot radius (300 K) are presented in Fig. 3, where we also show the $E_0^{(2)}(x)$ curve from Fig. 2 for comparison.

The $E_0^{(2)}(x)$ and $E_0^{(5)}(x)$ dependences follow from the experimental data of the same research team [28, 31, 34]. The first curve was obtained at 10 K, where the bulk CdSe forbidden gap amounts to $E_g = 1.84\,\text{eV}$; the second curve, at 300 K, where $E_g = 1.75\,\text{eV}$. Note that, within a wide range of parameter x values, an approximate equation $E_0^{(5)}(x) \approx E_0^{(2)}(x) - 1.84 + 1.75$ is valid. A small divergence occurs only for large x values, probably, due to the conduction band nonparabolicity. The noted equation means that many spectroscopic results obtained at a certain temperature can be extrapolated to the case of other temperature values simply by taking into consideration the temperature dependence of the forbidden gap of the bulk semiconductor.

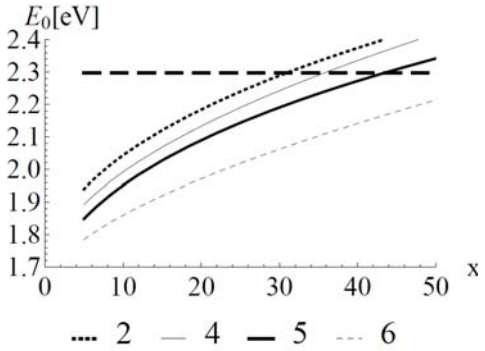

Fig. 3. Dependences of the fundamental transition energy vs. the mean quantum dot radius at 300 K: from [32, 33] (thin solid line *4*), [31] (thick solid line *5*), and [27] (dashed line *6*). The dotted line corresponds to the curve $E_0^{(2)}(x)$ from Fig. 2.

Let us transform the curves $E_0^{(4)}(x)$ and $E_0^{(6)}(x)$ is such a way that they are maximally close to each other and to the $E_0^{(5)}(x)$ curve. It is easy to see that, for not very large x values, we have $E_0^{(5)}(x) \lesssim E_0^{(4)}(x) - 0.05 \approx E_0^{(6)}(1.3x) + 0.05$. The transformed curves are presented in Fig. 4.

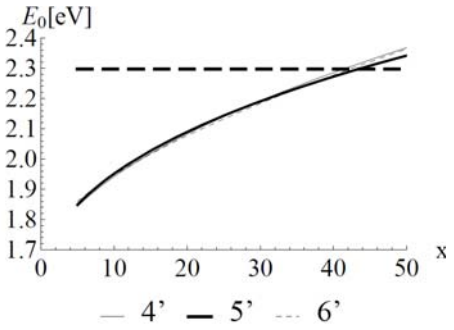

Fig. 4. Transformed curves $E_0^{(4')}(x) = E_0^{(4)}(x) - 0.05$ (thin solid line), $E_0^{(5')}(x) = E_0^{(5)}(x)$ (thick solid line), and $E_0^{(6')}(x) = E_0^{(6)}(1.3x) + 0.05$ (dashed line).

It follows from Fig. 4 that the curves $E_0^{(4)}(x)$ and $E_0^{(6)}(1.3x)$ have the same shape. Moreover, $E_0^{(4')}(x)$ and $E_0^{(6')}(x)$ are close to $E_0^{(5')}(x)$. Therefore, the divergence of the results of [32, 33] and [27] is probably associated with the fact that the radius of quantum dots in [27] by a factor of $\sqrt{1/1.3} \approx 0.9$ differs from the value given by the authors. If we evaluate the quantum dot size, for which the fundamental transition is, for example, in resonance with the second harmonic of YAP-laser, we obtain that, for each of the $E_0^{(4')}(x)$, $E_0^{(5')}(x)$, and $E_0^{(6')}(x)$ curves, the a value divergence is within 0.4 Å.

In conclusion, note that all the above curves can be sufficiently well approximated by a simple analytical dependence $E_0(x) = \alpha + \beta x + \gamma\sqrt{x}$, where α, β, and γ are certain numerical parameters.

References

[1] S. V. Gaponenko, Optical Properties of Semiconductor Nanocrystals (Cambridge, UK: Cambridge University Press, 2005).
[2] S. Nizamoglu, T. Qzel, E. Sari, and H. V. Demir, Nanotechnology 18, 065 709 (2007).
[3] A. I. Ekimov, A. A. Onushchenko, A. G. Plyukhin, and A. L. Efros, Sov. Phys.-JETP 61, 891 (1985), [Zh. Eksp. Teor. Fiz. 88, 1490 (1985)].
[4] A. I. Ekimov, A. L. Efros, and A. A. Onushchenco, Solid State Commun. 56, 921 (1985).
[5] A. I. Ekimov, A. L. Efros, M. G. Ivanov, A. A. Onushchenco, and S. K. Shumilov, Solid State Commun. 69, 565 (1989).
[6] Al. L. Efros A. L. and Efros, Sov. Phys. Semicond. 16, 772 (1982), [Fiz. Tekh. Poluprovodn., 8, 1209 (1982)].
[7] J. Xia, Phys. Rev. B 40, 8500 (1989).
[8] M. G. Bawendi, M. L. Steigerwald, and L. E. Brus, Anu. Rev. Phys. Chem. 41, 47 (1990).
[9] A. I. Ekimov, F. Hache, M. C. Schanne-Klein, D. Ricard, C. Flytzanis, I. A. Kudryavtsev, T. V. Yazeva, A. V. Rodina, and Al. L.Efros, J. Opt. Soc. Am. B 10, 100 (1993).
[10] S. W. Koch, Y. Z. Hu, and N. Peyghambarian, J. Cryst. Growth 117, 592 (1992).
[11] D. J. Norris and M. G. Bawendi, Phys. Rev. B 53, 16338 (1996).
[12] Al. L. Efros and M. Rosen, Phys. Rev. B 58, 7120 (1998).
[13] Al. L. Efros and M. Rosen, Annu. Rev. Mater. Sci. 30, 475 (2000).
[14] J. Xia and J. Li, Phys.Rev. B 60, 11540 (1999).
[15] G. B. Grigorian, E. M. Kazaryan, Al. L. Efros, and T. V. Yazeva, Sov. Phys. Sol. State 32, 1031 (1990), [Fiz. Tverd. Tela 32, 1772 (1990)].
[16] D. B. T. Thoai, Y. Z. Hu, and S. W. Koch, Phys. Rev. B 42, 11261 (1990).
[17] E. Rabani, B. Hetenyi, B. J. Berne, and L. E. Brus, J. Chem. Phys. 110, 5355 (1999).
[18] A. Franceschetti and A. Zunger, Phys. Rev. Lett. 78, 915 (1997).
[19] U. E. H. Laheld and G. T. Einevoll, Phys. Rev. B 55, 5184 (1997).
[20] J. Li and J. Xia, Phys. Rev. B 61, 15880 (2000).
[21] P. E. Lippens and M. Lannoo, Phys.Rev. B 39, 10935 (1989).
[22] T. Takagahara, Phys. Rev. B 47, 4569 (1993).
[23] L.-W. Wang and A. Zunger, Phys. Rev. B 53, 9579 (1996).
[24] Y. Z. Hu, M. Lindberg, and S. W. Koch, Phys. Rev. B 42, 1713 (1990).
[25] L. Banyai, P. Gilliot, Y. Z. Hu, and S. W. Koch, Phys. Rev. B 45, 14136 (1992).
[26] G. Pellegrini, G. Mattei, and P. Mazzoldi, J. Appl. Phys. 97, 073706 (2005).
[27] W. W. Yu, L. Qu, W. Guo, and X. Peng, Chem. Mater. 15, 2854 (2003).
[28] D. J. Norris, A. Sacra, C. B. Murray, and M. G. Bawendi, Phys. Rev. Lett. 72, 2612 (1994).
[29] S. Baskoutas and A. F. Terzis, J. Appl. Phys. 99, 013708 (2006).
[30] H. H. von Grünberg, Phys.Rev. B 55, 2293 (1997).
[31] C. B. Murray, D. J. Norris, and M. G. Bawendi, J. Am. Chem. Soc. 115, 8706 (1993).
[32] V. I. Klimov, J. Phys. Chem. B 104, 6112 (2000).
[33] V. I. Klimov, “Nanostructured matarials and nanotechnology”, (Academic Press, 2002) Chap. 13, Linear and Nonlinear Optical Spectroscopy of Semiconductor Nanocrystals, pp. 563-39.
[34] Al. L. Efros, M. Rosen, M. Kuno, M. Nirmal, D. J. Norris, and M. Bawendi, Phys.Rev. B 54, 4843 (1996).

OPTICALLY AND THERMALLY INDUCED MODIFICATIONS OF THE OPTICAL CONSTANTS OF AMORPHOUS $(As_4S_3Se_3)_{1-x}$:Sn_x THIN FILMS

O. V. Iaseniuc, M. S. Iovu, and I. A. Cojocaru

Institute of Applied Physics, Academy of Sciences of Moldova
Academiei str. 5, Chisinau, MD-2028 Republic of Moldova
E-mail: oxana.iaseniuc@gmail.com

(Received March 18, 2014)

Abstract

This paper represent the work that has been done to show optically and thermally induced changes of the optically constants in chalcogenide $(As_4S_3Se_3)_{1-x}$:Sn_x (x=0÷10 at.%) thin films. The kinetics of optically and thermally induced changes in chalcogenide films were measured by monitoring the change of optically constants, such as optical band gap E_g^{opt}, absorption coefficient α, and refractive index n, using a modified computer-controlled spectrophotometer; for data acquisition, the experimental set-up included a digital built-in PC-card PCI-1713A connected to the registration module. The relaxation of photodarkening in amorphous $(As_4S_3Se_3)_{1-x}$:Sn_x thin films, which is described by the stretched exponential function $T(t)/T(0) = A_0+Aexp[-(t-t_0)/\tau]^{(1-\beta)}$, was also investigated. Since the amorphous $(As_4S_3Se_3)_{1-x}$:Sn_x thin films exhibit photoinduced effects under the light irradiation with photon energy above the optical band gap ($h\nu \geq Eg$), they are promising materials for registration of optical and holographic information.

1. Introduction

The effect of photo-structural transformations in amorphous films of chalcogenide glasses under light irradiation and heat treatment is of great fundamental interest for the establishment of the general relationships impacting heat and light stresses on amorphous solids. This effect is characteristic of many amorphous chalcogenide materials; a lot of applications in optoelectronics and photonics have been initiated, especially as inorganic photoresists for submicron technology, as switching elements, optical fibers, etc. [1]. Of special interest is the system of chalcogenide glasses of the *As-S-S* type, which exhibits advantageous properties, such as reversibility and irreversibility of photostructural transformations, and are promising materials as registration media for holography, as photoresists, for fabrication of diffractive elements, and other optoelectronic applications [2]. Special interest in the applications of chalcogenide amorphous films is connected with doping with metal impurities, which alter the optical, photoelectrical, and transport properties of the host material [3]. The effect of foreign atom impurities in thermally deposited amorphous chalcogenide films is of practical interest as a tool for modifying optical properties and photosensitivity. According to ^{119}Sn Mössbauer spectroscopy in the As_2Se_3:Sn glassy system, new tetrahedral $Sn(Se_{1/2})_4$ and quasi-octahedral SnSe structural units can be formed, which affect the degree of photostructural transformations [4]. In addition, it has been shown that the Sn impurity introduced in the As_2Se_3 glass network reduces the photodarkening effect [5].

In the present paper, the transmission spectra of thin $(As_4S_3Se_3)_{1-x}$:Sn_x (x = 0–10 at %) amorphous films before and after light and heat treatment have been studied. The main aim of our investigation is to study the influence of heart treatment and light exposure on modification of optical constants of amorphous $(As_4S_3Se_3)_{1-x}$:Sn_x thin films. The obtained experimental results are interpreted on the basis of the structure of the Sn-doped chalcogenide glasses [5].

2. Experimental

Bulk chalcogenide glasses As_2S_3, As_2Se_3, $(As_2S_3)_{0.5}$:$(As_2Se_3)_{0.5}$, and $(As_4S_3Se_3)_{1-x}$:Sn_x ($0 \le x \le 10$ at.%) were prepared from the starting elements of 6N (As, S, Se, Sn) purity by a conventional melt quenching method. The starting component elements $As_4S_3Se_3$ and Sn were mixed in quartz ampoules and then evacuated to a pressure of $P \sim 10^{-5}$ torr, sealed and heated to a temperature of $T = 900^oC$ at a rate of 1^oC/min. The quartz tubes were held at this temperature for 48 h for homogenization and then slowly quenched in the disconnected furnace.

For the optical measurements, the thin-film samples with a thickness of $d = 1.5 \pm 0.02$ μm were prepared by flash thermal vacuum evaporation of the synthesized initial glasses onto glass substrates held at $T_{subs} = 100^oC$. For optical transmission spectra measurements, a Specord UV/VIS (λ = 300–800 nm) and a Specord 61 NIR instruments (λ = 800–3500 nm) (CARL ZEISS, Jena) and a Spectrum 100 FTIR Spectrometer (PerkinElmer) (λ = 1280–25000 nm) were used. For calculation of the optical constants from the transmission spectra, we used the method proposed by Swanepoel and Tauc [6, 7] and the PARAV-V1.0 computer program (www.chalcogenide.eu.org) [8]. To study the red shift edge of the transmission spectra of thin films, a halogen lamp (λ = 400–700 nm, with infrared filter, with a light density of 2×10^4 Lx) was used as a source of light exposure. To initiate photostructural transformations in thin film samples, continuous He-Ne lasers (λ = 633 nm, P = 0.6 mW and λ = 540 nm, P = 0.75 mW) were used. The relaxation of the transmission curves was measured *in-situ* both at λ = 630 nm and λ = 540 nm wavelengths during the light exposure. For data acquisition, the experimental set-up included a digital built-in PC-card PCI-1713A connected to the registration module. Thermally induced modifications of the optical constants of amorphous $(As_4S_3Se_3)_{1-x}$:Sn_x thin films by heat treatment at $T_{ann} = 100^oC$ during time t = 30 min with different amounts of Sn were studied.

3. Results and discussion

The mid-IR transmission spectra of As_2S_3 and some $As_4S_3Se_3$:Sn_x bulk glasses are shown in Fig. 1 and, as in the case of vitreous As_2S_3 doped with metals [9], are characterized by several well-resolved absorption bands. For vitreous As_2S_3, these bands are located at frequencies of ν = 3500 cm^{-1} (H_2O), ν = 3218 cm^{-1} (S-H)ν = 2482 cm^{-1} (S-H,Se-H), ν = 1857 cm^{-1} (As-H), ν = 1494 cm^{-1} (H_2O), and ν = 1003 cm^{-1} (AsO-As_2O_3. The characteristic absorption bands for pure As_2S_3 at ν = 5190, 3617, 3522, 1857, and 1597 cm^{-1} are significantly reduced upon doping with Sn [10]. At the same time, for the $(As_4S_3Se_3)_{0.98}$:$Sn_{0.02}$ glass, additional absorption bands appear. The observed changes upon doping in the mid infrared region are most likely related to interactions of a portion of the introduced metal ion impurities with the inherent impurities of the host glass, such as hydrogen and oxygen atoms. These interactions result in the reduction of the relative intensity of bands associated with O-H, S-H, As-O, and As-H bonds in the parent glass.

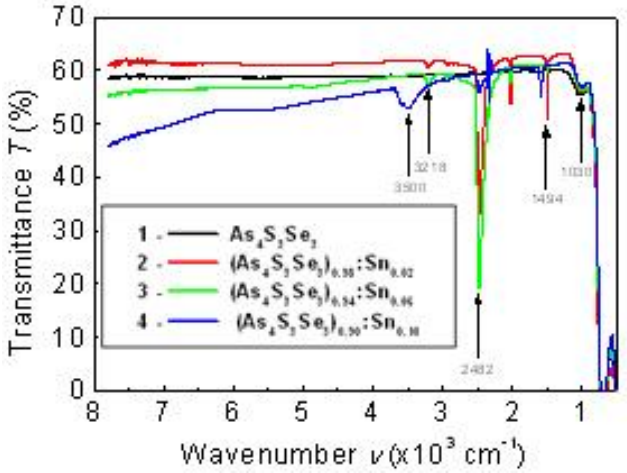

Fig. 1. Transmission spectra of some bulk samples of $As_4S_3Se_3$:Sn_x glasses.

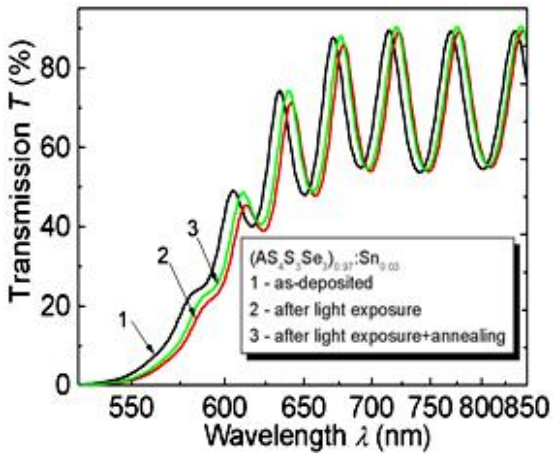

Fig. 2. Transmission spectra of the amorphous $(As_4S_3Se_3)_{0.97}$:$Sn_{0.03}$ thin film (1) as-deposited, (2) after light exposure, and (3) after annealing.

Under light exposure, a red shift of the fundamental absorption edge was observed (Fig. 2). It is evident from the transmission spectra (Figs. 2, 3) that heat treatment and light exposure of the samples lead to a slight reverse shift of the absorption edge in the initial position. Moreover, annealing of vitreous as-deposited thin films of $(As_4S_3Se_3)_{1-x}$:Sn_x does not change the optical constants, as evidenced by the transmission spectrum in Fig. 4.

The spectra of optical absorption edge (Fig. 3) of the As-S-Se system with tin impurity are characteristic of amorphous semiconductors. In the high absorption region close to the beginning of band-to-band optical transition, the absorptions exhibit a square-law energy dependence $\alpha \cdot h\nu = (h\nu - E_g^{op})^2$, widely known as the Tauc plot. This dependence gives a correct value of optical band gap E_g^{op} determined as the energy difference between the onsets of exponential tails of the allowed conduction bands [6].

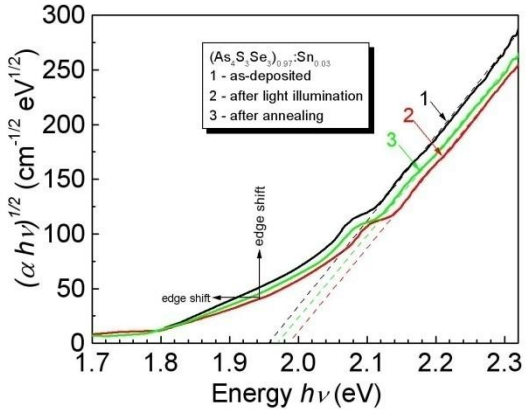

Fig. 3. Absorption spectra in the Tauc coordinates $(\alpha\ h\nu)^{1/2} = A(h\nu - Eg)$ of the amorphous $(As_4S_3Se_3)_{0.97}$:$Sn_{0.03}$ thin film: (1) as deposited, (2) after light exposure, and (3) after light exposure and heat treatment.

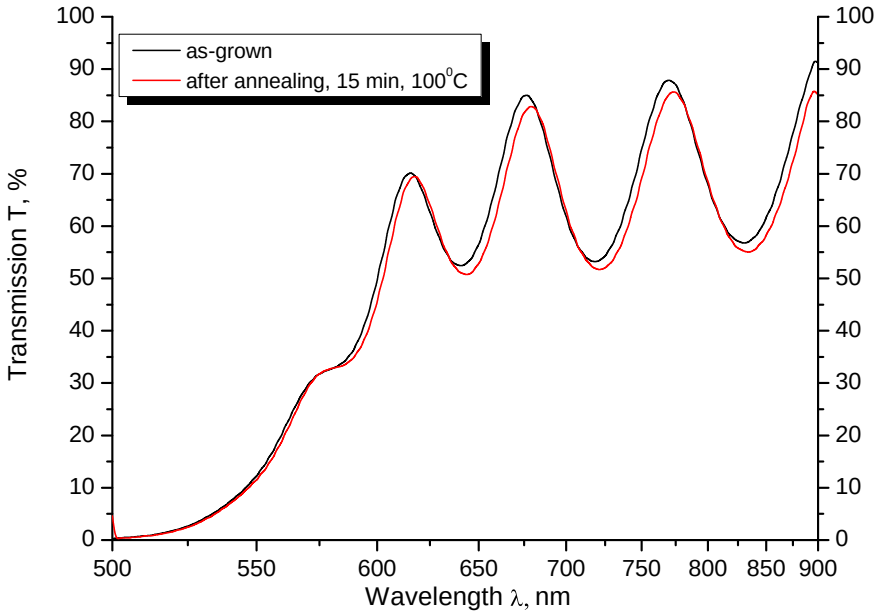

Fig. 4. Transmission spectra of the amorphous $(As_4S_3Se_3)_{0.97}:Sn_{0.03}$ thin films: (*1*) as-deposited and (*2*) after annealing.

From the experimental plots in Tauc coordinates $(\alpha h\nu)^{1/2}=A(h\nu - E_g^{op})$ the values of the optical band gap E_g^{opt} were estimated. The average energy change before and after heat treatment is $\Delta E_g^{opt}=0.02 \pm 0.01$eV.

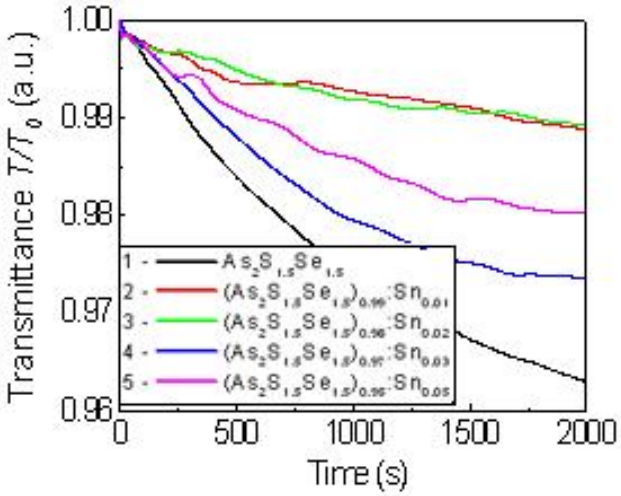

Fig. 5. Relaxation curves of photodarkening T(t)/T(0)=f(t) for amorphous $(As_3S_4Se_4)_{1-x}:Sn_x$ thin films. Excitation with a He-Ne laser at λ = 633 nm.

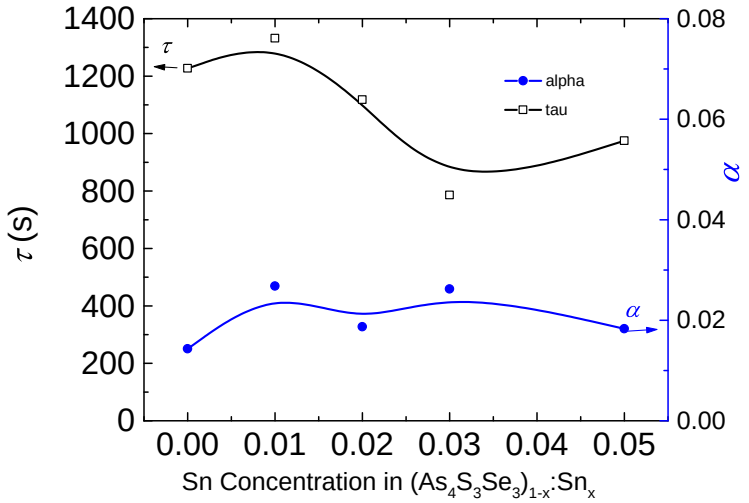

Fig. 6. Dependences of parameters τ and α vs. Sn concentration in amorphous $(As_3S_4Se_4)_{1-x}$:Sn_x thin films at excitation with λ = 633 nm.

The relaxation of relative optical transmission $T/T_0 = f(t)$ under light exposure at λ = 633 nm for amorphous $(As_4S_3Se_3)_{1-x}$:Sn_x thin films is shown in Fig. 4. At a constant light intensity, these dependences characterize the decay of the film optical transmittance with an increase in the dose of absorbed photons. The experimental curves show that the general tendency is that Sn additives in amorphous $(As_4S_3Se_3)_{1-x}$:Sn_x thin films decrease the photodarkening.

To obtain a unified basis for comparison of the transmission relaxation *T(t)/T(0)* curves, we used the so-called stretched exponential presentation for the relaxation curves in the form:

$$T(t)/T(0) = A_0 + A\exp[-(t-t_0)/\tau]^{(1-\alpha)},$$

here t is the exposure time, τ is the apparent time constant, A characterizes the exponent amplitude, t_0 and A_0 are the initial coordinates, and α is the dispersion parameter ($0 < \alpha < 1$). Figure 6 represents the dependences of parameters τ and vs. Sn concentration in amorphous $(As_3S_4Se_4)_{1-x}$:Sn_x thin films at excitation with λ = 633 nm. For the obtained relaxation curves, a rather wide scatter of parameters is observed for samples of the different composition. For doped samples, this dispersion may be caused by the fact that the concentration and distribution uniformity of the impurity is not adequately preserved along the film at deposition. However, the relaxation curves are significantly different in the case of non-doped $As_4S_3Se_3$. The main cause is the difference in thickness. For these samples, the effect of interference of light reflected at the front and rear film boundaries significantly changes the amount of absorbed light leading to a strong dependence of photodarkening at a fixed laser wavelength on film thickness [11].

The photodarkening phenomenon in chalcogenide glass films under illumination has no plain explanation up to now in spite of detailed investigation and a series of models advanced for interpreting it. The red shift of the absorption edge, which indicates the narrowing of the optical gap of the film at photodarkening, is believed to be due to the broadening of the valence band, the top of which is formed mainly by states of lone-electron pairs of the chalcogen atom. Several models have been proposed to substantiate this broadening with a particular individual atom regarded as an initial object of photoexcitation. Recently, a novel model for photodarkening in *a*-$As_2Se(S)_3$ has been proposed [12], in which photoexcited charge carriers in extended states are

considered to be responsible for photodarkening. This model was used for experimental results on photodarkening in amorphous $As_2Se_3:Sn_x$ [11]. It was shown that tin impurities strongly affect the network of the host glass inducing changes in both short-range and medium-range order; in particular they exert significant influence on the structural layers and the pattern of their relative motion.

4. Conclusions

The transmissions and optical absorption spectra of amorphous As-S-Se films doped with 1–10 at % Sn were studied before and after light exposure and heat treatment. It was shown that the doping of $As_4S_3Se_3$ glasses with tin impurities leads to a shift of the absorption edge in the red region of the spectrum and a decrease in the optical band gap. Under light exposure, amorphous $(As_4S_3Se_3)_{1-x}:Sn_x$ become darkened; that is, photostructural transformations take place, while the heat treatment imperceptibly reversed its structure to the initial position. In addition, it was observed that annealing of as-deposited thin films of the studied composition does not essentially change the shape of the spectra and does not lead to a shift of the fundamental absorption edge in any direction. The relaxation of the photodarkening effect in amorphous $(As_4S_3Se_3)_{1-x}:Sn_x$ thin films is described by stretched exponential function $T(t)/T(0) = A_0+Aexp[-(t-t_0)/\tau]^{(1-\alpha)}$. The main feature of the photodarkening effect in the samples under study is that the tin impurity suppresses this effect.

Acknowledgments. This work was supported by National Institutional project no. 11.817.05.03A. The authors are kindly grateful to Drs. D.F. Felix and A.Yu. Meshalkin for IR measurements.

References

[1] A. Andriesh, S. Sergheev, G. Triduh, and A. Meshalkin, J. Optoelectron. Adv. Mater. 9, 3007, (2007).
[2] A. Stronski, M. Vlcek, S. Kostyukevych, et al., Quantum Elelectron. Optoelelectron. 5 (3), 284, (2002).
[3] M. Iovu, S. Shutov, and L. Toth, Phys. Status Solidi (b), 195, 149, (1996).
[4] M. S. Iovu, S. D. Shutov, and M. Popescu , J. Non-Cryst. Sol., 299-309, 924, (2002).
[5] M. S. Iovu, P. Boolchand, and D. G. Georgiev, J. Optoelelectron. Adv. Mater. 7 (2), 763, (2005).
[6] J. Tauc, The optical properties of solids, North-Holland, Amsterdam, 1970.
[7] R. Swanepoel, J. Phys. E: Sci. Instrum., 16(12), 1214, (1983).
[8] A. Ganjoo and R. Golovchak, J. Optoelelectron. Adv. Mater. 10 (6), 1328, (2008).
[9] M. Iovu, S. Shutov, A. Andriesh, E. Kamitsos, C. Varsamis, D. Furniss, A. Seddon, and M. Popescu, J. Optoel. Adv. Mater. 3 (2), 443 (2001).
[10] O. V. Iaseniuc, M. S. Iovu, E. P. Colomeico, and E. Harea, Proc. 37-th Annual Congress of the American Romanian Academy of Arts and Sciences, June 04-09, 2013, Central Publishing House, Chisinau, 2013, R. Moldova, P.539-542.
[11] P. Boolchand, D. Georgiev, and M. Iovu, Chalcogen. Lett. 2 (4), 27, (2005).
[12] K. Shimakawa, N. Yoshida, A.Ganjoo, and Y. Kuzukawa, J. Singh, Phil. Mag. Lett., 77(3), 153, (1998).

PHOTOCONDUCTIVITY AND LIGHT INDUCED PHENOMENA IN AMORPHOUS $(As_4S_3Se_3)_{1-x}:Sn_x$ THIN FILMS

O. V. Iaseniuc, M. S. Iovu, I. A. Cojocaru, and A. M. Prisacar

Institute of Applied Physics, Academy of Sciences of Moldova,
str. Academiei 5, Chisinau, MD-28 Republic of Moldova
E-mail: oxana.iaseniuc@phys.asm.md

(Received May 05, 2014)

Abstract

Amorphous arsenic trisulfide (As_2S_3) and arsenic triselenide (As_2Se_3) are widely investigated amorphous materials due to their interesting electrical, optical, and photoelectrical properties. Mixed amorphous materials, such as (As_2S_3):(As_2Se_3), are of special interest for improving the physical properties and recording characteristics and extending the spectral range of photosensibility. Chalcogenide vitreous semiconductors (ChVSs) of the As-S-Se system exhibit photostructural transformations with reversible and irreversible properties and are promising materials as registration media for holography and optical information, for fabrication of diffractive elements, and other optoelectronic applications. Because many optoelectronic devices on amorphous semiconductors are based on the photoconductivity effect, it is of particular interest to study the steady-state and transient characteristics of photoconductivity. In this paper, experimental results for steady-state photoconductivity and holographic characteristics of amorphous $(As_4S_3Se_3)_{1-x}:Sn_x$ thin films are described. It was shown that the photoconductivity spectra depend on the polarity on the top illuminated electrode and on the Sn concentration in the host glass. The photosensitivity of amorphous $(As_4S_3Se_3)_{1-x}:Sn_x$ thin films is almost constant for all Sn-containing glasses. The Moss rule was used for determination of optical forbidden gap E_g from the photoconductivity spectra. It was demonstrated that the investigated amorphous films are sensitive to light irradiation and can be used as effective registration media for holographic information. The relaxation of photodarkening in amorphous $(As_4S_3Se_3)_{1-x}:Sn_x$ thin films was investigated; it was shown that the relaxation curves of transmittance $T/T_0 = f(t)$ can be described by stretch exponential function $T(t)/T(0) = A_0 + A\exp[-(t-t_0)/\tau]^{(1-\beta)}$. The kinetics of diffraction efficiency growth $\eta(t)$ was measured by registration of the laser intensity of the 1st interference maximum versus time exposure. With an increase in the Sn concentration in amorphous $(As_4S_3Se_3)_{1-x}:Sn_x$ thin films up to 6.0 at % Sn, diffraction efficiency η increases; at higher tin concentrations, it decreases.

1. Introduction

Photoconductivity represents a change in conductivity under the action of light radiation. Photoconductivity spectra can provide information about the generation, drift, and recombination of nonequilibrium current carriers [1]. In our previous works, some physical and optical properties of amorphous $(As_4S_3Se_3)_{1-x}:Sn_x$ thin films have been described [2, 3]. Chalcogenide vitreous semiconductors (ChVSs) of the As-S-Se system exhibit photostructural transformations with reversible and irreversible properties and are promising materials as registration media for

holography and optical information, for fabrication of diffractive elements, and other optoelectronic applications [4, 5]. Because many optoelectronic devices on amorphous semiconductors are based on the photoconductivity effect, it is of particular interest to study the steady-state and transient characteristics of photoconductivity. Evaporated amorphous thin films are shown to have a high degree of structural disorder depending on the composition and foreign impurities. The electrical, optical, and photoelectrical properties of chalcogenide glasses can be varied and regulated over an extensive range by modifying the composition and production technique. It was shown that the addition of a Sn impurity in amorphous As_2S_3 and AsSe thin films can provide a pronounced effect on the electrical and transport properties and optical and photoinduced phenomena [6-10]. In the last years, special attention has been paid to the influence on the photostructural transformation in amorphous thin films doped with metal impurity. It has been shown that a Sn impurity introduced in the As_2Se_3, AsSe and Sb_2S_3 glass network reduce the photodarkening effect. According to ^{119}Sn Mössbauer spectroscopy, in the As_2Se_3:Sn_x glassy system, new tetrahedral $Sn(Se_{1/2})_4$ and quasi-octahedral SnSe structural units can be formed and influence the photostructural transformations. A decrease in the optical gap of As_2Se_3 glass upon Sn alloying, most likely, results from a broadening of the valence band, the top of which is formed by Se lone-pair electrons. It was demonstrated that tin impurities has a strong effect on transient rather than on steady-state photoconductivity. The enhanced deep trapping in doped As_2Se_3 delays the recombination process and slows down the initial photocurrent relaxation. The features of transient photoconductivity were found to be primarily controlled by deep carrier trapping with the energy distribution and concentration of deep traps being determined by the structure and composition of doped amorphous films [8]. In this paper, experimental results of steady-state photoconductivity, photodarkening relaxation and holographic characteristics of amorphous $(As_4S_3Se_3)_{1-x}$:Sn_x thin films are described. The photoconductivity spectra are used to determine some optical parameters.

2. Experimental

The bulk $(As_4S_3Se_3)_{1-x}$:Sn_x chalcogenide glasses (x = 0–10.0 at % Sn) were prepared from the elements of high purity 6N (As, S, Se, Sn) by the conventional melt quenching method. Thin film samples with thickness L = 0.5–17.5 μm were prepared by flash thermal evaporation in a vacuum (P = 10^{-5} Torr) of the synthesized initial glass onto glass substrates held at T_{substr} = 100°C. The thin film samples had a sandwich configuration with two Al electrodes; the top electrode was transparent for the incident light. In all the cases, measurement of dark conductivity σ_d and photoconductivity σ_{ph} for amorphous semiconductors with the low conductivity was performed at a constant current, e.g., the case of low load resistance $R_L \angle\angle R_d R_{ph}$, where R_L is the load resistance, R_d the sample resistance in the dark, and R_{ph} is the sample resistance under illumination. Forasmuch as the calibrated resistance of an U5-11 electrometrical amplifier was used as a load resistance, the error of the measurements was determined by the scatter of load resistance R_L; it was less than 1.0 %. Specific conductivity σ_S of the sample was calculated according to the expression

$$\sigma_S = \frac{1}{R_S} \cdot \frac{L}{S} = \frac{U_L}{U - U_L} \cdot \frac{1}{R_L} \cdot \frac{L}{S} \qquad (1)$$

Here, R_S is the resistance of the sample, S is the area between the electrodes of the sample, U is the total voltage in the electrical circuit, and U_L is the voltage on load resistance R_L

In order to initiate the photostructural transformations in the thin film samples a red (λ = 633 nm, P = 0.6 mW) and green (λ = 543 nm, P = 0.75 mW) continuous He−Ne lasers were used simultaneously as sources of light exposure. The relaxation of the transmission curves was measured both at λ = 633 nm and λ = 543 nm wavelengths in-situ during the light excitation. The experimental set-up included a laser and a PCI-1713A digital build-in PC-card for data acquisition connected to a Si-photodetector. Special software was elaborated for automatic measurements. The microholograms in the amorphous thin films were registered by means of the interference of two Ar^+-laser beams (λ = 0.488 μm) with a power of W = 0.64 mW. The kinetics of diffraction efficiency growth $\eta(t)$ was measured by registration of the intensity of the 1st interference maximum versus time exposure at wavelength λ = 0.6328 μm. Diffraction efficiency η was calculated as a ratio of the intensity in the 1st diffraction maximum to the intensity of the transmitted laser beam across the sample.

3. Experimental results and discussion

The photoconductivity spectra can give the information regarding the processes of generation, drift and recombination of non-equilibrium current carriers. The photoconductivity, which is determined as an increase in conductivity under light illumination, can be defined by the expression

$$\sigma_{ph} = \frac{1}{L} e\mu_d \tau \beta N_0 [1 - \exp(-kL)] \tag{2}$$

Here, N_0 is the number of incident photons on the sample surface per second, L is the thickness of the sample, β describes the efficiency of the generation process μ_d is the drift mobility of the holes, τ is the recombination life time, e is the electron charge, and k is the absorption coefficient. The exponential term describes the light absorption in the sample of the investigated material and thickness.

Figure 1 shows the spectral distribution of photocurrent for amorphous $(As_4S_3Se_3)_{0.97}$:$Sn_{0.03}$ thin films at positive (curve *1*) and negative (curve *2*) polarities at the top illuminated electrode. For other $(As_4S_3Se_3)_{1-x}$:Sn_x ($0 \le x \le 10$ at % Sn), the shape of the curves of the spectral distribution of photocurrent is similar. In all cases, the photocurrent at positive polarity at the top illuminated electrode is higher and the maximum of the spectral distribution is shifted in the high energy region of the spectrum (Fig. 2). Since the investigated spectral region ($h\nu$ = (0.95–3.1 eV) corresponds to the region of the optical absorption edge and the values of absorption coefficient k change four- to fivefold in this region, the spectral distribution of photoconductivity is analyzed in the approximation of strong and weak absorption.

In the region of strong absorption $\exp(-kL) \angle\angle 1$, the light is absorbed near the surface of the sample and photoconductivity is determined by the expression

$$\sigma_{ph} = \frac{1}{L} \cdot e\mu_d \tau \beta N_0 . \tag{3}$$

In this region of energy of the incident photons in the absence of strong surface recombination, the photoconductivity weakly depends of the photon energy, which gives the possibility to determine the product $\beta\mu_d\tau$ and which is characteristic of the photosensibility of the investigated semiconductor material.

In the approximation of weak absorption, at $\exp(kL) \approx 1 - kL$, from expression (1) we

obtain

$$\sigma_{ph} = e\mu_d \tau \beta k N_0 . \quad (4)$$

Relation (4) suggests that, in the region of weak absorption, the dependence of the spectral dependence of photoconductivity vs. energy of incident photons is determined by the spectral distribution of absorption coefficient k because, in this region, the product $\beta\mu_d\tau$ very weakly depends on photon energy [11]. This gives the possibility to use the photoconductivity spectra for calculating the optical absorption spectra in this region.

The low energy portion of the $log(I_{ph}/N_0)$ dependence is described by the Urbach tail of absorption coefficient α. The Moss rule was used for determining the optical forbidden gap E_g from the photoconductivity spectra. Usually, in chalcogenide glasses, the absorption edge is broader than in crystalline analogues, which is caused by a broad energy distribution of electronic states in the band gap due to disorder and defects. The distribution of the localized states of the semiconductor, including band gap E_g depend on the structure of the investigated material. A well-known tool for determining the band gap of the semiconductor is long wavelength λ_0 at which the photosensitivity achieves half maximum, as is shown in Fig. 1. The dependence of the calculated values of E_g^+ versus Sn concentration in amorphous $(As_4S_3Se_3)_{1-x}$:Sn_x thin films is shown in Fig. 2 (right Y axis). This dependence has a minimum at about 6.0 at % Sn, which is probably attributed to the formation of new tetrahedral units $SnSe_2$.

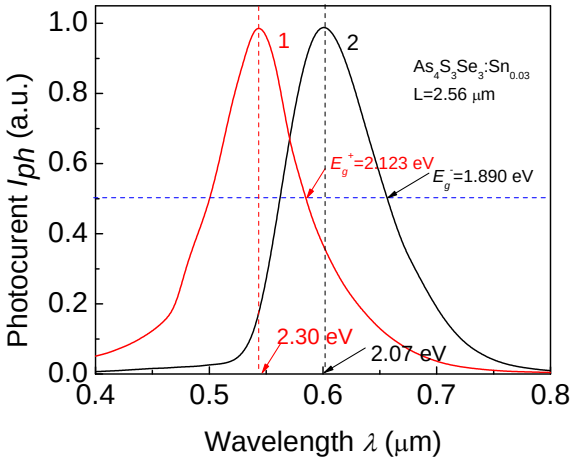

Fig. 1. Spectral distribution of photocurrent $I_{ph} = f(\lambda)$ for amorphous $(As_4S_3Se_3)_{0.97}$:$Sn_{0.03}$ thin films.

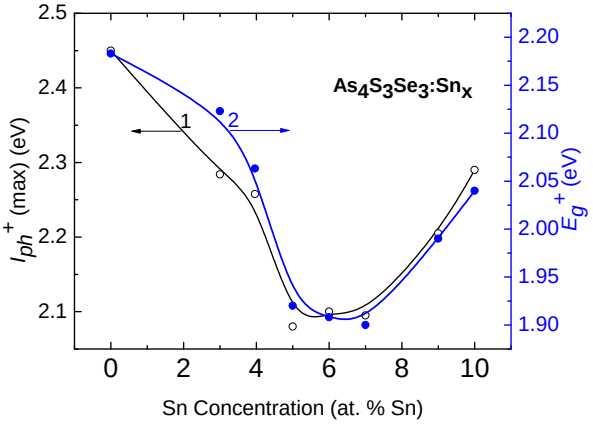

Fig. 2. Dependence of the maximum of the photocurrent $I_{ph}^+(max)$ and forbidden gap E_g^+ versus Sn concentration in amorphous $(As_4S_3Se_3)_{1-x}$:Sn_x thin films.

Figure 2 shows that the photocurrent is higher for the positive polarity on the illuminated top electrode and the maximum in the spectral distribution of photocurrent is displaced in the higher region of photon energy. At the negative polarity on the top illuminated electrode, the photocurrent decrease after the maximum. That is caused by the existence of a high concentration of recombination centers at the surface of the sample due to the presence of a lot of structural defects. For this reason, we can assume that the nonequilibrium carriers reaching the surface can be captured by the local centers and the recombination process is faster than in the bulk of the sample. The probability that the non-equilibrium carriers reach the surface is greater for the case where the incident light is absorbed in the small layer, e.g., at high absorption coefficients. For

this reason, we observe the fall of the photosensitivity in high energy region because, in the shot wavelength region, the absorption coefficient increases and the number of localized states involved in the optical transitions also increases.

Figure 3 shows the spectral distribution of photocurrent for some compositions of amorphous $(As_4S_3Se_3)_{1-x}$:Sn_x thin films. With an increase in the Sn concentration in amorphous $(As_4S_3Se_3)_{1-x}$:Sn_x thin films, the maximum of photocurrent $I_{ph}(max)$ and the values of optical band gap E_g are shifted to lower energies up to x = 6.0 at % Sn and, for higher concentrations, increase due to the formation of new tetrahedral structural units. The photosensitivity of amorphous $(As_4S_3Se_3)_{1-x}$:Sn_x thin films decreases upon the introduction of Sn into the host glass and is almost constant for all Sn-containing glasses. Figure 4 shows the normalized curves of the spectral distribution of photocurrent $log(I_{ph}/N_0) = f(h\nu)$ for amorphous $As_4S_3Se_3$ thin films. The same dependences are exhibited by all amorphous $(As_4S_3Se_3)_{1-x}$:Sn_x thin films with the different investigated compositions.

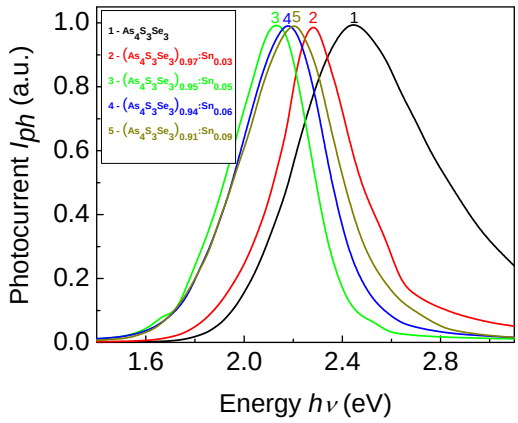

Fig. 3. Spectral distribution of photocurrent $I_{ph} = f(\lambda)$ for amorphous $(As_4S_3Se_3)_{1-x}$:Sn_x thin films.

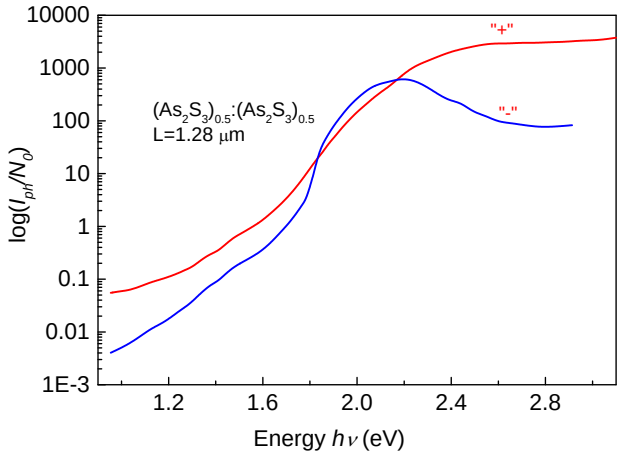

Fig. 4. Normalized curves of the spectral distribution of photocurrent $log(I_{ph}/N_0) = f(h\nu)$ for amorphous $As_4S_3Se_3$ thin films.

The amorphous $(As_4S_3Se_3)_{1-x}$:Sn_x thin films exhibit photoinduced effects under light irradiation with photon energy above the optical band gap ($h\nu \geq E_g$),which makes them promising materials for registration of optical and holographic information [2].

The relaxation of relative optical transmission $T/T_0 = f(t)$ under light exposure at wavelength λ = 633 nm and λ = 543 n for amorphous $(As_4S_3Se_3)_{1-x}$:Sn_x thin films is shown in Figs. 5 and 6, respectively.

At a constant light intensity, these dependences exhibit the decay of the film optical transmittance with an increase in the dose of absorbed photons. To obtain a unified basis for comparison of the transmission relaxation $T(t)/T_0$ curves, we used the so-called stretched exponential and single-exponential presentation for the relaxation curves in the form:

$$T(t)/T(0) = A_0 + A\exp[-(t-t_0)/\tau]^{(1-\beta)} \quad (5)$$

$$T(t)/T(0) = A_0 + A\exp[-(t-t_0)/\tau] \quad (6)$$

Here, t is the exposure time, τ is the apparent time constant, A characterizes the exponent amplitude, t_0 and A_0 are the initial coordinates, and α is the dispersion parameter ($0<\beta<1$).

For the obtained relaxation curves, a fairly wide scatter of parameters is observed for samples of the different composition. For doped samples, the cause of this dispersion may be that the concentration and distribution uniformity of impurity are not adequately preserved along the film during deposition. However, the relaxation curves are significantly different in the case of non-doped $As_4S_3Se_3$ as well. Comparison of the parameters of the relaxation curves for samples deposited at different incident angles has shown that, in the considered limits of distance from the center over the evaporator, the greatest effect of photodarkening is observed for the central samples, in contrast to the results reported in the literature for obliquely deposited films [12]. A slight decrease in the photodarkening amplitude with the distance from the center is due to a decrease in the film thickness.

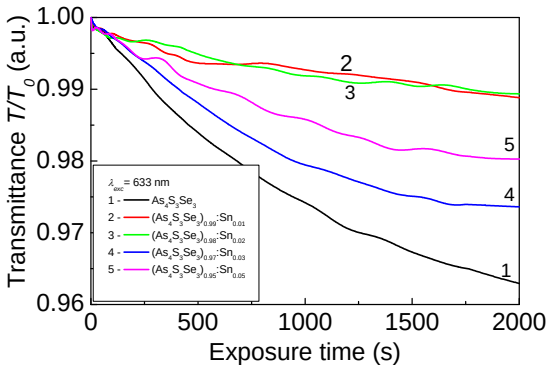

Fig. 5. Relaxation curves of photodarkening $T/T_0 = f(t)$ for amorphous $(As_4S_3Se_3)_{1-x}$:Sn_x thin films under light exposure at wavelength $\lambda = 633$ nm.

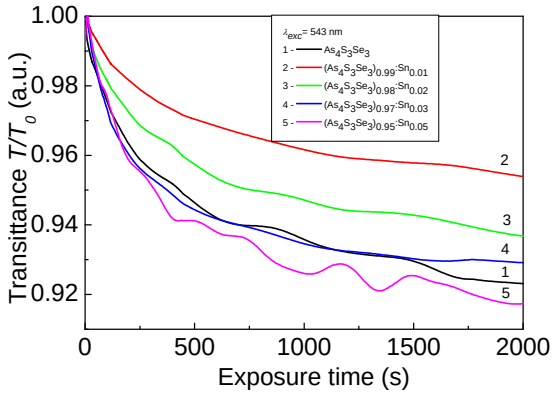

Fig. 6. Relaxation curves of photodarkening $T/T_0 = f(t)$ for amorphous $(As_4S_3Se_3)_{1-x}$:Sn_x thin films under light exposure at wavelength $\lambda = 543$ nm.

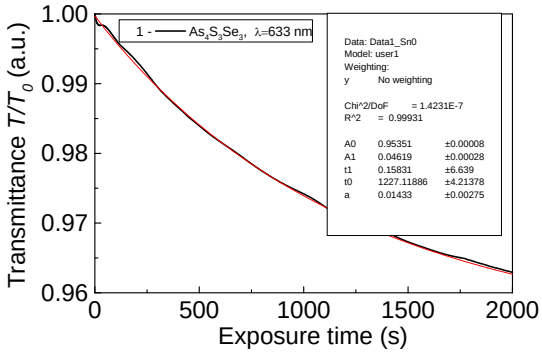

Fig. 7. Normalized optical transmittance kinetics for a He−Ne laser beam (λ = 633 nm) for amorphous $As_4S_3Se_3$ thin films.

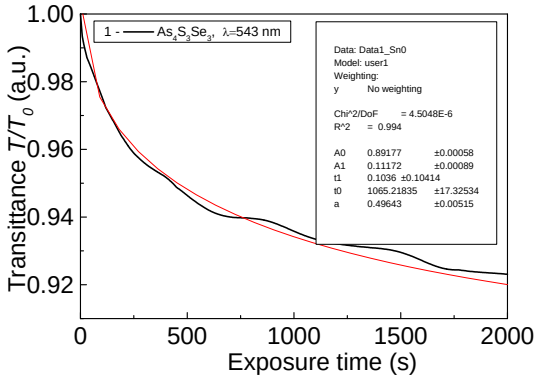

Fig. 8. Normalized optical transmittance kinetics for a He−Ne laser beam (λ = 543 nm) for amorphous $As_4S_3Se_3$ thin films.

The photodarkening phenomenon in chalcogenide glass films under illumination has no plain explanation up to now in spite of detailed investigation and a series of models advanced for interpretation of it. Several models have been put forward to substantiate this broadening

considering a particular individual atom as an initial object of photoexcitiation [13, 14]. Recently, a novel model for photodarkening in a-$As_2Se(S)_3$ has been proposed [15, 16], in which photoexcited charge carriers in extended states are considered to be responsible for photodarkening.

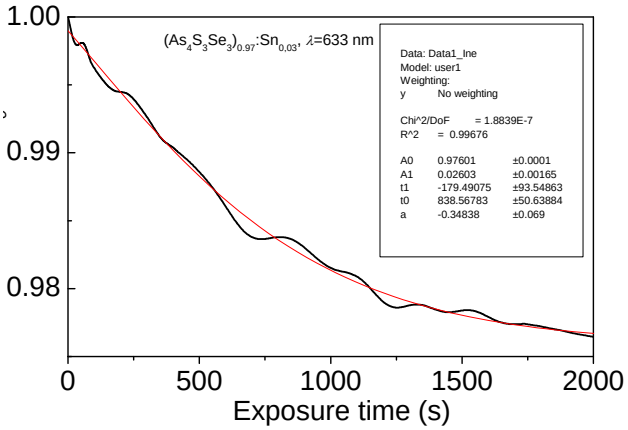

Fig. 9. Normalized optical transmittance kinetics for a He−Ne laser beam (λ = 633 nm) for amorphous $(As_4S_3Se_3)_{0.97}$:$Sn_{0.03}$ thin films.

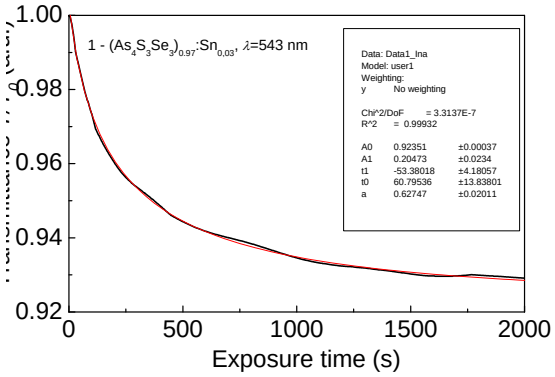

Fig. 10. Normalized optical transmittance kinetics for a He−Ne laser beam (λ = 543 nm) for amorphous $(As_4S_3Se_3)_{0.97}$:$Sn_{0.03}$ thin films.

Unlike the previous conceptions, the new model takes into account the layered cluster structure of a chalcogenide glass. During exposure, the layer is negatively charged due to capture of photoexcited electrons, and repulsive forces are built between the layers. These forces cause enlargement of the interlayer distance (leading to photoexpansion) and slip motion along the layers. The last-mentioned process alters the interaction of lone-pair electrons between the layers leading to a photodarkening effect. Earlier, in a structural model proposed for explanation of photodarkening phenomena, M. Popescu [17] has pointed out that distortion in the second and third coordination spheres should be taken into account as important factors.

The model of Shimakawa et al. [15, 16] offers a good basis for consideration of the effect on photodarkening of impurity atoms with coordination different from that of the host glass atoms, as in the case of tin. The foreign metal atoms provide bridging between the layers and hence reduce the slip motion, thus hindering the photodarkening. We suggest that this consideration is applicable in the case of tin impurity in amorphous $[(As_2S_3)_{0.5}$:$(As_2Se_3)_{0.5}]_{1-x}$:Sn_x thin films. Upon the addition of Sn, due to the tetrahedral arrangement of the sp^3 bonds with the chalcogens, the dopant atom inserted in the network increases the thickness of the layered configuration as revealed by the significant shift of the FSDP towards lower angles. This insertion corresponds in fact of introduction of the structural units of the $SnSe_2$ type in the network. The transition to a three-dimensionally (3D) network is preceded by the appearance of structural units of the SnSe type. Then, the direct consequence of this transition will be shown in the intensity of the FSDP which gradually disappears. The interruption of the two-dimensional structure and transition is probably due to a more ionic character of the Sn-Se bonds. Since tin tends to form directional bonds being introduced in the host glass and especially during annealing, some bridging bonds should appear between the layers. The structure of the glass that contains tin impurity requires therefore some excess slip forces; that is, it leads to greater

exposition doses and time constants.

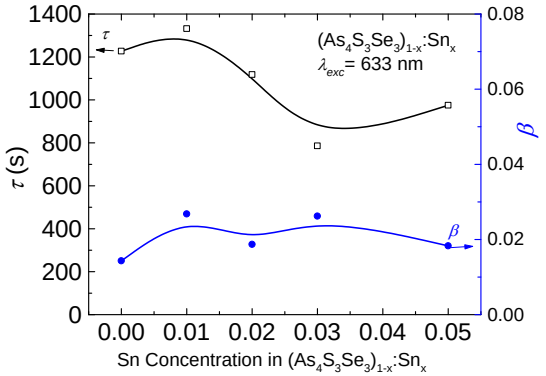

Fig. 11. Fitting parameters τ and β in equation (5) for the normalized optical transmittance kinetics for a He–Ne laser beam (λ = 633 nm) for amorphous $(As_4S_3Se_3)_{1-x}$:Sn_x thin films.

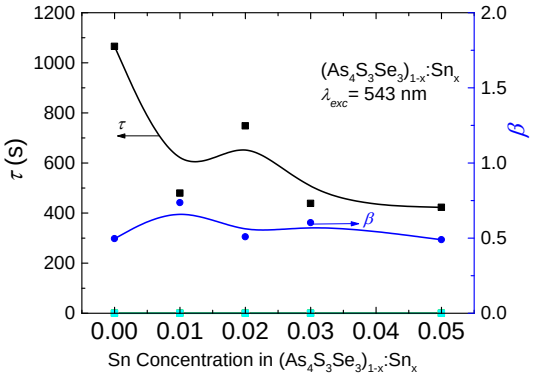

Fig. 12. Fitting parameters τ and β in equation (5) for the normalized optical transmittance kinetics for a He–Ne laser beam (λ = 543 nm) for amorphous $(As_4S_3Se_3)_{1-x}$:Sn_x thin films.

The stretched exponential photodarkening kinetics was numerically justified for thick amorphous As-Se films [18, 19]. It was shown that in-situ photodarkening kinetics are quite similar in amorphous $As_{40}Se_{60}$ and $As_{50}Se_{50}$ films and exhibit a strong tendency to non-dispersion (β values from equation (1) are slightly deviated around 0.6, while photodarkening in $As_{60}Se_{40}$ films mainly corresponds to single-exponential rule with β value close to 1.0). It was also established that the parameter β values depend on the thickness of the sample. If the film thickness is smaller than the penetration depth of the excitation light, the dispersion parameter β = 1, which indicates that the photodarkening kinetics can be presented by an exponential function (equation (6)). In our case, the penetration depth is defined by the excitation wavelength. It is evident that the penetration depth is higher if the amorphous film is excited at a longer wavelength (λ = 633 nm) than in the case of a shorter wavelength (λ = 543 nm).

The parameters τ and β from equations (5) and (6) were calculated by the computer fitting of the normalized optical transmittance kinetics curves for exposure of amorphous $(As_4S_3Se_3)_{1-x}$:Sn_x thin films to a He–Ne laser beam (λ = 633 and 543 nm). Figures 11 and 12 represent the fitting parameters τ and β according to equation (5) versus Sn concentration in amorphous $(As_4S_3Se_3)_{1-x}$:Sn_x thin films. We obtain that, if the thin amorphous film is excited at a longer wavelength (λ = 633 nm), the values of the dispersion parameter β are smaller, which means that dispersion is more pronounced.

The fact that the photodarkening kinetics may be described by a stretched exponential can be regarded as an indication of dispersion by a kinetic mechanism, i.e., the time dependence of the process rate [20]. The data allow concluding that the formation of photoinduced absorption is limited to a dispersive process with the exponent $\beta \cong 0.5$. Charge transport in chalcogenide glasses is known as highly dispersive due to wide distribution of capture times in multiple-trapping process [21]. For a-As_2Se_3-like glasses, the dispersive parameter β of hole transport is close to 0.5, in accordance with the value found from the stretched exponential presentation of photodarkening kinetics [9].

The transmission hologram gratings in amorphous $(As_4S_3Se_3)_{1-x}$:Sn_x thin films with a period Λ = 1μm were recorded by two symmetrically incident Ar^+ laser beams (DPSS-laser) of

equal intensity (λ = 532 нм), and the readout of the diffraction efficiency η was made using a diode laser beam (λ = 650 нм) in the first diffraction maximum.

The optical set-up is illustrated in Fig. 13. Diffraction efficiency η was defined as $\eta = \frac{I_d}{I_0}$, where I_0 is the intensity of the readout beam and I_d is the intensity of the first order diffracted beam. Figure 14 represents the growth of diffraction efficiency $\eta(t)$ during the registration of elementary microhologram in amorphous $(As_4S_3Se_3)_{1-x}$:Sn_x thin films. The kinetics of diffraction efficiency growth $\eta(t)$ was measured by registration of the laser intensity of the 1st interference maximum versus time exposure. With an increase in the Sn concentration in amorphous $(As_4S_3Se_3)_{1-x}$:Sn_x thin films up to 6.0 at % Sn, diffraction efficiency η increases, while for higher concentrations of tin, it decreases (Fig. 15.)

The dependence of the diffraction efficiency versus thin film thickness (L = 0.88−17.5 μm) was also investigated. Figure 16 represents the kinetics of the registration process of the gratings $\eta(t)$ for amorphous $As_4S_3Se_3$ thin films with different thickness. For amorphous $As_4S_3Se_3$ thin films, it was demonstrated that the maximum of diffraction efficiency η is obtained for the films with a thickness of about L = 4.0 μm. A similar dependence was previously obtained for amorphous $As_{40}S_{60}$ and $As_{55}Se_{45}$ thin films [22, 23]. The dependence of photodarkening for as-evaporated amorphous As-Se [24] and As_2Se_3:Pr(Dy) thin films was also found [25].

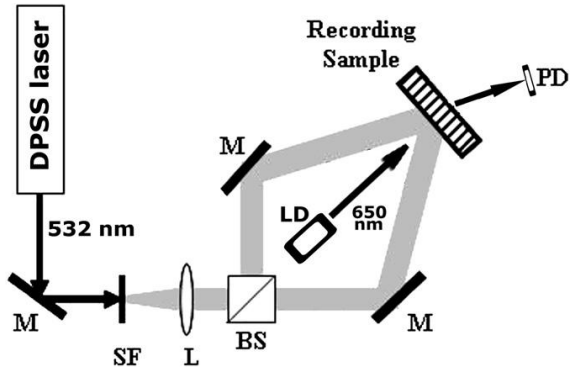

Fig. 13. Experimental set-up for Bragg grating recording in chalcogenide amorphous thin films: DPSS-laser (λ = 532 нм, 30 mW/cm^2), M-mirror, SF-spatial filter, L-lens, BS-beam splitter, LD-laser diode (λ = 650 нм), PD-photodiode.

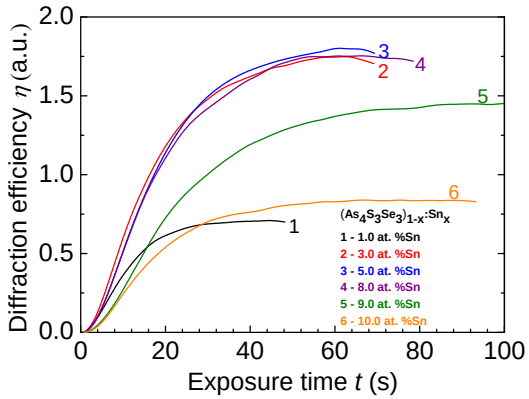

Fig. 14. Kinetics of diffraction efficiency $\eta(t)$ for different compositions of amorphous $(As_4S_3Se_3)_{1-x}$:Sn_x thin films.

The dependence of the photodarkening amplitude on the thickness of the amorphous thin film is due mainly to the dependence of the position of optical absorption edge, which regulates the amount of absorbed photons generating the photodarkening process. As in our case, for amorphous As_2S_3 [22] and As_3Se_2 [24] thin films, the diffraction efficiency and the photodarkening effect were achieved for the thickness of the amorphous film of about L = 4.0 μm. In addition to the thickness dependence of the position of the optical absorption edge, the thickness dependence of the photodarkening in amorphous As_2S_3 thin films was also explained by the strain induced by the lattice mismatch between the film and the substrate [26].

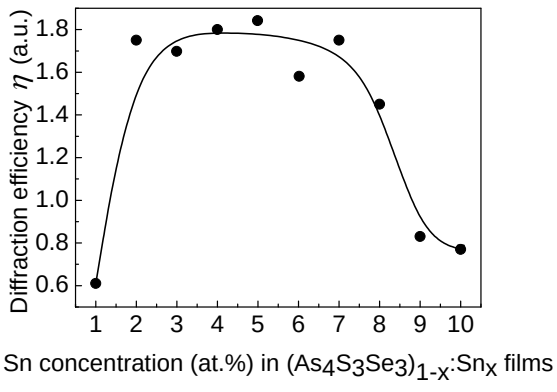

Fig. 15. Dependence of diffraction efficiency η versus Sn concentration in amorphous $(As_4S_3Se_3)_{1-x}:Sn_x$ thin films.

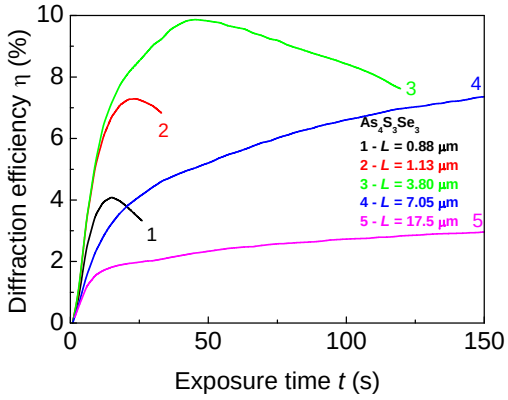

Fig. 16. Kinetics of diffraction efficiency $\eta(t)$ for amorphous $As_4S_3Se_3$ thin films with different thickness.

The thickness dependence of the photodarkening kinetics of optical transmittance in amorphous As-Se films also was interpreted on the basis of change in the penetration depth of the incident laser beam during exposure [18, 19]. It was shown that the photostructure transformations in an amorphous film depend on the thickness of the amorphous film and are fairly complicated depending on the nature of evolving changes in short- and long-range ordering near-neighbor interactions in the disordered lattice.

4. Conclusions

The experimental results of steady-state photoconductivity, relaxation of photodarkening and holographic characteristics of amorphous $(As_4S_3Se_3)_{1-x}:Sn_x$ thin films are described. It is shown that the photoconductivity spectra depend on the polarity on the top illuminated electrode and on the Sn concentration in the host glass. The photosensitivity of amorphous $(As_4S_3Se_3)_{1-x}:Sn_x$ thin films is almost constant for all Sn-containing glasses. The Moss rule is used for determination of optical forbidden gap E_g from the photoconductivity spectra. It is demonstrated that the investigated amorphous films are sensitive to light irradiation and can be used as effective registration media for holographic information. The relaxation of photodarkening in amorphous $(As_4S_3Se_3)_{1-x}:Sn_x$ thin films is investigated; it is shown that the relaxation curves of transmittance $T/T_0 = f(t)$ can be described the stretched exponential function $T(t)/T(0) = A_0+A\exp[-(t-t_0)/\tau]^{(1-\beta)}$. Diffraction efficiency η measured in the 1st interference maximum in amorphous $(As_4S_3Se_3)_{1-x}:Sn_x$ thin films increases upon doping with tin up to 6.0 at % Sn.

Acknowledgments. This work was supported by the SCSTD of the Academy of Sciences of Moldova, project no. 11.817.05.03A.

References

[1] M. Popescu, A. Andriesh, V. Ciumash, M. Iovu, S. Shutov, and D. Tsiuleanu, Physics of chalcogenide glasses, Editura Ştiinţifică Bucureşti – I.E.P. Ştiinţa Chişinău, 1996.

[2] O. V. Iaseniuc, D. V. Harea, M. S. Iovu, E. P. Colomeico, E. E. Harea, I. A. Cojocaru, D. F. Shepel, and A. Meshalkin, Spectroscopic study of amorphous As_2Se_3:Sn_x and $(As_2S_{1.5}Se_{1.5})_{1-x}$:$Sn_x$ thin films, Proc. SPIE 8411, Advanced Topics in Optoelectronics, Microelectronics, and Nanotechnologies VI, 8411OL (November 1, 2012).

[3] O. V. Iaseniuc, D. V. Harea, E. E. Harea, G. F. Volodina, and M. S. Iovu, Mold. J. Phys. Sci. 12(3-4), 181 (2013).

[4] A. V. Stronski, M. Vlcek, S. A. Kostyukevych, V. M. Tomchuk, E. V. Kostyukevych, S. V. Svechnikov, A. A. Kudreavtsev, N. L. Moskalenko, and A. A. Koptyukh, Sem. Phys., Quantum Electron. Optoelectron. 5(3), 284 (2002).

[5] M. Reinfelde, and J. Teteris, J. Optoelectron. Adv. Mater. 13(11-12), 1531 (2011).

[6] M. S. Iovu, S. D. Shutov, and L. Toth, Physica Status Solidi (b), 195, 149 (1996).

[7] M. S. Iovu, N. N. Syrbu, S. D. Shutov, I. A. Vasiliev, S. Z. Rebeja, E. P. Colomeico, M. Popescu, and F. Sava, Physica Status Solidi (a), 175(2), 623 (1999).

[8] M. S. Iovu, S. D. Shutov, V. I. Arkhipov, and G. J. Adriaenssens, J. Non-Cryst. Solids 299&302, 1008 (2002).

[9] P. Boolchand, D. G. Georgiev, and M. S. Iovu, Chalcogen. Lett. 2(4), 27 (2005).

[10] M. S. Iovu, D. V. Harea, I. A. Cojocaru, E. P. Colomeico, A. M. Prisacari, and V. G. Ciorba, J. Optoelectron. Adv. Mater. 9(10), 3138 (2007).

[11] G. Moddel, D. A. Anderson, Poyl, W., Phys. Rev. B22, 1918 (1980).

[12] Y. Kuzukawa, A. Ganjoo, and K. Shimakawa, Phil. Mag. B79(2), 249 (1999).

[13] G. Pfeiffer, M. A. Paesler, S. C. Agarwal, J. Non-Cryst. Solids, 130, 111 (1991)

[14] K. Shimakawa, A. Kolobov, and S. R. Elliot, Adv. Phys. 44, 775 (1995).

[15] K. Shimakawa, N. Yoshida, A. Ganjoo, Y. Kuzukawa, and J. Singh, Phil. Mag. Lett., 77**,** 153 (1998).

[16] A. Ganjoo, N. Yoshida, and K. Shimakawa, Photoinduced changes on the structural and electronic properties of amorphous semiconductors, Recent Research Developments in Applied Physics, ed. M.Kawasaki, N. Ashgritz and R. Anthony (Research Signpost, Trivandrum, 2, 129-150 (1999).

[17] M. Popescu, J. Non-Cryst. Solids, 90(1-3), 533 (1987).

[18] V. O. Balitska, M. S. Iovu, and O. I. Shpotyuk, J. Optoelectron. Adv. Mater. 14(7), 590 (2012).

[19] V. O. Balitska, M. S. Iovu, and O. I. Shpotyuk, J. Non-Cryst. Solids, 379, 182 (2013).

[20] D. L. Gisom, M. T. Gingerich, E. J. Frieble, Phys. Rev. Lett., 71, 1019 (1993).

[21] G. Pfister, and H. Sher, Adv. Phys. 27(5), 747 (1978).

[22] J. J. Teteris, Optoelectron. Adv. Mater. 4(3), 687 (2002).

[23] J. Teteris, and M. Reinfelde, J. Optoelectron. Adv. Mater. 7(5), 2581 (2005).

[24] M. S. Iovu, V. G. Ciorba, E. P. Colomeico, M. A. Iovu, A. M. Nastas, A. Prisacari, M. Popescu, and O. I. Shpotyuk, J. Optoelectron. Adv. Mater. 7(5), 2333 (2005).

[25] M. S. Iovu, S. D. Shutov, P. Boolchand, E. P. Colomeico, V. G. Ciorba, S. M. Iovu, and M. Popescu, J. Optoelectron. Adv. Mater. 4(4), 857 (2002).

[26] K. Hayashi, and N. Mitsuishi, J. Non-Cryst. Solids 299&302, 949 (2002).

BOSE–EINSTEIN CONDENSATION OF TWO-DIMENSIONAL POLARITONS IN MICROCAVITY UNDER THE INFLUENCE OF THE LANDAU QUANTIZATION AND RASHBA SPIN–ORBIT COUPLING

S. A. Moskalenko[1], E. V. Dumanov[1,2], I. V. Podlesny[1], M. A. Liberman[3,4], B. V. Novikov[5], S. S. Rusu[1,2], and V. M. Bajireanu[1]

[1]*Institute of Applied Physics, Academy of Sciences of Moldova, Academiei str. 5, Chisinau, MD-2028 Republic of Moldova*

[2]*Technical University of Moldova, bd. Stefan cel Mare 168, Chisinau, MD2004 Republic of Moldova*

[3] *Nordita, KTH Royal Institute of Technology and Stockholm University, Roslagstullsbacken 23, Stockholm, 10691 Sweden*

[4]*Moscow Institute of Physics and Technology, Instststitutskii per. 9, Dolgoprudnyi, Moskow oblast, 141700 Russia*

[5]*Department of Solid State Physics, Institute of Physics, St.Petersburg State University, Ulyanovskaya str. 1, Petrodvorets, St. Petersburg, 198504 Russia*

(Received February 24, 2014)

Abstract

The Bose-Einstein condensation (BEC) of the two-dimensional (2D) magnetoexciton–polaritons in microcavity, where the Landau quantization of the electron and hole states accompanied by the Rashba spin–orbit coupling plays the main role, was investigated. The Landau quantization levels of the 2D heavy holes with nonparabolic dispersion law and third-order chirality terms both induced by the external electric field perpendicular to the semiconductor quantum well and strong magnetic field B give rise to a nonmonotonous dependence of the magnetoexciton energy levels and the polariton energy branches on B. The Hamiltonian describing the Coulomb electron–electron and electron–radiation interactions was expressed in terms of the two-particle integral operators, such as density operators $\hat{\rho}(\vec{Q})$ and $\hat{D}(\vec{Q})$ representing the optical and acoustical plasmons and magnetoexciton creation and annihilation operators $\Psi_{ex}^{\dagger}(\vec{k}_{\parallel}), \Psi_{ex}(\vec{k}_{\parallel})$ with in-plane wave vectors $\vec{k}_{\parallel}$ and $\vec{Q}$. Polariton creation and annihilation operators $L_{ex}^{\dagger}(\vec{k}_{\parallel}), L_{ex}(\vec{k}_{\parallel})$ were introduced using the Hopfield coefficients and neglecting the antiresonant terms because the photon energies exceed the energy of the cavity mode. The BEC of the magnetoexciton–polariton takes place on the lower polariton branch at point $\vec{k}_{\parallel} = 0$ with the quantized value of the longitudinal component of the light wave vector, as in the point of the cavity mode.

The unitary coherent transformation of the obtained Hamiltonian leading to the breaking of its gauge symmetry was written as a Glauber-type coherent transformation using polariton operators $L_0^{\dagger}, L_0$ instead of the true Bose operators. It can be represented in a factorized form as a product of two unitary transformations acting separately on the magnetoexciton and photon subsystems. The first of them is similar to the Keldysh–Kozlov–Kapaev unitary transformation, whereas the second one is equivalent to the Bogoliubov canonical displacement transformation. It

was shown that the first transformation leads not only to the Bogoliubov u-v transformations of the electron and hole single-particle Fermi operators but also to the similar transformation of the two-particle integral operators. It becomes possible due to the extensive N-fold degeneracy of the lowest Landau levels (LLLs) in Landau gauge description, where N is proportional to the layer surface area S. In both cases, the u-v coefficients depend on the LLL filling factor, but in the last case, this dependence is doubled. The breaking of the gauge symmetry gives rise to the new mixed states expressed through the coherent superposition of the algebraic sum of the magnetoexciton creation and annihilation operators $(e^{i\alpha}\Psi_{ex}(-\vec{k}_{\|})+\Psi^{\dagger}_{ex}(\vec{k}_{\|})e^{-i\alpha})$ and density operator $\hat{D}(\vec{k}_{\|})$ representing the acoustical plasmon. In contrast, density operator $\hat{\rho}(\vec{Q})$ representing the optical plasmon does not take part in these superpositions.

1. Introduction

The present article is based on the background previous papers and monographs [1–16] as well on the recent contribution [17–26].

In [17], the Hamiltonian of the electron-radiation interaction in the second quantization representation for the case of 2D coplanar electron–hole (e–h) systems in a strong perpendicular magnetic field was derived. The s-type conduction band electrons with spin projections $s_z = \pm 1/2$ along the magnetic field direction and the heavy holes with total momentum projections $j_z = \pm 3/2$ in the p-type valence band were taken into account. The periodic parts of their Bloch wave functions are similar to $(x \pm iy)$ expressions with the orbital momentum projection $M_v = \pm 1$ on the same selected direction. The envelope parts of the Bloch wave functions have the forms of plane waves in the absence of a magnetic field. In its presence, they completely changed due to the Landau quantization event. In [17–26], the Landau quantization of the 2D electrons and holes is described in the Landau gauge and is characterized by the oscillator-type motion in one in-plane direction giving rise to discrete Landau levels enumerated by the quantum numbers n_e and n_h and by the free translation motion in another in-plane direction perpendicular to previous one. The one-dimensional (1D) plane waves describing this motion are marked by the 1D wave numbers p and q. In [18], the Landau quantization of the 2D electrons with non-parabolic dispersion law, pseudospin components and chirality terms were investigated. On this base, in [19], the influence of the Rashba spin–orbit coupling (RSOC) on the 2D magnetoexcitons was discussed. The spinor-type wave functions of the conduction and valence electrons in the presence of the RSOC have different numbers of Landau quantization levels for different spin projections. As was demonstrated in [18, 19, 22], the difference between these numbers is determined by the order of the chirality terms. Their origin is due to the influence of the external electric field applied to the layer parallel to the direction of the magnetic field. In [19], two lowest Landau levels (LLLs) of the conduction electron and four LLLs for the holes were used to calculate the matrix elements of the Coulomb interaction between the charged carriers as well as the matrix elements of the electron-radiation interaction. On these bases, the ionization potentials of the new magnetoexcitons and the probabilities of the quantum transitions from the ground state of the crystal to the magnetoexciton states were calculated. In the present description the number of the hole and magnetoexciton states will be enlarged and the formation of magnetopolaritons taking into account the RSOC will be described. A simpler version of magnetopolariton without taking into account the RSOC was described in [21] for the case of

interband quantum transitions and in [23] for the case of intraband quantum transitions.

The paper is organized as follows. In section 2, the results concerning the Landau quantization of the 2D heavy holes, as well as of the electrons, in the conduction band taking into account the Rashba spin–orbit interaction were described. On this base, the Hamiltonians describing the electron-radiation interaction and of the Coulomb electron–electron interaction in the presence of the Rashba spin–orbit coupling were deduced in sections 3 and 4, respectively. Section 5 is focused on the description of the magnetoexcitons in the model of a Bose gas. In section 6, the breaking of the gauge symmetry of the obtained Hamiltonians is introduced and the mixed photon–magnetoexciton–acoustical plasmon states are discussed. Section 7 offers conclusions.

First of all, we will describe the Landau quantization of the 2D heavy holes following [19, 22].

2. Landau quantization of the 2D heavy holes

The full Landau-Rashba Hamiltonian for 2D heavy holes was discussed in [19] following formulas (13)–(20). It can be expressed through the Bose-type creation and annihilation operators $a^{\dagger}$, a acting on the Fock quantum states $|n\rangle = \frac{(a^{\dagger})^n}{\sqrt{n!}}|0\rangle$, where $|0\rangle$ is the vacuum state of the harmonic oscillator. The Hamiltonian has the form [22]

$$\hat{H}_h = \hbar\omega_{ch}\left\{\left[\left(a^{\dagger}a+\frac{1}{2}\right)+\delta\left(a^{\dagger}a+\frac{1}{2}\right)^2\right]\hat{I}+i\beta 2\sqrt{2}\begin{vmatrix}0 & (a^{\dagger})^3\\ -a^3 & 0\end{vmatrix}\right\},$$
$$\hat{I}=\begin{vmatrix}1 & 0\\ 0 & 1\end{vmatrix} \tag{1}$$

with the denotations

$$\omega_{ch}=\frac{|e|H}{m_h c},\ \delta=\frac{|\delta_h E_z|\hbar^4}{l^4\hbar\omega_{ch}},\ \beta=\frac{\beta_h E_z}{l^3\hbar\omega_{ch}},\ l=\sqrt{\frac{\hbar c}{|e|H}}. \tag{2}$$

Parameter δ_h is not well known; therefore, different versions mentioned below were considered.

The exact solutions of the Pauli-type Hamiltonian are described by formulas (21)–(31) of [19]. In more detail, they were described in [22] and have the spinor form

$$\hat{H}_h\begin{vmatrix}f_1\\ f_2\end{vmatrix}=E_h\begin{vmatrix}f_1\\ f_2\end{vmatrix},\ f_1=\sum_{n=0}^{\infty}c_n|n\rangle,\ f_2=\sum_{n=0}^{\infty}d_n|n\rangle,\ \sum_{n=0}^{\infty}|c_n|^2+\sum_{n=0}^{\infty}|d_n|^2=1. \tag{3}$$

The first three solutions depend only on one quantum number m with values 0, 1, 2 as follows [6]:

$$E_h(m=0)=\hbar\omega_{ch}\left(\frac{1}{2}+\frac{\delta}{4}\right);|\Psi(m=0)\rangle=\begin{vmatrix}|0\rangle\\ 0\end{vmatrix},$$
$$E_h(m=1)=\hbar\omega_{ch}\left(\frac{3}{2}+\frac{9\delta}{4}\right);|\Psi(m=1)\rangle=\begin{vmatrix}|1\rangle\\ 0\end{vmatrix}, \tag{4}$$

$$E_h(m=2)=\hbar\omega_{ch}\left(\frac{5}{2}+\frac{25\delta}{4}\right);\left|\Psi(m=2)\right\rangle=\begin{vmatrix}\left|2\right\rangle\\0\end{vmatrix}.$$

All other solutions with $m\geq 3$ depend on two quantum numbers $(m-5/2)$ and $(m+1/2)$ and have the general expression

$$\varepsilon_h^{\pm}(m-\frac{5}{2};m+\frac{1}{2})=\frac{E_h^{\pm}(m-5/2;m+1/2)}{\hbar\omega_{ch}}=(m-1)+\frac{\delta}{8}\left[(2m+1)^2+(2m-5)^2\right]\pm$$
$$\pm\left(\frac{3}{2}+\frac{\delta}{8}\left[(2m+1)^2-(2m-5)^2\right]\right)^2+8\beta^2m(m-1)(m-2))^{1/2},\ m\geq 3. \tag{5}$$

The respective wave functions for $m=3$ and $m=4$ are

$$\left|\Psi_h^{\pm}(m=3)\right\rangle=\begin{vmatrix}c_3\left|3\right\rangle\\d_0\left|0\right\rangle\end{vmatrix}\text{and}\left|\Psi_h^{\pm}(m=4)\right\rangle=\begin{vmatrix}c_4\left|4\right\rangle\\d_1\left|1\right\rangle\end{vmatrix}. \tag{6}$$

They depend on coefficients c_m and d_{m-3}, which obey to the equations

$$c_m\left(m+\frac{1}{2}+\frac{\delta}{4}(2m+1)^2-\varepsilon_h\right)=-i\beta 2\sqrt{2}\sqrt{m(m-1)(m-2)}d_{m-3},$$
$$d_{m-3}\left(m-\frac{5}{2}+\frac{\delta}{4}(2m-5)^2-\varepsilon_h\right)=i\beta 2\sqrt{2}\sqrt{m(m-1)(m-2)}c_m, \tag{7}$$
$$|c_m|^2+|d_{m-3}|^2=1.$$

There are two different solutions $\varepsilon_h^{\pm}(m)$ at a given value of $m\geq 3$ and two different pairs of the coefficients $(c_m^{\pm},d_{m-3}^{\pm})$.

The dependences of parameters ω_{ch}, β, and δ on the electric and magnetic fields strengths may be represented for the GaAs-type quantum wells as follows $H=y$ T; $E_z=x$ kV/cm; $m_h=0.25m_0$; $\hbar\omega_{ch}=0.4y$ meV; $\beta=1.062\cdot10^{-2}x\sqrt{y}$; $\delta=10^{-4}Cxy$ with unknown parameter C, which will be varied in a larger interval of values. We cannot neglect the parameter C putting it equal to zero because, in this case, as was argued in [19] formula (10), the lower spinor branch of the heavy hole dispersion law

$$E_h^-(k_{\|})=\frac{\hbar^2\vec{k}_{\|}^2}{2m_h}-\left|\frac{\beta_hE_z}{2}\right|\left|\vec{k}_{\|}\right|^3$$

has an unlimited decreasing, deeply penetrating inside the semiconductor energy gap at great values of $\left|\vec{k}_{\|}\right|$. To avoid this unphysical situation, a positive quartic term $\left|\delta_hE_z\right|\vec{k}_{\|}^4$ was added in the starting Hamiltonian. The new dependences were compared with the drawings calculated in Fig. 2 of [19] in the case $E_z=10$ kV/cm and $C=10$. Four LLLs for heavy holes were selected in [19]. In addition to them, in [22], three other levels were studied as follows:

$$
\begin{aligned}
E_h(R_1) &= E_h^-(\frac{1}{2},\frac{7}{2});\\
E_h(R_2) &= E_h(m=0);\\
E_h(R_3) &= E_h^-(\frac{3}{2},\frac{9}{2});\\
E_h(R_4) &= E_h(m=1);\\
E_h(R_5) &= E_h^-(\frac{5}{2},\frac{11}{2});\\
E_h(R_6) &= E_h(m=2);\\
E_h(R_7) &= E_h^-(\frac{7}{2},\frac{13}{2}).
\end{aligned}
\tag{8}
$$

Their dependences on the magnetic field strength were represented in Figs. 1 and 2 of [22] at different parameters x and C; they are reproduced below.

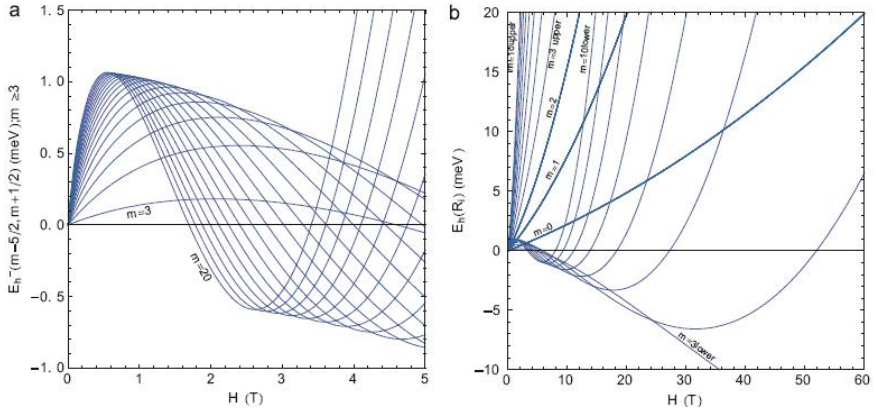

Fig. 1. (a) The lower branches of the heavy hole Landau quantization levels $E_h^-(m-5/2;m+1/2)$ for $m\geq 3$ at parameters $E_z=10$ kV/cm and $C=5.5$; (b) a general view of all the heavy hole Landau quantization levels with m=0,1,...,10 at the same parameters E_z and C. They are reproduced from Fig. 1 of [22].

The general view of the lower branches $E_h^-(m-\frac{5}{2},m+\frac{1}{2})$ of the heavy hole Landau quantization levels with $m\geq 3$ as a function of magnetic field strength is represented in Fig. 1a following formula (5). The upper branches exhibit a simpler monotonous behavior and are drawn together with some curves of the lower branches in Fig. 1b. All the lower branches in their initial parts have a linear increasing behavior up till they achieve the maximal values succeeded by the minimal values in the middle parts of their evolutions being transformed in the final quadratic increasing dependences. The values of the magnetic field strength corresponding to the minima and to the maxima decrease with increasing number m. These peculiarities can be compared with the case of Landau quantization of the 2D electron in the biased bilayer graphene described in [18]. The last-mentioned case is characterized by the initial dispersion law without parabolic part and by second order chirality terms. They both lead to dependences on magnetic field strength for the lower dispersion branches with sharp initial decreasing parts and minimal values succeeded by the quadratic increasing behavior. The differences between the initial dispersion

laws and chirality terms in two cases of bilayer graphene and of heavy holes lead to different intersections and degeneracies of the Landau levels.

The spinor-type envelope wave functions of the heavy holes in the coordinate representation look as follows [22]:

$$\begin{aligned}
&\left|\psi_h(\varepsilon_m,q;x,y)\right\rangle=\frac{e^{iqx}}{\sqrt{L_x}}\begin{vmatrix}\varphi_m(y+ql^2)\\0\end{vmatrix},\\
&m=0,1,2.\\
&\left|\psi_h(\varepsilon_m^{\pm},q;x,y)\right\rangle=\frac{e^{iqx}}{\sqrt{L_x}}\begin{vmatrix}c_m^{\pm}\varphi_m(y+ql^2)\\d_{m-3}^{\pm}\varphi_{m-3}(y+ql^2)\end{vmatrix},\\
&m\geq 3
\end{aligned}\tag{9}$$

The valence electrons in comparison with the holes are characterized by the opposite signs of the spin projections, wave vector, and charge. The respective envelope wave functions can be obtained from the previous ones by the procedure

$$\left|\psi_v(\varepsilon,q;x,y)\right\rangle=i\hat{\sigma}_y\left|\psi_h(\varepsilon,-q;x,y)\right\rangle^*\tag{10}$$

where $\hat{\sigma}_y$ is the Pauli matrix. In coordinate representation, they are as follows:

$$\begin{aligned}
&\left|\psi_v(\varepsilon_m,q;x,y)\right\rangle=\frac{e^{iqx}}{\sqrt{L_x}}\begin{vmatrix}0\\-\varphi_m^*(y-ql^2)\end{vmatrix},\\
&m=0,1,2.\\
&\left|\psi_v(\varepsilon_m^{\pm},q;x,y)\right\rangle=\frac{e^{iqx}}{\sqrt{L_x}}\begin{vmatrix}d_{m-3}^{\pm *}\varphi_{m-3}^*(y-ql^2)\\-c_m^{\pm *}\varphi_m^*(y-ql^2)\end{vmatrix},\\
&m\geq 3
\end{aligned}\tag{11}$$

To obtain the full valence electron Bloch wave functions, expressions (11) must be multiplied by the periodic parts. In the p-type valence band, they have the form $\frac{1}{\sqrt{2}}(U_{v,p,x,q}(x,y)\pm iU_{v,p,y,q}(x,y))$ and are characterized by the orbital momentum projections $M_v=\pm 1$, respectively. The hole orbital projections $M_h=-M_v$ have opposite signs in comparison with the valence electron. The full Bloch wave functions of the valence electrons are now characterized by a supplementary quantum number M_v side by side with the previous ones ε_m, $\varepsilon^{\pm}{}_m$ and q as follows:

$$\begin{aligned}
&\left|\psi_v(M_v,\varepsilon_m,q;x,y)\right\rangle=\frac{1}{\sqrt{2}}(u_{v,p,x,q}(\vec{r})\pm iU_{v,p,y,q}(\vec{r}))\frac{e^{iqx}}{\sqrt{L_x}}\begin{vmatrix}0\\-\varphi_m^*(y-ql^2)\end{vmatrix},\\
&m=0,1,2;M_v=\pm 1,\\
&\left|\psi_v(M_v,\varepsilon_m^{\pm},q;x,y)\right\rangle=\frac{1}{\sqrt{2}}(u_{v,p,x,q}(\vec{r})\pm iU_{v,p,y,q}(\vec{r}))\frac{e^{iqx}}{\sqrt{L_x}}\begin{vmatrix}d_{m-3}^{\pm *}\varphi_{m-3}^*(y-ql^2)\\-c_m^{\pm *}\varphi_m^*(y-ql^2)\end{vmatrix},\\
&m\geq 3, M_v=\pm 1.
\end{aligned}\tag{12}$$

From this multitude of valence electron wave functions, the more important of them are characterized by the values of ε_m^- with $m=3$ and 4 as well as by ε_m with $m=0,1$. These four

lowest hole energy levels being combined with two projections $M_h \pm 1$ form a set of eight lowest hole states, which will be taken into account below.

Now, for completeness, we will remember the main results obtained by Rashba [1] in the case of the electron conduction band. They are required to obtain a full description of the 2D e–h pair and of a 2D magnetoexciton under the condition of the Landau quantization under the influence of the RSOC.

The LLL of the conduction electron in the presence of the RSOC was obtained in [1]:

$$\left|\Psi_{\mathrm{e}}\left(R_1, p; x_e, y_e\right)\right\rangle = \frac{\mathrm{e}^{ipx_{\mathrm{e}}}}{\sqrt{L_x}}\left|\begin{matrix} a_0\varphi_0(y_{\mathrm{e}}). \\ b_1\varphi_1(y_{\mathrm{e}}) \end{matrix}\right|;$$

$$\varepsilon_{\mathrm{e}R_1} = 1 - \sqrt{\frac{1}{4} + 2\alpha^2}; |a_0|^2 + |b_1|^2 = 1 \tag{13}$$

$$|a_0|^2 = \frac{1}{1 + \dfrac{2\alpha^2}{\left[\dfrac{1}{2} + \sqrt{\dfrac{1}{4} + 2\alpha^2}\right]^2}}; |b_1|^2 = \frac{2\alpha^2 |a_0|^2}{\left[\dfrac{1}{2} + \sqrt{\dfrac{1}{4} + 2\alpha^2}\right]^2}.$$

The next electron level higher situated on the energy scale is characterized by the pure spin oriented state

$$\left|\Psi_{\mathrm{e}}\left(R_2, p; x_{\mathrm{e}}, y_{\mathrm{e}}\right)\right\rangle = \frac{\mathrm{e}^{ipx_{\mathrm{e}}}}{\sqrt{L_x}}\left|\begin{matrix} 0 \\ \varphi_0(y_{\mathrm{e}}) \end{matrix}\right|; \varepsilon_{\mathrm{e}R_2} = \frac{1}{2}. \tag{14}$$

Two LLLs for conduction electron are characterized by the values of $m_{\mathrm{e}} = 0.067 m_0$, $\hbar\omega_{\mathrm{ce}} = 1.49\ \mathrm{meV}\cdot y$ and parameter $\alpha = 8\cdot 10^{-3} x / \sqrt{y}$. They are denoted as

$$E_{\mathrm{e}}(R_1) = \hbar\omega_{\mathrm{ce}}\left(1 - \sqrt{\frac{1}{4} + 2\alpha^2}\right),$$

$$E_{\mathrm{e}}(R_2) = \hbar\omega_{\mathrm{ce}}\frac{1}{2}. \tag{15}$$

The lowest Landau energy level for electron $E_{\mathrm{e}}(R_1)$ has a nonmonotonous anomalous dependence on magnetic field strength near the point $H = 0\ \mathrm{T}$. It is due to the singular dependence of the RSOC parameter $\alpha^2 = 6.4\cdot 10^{-5} x^2 / y$, which, in the total energy level expression, is compensated for by factor $\hbar\omega_{\mathrm{ce}}$ of the cyclotron energy, where $\hbar\omega_{\mathrm{ce}} = 1.49\, y$ meV. As earlier, parameters x and y are related with electric field $E_z = x$ kV/cm and magnetic field $H = y$ T. The second electron Landau energy level has a simple linear dependence on H.

The full Bloch wave functions for conduction electrons including their s-type periodic parts look as follows:

$$\left|\psi_c(s, R_1, p; x, y)\right\rangle = U_{c,s,p}(\vec{r})\frac{e^{ipx}}{\sqrt{L_x}}\left|\begin{matrix} a_0\varphi_0(y - pl^2) \\ b_1\varphi_1(y - pl^2) \end{matrix}\right|,$$

$$\left|\psi_c(s, R_2, p; x, y)\right\rangle = U_{c,s,p}(\vec{r})\frac{e^{ipx}}{\sqrt{L_x}}\left|\begin{matrix} 0 \\ \varphi_0(y - pl^2) \end{matrix}\right|. \tag{16}$$

Two lowest Rashba-type states for conduction electron will be combined with eight LLLs for heavy holes and with the corresponding states of the valence electrons. The e–h pair will be characterized by 16 states. Heaving the full set of the electron Bloch wave functions in conduction and in the valence bands one can construct the Hamiltonian describing in second quantization representation the Coulomb electron-electron interaction as well as the electron-radiation interaction. These tow tasks will be described in the next sections of our review paper. The results obtained earlier in [19, 22] taking into account only 8 e–h states will be supplemented below.

3. Electron-radiation interaction in the presence of the Rashba spin-orbit coupling

In [17, 21] the Hamiltonian of the electron-radiation interaction in the second quantization representation for the case of two-dimensional (2D) coplanar e–h system in a strong perpendicular magnetic field was discussed. The s-type conduction-band electrons with spin projections $s_z = \pm 1/2$ along the magnetic field direction and the heavy holes with the total momentum projections $j_z = \pm 3/2$ in the p-type valence band were taken into account. Their orbital Bloch wave functions are similar to $(x \pm iy)$ expressions with the orbital momentum projections $M = \pm 1$ on the same selected direction. The Landau quantization of the 2D electrons and holes was described in the Landau gauge with oscillator type motion in one in-plane direction characterized by the quantum numbers n_e and n_h and with the free translational motion described by the uni-dimensional(1D) wave numbers p and q in another in-plane direction perpendicular to the previous one. The electron and hole creation and annihilation operators $a^+_{s_z,n_e,p}$, $a_{s_z,n_e,p}$, and $b^+_{j_z,n_h,q}$, $b_{j_z,n_h,q}$ were introduced correspondingly. The Zeeman effect and the Rashba spin–orbit coupling in [17, 21] were not taken into account.

The electrons and holes have a free orbital motion on the surface of the layer with the area S and are completely confined in $\vec{a}_3$ direction. The degeneracy of their Landau levels equals $N = S/(2\pi l_0^2)$, where l_0 is the magnetic length. In contrast, the photons were supposed to move in any direction in the three-dimensional (3D) space with the wave vector $\vec{k}$ arbitrary oriented as regards the 2D layer as it is represented in the Fig.2 reproduced from [17]. There are three unit vectors $\vec{a}_1$, $\vec{a}_2$, $\vec{a}_3$, the first two being in-plane oriented, whereas the third $\vec{a}_3$ is perpendicular to the layer. We will use the 3D and 2D wave vectors $\vec{k}$ and $\vec{k}_\parallel$ and will introduce circular polarization vectors $\vec{\sigma}_M$ for the valence electrons, heavy holes, and magnetoexcitons as follows:

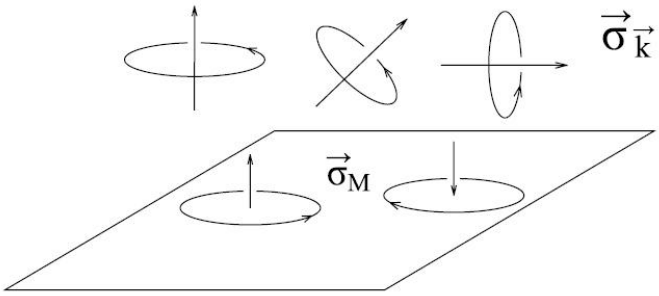

Fig. 2. Reciprocal orientations of circularly polarized vectors $\vec{\sigma}_{\vec{k}}$ and $\vec{\sigma}_M$ reproduced from [17].

$$\vec{k}=\vec{k}_{\parallel}+\vec{a}_3k_z;\vec{k}_{\parallel}=\vec{a}_1k_x+\vec{a}_2k_y;\vec{\sigma}_M=\frac{1}{\sqrt{2}}(\vec{a}_1\pm i\vec{a}_2);M=\pm1. \tag{17}$$

The photons are characterized by two linear vectors $\vec{e}_{k,j}$ or by two circular polarization vectors $\vec{\sigma}_{\vec{k}}^{\pm}$ obeying the transversality conditions:

$$\vec{\sigma}_{\vec{k}}^{\pm}=\frac{1}{\sqrt{2}}(\vec{e}_{\vec{k},1}\pm i\vec{e}_{\vec{k},2});(\vec{e}_{k,j}\cdot\vec{k})=0;\ j=1,2. \tag{18}$$

The photon creation and annihilation operators can be introduced in two different polarizations as follows:

$$\begin{aligned}&C_{\vec{k},\pm}=\frac{1}{\sqrt{2}}\left(C_{\vec{k},1}\pm iC_{\vec{k},2}\right);\left(C_{\vec{k},\pm}\right)^{\dagger}=\frac{1}{\sqrt{2}}\left(C_{\vec{k},1}^{\dagger}\mp iC_{\vec{k},2}^{\dagger}\right);\\&\sum_{j=1}^{2}\vec{e}_{\vec{k},j}C_{\vec{k},j}=C_{\vec{k},-}\vec{\sigma}_{\vec{k}}^{+}+C_{\vec{k},+}\vec{\sigma}_{\vec{k}}^{-};\\&\sum_{j=1}^{2}\vec{e}_{\vec{k},j}C_{\vec{k},j}^{\dagger}=\left(C_{\vec{k},-}\right)^{\dagger}\vec{\sigma}_{\vec{k}}^{-}+\left(C_{\vec{k},+}\right)^{\dagger}\vec{\sigma}_{\vec{k}}^{+}.\end{aligned} \tag{19}$$

The reciprocal orientations of circular polarizations $\vec{\sigma}_{\vec{k}}^{\pm}$ and $\vec{\sigma}_M$ will determine the values of scalar products $(\vec{\sigma}_{\vec{k}}^{\pm}\cdot\vec{\sigma}_M^{*})$. The electron-radiation interaction describing only the band-to-band quantum transitions with the participation of the e–h pairs in the presence of a strong perpendicular magnetic field was obtained in [17] and can be used as initial expression for obtaining the interaction of 2D magnetoexcitons with the electromagnetic field.

These results will be generalized below taking into account the Rashba spin−orbit coupling, which means the use of the spinor-type wave functions (12) and (16) instead of the scalar ones [17, 21]. The Hamiltonian looks as

$$\begin{aligned}&H_{e-rad}=\left(-\frac{e}{m_0}\right)\sum_{\vec{k}(\vec{k}_{\parallel},\vec{k}_z)}\sqrt{\frac{2\pi\hbar}{V\omega_{\vec{k}}}}\sum_{i=1,2}\sum_{M_v=\pm1}\sum_{\varepsilon=\varepsilon_m,\varepsilon_m^{-}}\sum_{g,q}\{[C_{\vec{k},-}\vec{\sigma}_{\vec{k}}^{+}+C_{\vec{k},+}\vec{\sigma}_{\vec{k}}^{-}]\bullet\\&\bullet[\vec{P}(c,R_i,g;v,M_v,\varepsilon,q;\vec{k})a_{c,R_i,g}^{\dagger}a_{v,M_v,\varepsilon,q}+\vec{P}(v,M_v,\varepsilon,q;c,R_i,g;\vec{k})a_{v,M_v,\varepsilon,q}^{\dagger}a_{c,R_i,g}]+\\&+[(C_{\vec{k},-})^{\dagger}\vec{\sigma}_{\vec{k}}^{-}+(C_{\vec{k},+})^{\dagger}\vec{\sigma}_{\vec{k}}^{+}]\bullet[\vec{P}(c,R_i,g;v,M_v,\varepsilon,q;-\vec{k})\times\\&\times a_{c,R_i,g}^{\dagger}a_{v,M_v,\varepsilon,q}+\vec{P}(v,M_v,\varepsilon,q;c,R_i,g;-\vec{k})a_{v,M_v,\varepsilon,q}^{\dagger}a_{c,R_i,g}]\}\end{aligned} \tag{20}$$

The matrix elements will be discussed below. One of them has the form

$$\begin{aligned}&\vec{P}(c,R_1,g;v,M_v,\varepsilon^{-}{}_m,q;\vec{k})=\int d^2\vec{r}\left\langle\hat{\psi}_{c,R_i,g}(\vec{r})\middle|e^{i\vec{k}\vec{r}}\hat{\vec{p}}\middle|\hat{\psi}_{v,M_v,\varepsilon^{-}{}_m,q}(\vec{r})\right\rangle=\\&\frac{a_0^{*}d_{m-3}^{-*}}{\sqrt{2}L_x}\int d^2\vec{r}U_{c,s,g}^{*}(\vec{r})e^{-igx}\varphi_0^{*}(y-gl^2)e^{i\vec{k}\vec{r}}(\vec{a}_1\hat{p}_x+\vec{a}_2\hat{p}_y)(U_{v,p,x,q}(\vec{r})\pm iU_{v,p,y,q}(\vec{r}))e^{iqx}\varphi_{m-3}^{*}(y-pl^2)-\\&-\frac{b_1^{*}c_m^{-*}}{\sqrt{2}L_x}\int d^2\vec{r}U_{c,s,g}^{*}(\vec{r})e^{-igx}\varphi_1^{*}(y-gl^2)e^{i\vec{k}\vec{r}}(\vec{a}_1\hat{p}_x+\vec{a}_2\hat{p}_y)(U_{v,p,x,q}(\vec{r})\pm iU_{v,p,y,q}(\vec{r}))e^{iqx}\varphi_m^{*}(y-pl^2)\end{aligned} \tag{21}$$

One can represent the 2D coordinate vector $\vec{r}$ as a sum $\vec{r}=\vec{R}+\vec{\rho}$ of lattice point vector $\vec{R}$ and small vector $\vec{\rho}$ changing inside the unit lattice cell with lattice constant a_0 and volume $v_0=a_0^3$.

Any 2D semiconductor layer has at least minimal width a_0 and periodic parts $U_{nk}(\vec{r})$ are determined inside the elementary lattice cell. Periodic parts $U_{nk}(\vec{r})$ do not depend on $\vec{R}$ because $U_{nk}(\vec{R}+\vec{\rho})=U_{nk}(\vec{\rho})$. On the other hand, envelope functions $\varphi_n(\vec{r})$ describing the Landau quantization have a spread of the order of magnetic length l_0 which is much greater than a_0 ($l_0 >> a_0$). It means that they hardly depend on $\vec{\rho}$, i.e., $\varphi_n(\vec{R}+\vec{\rho})\cong\varphi_n(\vec{R})$. The matrix elements (21) contains some functions that do not depend on $\vec{R}$ and other ones that do not depend on $\vec{\rho}$. Only the plane wave $e^{i\vec{k}\vec{r}}=e^{i\vec{k}\vec{R}+i\vec{k}\vec{\rho}}$ contains both of them. Derivative $\frac{\partial}{\partial\vec{r}}$ acts in the same manner on functions $U_{nk}(\vec{\rho})$ and $\varphi_n(\vec{R})$ because $\vec{R}$ and $\vec{\rho}$ are the components of $\vec{r}$. These properties suggested transforming the 2D integral on variable $\vec{r}$ in two separate integrals on variables $\vec{R}$ and $\vec{\rho}$ as follows:

$$\int d^2\vec{r}A(\vec{R})B(\vec{\rho})=\sum_{\vec{R}}A(\vec{R})\int d^2\vec{\rho}B(\vec{\rho})=\sum_{\vec{R}}A(\vec{R})a_0^2\frac{1}{v_0}\int d^3\vec{\rho}B(\vec{\rho})=\int d^2\vec{R}A(\vec{R})\frac{1}{v_0}\int_{v_0}d\vec{\rho}B(\vec{\rho}) \qquad (22)$$

Here the small value of a_0^2 is substituted by the infinitesimal differential value $d^2\vec{R}$ because $A(\vec{R})$ is a smooth function on $\vec{R}$. The integrals on te volume v_0 of the elementary lattice cell contain the quickly oscillating periodic parts $U_{c,s,g}(\vec{\rho})$ and $U_{v,p,i,q}(\vec{\rho})$ belonging to s-type conduction band and to p-type valence band. They have different parities and obey to selection rules

$$\begin{aligned}&\frac{1}{v_0}\int_{v_0}d\vec{\rho}U^*_{c,s,g}(\vec{\rho})e^{ik_y\rho_y}U_{v,p,i,q}(\vec{\rho})=0,\ \ i,j=x,y\\&\frac{1}{v_0}\int_{v_0}d\vec{\rho}U^*_{c,s,g}(\vec{\rho})e^{ik_y\rho_y}\frac{\partial}{\partial\rho_i}U_{v,p,j,q}(\vec{\rho})=0,\ \ \text{if } i\neq j\end{aligned} \qquad (23)$$

The case $i=j$ is different from zero and gives rise to the expression

$$\frac{1}{v_0}\int_{v_0}d\vec{\rho}U^*_{c,s,g}(\vec{\rho})e^{ik_y\rho_y}\frac{\partial}{\partial\rho_i}U_{v,pi,g-k_x}(\vec{\rho})=P_{cv}(\vec{k}_{\|},g) \qquad (24)$$

The last integral in the zeroth approximation is of the allowed type in the definition of Elliott [26, 27] and can be considered as a constant $P_{cv}(\vec{k}_{\|},g)\approx P_{cv}(0)$ which does not depend on wave vectors $\vec{k}_{\|}$ and g. Due to these selection rules, derivatives $\partial/\partial\vec{r}$ in expression (21) must be taken only from the periodic parts $U_{v,p,i,q}(\vec{\rho})$ because all other integrals vanish.

The integration on variable R_x engages only the plane wave functions and gives rise to the selection rule for the 1D wave numbers g,q,k_x as follows:

$$\frac{1}{L_x}\int\ e^{iR_x(q-g+k_x)}=\frac{2\pi}{L_x}\delta(q-g+k_x)=\delta_{kr}(q,g-k_x) \qquad (25)$$

The integral on variable R_y engages only Landau quantization functions $\varphi_n(R_y)$ and gives rise to the third selection rule concerning numbers n_e and n_h of the Landau levels for electrons and holes. It looks as

$$\int_{-\infty}^{\infty} dR_y \varphi^*_{n_e}(R_y - gl_0^2)\varphi^*_{n_h}(R_y - (g-k_x)l_0^2)e^{ik_y R_y} = e^{ik_y g l_0^2} e^{-i\frac{k_x k_y}{2}l_0^2}\tilde{\phi}(n_e, n_h; \vec{k}_\parallel), \quad (26)$$

where

$$\tilde{\phi}(n_e, n_h; \vec{k}_\parallel) = \int_{-\infty}^{\infty} dy \varphi_{n_e}(y - \frac{k_x l_0^2}{2})\varphi_{n_h}(y + \frac{k_x l_0^2}{2})e^{ik_y y},$$

$$e^{-i\frac{k_x k_y}{2}l_0^2}\tilde{\phi}(n_e, n_h; \vec{k}_\parallel) = \phi(n_e, n_h; \vec{k}_\parallel).$$

Here, we took into account that Landau quantization functions $\varphi_n(y)$ are real.

This selection rule coincides with formula (30) in the absence of the RSOC, and its interpretation remains the same. Once again one can underlain that, during the dipole-active band-to-band quantum transition, the numbers of the Landau levels in the initial starting band, as well as in the final arriving band, coincide, i.e., $n_e = n_h$. It is equally true both in the absence and in the presence of the RSOC.

Three separate integrations on $\vec{\rho}, R_x$ and R_y taking into account selection rules (23), (25), and (26) lead to the expression

$$\vec{P}(c, R_1, g; v, M_v, \varepsilon_m^-, q; \vec{k}_\parallel) = \delta_{kr}(q, g - k_x)\vec{\sigma}_{M_v} P_{cv}(0) e^{ik_y g l_0^2} \times$$
$$\times e^{-i\frac{k_x k_y}{2}l_0^2}[a_0^* d_{m-3}^{-*}\tilde{\phi}(0, m-3; \vec{k}_\parallel) - b_1^* c_m^{-*}\tilde{\phi}(1, m; \vec{k}_\parallel)], \quad (27)$$
$$m \geq 3$$

Here, the vectors of circular polarizations $\vec{\sigma}_{M_v}$ describing the valence electron states were introduced following formula (17). One can introduce also the vectors of the heavy hole circular polarizations $\vec{\sigma}_{M_h}$ in the form

$$\vec{\sigma}_{M_v} = \frac{1}{\sqrt{2}}(\vec{a}_1 \pm i\vec{a}_2), \quad M_v = \pm 1,$$
$$\vec{\sigma}_{M_h} = \vec{\sigma}^*_{M_v} = \frac{1}{\sqrt{2}}(\vec{a}_1 \mp i\vec{a}_2), \quad M_h = \mp 1 \quad (28)$$

The magnetoexciton states are characterized by quantum numbers M_h, R_i, ε and by wave vectors $\vec{k}_\parallel$.

The general expressions for the matrix elements are as follows:

$$\vec{P}(c, R_i, g; v, M_v, \varepsilon, q; \vec{k}_\parallel) = \delta_{kr}(q, g - k_x)\vec{\sigma}_{M_v} P_{cv}(0) e^{ik_y g l_0^2} T(cR_i, \varepsilon; \vec{k}_\parallel) e^{-i\frac{k_x k_y}{2}l_0^2}, \quad (29)$$
$$i = 1, 2,\ \mathrm{M}_v = \pm 1,\ \varepsilon = \varepsilon_m,\ \text{with } m = 0, 1, 2, \text{ and } \varepsilon = \varepsilon_m^-,\ \text{with } m \geq 3$$

Coefficients $T(cR_i, \varepsilon; \vec{k}_\parallel)$ have the forms

$$
\begin{aligned}
&T(R_1,\varepsilon_m^-;\vec{k}_\parallel)=[a_0^* d_{m-3}^{-*}\tilde{\phi}(0,m-3;\vec{k}_\parallel)-b_1^* c_m^{-*}\tilde{\phi}(1,m;\vec{k}_\parallel)],\\
&m\geq 3,\\
&T(R_1,\varepsilon_m;\vec{k}_\parallel)=[-b_1^*\tilde{\phi}(1,m;\vec{k}_\parallel)],\\
&m=0,1,2,\\
&T(R_2,\varepsilon_m^-;\vec{k}_\parallel)=[-c_m^{-*}\tilde{\phi}(0,m;\vec{k}_\parallel)],\\
&m\geq 3,\\
&T(R_2,\varepsilon_m;\vec{k})=[-\tilde{\phi}(0,m;\vec{k}_\parallel)],\\
&m=0,1,2
\end{aligned}
\tag{30}
$$

The other matrix elements can be calculated in a similar way. They are

$$
\begin{aligned}
&\vec{P}(v,M_v,\varepsilon,q;c,R_i,g;-\vec{k}_\parallel)=\vec{P}^*(c,R_i,g;v,M_v,\varepsilon,q;\vec{k}_\parallel)=\\
&=\delta_{kr}(q,g-k_x)\vec{\sigma}_{M_v}^* P_{cv}^*(0)e^{-ik_y g l_0^2}e^{i\frac{k_x k_y}{2}l_0^2}T^*(R_i,\varepsilon;\vec{k}_\parallel),\\
&\vec{P}(c,R_i,g;v,M_v,\varepsilon,q;-\vec{k}_\parallel)=\delta_{kr}(q,g+k_x)\vec{\sigma}_{M_v}P_{cv}(0)e^{-ik_y g l_0^2}e^{-i\frac{k_x k_y}{2}l_0^2}T(R_i,\varepsilon;-\vec{k}_\parallel),\\
&\vec{P}(v,M_v,\varepsilon,q;c,R_i,g;\vec{k}_\parallel)=\delta_{kr}(q,g+k_x)\vec{\sigma}_{M_v}^* P_{cv}^*(0)e^{ik_y g l_0^2}e^{i\frac{k_x k_y}{2}l_0^2}T^*(R_i,\varepsilon;-\vec{k}_\parallel)
\end{aligned}
\tag{31}
$$

They permit calculating the electron operator parts in Hamiltonian (20) and expressing them in terms of the magnetoexciton creation and annihilation operators determined as follows:

$$
\hat{\psi}_{ex}^\dagger(\vec{k}_\parallel,M_h,R_i,\varepsilon)=\frac{1}{\sqrt{N}}\sum_t e^{ik_y t l_0^2}a^\dagger_{R_i,\frac{k_x}{2}+t}b^\dagger_{M_h,\varepsilon,\frac{k_x}{2}-t}
\tag{32}
$$

Here, he electron and hole creation and annihilation operator were introduced

$$
\begin{aligned}
&a_{R_i,g}=a_{c,R_i,g},\\
&a_{v,M_v,\varepsilon,q}=b^\dagger_{-M_h,\varepsilon,-q}
\end{aligned}
\tag{33}
$$

Here, we have supposed that the Coulomb electron–hole interaction leading to the formation of the magnetoexciton is greater than the magnetoexciton–photon interaction leading to the formation of the magnetopolariton. It means that the ionization potential of the magnetoexciton I_l is greater than the Rabi energy $\hbar|\omega_R|\approx\frac{|e|}{m_0 l_0}|P_{cv}(0)|\sqrt{\frac{\hbar}{L_z\omega_{\vec{k}}}}$. It was determined in [21].

The existence of the phase factors of the type $e^{\pm ik_y g l_0^2}$ in expressions (29) and (31) similar with that appearing in the definitions of the magnetoexciton creation operators permits obtaining the expressions

$$\begin{aligned}
&\sum_{q,g}\vec{P}(c,R_i,g;v,M_v,\varepsilon,q;\vec{k}_\parallel)a^\dagger_{c,R_i,g}a_{v,M_v,\varepsilon,q}=\\
&=\vec{\sigma}^*_{M_h}P_{cv}(0)T(R_i,\varepsilon;\vec{k}_\parallel)\sqrt{N}\hat{\psi}^\dagger_{ex}(\vec{k}_\parallel,M_h,R_i,\varepsilon),\\
&\sum_{q,g}\vec{P}(v,M_v,\varepsilon,q;c,R_i,g;-\vec{k}_\parallel)a^\dagger_{v,M_v,\varepsilon,q}a_{c,R_i,g}=\\
&=\vec{\sigma}_{M_h}P^*{}_{cv}(0)T^*(R_i,\varepsilon;\vec{k}_\parallel)\sqrt{N}\hat{\psi}_{ex}(\vec{k}_\parallel,M_h,R_i,\varepsilon),\\
&\sum_{q,g}\vec{P}(c,R_i,g;v,M_v,\varepsilon,q;-\vec{k}_\parallel)a^\dagger_{c,R_i,g}a_{v,M_v,\varepsilon,q}=\\
&=\vec{\sigma}^*_{M_h}P_{cv}(0)T(R_i,\varepsilon;-\vec{k}_\parallel)\sqrt{N}\hat{\psi}^\dagger_{ex}(-\vec{k}_\parallel,M_h,R_i,\varepsilon),\\
&\sum_{q,g}\vec{P}(v,M_v,\varepsilon,q;c,R_i,g;\vec{k}_\parallel)a^\dagger_{v,M_v,\varepsilon,q}a_{c,R_i,g}=\\
&=\vec{\sigma}_{M_h}P^*{}_{cv}(0)T^*(R_i,\varepsilon;-\vec{k}_\parallel)\sqrt{N}\hat{\psi}_{ex}(-\vec{k}_\parallel,M_h,R_i,\varepsilon),
\end{aligned}\tag{34}$$

In [21], the Hamiltonian of the electron-radiation interaction was deduced in the absence of the RSOC. In its presence, the mentioned Hamiltonian also can be expressed in a compact form in terms of the photon and magnetoexciton creation and annihilation operators. As earlier, we introduced the values $N=S/2\pi l_0^2$, $V=SL_z$, where L_z is the size of the 3D space in direction perpendicular to the layer. In the case of microcavity L_z equals cavity length L_c. The electron-radiation interaction has the form

$$\begin{aligned}
&\hat{H}_{e-rad}=\left(-\frac{e}{m_0 l_0}\right)\sum_{\vec{k}(\vec{k}_\parallel,k_z)}\sum_{M_h=\pm1}\sum_{i=1,2}\sum_{\varepsilon=\varepsilon_m,\varepsilon_m^-}\sqrt{\frac{\hbar}{L_z\omega_{\vec{k}}}}\times\\
&\times\Big\{P_{cv}(0)T\left(R_i,\varepsilon,\vec{k}_\parallel\right)\Big[C_{\vec{k},-}\left(\vec{\sigma}^+_{\vec{k}}\cdot\vec{\sigma}^*_{M_h}\right)+C_{\vec{k},+}\left(\vec{\sigma}^-_{\vec{k}}\cdot\vec{\sigma}^*_{M_h}\right)\Big]\hat{\Psi}^\dagger_{ex}(\vec{k}_\parallel,M_h,R_i,\varepsilon)+\\
&+P^*{}_{cv}(0)T^*\left(R_i,\varepsilon,\vec{k}_\parallel\right)\Big[\left(C_{\vec{k},-}\right)^\dagger\left(\vec{\sigma}^-_{\vec{k}}\cdot\vec{\sigma}_{M_h}\right)+\left(C_{\vec{k},+}\right)^\dagger\left(\vec{\sigma}^+_{\vec{k}}\cdot\vec{\sigma}_{M_h}\right)\Big]\hat{\Psi}_{ex}(\vec{k}_\parallel,M_h,R_i,\varepsilon)+\\
&+P_{cv}(0)T\left(R_i,\varepsilon,-\vec{k}_\parallel\right)\Big[\left(C_{\vec{k},-}\right)^\dagger\left(\vec{\sigma}^-_{\vec{k}}\cdot\vec{\sigma}^*_{M_h}\right)+\left(C_{\vec{k},+}\right)^\dagger\left(\vec{\sigma}^+_{\vec{k}}\cdot\vec{\sigma}^*_{M_h}\right)\Big]\hat{\Psi}^\dagger_{ex}(-\vec{k}_\parallel,M_h,R_i,\varepsilon)+\\
&+P^*{}_{cv}(0)T^*\left(R_i,\varepsilon,-\vec{k}_\parallel\right)\Big[C_{\vec{k},-}\left(\vec{\sigma}^+_{\vec{k}}\cdot\vec{\sigma}_{M_h}\right)+C_{\vec{k},+}\left(\vec{\sigma}^-_{\vec{k}}\cdot\vec{\sigma}_{M_h}\right)\Big]\hat{\Psi}_{ex}(-\vec{k}_\parallel,M_h,R_i,\varepsilon)\Big\}
\end{aligned}\tag{35}$$

This expression is similar to the Hamiltonian in the absence of the RSOC. Now the Coulomb interaction between charged carriers in the presence of the RSOC will be investigated.

4. The Coulomb interaction in the 2D electron-hole system under the influence of the Rashba spin-orbit coupling

The Coulomb interaction in the 2D e–h system taking into account the Rashba spin–orbit coupling was discussed in [19, 22]. Below, we will remind these results including all valence electron states (12). In the present description, the multicomponent electron field contains a larger variety of the valence band states than in [19, 22]. For the very beginning, the properties of the density operator of electron field $\hat{\rho}(\vec{r})$ and of its Fourier components $\hat{\rho}(\vec{Q})$ will be discussed. To this end, the Fermi-type creation and annihilation operators of the electron on different states

were introduced. They are denoted as $a^{\dagger}_{R_i,g}, a_{R_i,g}$ for the conduction band Rashba-type states (16) $\left|\psi_c(R_i,g;r)\right\rangle$, as $a^{\dagger}_{M_v,\varepsilon_m,g}, a_{M_v,\varepsilon_m,g}$ for the spinor valence band states (12) $\left|\psi_v(M_v,\varepsilon_m,g;r)\right\rangle$ and as $a^{\dagger}_{M_v,\varepsilon_m^-,g}, a_{M_v,\varepsilon_m^-,g}$ for other spinor valence band states (12) $\left|\psi_v(M_v,\varepsilon_m^-,g;r)\right\rangle$. These spinor-type functions have a form of a column with two components corresponding to two spin projections on the direction of the magnetic field. The conjugate functions $\left\langle\psi_c(R_i,g;r)\right|$, $\left\langle\psi_c(R_i,g;r)\right|$ and $\left\langle\psi_v(M_v,\varepsilon_m^-,g;r)\right|$ have a form of a row with two components conjugate to the components of the columns. With the aid of the electron creation and annihilation operators and the spinor-type wave functions, creation and annihilation operators $\hat{\Psi}^{\dagger}(r)$ and $\hat{\Psi}(r)$ of the multi-component electron field can be written as

$$\begin{aligned}
&\hat{\Psi}(r)=\sum_{i=1,2}\sum_{g}\left|\psi_c(R_i,g;r)\right\rangle a_{R_i,g}+\sum_{M_v}\sum_{\varepsilon_m}\sum_{g}\left|\psi_v(M_v,\varepsilon_m,g;r)\right\rangle a_{M_v,\varepsilon_m,g}+\\
&+\sum_{M_v}\sum_{\varepsilon_m^-}\sum_{g}\left|\psi_v(M_v,\varepsilon_m^-,g;r)\right\rangle a_{M_v,\varepsilon_m^-,g},\\
&\hat{\Psi}^{\dagger}(r)=\sum_{i=1,2}\sum_{g}\left\langle\psi_c(R_i,g;r)\right| a^{\dagger}_{R_i,g}+\sum_{M_v}\sum_{\varepsilon_m}\sum_{g}\left\langle\psi_v(M_v,\varepsilon_m,g;r)\right| a^{\dagger}_{M_v,\varepsilon_m,g}+\\
&+\sum_{M_v}\sum_{\varepsilon_m^-}\sum_{g}\left\langle\psi_v(M_v,\varepsilon_m^-,g;r)\right| a^{\dagger}_{M_v,\varepsilon_m^-,g}
\end{aligned} \tag{36}$$

The density operator of electron field $\hat{\rho}(\vec{r})$ and its Fourier components $\hat{\rho}(\vec{Q})$ are determined by the expressions

$$\begin{aligned}
&\hat{\rho}(\vec{r})=\hat{\Psi}^{\dagger}(r)\hat{\Psi}(r),\\
&\hat{\rho}(\vec{Q})=\int d^2\vec{r}\,\hat{\rho}(\vec{r})e^{i\vec{Q}\vec{r}}
\end{aligned} \tag{37}$$

The density operator looks as

$$\hat{\rho}(\vec{r}) = \sum_{i,j=1,2}\sum_{g,q} a^{\dagger}_{R_j,q} a_{R_i,g} \left\langle \psi_c(R_j,q;r)\,|\,\psi_c(R_i,g;r)\right\rangle +$$
$$+ \sum_{M_v,M_v'}\sum_{\varepsilon_m,\varepsilon_{m'}}\sum_{g,q} a^{\dagger}_{M_v',\varepsilon_{m'},q} a_{M_v,\varepsilon_m,g} \left\langle \psi_v(M_v',\varepsilon_{m'},q;r)\middle|\psi_v(M_v,\varepsilon_m,g;r)\right\rangle +$$
$$+ \sum_{M_v,M_v'}\sum_{\varepsilon_m^-,\varepsilon_{m'}^-}\sum_{g,q} a^{\dagger}_{M_v',\varepsilon_{m'}^-,q} a_{M_v,\varepsilon_m^-,g} \left\langle \psi_v(M_v',\varepsilon_{m'}^-,q;r)\middle|\psi_v(M_v,\varepsilon_m^-,g;r)\right\rangle +$$
$$+ \sum_{M_v,M_v'}\sum_{\varepsilon_{m'},\varepsilon_m^-}\sum_{g,q} a^{\dagger}_{M_v',\varepsilon_{m'},q} a_{M_v,\varepsilon_m^-,g} \left\langle \psi_v(M_v',\varepsilon_{m'},q;r)\middle|\psi_v(M_v,\varepsilon_m^-,g;r)\right\rangle +$$
$$+ \sum_{M_v,M_v'}\sum_{\varepsilon_{m'}^-,\varepsilon_m}\sum_{g,q} a^{\dagger}_{M_v',\varepsilon_{m'}^-,q} a_{M_v,\varepsilon_m,g} \left\langle \psi_v(M_v',\varepsilon_{m'}^-,q;r)\middle|\psi_v(M_v,\varepsilon_m,g;r)\right\rangle +$$
$$+ \sum_{i=1,2}\sum_{M_v}\sum_{\varepsilon_m}\sum_{g,q} a^{\dagger}_{R_i,q} a_{M_v,\varepsilon_m,g} \left\langle \psi_c(R_i,q;r)\,|\,\psi_v(M_v,\varepsilon_m,g;r)\right\rangle +$$
$$+ \sum_{i=1,2}\sum_{M_v}\sum_{\varepsilon_m^-}\sum_{g,q} a^{\dagger}_{R_i,q} a_{M_v,\varepsilon_m^-,g} \left\langle \psi_c(R_i,q;r)\,|\,\psi_v(M_v,\varepsilon_m^-,g;r)\right\rangle +$$
$$+ \sum_{i=1,2}\sum_{M_v}\sum_{\varepsilon_m}\sum_{g,q} a^{\dagger}_{M_v,\varepsilon_m,q} a_{R_i,g} \left\langle \psi_v(M_v,\varepsilon_m,q;r)\,|\,\psi_c(R_i,g;r)\right\rangle +$$
$$+ \sum_{i=1,2}\sum_{M_v}\sum_{\varepsilon_m^-}\sum_{g,q} a^{\dagger}_{M_v,\varepsilon_m^-,q} a_{R_i,g} \left\langle \psi_v(M_v,\varepsilon_m^-,q;r)\,|\,\psi_c(R_i,g;r)\right\rangle \qquad (38)$$

Fourier components $\hat{\rho}(\vec{Q})$ of the density operator determine the Coulomb interaction between the electrons. They will be calculated below taking into account spinor-type wave functions (12) and (16). For example, the first term in expressions (38) looks as

$$\hat{\rho}_{c-c}(R_1;R_1;\vec{Q}) = \sum_{q,g} a^{\dagger}_{R_1,q} a_{R_1,g} \left\langle \psi_c(R_1,q;\vec{r})\middle|\psi_c(R_1,g;\vec{r})\right\rangle =$$
$$= \sum_{q,g} a^{\dagger}_{R_1,q} a_{R_1,g} \int d^2\vec{r}\, U^{*}_{c,s,q}(\vec{r}) U_{c,s,g}(\vec{r}) \frac{e^{i(g+Q_x-q)x}}{L_x} \times \qquad (39)$$
$$\times[\left|a_0\right|^2 \varphi_0^{*}(y-ql_0^2)\varphi_0(y-gl_0^2) + \left|b_1\right|^2 \varphi_1^{*}(y-ql_0^2)\varphi_1(y-gl_0^2)],$$
$$\vec{r} = \vec{R} + \vec{\rho}$$

Following formula (22), it is necessary to separate the integration of the quickly varying periodic parts on volume v_0 of the elementary lattice cell and the integration of the slowly varying envelope parts on lattice point vectors $\vec{R}$ as follows:

$$\frac{1}{v_0}\int_{v_0} d\rho U^{*}_{c,s,g+Q_x}(\rho) U_{c,s,g}(\rho) e^{iQ_y\rho_y} = 1 + O(\vec{Q}),$$
$$\frac{1}{L_x}\int e^{i(g-q+Q_x)R_x} dR_x = \delta_{kr}(q, g+Q_x), \qquad (40)$$
$$\tilde{\phi}(n,m;\vec{Q}) = \int dR_y \varphi_n^{*}\left(R_y - \frac{Q_x l_0^2}{2}\right)\varphi_m\left(R_y + \frac{Q_x l_0^2}{2}\right) e^{iQ_y R_y} = \tilde{\phi}^{*}(m,n;-\vec{Q})$$

Here $O(\vec{Q})$ is an infinitesimal value much smaller than unity, tending to zero in the limit $Q \to 0$. It will be neglected in all calculations below. The calculation gives rise to the final form

$$\hat{\rho}_{c-c}(R_1;R_1;\vec{Q}) = [|a_0|^2\,\tilde{\phi}(0,0;\vec{Q}) + |b_1|^2\,\tilde{\phi}(1,1;\vec{Q})]\hat{\rho}(R_1;R_1;\vec{Q}) = \tilde{S}(R_1;R_1;\vec{Q})\hat{\rho}(R_1;R_1;\vec{Q}),$$
$$\hat{\rho}(R_1;R_1;\vec{Q}) = \sum_t e^{iQ_y t l_0^2} a^{\dagger}_{R_1,t+\frac{Q_x}{2}} a_{R_1,t-\frac{Q_x}{2}}, \tag{41}$$
$$\tilde{S}(R_1;R_1;\vec{Q}) = [|a_0|^2\,\tilde{\phi}(0,0;\vec{Q}) + |b_1|^2\,\tilde{\phi}(1,1;\vec{Q})]$$

Expression (41) looks as a product of one numeral factor $\tilde{S}(R_1;R_1;\vec{Q})$, which concerns the concrete electron spinor state and another operator type factor of the general form

$$\hat{\rho}(\xi,\eta;\vec{Q}) = \sum_t e^{iQ_y t l_0^2} a^{\dagger}_{\xi,t+\frac{Q_x}{2}} a_{\eta,t-\frac{Q_x}{2}} = \hat{\rho}^{\dagger}(\eta,\xi;-\vec{Q}) \tag{42}$$

It will be met in all expressions listed below, but with different meanings of ξ and η, as follows:

$$\begin{aligned}
&\hat{\rho}_{c-c}(R_2;R_2;\vec{Q}) = \tilde{S}(R_2;R_2;\vec{Q})\hat{\rho}(R_2;R_2;\vec{Q}),\\
&\tilde{S}(R_2;R_2;\vec{Q}) = \tilde{\phi}(0,0;\vec{Q}),\\
&\hat{\rho}_{c-c}(R_1;R_2;\vec{Q}) = \tilde{S}(R_1;R_2;\vec{Q})\hat{\rho}(R_1;R_2;\vec{Q}),\\
&\tilde{S}(R_1;R_2;\vec{Q}) = b_1^{*}\tilde{\phi}(1,0;\vec{Q}),\\
&\hat{\rho}_{c-c}(R_2;R_1;\vec{Q}) = \tilde{S}(R_2;R_1;\vec{Q})\hat{\rho}(R_2;R_1;\vec{Q}) = \rho^{\dagger}_{c-c}(R_1;R_2;-\vec{Q}),\\
&\tilde{S}(R_2;R_1;\vec{Q}) = b_1\,\tilde{\phi}(0,1;\vec{Q})
\end{aligned} \tag{43}$$

One of the valence electron density fluctuation operator looks as

$$\begin{aligned}
&\hat{\rho}_{v-v}(M_v,\varepsilon_m^-,M_v',\varepsilon_{m'}^-;\vec{Q}) = \sum_{q,g} a^{\dagger}_{M_v,\varepsilon_m^-,q} a_{M_v',\varepsilon_{m'}^-,g} \int d^2\vec{r} e^{i\vec{Q}\vec{r}} \left\langle \psi_v(M_v,\varepsilon_m^-,q;\vec{r}) \middle| \psi_v(M_v',\varepsilon_{m'}^-,g;\vec{r}) \right\rangle =\\
&= \tilde{S}(M_v,\varepsilon_m^-;M_v',\varepsilon_{m'}^-;\vec{Q})\hat{\rho}(M_v,\varepsilon_m^-;M_v,\varepsilon_{m'}^-\vec{Q}),\\
&\tilde{S}(M_v,\varepsilon_m^-;M_v',\varepsilon_{m'}^-;\vec{Q}) = \delta_{M_v,M_v'}[d^-_{m-3}d^{-*}_{m'-3}\tilde{\phi}(m-3,m'-3;\vec{Q}) + c^-_m c^{-*}_{m'}\tilde{\phi}(m,m';\vec{Q})],\\
&m,m' \geq 3
\end{aligned} \tag{44}$$

Here, we have taken into account the following property of the valence band periodic parts

$$\begin{aligned}
&\frac{1}{v_0}\int_{v_0} d\vec{\rho} U^{*}_{v,p,i,g+Q_x}(\rho) U_{v,p,j,g}(\rho) e^{iQ_y\rho_y} = \delta_{ij} + O(\vec{Q}),\\
&i,j = x,y
\end{aligned} \tag{45}$$

They lead to Kronecker symbol $\delta_{M_v,M_v'}$ in expression (50) and in the next ones concerning the valence band as follows:

$$\begin{aligned}
&\hat{\rho}_{v-v}(M_v,\varepsilon_m;M_v',\varepsilon_{m'};\vec{Q}) = \tilde{S}(M_v,\varepsilon_m;M_v',\varepsilon_{m'};\vec{Q})\hat{\rho}(M_v,\varepsilon_m;M_v,\varepsilon_{m'};\vec{Q}),\\
&\tilde{S}(M_v,\varepsilon_m;M_v',\varepsilon_{m'};\vec{Q}) = \delta_{M_v,M_v'}\tilde{\phi}(m,m';\vec{Q}),\\
&m,m' = 0,1,2,\\
&\hat{\rho}_{v-v}(M_v',\varepsilon_{m'};M_v,\varepsilon_m^-;\vec{Q}) = \tilde{S}(M_v',\varepsilon_{m'};M_v,\varepsilon_m^-;\vec{Q})\hat{\rho}(M_v,\varepsilon_{m'};M_v,\varepsilon_m^-;\vec{Q}),\\
&\tilde{S}(M_v',\varepsilon_{m'};M_v,\varepsilon_m^-;\vec{Q}) = \delta_{M_v,M_v'}c_m^{-*}\tilde{\phi}(m',m;\vec{Q}),\\
&m' = 0,1,2,\ m \geq 3,\\
&\hat{\rho}_{v-v}(M_v,\varepsilon_m^-;M_v',\varepsilon_{m'};\vec{Q}) = \tilde{S}(M_v,\varepsilon_m^-;M_v',\varepsilon_{m'};\vec{Q})\hat{\rho}(M_v,\varepsilon_m^-;M_v,\varepsilon_{m'};\vec{Q}),\\
&\tilde{S}(M_v,\varepsilon_m^-;M_v',\varepsilon_{m'};\vec{Q}) = \delta_{M_v,M_v'}c_m^-\tilde{\phi}(m,m';\vec{Q}),\\
&m \geq 3,\ m' = 0,1,2
\end{aligned} \tag{46}$$

As usual, they obey to the equalities

$$\begin{aligned}
&\hat{\rho}_{v-v}^{\dagger}(\xi;\eta;\vec{Q}) = \hat{\rho}_{v-v}(\eta;\xi;-\vec{Q}),\\
&\hat{\rho}(\xi;\eta;\vec{Q}) = \hat{\rho}^{\dagger}(\eta;\xi;-\vec{Q}),\\
&\tilde{\phi}(n;m;\vec{Q}) = \tilde{\phi}^{*}(m;n;-\vec{Q}),\\
&\tilde{S}(\xi;\eta;\vec{Q}) = \tilde{S}^{*}(\eta;\xi;-\vec{Q})
\end{aligned} \tag{47}$$

Up till now, we have dealt with intraband density operators $\hat{\rho}_{c-c}(\xi;\eta;\vec{Q})$ and $\hat{\rho}_{v-v}(\xi;\eta;\vec{Q})$. Interband density operators $\hat{\rho}_{c-v}(\xi;\eta;\vec{Q})$ and $\hat{\rho}_{v-c}(\xi;\eta;\vec{Q})$ depend on the interband exchange electron densities of the type $U_{c,s,g+Q_x}^{*}(\rho)\frac{1}{\sqrt{2}}(U_{v,p,x,g}(\rho) \pm iU_{v,p,y,g}(\rho))$ and its complex conjugate value. They contain the quickly oscillating periodic parts with different parities and the orthogonality integral on the elementary lattice cell has an infinitesimal value

$$\frac{1}{v_0}\int_{v_0} d\rho U_{c,s,g+Q_x}^{*}(\rho)e^{iQ_y\rho_y}\frac{1}{\sqrt{2}}(U_{v,p,x,g}(\rho) \pm iU_{v,p,y,g}(\rho)) = O(\vec{Q}) \tag{48}$$

This integral is different from zero if one takes into account, for example, term $iQ_y\rho_y$ appearing in the series expansion of function $e^{iQ_y\rho_y}$. It gives rise to interband dipole momentum $\vec{d}_{cv}$ with the component

$$\begin{aligned}
&d_{cv,y} = \frac{e}{v_0}\int_{v_0} d\rho U_{c,s,g}^{*}(\rho)\rho_y U_{v,p,y,g}(\rho),\\
&O(\vec{Q}) \approx Q_y d_{cv,y}
\end{aligned} \tag{49}$$

The Coulomb interaction depending on interband exchange electron densities $\hat{\rho}_{cv}(\vec{Q})\hat{\rho}_{vc}(-\vec{Q})$ has a form of the dipole–dipole interaction instead of the charge–charge interaction, which takes place only in the intraband cases. It is known as a long-range Coulomb interaction and gives rise to the longitudinal-transverse splitting of the three-fold degenerate levels of the dipole-active excitons in the cubic crystals [28, 29]. These effects with the participation of the 2D

magnetoexcitons have not been investigated up till now, to the best of our knowledge, and remain outside the present review article.

Density operator $\hat{\rho}(\vec{Q})$ in the frame of electron spinor states (12) and (16) looks as

$$\begin{aligned}
\hat{\rho}(\vec{Q}) = &\sum_{i,j} \hat{\rho}_{c-c}(R_i;R_j;\vec{Q}) + \sum_{M_v,M_v'} \sum_{\varepsilon_m,\varepsilon_{m'}} \hat{\rho}_{v-v}(M_v,\varepsilon_m;M_v',\varepsilon_{m'};\vec{Q}) + \\
&+ \sum_{M_v,M_v'} \sum_{\varepsilon_m^-,\varepsilon_{m'}^-} \hat{\rho}_{v-v}(M_v,\varepsilon_m^-;M_v',\varepsilon_{m'}^-;\vec{Q}) + \sum_{M_v,M_v'} \sum_{\varepsilon_m^-,\varepsilon_{m'}} \hat{\rho}_{v-v}(M_v',\varepsilon_{m'};M_v,\varepsilon_m^-;\vec{Q}) + \\
&+ \sum_{M_v,M_v'} \sum_{\varepsilon_m^-,\varepsilon_{m'}} \hat{\rho}_{v-v}(M_v,\varepsilon_m^-;M_v',\varepsilon_{m'};\vec{Q}) + \sum_{i} \sum_{M_v} \sum_{\varepsilon_m} \hat{\rho}_{c-v}(R_i;M_v,\varepsilon_m;\vec{Q}) + \\
&+ \sum_{i} \sum_{M_v} \sum_{\varepsilon_m^-} \hat{\rho}_{c-v}(R_i;M_v,\varepsilon_m^-;\vec{Q}) + \sum_{i} \sum_{M_v} \sum_{\varepsilon_m} \hat{\rho}_{v-c}(M_v,\varepsilon_m;R_i;\vec{Q}) + \\
&+ \sum_{i} \sum_{M_v} \sum_{\varepsilon_m^-} \hat{\rho}_{v-c}(M_v,\varepsilon_m^-;R_i;\vec{Q})
\end{aligned} \tag{50}$$

The first five terms of this expression depend on the intraband electron densities and determine the charge–charge Coulomb interaction. The last four terms depend on the interband electron densities and lead to the dipole–dipole long-range Coulomb interaction.

The strength of the Coulomb interaction is determined by coefficients a_n, b_n, c_n, d_n of the spinor-type wave function (12) and (16) as well as by the normalization and orthogonality-type integrals $\tilde{\phi}(n,m,\vec{Q})$. They have the properties:

$$\begin{aligned}
&\tilde{\phi}(n,m,\vec{Q}) = e^{-\frac{Q^2 l^2}{4}} A_{n,m}(\vec{Q}) \\
&A_{n,m}(0) = \delta_{n,m}
\end{aligned} \tag{51}$$

Diagonal coefficients $A_{n,n}(\vec{Q})$ with $n = 0,1,3$ will be calculated below. The nondiagonal coefficients with $n \neq m$ in the limit $Q \to 0$ are proportional to vector components Q_i in a degree of $|n-m|$. They can be neglected in the zeroth order approximation together with other corrections denoted as $O(\vec{Q})$. It essentially diminishes the number of the actual components of density operator $\hat{\rho}(\vec{Q})$.

In the zeroth order approximation, neglecting the corrections of the order $O(\vec{Q})$, we will deal only with diagonal terms that permit the simplified denotations

$$\begin{aligned}
&\hat{\rho}(\xi;\xi;\vec{Q}) = \hat{\rho}(\xi;\vec{Q}), \\
&\tilde{S}(\xi;\xi;\vec{Q}) = \tilde{S}(\xi;\vec{Q}) = e^{-\frac{Q^2 l_0^2}{4}} S(\xi;\vec{Q})
\end{aligned} \tag{52}$$

The concrete values of coefficients $S(\xi;\vec{Q})$ are

$$\begin{aligned}
&S(R_1;\vec{Q}) = [|a_0|^2 A_{0,0}(\vec{Q}) + |b_1|^2 A_{1,1}(\vec{Q})], \\
&S(R_2;\vec{Q}) = A_{0,0}(\vec{Q}), \\
&S(\varepsilon_m;\vec{Q}) = A_{m,m}(\vec{Q}), m = 0,1,2, \\
&S(\varepsilon_m^-;\vec{Q}) = [|d_{m-3}^-|^2 A_{m-3,m-3}(\vec{Q}) + |c_m^-|^2 A_{m,m}(\vec{Q})], \\
&m \geq 3
\end{aligned} \tag{53}$$

The calculated values of $A_{m,m}(\vec{Q})$ equal

$$A_{0,0}(\vec{Q})=1,\ A_{1,1}(\vec{Q})=\left(1-\frac{Q^2l_0^2}{2}\right),$$
$$A_{3,3}(\vec{Q})=1-\frac{3}{2}Q^2l_0^2+\frac{3}{8}Q^4l_0^4-\frac{1}{48}Q^6l_0^6 \tag{54}$$

The diagonal part of density operator $\hat{\rho}(\vec{Q})$ looks as

$$\hat{\rho}(\vec{Q})=e^{-\frac{Q^2l_0^2}{4}}\{\sum_i S(R_i;\vec{Q})\hat{\rho}(R_i;\vec{Q})+\sum_{M_v}\sum_{\varepsilon_m} S(M_v,\varepsilon_m;\vec{Q})\hat{\rho}(M_v,\varepsilon_m;\vec{Q})+$$
$$+\sum_{M_v}\sum_{\varepsilon_m^-} S(M_v,\varepsilon_m^-;\vec{Q})\hat{\rho}(M_v,\varepsilon_m^-;\vec{Q})\} \tag{55}$$

It contains two separate contributions from the conduction and valence bands. The latter contribution in turn can be represented as due to the electrons of the full filled valence band extracting the contribution of the holes created in its frame. To show it, one can introduce the hole creation and annihilation operators as follows:

$$b^{\dagger}_{M_h,\varepsilon,q}=a_{v,-M_v,\varepsilon,-q},$$
$$b_{M_h,\varepsilon,q}=a^{\dagger}_{v,-M_v,\varepsilon,-q},$$
$$\varepsilon=\varepsilon_m, m=0,1,2,$$
$$\varepsilon=\varepsilon_m^-, m\geq 3 \tag{56}$$

This leads to the relation

$$\hat{\rho}_v(-M_v,\varepsilon,\vec{Q})=N\delta_{kr}(\vec{Q},0)-\hat{\rho}_h(M_h,\varepsilon,\vec{Q}),$$
$$N=\frac{S}{2\pi l_0^2} \tag{57}$$

where hole density operator $\rho_h(M_h,\varepsilon,\vec{Q})$ looks as

$$\hat{\rho}_h(M_h,\varepsilon,\vec{Q})=\sum_t e^{-iQ_y t l_0^2}b^{\dagger}_{M_h,\varepsilon,t+\frac{Q_x}{2}}b_{M_h,\varepsilon,t-\frac{Q_x}{2}} \tag{58}$$

The constant part $N\delta_{kr}(\vec{Q},0)$ in (57) created by electron of the full filled valence band is compensated by the influence of the positive electric charges of the background nuclei. In the jelly model of the system, their presence is taken into account excluding the point $\vec{Q}=0$ from the Hamiltonian of the Coulomb interaction [29]. Taking into account the fully neutral system of the bare electrons and the positive jelly background, we will operate only with the conduction band electrons and with the holes in the valence band. In this electron–hole description, density operator $\hat{\rho}(\vec{Q})$ becomes equal to

$$\hat{\rho}(\vec{Q})=\hat{\rho}_e(\vec{Q})-\hat{\rho}_h(\vec{Q}),$$
$$\vec{Q}\neq 0 \tag{59}$$

where

$$\hat{\rho}_h(\vec{Q}) = \sum_{M_h,\varepsilon_m} \tilde{S}(\varepsilon_m;\vec{Q})\hat{\rho}_h(M_h,\varepsilon_m;\vec{Q}) + \sum_{M_h,\varepsilon_m^-} \tilde{S}(\varepsilon_m^-;\vec{Q})\hat{\rho}_h(M_h,\varepsilon_m^-;\vec{Q}) =$$

$$= e^{-\frac{Q^2 l_0^2}{4}}\{\sum_{M_h,\varepsilon_m} S(\varepsilon_m;\vec{Q})\hat{\rho}_h(M_h,\varepsilon_m;\vec{Q}) + \sum_{M_h,\varepsilon_m^-} S(\varepsilon_m^-;\vec{Q})\hat{\rho}_h(M_h,\varepsilon_m^-;\vec{Q})\}, \tag{60}$$

$$\hat{\rho}_e(\vec{Q}) = \hat{\rho}_c(\vec{Q}) = \sum_{i=1,2} \tilde{S}(R_i;\vec{Q})\hat{\rho}_e(R_i;\vec{Q}) = e^{-\frac{Q^2 l_0^2}{4}} \sum_{i=1,2} S(R_i;\vec{Q})\hat{\rho}_e(R_i;\vec{Q})$$

The Hamiltonian of the Coulomb interaction of the initial bare electrons can be expressed in terms of the electron field and density operators (36) and (50) as follows:

$$\begin{aligned} H_{Coul} &= \frac{1}{2}\int d\vec{1}\int d\vec{2}\hat{\Psi}^\dagger(1)\hat{\Psi}^\dagger(2)V(1-2)\hat{\Psi}(2)\hat{\Psi}(1) = \\ &= \frac{1}{2}\sum_{\vec{Q}} V(\vec{Q})\int d\vec{1}\int d\vec{2}e^{i\vec{Q}(\vec{1}-\vec{2})}\hat{\Psi}^\dagger(1)\hat{\rho}(2)\hat{\Psi}(1) = \\ &= \frac{1}{2}\sum_{\vec{Q}} V(\vec{Q})\int\int d\vec{r}e^{i\vec{Q}\vec{r}}\hat{\Psi}^\dagger(\vec{r})\hat{\rho}(-\vec{Q})\hat{\Psi}(\vec{r}), \\ V(\vec{Q}) &= \frac{2\pi e^2}{\varepsilon_0 S|\vec{Q}|} \end{aligned} \tag{61}$$

$V(\vec{Q})$ is the Fourier transform of the Coulomb interaction of the electrons situated on the surface of the 2D layer with area S and dielectric constant ε_0 of the medium. The expression $\hat{\Psi}^\dagger(\vec{r})\hat{\rho}(-\vec{Q})\hat{\Psi}(\vec{r})$ contains density operator $\hat{\rho}(-\vec{Q})$ intercalated between field operators $\hat{\Psi}^\dagger(\vec{r})$ and $\hat{\Psi}(\vec{r})$. Operator $\hat{\Psi}(\vec{r})$ cannot be transposed over operator $\hat{\rho}(-\vec{Q})$ because they do not commute, but its nonoperator part expressed through the spinor-type wave function can be transposed forming together with the conjugate wave function of field operator $\hat{\Psi}^\dagger(\vec{r})$ a scalar.

After the integration on coordinate $\vec{r}$, the quadratic intercalated density operators will appear in the form

$$\begin{aligned} K(\xi;\eta;x;\eta;\vec{Q}) &= \sum_t e^{iQ_y t l_0^2} a^\dagger_{\xi,t+\frac{Q_x}{2}} \hat{\rho}(x;y;-\vec{Q}) a_{\eta,t-\frac{Q_x}{2}} = \\ &= \sum_t\sum_s e^{iQ_\eta t l_0^2} e^{-iQ_y s l_0^2} a^\dagger_{\xi,t+\frac{Q_x}{2}} a^\dagger_{x,s-\frac{Q_x}{2}} a_{y,s+\frac{Q_x}{2}} a_{\eta,t-\frac{Q_x}{2}} = \\ &= \hat{\rho}(\xi;\eta;\vec{Q})\hat{\rho}(x;y;-\vec{Q}) - \delta_{\eta,x}\hat{\rho}(\xi;y;0) \end{aligned} \tag{62}$$

The same relations remain in the electron–hole description.

The commutation relations between the density operators are the following:

$$\hat{\rho}(\xi;\eta;\vec{Q}) = \sum_t e^{iQ_y t l_0^2} a^{\dagger}_{\xi,t+\frac{Q_x}{2}} a_{\eta,t-\frac{Q_x}{2}},$$

$$\hat{\rho}(x;y;\vec{P}) = \sum_t e^{iP_y t l_0^2} a^{\dagger}_{x,t+\frac{P_x}{2}} a_{y,t-\frac{P_x}{2}},$$

$$[\hat{\rho}(\xi;\eta;\vec{Q}),\hat{\rho}(x;y;\vec{P})] = \delta_{x,\eta}\hat{\rho}(\xi;y;\vec{P}+\vec{Q})e^{\frac{i[\vec{P}\times\vec{Q}]_z l_0^2}{2}} - \delta_{\xi,y}\hat{\rho}(x;\eta;\vec{P}+\vec{Q})e^{\frac{-i[\vec{P}\times\vec{Q}]_z l_0^2}{2}} = \tag{63}$$

$$= \cos\left(\frac{[\vec{P}\times\vec{Q}]_z l_0^2}{2}\right)[\delta_{x,\eta}\hat{\rho}(\xi;y;\vec{P}+\vec{Q}) - \delta_{\xi,y}\hat{\rho}(x;\eta;\vec{P}+\vec{Q})] +$$

$$+ i\sin\left(\frac{[\vec{P}\times\vec{Q}]_z l_0^2}{2}\right)[\delta_{x,\eta}\hat{\rho}(\xi;y;\vec{P}+\vec{Q}) + \delta_{\xi,y}\hat{\rho}(x;\eta;\vec{P}+\vec{Q})]$$

Factor $e^{-\frac{Q^2 l_0^2}{4}}$ arising from the product of the density operators $\hat{\rho}(\vec{Q})$ and $\hat{\rho}(-\vec{Q})$ being multiplied by coefficient $V(\vec{Q})$ gives rise to coefficient $W(\vec{Q})$ describing the effective Coulomb interaction under the conditions of the Landau quantization

$$W(\vec{Q}) = V(\vec{Q})e^{-\frac{Q^2 l_0^2}{2}} \tag{64}$$

Excluding the intercalations, the Hamiltonian of the Coulomb interaction in the presence of the Landau quantization and Rashba spin–orbit coupling has the form:

$$H_{Coul} = \frac{1}{2}\sum_{\vec{Q}} W(\vec{Q})\{\sum_{i,j} S(R_i;\vec{Q})S(R_j;-\vec{Q})[\hat{\rho}(R_i;\vec{Q})\hat{\rho}(R_j;-\vec{Q}) - \delta_{i,j}\hat{\rho}(R_i;0)] +$$

$$+ \sum_{M_\nu,M'_\nu}\sum_{\varepsilon_m,\varepsilon_{m'}} S(M_\nu,\varepsilon_m;\vec{Q})S(M'_\nu,\varepsilon_{m'};-\vec{Q})[\hat{\rho}(M_\nu,\varepsilon_m;\vec{Q})\hat{\rho}(M'_\nu,\varepsilon_{m'};-\vec{Q}) - \delta_{M_\nu,M'_\nu}\delta_{m,m'}\hat{\rho}(M_\nu,\varepsilon_m;0)] +$$

$$+ \sum_{M_\nu,M'_\nu}\sum_{\varepsilon^-_m,\varepsilon^-_{m'}} S(M_\nu,\varepsilon^-_m;\vec{Q})S(M'_\nu,\varepsilon^-_{m'};-\vec{Q})[\hat{\rho}(M_\nu,\varepsilon^-_m;\vec{Q})\hat{\rho}(M'_\nu,\varepsilon^-_{m'};-\vec{Q}) - \delta_{M_\nu,M'_\nu}\delta_{m,m'}\hat{\rho}(M_\nu,\varepsilon^-_m;0)] +$$

$$+ \sum_{i=1,2}\sum_{M_\nu,\varepsilon_m} S(R_i;\vec{Q})S(M_\nu,\varepsilon_m;-\vec{Q})\hat{\rho}(R_i;\vec{Q})\hat{\rho}(M_\nu,\varepsilon_m;-\vec{Q}) +$$

$$+ \sum_{i=1,2}\sum_{M_\nu,\varepsilon^-_m} S(R_i;\vec{Q})S(M_\nu,\varepsilon^-_m;-\vec{Q})\hat{\rho}(R_i;\vec{Q})\hat{\rho}(M_\nu,\varepsilon^-_m;-\vec{Q}) +$$

$$+ \sum_{i=1,2}\sum_{M_\nu,\varepsilon_m} S(M_\nu,\varepsilon_m;\vec{Q})S(R_i;-\vec{Q})\hat{\rho}(M_\nu,\varepsilon_m;\vec{Q})\hat{\rho}(R_i;-\vec{Q}) +$$

$$+ \sum_{i=1,2}\sum_{M_\nu,\varepsilon^-_m} S(M_\nu,\varepsilon^-_m;\vec{Q})S(R_i;-\vec{Q})\hat{\rho}(M_\nu,\varepsilon^-_m;\vec{Q})\hat{\rho}(R_i;-\vec{Q}) +$$

$$+ \sum_{M_\nu,M'_\nu}\sum_{\varepsilon_m,\varepsilon^-_{m'}} S(M_\nu,\varepsilon_m;\vec{Q})S(M'_\nu,\varepsilon^-_{m'};-\vec{Q})\hat{\rho}(M_\nu,\varepsilon_m;\vec{Q})\hat{\rho}(M'_\nu,\varepsilon^-_{m'};-\vec{Q}) +$$

$$+ \sum_{M_\nu,M'_\nu}\sum_{\varepsilon^-_m,\varepsilon_{m'}} S(M_\nu,\varepsilon^-_m;\vec{Q})S(M'_\nu,\varepsilon_{m'};-\vec{Q})\hat{\rho}(M_\nu,\varepsilon^-_m;\vec{Q})\hat{\rho}(M'_\nu,\varepsilon_{m'};-\vec{Q})\} \tag{65}$$

The Hamiltonian of the Coulomb interaction in the electron–hole representation looks as

$$H_{Coul}=\frac{1}{2}\sum_{\vec{Q}} W(\vec{Q})\{\sum_{i,j} S(R_i;\vec{Q})S(R_j;-\vec{Q})[\hat{\rho}_e(R_i;\vec{Q})\hat{\rho}_e(R_j;-\vec{Q})-\delta_{i,j}\hat{\rho}_e(R_i;0)]+$$
$$+\sum_{M_h,M_h'}\sum_{\varepsilon_m,\varepsilon_{m'}} S(M_h,\varepsilon_m;\vec{Q})S(M_h',\varepsilon_{m'};-\vec{Q})[\hat{\rho}_h(M_h,\varepsilon_m;\vec{Q})\hat{\rho}_h(M_h',\varepsilon_{m'};-\vec{Q})-\delta_{M_h,M_h'}\delta_{m,m'}\hat{\rho}_h(M_h,\varepsilon_m;0)]+$$
$$+\sum_{M_h,M_h'}\sum_{\varepsilon_m^-,\varepsilon_{m'}^-} S(M_h,\varepsilon_m^-;\vec{Q})S(M_h',\varepsilon_{m'}^-;-\vec{Q})[\hat{\rho}_h(M_h,\varepsilon_m^-;\vec{Q})\hat{\rho}_h(M_h',\varepsilon_{m'}^-;-\vec{Q})-\delta_{M_h,M_h'}\delta_{m,m'}\hat{\rho}_h(M_h,\varepsilon_m^-;0)]+$$
$$+\sum_{M_h,M_h'}\sum_{\varepsilon_m,\varepsilon_{m'}^-} S(M_h,\varepsilon_m;\vec{Q})S(M_h',\varepsilon_{m'}^-;-\vec{Q})\hat{\rho}_h(M_h,\varepsilon_m;\vec{Q})\hat{\rho}_h(M_h',\varepsilon_{m'}^-;-\vec{Q})+$$
$$+\sum_{M_h,M_h'}\sum_{\varepsilon_m^-,\varepsilon_{m'}} S(M_h,\varepsilon_m^-;\vec{Q})S(M_h',\varepsilon_{m'};-\vec{Q})\hat{\rho}_h(M_h,\varepsilon_m^-;\vec{Q})\hat{\rho}_h(M_h',\varepsilon_{m'};-\vec{Q})-$$
$$-\sum_{i}\sum_{M_h,\varepsilon_m} S(R_i;\vec{Q})S(M_h,\varepsilon_m;-\vec{Q})\hat{\rho}_e(R_i;\vec{Q})\hat{\rho}_h(M_h,\varepsilon_m;-\vec{Q})-$$
$$-\sum_{i}\sum_{M_h,\varepsilon_m^-} S(R_i;\vec{Q})S(M_h,\varepsilon_m^-;-\vec{Q})\hat{\rho}_e(R_i;\vec{Q})\hat{\rho}_h(M_h,\varepsilon_m^-;-\vec{Q})-$$
$$-\sum_{i}\sum_{M_h,\varepsilon_m} S(M_h,\varepsilon_m;\vec{Q})S(R_i;-\vec{Q})\hat{\rho}_h(M_h,\varepsilon_m;\vec{Q})\hat{\rho}_e(R_i;-\vec{Q})-$$
$$-\sum_{i}\sum_{M_h,\varepsilon_m^-} S(M_h,\varepsilon_m^-;\vec{Q})S(R_i;-\vec{Q})\hat{\rho}_h(M_h,\varepsilon_m^-;\vec{Q})\hat{\rho}_e(R_i;-\vec{Q})\} \quad (66)$$

In the concrete variant named as F_1, where the electrons are in state R_1, whereas the holes are in state ε_3^- with a given value of M_h, Hamiltonian (66) looks as

$$H_{Coul}(R_1;\varepsilon_3^-)=\frac{1}{2}\sum_{\vec{Q}} W(\vec{Q})\{(|a_0|^2+|b_1|^2 A_{1,1}(\vec{Q}))^2[\hat{\rho}_e(R_1;\vec{Q})\hat{\rho}_e(R_1;-\vec{Q})-\hat{\rho}_e(R_1;0)]+$$
$$+(|d_0^-|^2+|c_3^-|^2 A_{3,3}(\vec{Q}))^2[\hat{\rho}_h(M_h,\varepsilon_3^-;\vec{Q})\hat{\rho}_h(M_h,\varepsilon_3^-;-\vec{Q})-\hat{\rho}_h(M_h,\varepsilon_3^-;0)]- \quad (67)$$
$$-2(|a_0|^2+|b_1|^2 A_{1,1}(\vec{Q}))(|d_0^-|^2+|c_3^-|^2 A_{3,3}(\vec{Q}))\hat{\rho}_e(R_1;\vec{Q})\hat{\rho}_h(M_h,\varepsilon_3^-;-\vec{Q})\}$$

In the absence of the RSOC, we have $a_0=d_0^-=1$ and $b_1=c_3^-=0$. In the variant $F_1=(R_1,\varepsilon_3^-)$ described by Hamiltonian (67), the 2D magnetoexciton can be described by the wave function

$$\left|\Psi_{ex}(F_1,\vec{K})\right\rangle=\frac{1}{\sqrt{N}}\sum_t e^{iK_y t l_0^2} a^{\dagger}_{R_1,\frac{K_x}{2}+t} b^{\dagger}_{M_h,\varepsilon_3^-,\frac{K_x}{2}-t}\left|0\right\rangle \quad (68)$$

where $\left|0\right\rangle$ is the vacuum state determined by the equalities

$$a_{\xi,t}\left|0\right\rangle=b_{\eta,t}\left|0\right\rangle=0 \quad (69)$$

In [22], other seven combinations of the electron and hole states were considered as follows:

$$F_2=(R_2,\varepsilon_3^-),F_3=(R_1,\varepsilon_0),F_4=(R_2,\varepsilon_0),F_5=(R_1,\varepsilon_4^-),$$
$$F_6=(R_2,\varepsilon_4^-),F_7=(R_1,\varepsilon_1),F_8=(R_2,\varepsilon_1) \quad (70)$$

In all these cases, the exciton creation energies were calculated using the formulas

$$E_{ex}(F_n,\vec{k})=E_{cv}(F_n)-I_{ex}(F_n,\vec{k})$$
$$E_{cv}(F_n)-E_g=E_e(\xi)+E_h(\eta), \quad (71)$$
$$F_n=(\xi,\eta)$$

Here, E_g is the semiconductor energy gap in the absence of a magnetic field. $I_{ex}(F_n,\vec{k})$ is the ionization potential of the magnetoexciton moving with wave vector $\vec{k}$.

The Hamiltonian of the Coulomb electron-electron interaction in the case of e–h pairs with the electrons in the degenerate state (S_e,R_1) and the holes in the degenerate state $(S_h,M_h,\varepsilon_m^-)$ has the form

$$\begin{aligned}
&H_{Coul}(R_1,\varepsilon_m^-)=\\
&=\frac{1}{2}\sum_{\vec{Q}}\ \Big\{W_{e-e}(R_1;\vec{Q})\Big[\hat{\rho}_e(R_1;\vec{Q})\,\hat{\rho}_e(R_1;-\vec{Q})-\hat{N}_e(R_1)\Big]+\\
&+W_{h-h}(\varepsilon_m^-;\vec{Q})\Big[\hat{\rho}_h(M_h,\varepsilon_m^-;\vec{Q})\hat{\rho}_h(M_h,\varepsilon_m^-;-\vec{Q})-\hat{N}_h(M_h,\varepsilon_m^-)\Big]-\\
&-2W_{e-h}(R_1,\varepsilon_m^-;\vec{Q})\hat{\rho}_e(R_1;\vec{Q})\hat{\rho}_h(M_h,\varepsilon_m^-;-\vec{Q})\Big\}
\end{aligned}\tag{72}$$

Once again, the electron and hole density operators are recalled:

$$\begin{aligned}
&\hat{\rho}_e(R_1;\vec{Q})=\sum_t\ e^{iQ_y tl_0^2}a^{\dagger}_{R_1,t+\frac{Q_x}{2}}a_{R_1,t-\frac{Q_x}{2}},\\
&\hat{\rho}_h(M_h,\varepsilon_m^-;\vec{Q})=\sum_t\ e^{-iQ_y tl_0^2}b^{\dagger}_{M_h,\varepsilon_m^-,t+\frac{Q_x}{2}}b_{M_h,\varepsilon_m^-,t-\frac{Q_x}{2}},\\
&\hat{N}_e(R_1)=\hat{\rho}_e(R_1;0),\quad \hat{N}_h(M_h,\varepsilon_m^-)=\hat{\rho}_h(M_h,\varepsilon_m^-;0)
\end{aligned}\tag{73}$$

Coefficients $W_{i-j}(\vec{Q})$ in (72) are

$$\begin{aligned}
&W_{e-e}(R_1;\vec{Q})=W(\vec{Q})\Big(|a_0|^2A_{0,0}(\vec{Q})+|b_1|^2A_{1,1}(\vec{Q})\Big)^2,\\
&W_{h-h}(\varepsilon_m^-;\vec{Q})=W(\vec{Q})\Big(|d_{m-3}^-|^2A_{m-3,m-3}(\vec{Q})+|c_m^-|^2A_{m,m}(\vec{Q})\Big)^2,\ \ m\ge 3,\\
&W_{e-h}(R_1,\varepsilon_m^-;\vec{Q})=W(\vec{Q})\Big(|a_0|^2A_{0,0}(\vec{Q})+|b_1|^2A_{1,1}(\vec{Q})\Big)\times\\
&\times\Big(|d_{m-3}^-|^2A_{m-3,m-3}(\vec{Q})+|c_m^-|^2A_{m,m}(\vec{Q})\Big),\ m\ge 3
\end{aligned}\tag{74}$$

The normalization conditions take place

$$\begin{aligned}
&|a_0|^2+|b_1|^2=1,\\
&|d_{m-3}^-|^2+|c_m^-|^2=1,\\
&m\ge 3
\end{aligned}\tag{75}$$

In the actual case $m=3$ we obtain

$$W_{e-e}(R_1;\vec{Q})=W(\vec{Q})\left(1-\frac{|b_1|^2}{2}Q^2l_0^2\right)^2,$$

$$W_{h-h}(\varepsilon_3^-;\vec{Q})=W(\vec{Q})\left(1-\frac{|c_3^-|^2}{2}\left(3Q^2l_0^2-\frac{3}{4}Q^4l_0^4+\frac{1}{24}Q^6l_0^6\right)\right)^2,$$

$$W_{e-h}(R_1,\varepsilon_3^-;\vec{Q})=W(\vec{Q})\left(1-\frac{|b_1|^2}{2}Q^2l_0^2\right)\left(1-\frac{|c_3^-|^2}{2}\left(3Q^2l_0^2-\frac{3}{4}Q^4l_0^4+\frac{1}{24}Q^6l_0^6\right)\right), \quad (76)$$

$$W(\vec{Q})=e^{-\frac{Q^2l_0^2}{2}}V(\vec{Q}),\quad V(\vec{Q})=\frac{2\pi e^2}{\varepsilon_0 S|\vec{Q}|}$$

The terms proportional to $\hat{N}_e(R_1)$ and $\hat{N}_h(M_h,\varepsilon_m^-)$ in (72) have coefficients $I_e(R_1)$ and $I_h(\varepsilon_m^-)$, which describe the Coulomb self-actions of the electrons and holes, are listed below together with the binding energy of the electron and the hole forming the magnetoexciton. The last value is determined by the diagonal matrix element of Hamiltonian (72) calculated with wave function (68) as follows:

$$\left\langle\Psi_{ex}(F_1,\vec{k})\middle|H_{Coul}\middle|\Psi_{ex}(F_1,\vec{k})\right\rangle=-I_l(F_1)+E(F_1,\vec{k}),$$

$$I_l(F_1)=I_l(R_1;\varepsilon_m^-)=\sum_{\vec{Q}}W_{e-h}(R_1;\varepsilon_m^-;\vec{Q}),$$

$$E(F_1,\vec{k})=E(R_1;\varepsilon_m^-;\vec{k})=2\sum_{\vec{Q}}W_{e-h}(R_1;\varepsilon_m^-;\vec{Q})\sin^2\left(\frac{[\vec{k}\times\vec{Q}]_z l_0^2}{2}\right), \quad (77)$$

$$\lim_{\vec{k}\to\infty}E(R_1;\varepsilon_m^-;\vec{k})=I_l(R_1;\varepsilon_m^-),$$

$$I_e(R_1)=\frac{1}{2}\sum_{\vec{Q}}W_{e-e}(R_1;\vec{Q}),\ I_h(\varepsilon_m^-)=\frac{1}{2}\sum_{\vec{Q}}W_{h-h}(\varepsilon_m^-;\vec{Q}),$$

$$I_S(R_1;\varepsilon_m^-)=I_e(R_1)+I_h(\varepsilon_m^-)$$

The binding energy of the magnetoexciton and its ionization potential, which has the opposite sign as compared with the binding energy, tend to zero when wave vector $\vec{k}$ tends to infinity and the magnetoexciton is transformed into a free e–h pair:

$$H_{mex,1}=\left(\frac{E_g^0}{2}+E_e(R_1)-I_e(R_1)-\mu_e\right)\hat{N}_e(R_1)+$$
$$+\left(\frac{E_g^0}{2}+E_h(M_h,\varepsilon_m^-)-I_h(\varepsilon_m^-)-\mu_h\right)\hat{N}_h(M_h,\varepsilon_m^-) \quad (78)$$

Here, semiconductor energy band gap E_g^0 in the absence of the Landau quantization was introduced.

Now, instead of electron and hole density operators $\hat{\rho}_e(\vec{Q})$ and $\hat{\rho}_h(\vec{Q})$, we will introduce the density operators of the optical plasmon denoted as $\hat{\rho}(\vec{Q})$ and the acoustical plasmon denoted as $\hat{D}(\vec{Q})$ following the relations

$$\begin{aligned}
&\hat{\rho}(\vec{Q}) = \hat{\rho}_e(\vec{Q}) - \hat{\rho}_h(\vec{Q}),\\
&\hat{D}(\vec{Q}) = \hat{\rho}_e(\vec{Q}) + \hat{\rho}_h(\vec{Q}),\\
&\hat{\rho}_e(\vec{Q}) = \frac{\hat{\rho}(\vec{Q}) + \hat{D}(\vec{Q})}{2},\\
&\hat{\rho}_h(\vec{Q}) = \frac{\hat{D}(\vec{Q}) - \hat{\rho}(\vec{Q})}{2}
\end{aligned} \tag{79}$$

Here, for simplicity, many indices that label the electron, hole, and plasmon density operators are omitted. But they must be kept in mind and may be restored in concrete cases.

In the plasmon representation, Hamiltonian $H_{mex,1}$ (78) looks as

$$\begin{aligned}
H_{mex,1} = &\left(E_{mex}(R_1; M_h, \varepsilon_m^-) - \mu_{mex}\right)\frac{\hat{D}(0)}{2} +\\
&+\left(G_{e-h}(R_1; M_h, \varepsilon_m^-) - \mu_e + \mu_h\right)\frac{\hat{\rho}(0)}{2}
\end{aligned} \tag{80}$$

Here, the sums and differences of the Landau quantization level energies, the Coulomb self-interaction terms, and the chemical potentials are defined as follows:

$$\begin{aligned}
&E_{mex}(R_1; M_h, \varepsilon_m^-) = E_g(R_1; M_h, \varepsilon_m^-) - I_l(R_1; \varepsilon_m^-),\\
&E_g(R_1; M_h, \varepsilon_m^-) = E_g^0 + E_e(R_1) + E_h(M_h, \varepsilon_m^-),\\
&\mu_{ex} = \mu_e + \mu_h,\\
&G_{e-h}(R_1; M_h, \varepsilon_m^-) = E_e(R_1) - E_h(M_h, \varepsilon_m^-) - I_e(R_1) + I_h(\varepsilon_m^-)
\end{aligned} \tag{81}$$

The remaining part $H_{mex,2}$ of Hamiltonian (72), after the excluding of the linear terms, is quadratic in the plasmon density operators. It has the form

$$\begin{aligned}
H_{mex,2} = &\frac{1}{2}\sum_{\vec{Q}}\Big\{W_{0-0}(\vec{Q})\hat{\rho}(\vec{Q})\hat{\rho}(-\vec{Q}) + W_{a-a}(\vec{Q})\hat{D}(\vec{Q})\hat{D}(-\vec{Q}) +\\
&+W_{0-a}(\vec{Q})\left(\hat{\rho}(\vec{Q})\hat{D}(-\vec{Q}) + \hat{D}(\vec{Q})\hat{\rho}(-\vec{Q})\right)\Big\}
\end{aligned} \tag{82}$$

The new coefficients are expressed in terms of the former ones by the formulas

$$\begin{aligned}
&W_{0-0}(\vec{Q}) = \frac{1}{4}\left(W_{e-e}(\vec{Q}) + W_{h-h}(\vec{Q}) + 2W_{e-h}(\vec{Q})\right),\\
&W_{a-a}(\vec{Q}) = \frac{1}{4}\left(W_{e-e}(\vec{Q}) + W_{h-h}(\vec{Q}) - 2W_{e-h}(\vec{Q})\right),\\
&W_{0-a}(\vec{Q}) = \frac{1}{4}\left(W_{e-e}(\vec{Q}) - W_{h-h}(\vec{Q})\right)
\end{aligned} \tag{83}$$

In the case of the e–h pairs of the type $(R_1; \varepsilon_m^-)$ they take the form

$$W_{0-0}(R_1;\varepsilon_m^-;\vec{Q})=\frac{1}{4}\left(W_{e-e}(R_1;\vec{Q})+W_{h-h}(\varepsilon_m^-;\vec{Q})+2W_{e-h}(R_1;\varepsilon_m^-;\vec{Q})\right)=$$
$$=\frac{W(\vec{Q})}{4}\left(|a_0|^2 A_{0,0}(\vec{Q})+|b_1|^2 A_{1,1}(\vec{Q})+|d_{m-3}^-|^2 A_{m-3,m-3}(\vec{Q})+|c_m^-|^2 A_{m,m}(\vec{Q})\right)^2,$$
$$W_{a-a}(R_1;\varepsilon_m^-;\vec{Q})=\frac{1}{4}\left(W_{e-e}(R_1;\vec{Q})+W_{h-h}(\varepsilon_m^-;\vec{Q})-2W_{e-h}(R_1;\varepsilon_m^-;\vec{Q})\right)=$$
$$=\frac{W(\vec{Q})}{4}\left(|a_0|^2 A_{0,0}(\vec{Q})+|b_1|^2 A_{1,1}(\vec{Q})-|d_{m-3}^-|^2 A_{m-3,m-3}(\vec{Q})-|c_m^-|^2 A_{m,m}(\vec{Q})\right)^2, \quad (84)$$
$$W_{0-a}(R_1;\varepsilon_m^-;\vec{Q})=\frac{1}{4}\left(W_{e-e}(R_1;\vec{Q})-W_{h-h}(\varepsilon_m^-;\vec{Q})\right)=$$
$$=\frac{W(\vec{Q})}{4}\left[\left(|a_0|^2 A_{0,0}(\vec{Q})+|b_1|^2 A_{1,1}(\vec{Q})\right)^2-\left(|d_{m-3}^-|^2 A_{m-3,m-3}(\vec{Q})+|c_m^-|^2 A_{m,m}(\vec{Q})\right)^2\right]$$

In a special case $m=3$ we have

$$W_{0-0}(R_1;\varepsilon_m^-;\vec{Q})=W(\vec{Q})\left(1-\frac{|b_1|^2}{4}Q^2l_0^2-\frac{|c_m^-|^2}{4}\left(3Q^2l_0^2-\frac{3}{4}Q^4l_0^4+\frac{1}{24}Q^6l_0^6\right)\right)^2,$$
$$W_{a-a}(R_1;\varepsilon_m^-;\vec{Q})=W(\vec{Q})\left(-\frac{|b_1|^2}{4}Q^2l_0^2+\frac{|c_m^-|^2}{4}\left(3Q^2l_0^2-\frac{3}{4}Q^4l_0^4+\frac{1}{24}Q^6l_0^6\right)\right)^2, \quad (85)$$
$$W_{0-a}(R_1;\varepsilon_m^-;\vec{Q})=W(\vec{Q})\left[\left(1-\frac{|b_1|^2}{4}Q^2l_0^2-\frac{|c_m^-|^2}{4}\left(3Q^2l_0^2-\frac{3}{4}Q^4l_0^4+\frac{1}{24}Q^6l_0^6\right)\right)\times\right.$$
$$\left.\times\left(-\frac{|b_1|^2}{4}Q^2l_0^2+\frac{|c_m^-|^2}{4}\left(3Q^2l_0^2-\frac{3}{4}Q^4l_0^4+\frac{1}{24}Q^6l_0^6\right)\right)\right]$$

Side by side with the magnetoexciton subsystem, the photon subsystem does exist. In our case, it is composed of photons with a given circular polarization, for example, $\vec{\sigma}_{\vec{k}}^+$. Their wave vectors $\vec{k}=\vec{a}_3\frac{\pi}{L_c}+\vec{k}_\parallel$ have the same quantized longitudinal component equal to $\frac{\pi}{L_c}$, where L_c is the resonator length and arbitrary values of the in-plane 2D vectors $\vec{k}_\parallel$. The photon energies are $\hbar\omega_{\vec{k}}=\frac{\hbar c}{n_0}\sqrt{\frac{\pi^2}{L_c^2}+\vec{k}_\parallel^{\,2}}$, where n_0 is the refractive index of the microcavity. The full number of the photons captured into the resonator is determined by their chemical potential μ_{ph}.

The zeroth order Hamiltonian of the photons in the microcavity looks as

$$H_{0,ph}=\sum_{\vec{k}_\parallel}\left(\hbar\omega_{\vec{k}}-\mu_{ph}\right)c_{\vec{k},\sigma}^\dagger c_{\vec{k},\sigma} \quad (86)$$

where $c_{\vec{k},\sigma}^\dagger, c_{\vec{k},\sigma}$ are the creation and annihilation photon operators and σ denotes a definite circular polarization. Only the case $\sigma=-$ will be considered. It must be supplemented by the

Hamiltonian of the magnetoexciton–photon interaction deduced above in a more general case. In the case of dipole-active band-to-band quantum transition with the combination of the e–h states (R_1, ε_3^-) we have

$$H_{mex-ph} = \sum_{\vec{k}_\parallel} \Big[\varphi(\vec{k}_\parallel; R_1; \varepsilon_3^-) \left(\vec{\sigma}_{\vec{k}}^{+} \bullet \vec{\sigma}_{M_h}^{*} \right) c_{\vec{k},-}^{\dagger} \hat{\Psi}_{ex}^{\dagger}(\vec{k}_\parallel) + \\ + \varphi^{*}(\vec{k}_\parallel; R_1; \varepsilon_3^-) \left(\vec{\sigma}_{\vec{k}}^{-} \bullet \vec{\sigma}_{M_h} \right) c_{\vec{k},-}^{\dagger} \hat{\Psi}_{ex}(\vec{k}_\parallel) \Big] \tag{87}$$

The interaction coefficient is as follows:

$$\varphi(\vec{k}_\parallel; R_1; \varepsilon_3^-) = \left(-\frac{e}{m_0 l_0} \right) \sqrt{\frac{\hbar}{L_c \omega_{\vec{k}}}} P_{cv}(0) T(\vec{k}_\parallel; R_1; \varepsilon_3^-), \\ T(\vec{k}_\parallel; R_1; \varepsilon_3^-) = a_0^{*} d_0^{-*} \tilde{\phi}(0,0; \vec{k}_\parallel) - b_1^{*} c_3^{-*} \tilde{\phi}(1,3; \vec{k}_\parallel) \tag{88}$$

The magnetoexciton creation and annihilation operators were written in a shortened form in (87) because there are too many indices in its full description as follows:

$$\hat{\Psi}_{ex}^{\dagger}(\vec{Q}) = \hat{\Psi}_{ex}^{\dagger}(\vec{Q}; R_1; M_h, \varepsilon_3^-) = \frac{1}{\sqrt{N}} \sum_t e^{iQ_y t l_0^2} a^{\dagger}_{R_1, t+\frac{Q_x}{2}} b^{\dagger}_{M_h, \varepsilon_3^-, -t+\frac{Q_x}{2}} \tag{89}$$

The full Hamiltonian of the magnetoexciton–photon system for a more actual combination (R_1, ε_3^-) may be written

$$H = H_{mex,1} + H_{0,ph} + H_{mex-ph} + H_{mex,2} \tag{90}$$

Its remarkable peculiarity is the presence only of the two-particle integral plasmon and magnetoexciton operators, rather than of the single-particle electron and hole Fermi operators. It permits considerably simplifying the deduction of their equations of motion. For this reason, the commutation relations between the full set of four two-particle integral operators $\hat{\rho}(\vec{Q}), \hat{D}(\vec{Q}), \hat{\Psi}_{ex}^{\dagger}(\vec{Q})$ and $\hat{\Psi}_{ex}(\vec{Q})$ are needed. They are listed below

$$\left[\hat{\rho}(\vec{Q}), \hat{\rho}(\vec{P}) \right] = \left[\hat{D}(\vec{Q}), \hat{D}(\vec{P}) \right] = 2i \sin\left(Z(\vec{P}, \vec{Q}) \right) \hat{\rho}\left(\vec{Q} + \vec{P} \right), \\ \left[\hat{\rho}(\vec{Q}), \hat{D}(\vec{P}) \right] = 2i \sin\left(Z(\vec{P}, \vec{Q}) \right) \hat{D}\left(\vec{P} + \vec{Q} \right), \\ \left[\hat{\Psi}_{ex}(\vec{P}), \hat{\Psi}_{ex}^{\dagger}(\vec{Q}) \right] = \delta_{kr}(\vec{P}, \vec{Q}) - \frac{1}{N} [i \sin\left(Z(\vec{Q}, \vec{P}) \right) \hat{\rho}\left(\vec{Q} - \vec{P} \right) + \cos\left(Z(\vec{Q}, \vec{P}) \right) \hat{D}\left(\vec{Q} - \vec{P} \right)], \\ Z(\vec{P}, \vec{Q}) = -Z(\vec{Q}, \vec{P}) = \frac{[\vec{P} \times \vec{Q}]_z l_0^2}{2} = -Z(\vec{P}, -\vec{Q}) = Z(-\vec{Q}, \vec{P}), \\ \left[\hat{\Psi}_{ex}(\vec{P}), \hat{\Psi}_{ex}^{\dagger}(\vec{P}) \right] = 1 - \frac{1}{N} \hat{D}(0), \\ \left[\hat{\rho}(\vec{Q}), \hat{\Psi}_{ex}^{\dagger}(\vec{P}) \right] = 2i \sin\left(Z(\vec{P}, \vec{Q}) \right) \hat{\Psi}_{ex}^{\dagger}(\vec{P} + \vec{Q}), \\ \left[\hat{\rho}(\vec{Q}), \hat{\Psi}_{ex}(\vec{P}) \right] = -2i \sin\left(Z(\vec{P}, \vec{Q}) \right) \hat{\Psi}_{ex}(\vec{P} - \vec{Q}), \\ \left[\hat{D}(\vec{Q}), \hat{\Psi}_{ex}^{\dagger}(\vec{P}) \right] = 2 \cos\left(Z(\vec{P}, \vec{Q}) \right) \hat{\Psi}_{ex}^{\dagger}(\vec{P} + \vec{Q}), \\ \left[\hat{D}(\vec{Q}), \hat{\Psi}_{ex}(\vec{P}) \right] = -2 \cos\left(Z(\vec{P}, \vec{Q}) \right) \hat{\Psi}_{ex}(\vec{P} - \vec{Q}) \tag{91}$$

5. The magnetoexcitons in the Bose-gas model description

The Hamiltonian describing the 2D e–h pairs with electrons and holes situated on the given Landau quantization levels and interacting between themselves through the Coulomb forces was represented as a sum: $H_{mex,1}+H_{mex,2}$. It is expressed in terms of plasmon density operators $\hat{\rho}(\vec{Q})$ and $\hat{D}(\vec{Q})$. It is useful to represent it in the model of weakly interacting Bose gas. To this end, the wave functions describing the free single magnetoexcitons $\left|\psi_{mex}(\vec{P})\right\rangle$ as well as the pairs of the free magnetoexcitons with wave vectors $\vec{P}$ and $\vec{R}$ $\left|\psi_{mex}(\vec{P}),\psi_{mex}(\vec{R})\right\rangle$ were introduced:

$$\begin{aligned}
&\left|\psi_{ex}(\vec{P})\right\rangle=\hat{\Psi}^{\dagger}_{ex}(\vec{P})\left|0\right\rangle,\\
&\left\langle\psi_{ex}(\vec{P})\right|=\left\langle 0\right|\hat{\Psi}_{ex}(\vec{P}),\\
&\left|\psi_{ex}(\vec{P}),\psi_{ex}(\vec{R})\right\rangle=\hat{\Psi}^{\dagger}_{ex}(\vec{P})\hat{\Psi}^{\dagger}_{ex}(\vec{R})\left|0\right\rangle,\\
&\left\langle\psi_{ex}(\vec{P}),\psi_{ex}(\vec{R})\right|=\left\langle 0\right|\hat{\Psi}_{ex}(\vec{R})\hat{\Psi}_{ex}(\vec{P})
\end{aligned} \tag{92}$$

where $\left|0\right\rangle$ is the vacuum state of the semiconductor. They were used to calculate the matrix elements

$$\begin{aligned}
&E_{mex}(\vec{P})=\left\langle\psi_{ex}(\vec{P})\right|H_{mex,1}+H_{mex,2}\left|\psi_{ex}(\vec{P})\right\rangle,\\
&W(\vec{P}_1,\vec{R}_1;\vec{P}_2,\vec{R}_2)=\left\langle\psi_{ex}(\vec{P}_1)\psi_{ex}(\vec{R}_1)\right|H_{mex,1}+H_{mex,2}\left|\psi_{ex}(\vec{P}_2)\psi_{ex}(\vec{R}_2)\right\rangle
\end{aligned} \tag{93}$$

With these matrix elements and with the magnetoexciton creation and annihilation operators, the new Hamiltonian in the model of weakly interacting Bose gas can be constructed. It looks as

$$\begin{aligned}
&\hat{H}=\hat{H}_0+\hat{H}_{\text{int}},\\
&\hat{H}_0=\sum_{\vec{P}}E_{mex}(\vec{P})\hat{\Psi}^{\dagger}_{ex}(\vec{P})\hat{\Psi}_{ex}(\vec{P}),\\
&\hat{H}_{\text{int}}=\sum_{\vec{P}_1,\vec{R}_1,\vec{P}_2,\vec{R}_2}W(\vec{P}_1,\vec{R}_1;\vec{P}_2,\vec{R}_2)\hat{\Psi}^{\dagger}_{ex}(\vec{P}_1)\hat{\Psi}^{\dagger}_{ex}(\vec{R}_1)\hat{\Psi}_{ex}(\vec{R}_2)\hat{\Psi}_{ex}(\vec{P}_2),\\
&\vec{P}_1+\vec{R}_1=\vec{P}_2+\vec{R}_2
\end{aligned} \tag{94}$$

Recall that the magnetoexciton creation and annihilation operators in turn are constructed from electron and hole creation and annihilation Fermi-type operators $a^{\dagger}_p,a_p,b^{\dagger}_p,b_p$ as follows:

$$\hat{\Psi}^{\dagger}_{ex}(\vec{P})=\frac{1}{\sqrt{N}}\sum_t e^{iP_y tl_0^2}a^{\dagger}_{t+\frac{P_x}{2}}b^{\dagger}_{-t+\frac{P_x}{2}} \tag{95}$$

and their composition in all calculations is taken into account. Some of them are demonstrated below using commutation relations (91):

$$
\begin{aligned}
&a_p\left|0\right\rangle = b_p\left|0\right\rangle = 0,\\
&\hat{\rho}(\vec{Q})\left|0\right\rangle = \hat{D}(\vec{Q})\left|0\right\rangle = \hat{\Psi}_{ex}(\vec{Q})\left|0\right\rangle = 0,\\
&\hat{D}(0)\hat{\Psi}^{\dagger}_{ex}(\vec{P})\left|0\right\rangle = 2\hat{\Psi}^{\dagger}_{ex}(\vec{P})\left|0\right\rangle,\\
&\hat{\rho}(0)\hat{\Psi}^{\dagger}_{ex}(\vec{P})\left|0\right\rangle = 0,\\
&\hat{\rho}(\vec{Q})\hat{\rho}(-\vec{Q})\hat{\Psi}^{\dagger}_{ex}(\vec{P})\left|0\right\rangle = 4\sin^2(Z(\vec{P},\vec{Q}))\hat{\Psi}^{\dagger}_{ex}(\vec{P})\left|0\right\rangle,\\
&\hat{D}(\vec{Q})\hat{D}(-\vec{Q})\hat{\Psi}^{\dagger}_{ex}(\vec{P})\left|0\right\rangle = 4\cos^2(Z(\vec{P},\vec{Q}))\hat{\Psi}^{\dagger}_{ex}(\vec{P})\left|0\right\rangle,\\
&(\hat{\rho}(\vec{Q})\hat{D}(-\vec{Q}) + \hat{D}(\vec{Q})\hat{\rho}(-\vec{Q}))\hat{\Psi}^{\dagger}_{ex}(\vec{P})\left|0\right\rangle = 0
\end{aligned}
\tag{96}
$$

In the present model, the main role is played by the magnetoexciton creation and annihilation operators, rather than by the plasmon density operators.

Magnetoexciton creation energy $E_{mex}(\vec{P})$ from Hamiltonian H_0 consists of three parts:

$$
\begin{aligned}
&E_{mex}(\vec{P}) = E_{mex}(R_1; M_h, \varepsilon_m^-; \vec{P}) = E_g(R_1; M_h, \varepsilon_m^-) - I_S(R_1; \varepsilon_m^-) +\\
&+2\sum_{\vec{Q}} W_{0-0}(R_1; \varepsilon_m^-; \vec{Q})\sin^2(Z(\vec{P},\vec{Q})) + 2\sum_{\vec{Q}} W_{a-a}(R_1; \varepsilon_m^-; \vec{Q})\cos^2(Z(\vec{P},\vec{Q})) =\\
&= E_g(M_h, \varepsilon_m^-; R_1) - I_l(R_1; \varepsilon_m^-) + E(R_1; \varepsilon_m^-; \vec{P})
\end{aligned}
\tag{97}
$$

The first component $E_g(S_e, R_1; S_h, M_h, \varepsilon_m^-)$ plays the role of the band gap, whereas difference $I_l(\varepsilon_m^-; R_1) - E(R_1; \varepsilon_m^-; \vec{P})$ determines the resulting ionization potential of the moving magnetoexciton with wave vector $\vec{P}$. In the limiting case $\vec{P} \to \infty$, when $\lim_{\vec{P}\to\infty} E(R_1; \varepsilon_m^-; \vec{P}) = I_l(R_1; \varepsilon_m^-)$, the resulting ionization potential vanishes and the e–h pair becomes unbound. Nevertheless, the presence of positive term $E(R_1; \varepsilon_m^-; \vec{P})$ in formula (97) plays the role of the kinetic energy of the magnetoexciton at least in the region of the small values of wave vector $\vec{P}$, where this term can be represented in a quadratic form $\frac{\hbar^2 P^2}{2M(B)}$ with effective mass $M(B)$ depending on magnetic field strength *B*. Zeroth-order Hamiltonian H_0 (94), together with the similar Hamiltonian for the cavity photons and with the Hamiltonian describing the magnetoexciton–photon interaction, gives rise to quadratic Hamiltonian H_2 forming the base of the polariton conception. It looks as

$$
\begin{aligned}
&H_2 = \sum_{\vec{k}_\parallel} E_{mex}(\vec{k}_\parallel)\hat{\Psi}^{\dagger}_{ex}(\vec{k}_\parallel)\hat{\Psi}_{ex}(\vec{k}_\parallel) + \sum_{\vec{k}_\parallel} \hbar\omega_{\vec{k}} c^{\dagger}_{\vec{k},-} c_{\vec{k},-} +\\
&+\sum_{\vec{k}_\parallel}\left[\varphi(\vec{k}_\parallel)(\vec{\sigma}^{+}_{\vec{k}} \bullet \vec{\sigma}^{*}_{M_h}) c_{\vec{k},-}\hat{\Psi}^{\dagger}_{ex}(\vec{k}_\parallel) + \varphi^{*}(\vec{k}_\parallel)(\vec{\sigma}^{-}_{\vec{k}} \bullet \vec{\sigma}_{M_h}) c^{\dagger}_{\vec{k},-}\hat{\Psi}_{ex}(\vec{k}_\parallel)\right]
\end{aligned}
\tag{98}
$$

In this expression, the chemical potentials of the magnetoexcitons and the photons are omitted until the single-particle polariton formation is investigated. They will be restored when the collective properties of the polaritons will be discussed. The diagonalization of quadratic form (98) is achieved introducing the polariton creation and annihilation operators $\hat{L}^{\dagger}_{\vec{k}_\parallel}, \hat{L}_{\vec{k}_\parallel}$ in the form

of a linear superposition

$$\hat{L}_{\vec{k}_\parallel} = x(\vec{k}_\parallel)\Psi_{ex}(\vec{k}_\parallel) + y(\vec{k}_\parallel)c_{\vec{k},-} \tag{99}$$

It is a simplified form without the antiresonant terms because they are not introduced in the starting Hamiltonian H_2 (98). Quantities $x(\vec{k}_\parallel)$ and $y(\vec{k}_\parallel)$ are known as Hopfield coefficients [28, 29]. In the case where the scalar product of two circular polarized vectors equals 1, the energy spectrum of two polariton branches looks as

$$\hbar\omega(\vec{k}_\parallel) = \frac{E_{mex}(\vec{k}_\parallel) + \hbar\omega_{\vec{k}}}{2} \pm \frac{1}{2}\sqrt{(E_{mex}(\vec{k}_\parallel) - \hbar\omega_{\vec{k}})^2 + 4\,|\,\varphi(\vec{k}_\parallel)\,|^2} \tag{100}$$

The Rabi frequency for the e–h pair in the states (R_1, ε_3^-) is as follows:

$$|\,\omega_R\,| = \left|\frac{\varphi(0)}{\hbar}\right| = \frac{e}{m_0 l_0}\sqrt{\frac{1}{L_c\hbar\omega_k}}\,\left|P_{cv}(0)a_0 d_0\right|\left|\vec{\sigma}_{\vec{k}}^{-} \bullet \vec{\sigma}_{M_h}\right| \tag{101}$$

In the absence of the RSOI, coefficients $a_0 = d_0 = 1$ and expression (101) coincides with formula (12) in [21].

The Hopfield coefficients obey to the normalization condition and are equal to

$$\begin{aligned}
&\left|x(\vec{k}_\parallel)\right|^2 = \frac{\left(\hbar\omega_p(\vec{k}_\parallel) - \hbar\omega_{\vec{k}}\right)^2}{\left(\hbar\omega_p(\vec{k}_\parallel) - \hbar\omega_{\vec{k}}\right)^2 + |\,\varphi(\vec{k}_\parallel)(\vec{\sigma}_{\vec{k}}^{-} \bullet \vec{\sigma}_{M_h})\,|^2},\\
&\left|y(\vec{k}_\parallel)\right|^2 = \frac{|\,\varphi(\vec{k}_\parallel)(\vec{\sigma}_{\vec{k}}^{-} \bullet \vec{\sigma}_{M_h})\,|^2}{\left(\hbar\omega_p(\vec{k}_\parallel) - \hbar\omega_{\vec{k}}\right)^2 + |\,\varphi(\vec{k}_\parallel)(\vec{\sigma}_{\vec{k}}^{-} \bullet \vec{\sigma}_{M_h})\,|^2},\\
&\left|x(\vec{k}_\parallel)\right|^2 + \left|y(\vec{k}_\parallel)\right|^2 = 1,\\
&\varphi(\vec{k}_\parallel)(\vec{\sigma}_{\vec{k}}^{+} \bullet \vec{\sigma}_{M_h}^{*}) = |\,\varphi(\vec{k}_\parallel)(\vec{\sigma}_{\vec{k}}^{-} \bullet \vec{\sigma}_{M_h})\,|\,e^{i\gamma(\vec{k}_\parallel)},\\
&|\,(\vec{\sigma}_{\vec{k}}^{-} \bullet \vec{\sigma}_{M_h})\,| = \left|(\vec{\sigma}_{\vec{k}}^{+} \bullet \vec{\sigma}_{M_h}^{*})\right|,\\
&x(\vec{k}_\parallel) = \left|x(\vec{k}_\parallel)\right|e^{i\alpha(\vec{k}_\parallel)},\ y(\vec{k}_\parallel) = \left|y(\vec{k}_\parallel)\right|e^{i\beta(\vec{k}_\parallel)},\\
&\alpha(\vec{k}_\parallel) - \beta(\vec{k}_\parallel) + \gamma(\vec{k}_\parallel) = 0
\end{aligned} \tag{102}$$

The last equality results from the fact that polariton energy spectrum $\hbar\omega_p(\vec{k}_\parallel)$, the magnetoexciton and cavity photon bare energies are real entities. This relation will be used below at point $\vec{k}_\parallel = 0$ where these phases will be simply denoted as α, β and γ.

Now the breaking of the gauge symmetry of the 2D magnetoexciton–photon system leading to the BEC of the magnetopolaritons on the lower polariton branch at point $\vec{k}_\parallel = 0$ will be discussed.

6. Breaking of the gauge symmetry and the mixed photon–magnetoexciton–acoustical plasmon states

A method to introduce the coherent macroscopic polariton states in a system of 2D e–h

pairs and photons captured in the microcavity was proposed in [30, 31]. It was assumed that the e–h pairs were excited on the quantum well embedded into the microcavity and interacted with the photons captured in the resonator giving rise to the 2D Wannier–Mott excitons and polariton formation. As was shown in [30], the proposed method is equivalent to the u-v Bogoliubov transformation for the electron and hole Fermi operators and to Bogoliubov displacement transformation for the photon Bose operators. This method will be now applied to the case of 2D magnetoexcitons and photons in microcavity with the aim to investigate the BEC of magnetopolaritons in the state with $\vec{k}_{\|}=0$ on the lower polariton branch. The unitary transformation proposed in [30] looks as

$$D(\sqrt{N_p})=\exp\left(\sqrt{N_p}\left(L_0^{\dagger}-L_0\right)\right) \tag{103}$$

where N_p is a macroscopic number of the condensed polaritons at point $\vec{k}_{\|}=0$ of the lower polariton branch. The cavity photon with $\vec{k}_{\|}=0$ has a quantized longitudinal projection of its wave vector $\vec{k}$ equal to π/L_c. Only the photons with a given circular polarization are considered. In this case, we have

$$\begin{aligned}&\hat{L}_0=x(0)\Psi_{ex}(0)+y(0)c_{\frac{\pi}{L_c},-},\\ &x(0)=|x(0)|e^{i\alpha},\\ &y(0)=|y(0)|e^{i\beta}\end{aligned} \tag{104}$$

and the starting unitary transformation can be factorized in two independent unitary transformations acting separately in two subsystems of magnetoexcitons and of the photons as follows:

$$\begin{aligned}&D(\sqrt{N_p})=D_{ex}(\sqrt{N_p}\,|x(0)|)D_{ph}(\sqrt{N_p}\,|y(0)|),\\ &D_{ex}(\sqrt{N_p}\,|x(0)|)=\exp\left[\sqrt{N_p}\,|x(0)|\left(e^{-i\alpha}\hat{\Psi}_{ex}^{\dagger}(0)-e^{i\alpha}\hat{\Psi}_{ex}(0)\right)\right],\\ &D_{ph}(\sqrt{N_p}\,|y(0)|)=\exp\left[\sqrt{N_p}\,|y(0)|\left(e^{-i\beta}c^{\dagger}_{\frac{\pi}{L_c},-}-e^{i\beta}c_{\frac{\pi}{L_c},-}\right)\right]\end{aligned} \tag{105}$$

Taking into account the expressions for the magnetoexciton operators

$$\begin{aligned}&\hat{\Psi}_{ex}^{\dagger}(0)=\frac{1}{\sqrt{N}}\sum_t a_t^{\dagger}b_{-t}^{\dagger},\\ &\hat{\Psi}_{ex}(0)=\frac{1}{\sqrt{N}}\sum_t b_{-t}a_t\end{aligned} \tag{106}$$

one can transcribe operator $D_{ex}(\sqrt{N_p}\,|x(0)|)$ in the form $D_{ex}(\sqrt{N_p}\,|x(0)|)=e^{z}=\prod_t e^{z_t}$, where

$$\begin{aligned}&z=\sqrt{N_p}\,|x(0)|\left(e^{-i\alpha}\hat{\Psi}_{ex}^{\dagger}(0)-e^{i\alpha}\hat{\Psi}_{ex}(0)\right)=\sum_t z_t,\\ &z_t=\nu_p\,|x(0)|\left(e^{-i\alpha}a_t^{\dagger}b_{-t}^{\dagger}-e^{i\alpha}b_{-t}a_t\right)\end{aligned} \tag{107}$$

The unitary transformations of the Fermi operator are

$$
\begin{aligned}
&D_{ex}(\sqrt{N_p}\,|x(0)|)a_t D_{ex}^{-1}(\sqrt{N_p}\,|x(0)|) = e^{z_t}a_t e^{-z_t} = \alpha_t = \\
&= a_t\cos(v_p\,|x(0)|) - b_{-t}^{\dagger}e^{-i\alpha}\sin(v_p\,|x(0)|), \\
&D_{ex}(\sqrt{N_p}\,|x(0)|)b_{-t} D_{ex}^{-1}(\sqrt{N_p}\,|x(0)|) = e^{z_t}b_{-t}e^{-z_t} = \beta_{-t} = \\
&= b_{-t}\cos(v_p\,|x(0)|) + a_t^{\dagger}e^{-i\alpha}\sin(v_p\,|x(0)|)
\end{aligned}
\tag{108}
$$

Here, the filling factor of the Bose-Einstein condensate was introduced

$$\frac{N_p}{N} = v_p^2 \tag{109}$$

Side by side with unitary transformations (108) for the single-particle Fermi operators, one can also obtain the transformations for the two-particle integral operators. They were obtained using commutation relations (91) and look as follows

$$
\begin{aligned}
&e^{\hat{z}}\frac{\hat{D}(\vec{Q})}{\sqrt{N}}e^{-\hat{z}} = \frac{\hat{D}(\vec{Q})}{\sqrt{N}}\cos(2v_p\,|x(0)|) - \hat{\theta}(\vec{Q})\sin(2v_p\,|x(0)|), \\
&e^{\hat{z}}\hat{\theta}(\vec{Q})e^{-\hat{z}} = \hat{\theta}(\vec{Q})\cos(2v_p\,|x(0)|) + \frac{\hat{D}(\vec{Q})}{\sqrt{N}}\sin(2v_p\,|x(0)|), \\
&\hat{\theta}(\vec{Q}) = e^{-i\alpha}\hat{\Psi}_{ex}^{\dagger}(\vec{Q}) + e^{i\alpha}\hat{\Psi}_{ex}(-\vec{Q}),\ e^{\hat{z}}\hat{\rho}(\vec{Q})e^{-\hat{z}} = \hat{\rho}(\vec{Q}), \\
&e^{z}e^{-i\alpha}\Psi_{ex}^{\dagger}(\vec{Q})e^{-z} = e^{-i\alpha}\Psi_{ex}^{\dagger}(\vec{Q}) + \frac{1}{2}\sin\left(2v_p\,|\,x(0)\,|\right)\frac{D(\vec{Q})}{\sqrt{N}} + \frac{1}{2}[\cos\left(2v_p\,|\,x(0)\,|\right) - 1]\theta(\vec{Q}), \\
&e^{z}e^{i\alpha}\Psi_{ex}(-\vec{Q})e^{-z} = e^{i\alpha}\Psi_{ex}(-\vec{Q}) + \frac{1}{2}\sin\left(2v_p\,|\,x(0)\,|\right)\frac{D(\vec{Q})}{\sqrt{N}} + \frac{1}{2}[\cos\left(2v_p\,|\,x(0)\,|\right) - 1]\theta(\vec{Q})
\end{aligned}
\tag{110}
$$

As one can see, the superposition of the magnetoexciton creation and annihilation operators in the form $\theta(\vec{Q})$ forms a coherent mixed state with acoustical plasmon density operator $\frac{\hat{D}(\vec{Q})}{\sqrt{N}}$. These mixed magnetoexciton–plasmon states were discussed in [32–34].

The full Hamiltonian of the magnetoexciton-photon system consists of four parts as follows:

$$\hat{H} = \hat{H}_{mex,1} + \hat{H}_{0,ph} + \hat{H}_{mex,2} + \hat{H}_{mex-ph} \tag{111}$$

It will be subjected to unitary gauge transformation (105), which means calculation of the following unitary transformations:

$$
\begin{aligned}
&D_{ex}(\sqrt{N_p}\,|\,x(0)\,|)(\hat{H}_{mex,1} + \hat{H}_{mex,2})D_{ex}^{-1}(\sqrt{N_p}\,|\,x(0)\,|), \qquad D_{ph}(\sqrt{N_p}\,|\,y(0)\,|)\hat{H}_{0,ph}D_{ph}^{-1}(\sqrt{N_p}\,|\,y(0)\,|), \\
&D_{ex}(\sqrt{N_p}\,|\,x(0)\,|)D_{ph}(\sqrt{N_p}\,|\,y(0)\,|)\hat{H}_{mex-ph}D_{ph}^{-1}(\sqrt{N_p}\,|\,y(0)\,|)D_{ex}^{-1}(\sqrt{N_p}\,|\,x(0)\,|)
\end{aligned}
$$

The first of them is

$$\hat{\tilde{H}}_{mex,1} = D_{ex}(\sqrt{N_p} \mid x(0) \mid)\hat{H}_{mex,1}D_{ex}^{-1}(\sqrt{N_p} \mid x(0) \mid) =$$
$$= \left(E_{mex}(R_1; M_h, \varepsilon_m^-) - \mu_{ex}\right)\cos(2\nu_p \mid x(0) \mid)\frac{\hat{D}(0)}{2} +$$
$$+(G_{e-h}(R_1; M_h, \varepsilon_m^-) - \mu_e + \mu_h)\frac{\hat{\rho}(0)}{2} - \qquad (112)$$
$$-\frac{\sqrt{N}}{2}\sin(2\nu_p \mid x(0) \mid)\left(E_{mex}(R_1; M_h, \varepsilon_m^-) - \mu_{ex}\right)\hat{\theta}(0),$$
$$\mu_{ex} = \mu_e + \mu_h$$

The second one looks as

$$\hat{\tilde{H}}_{mex,2} = D_{ex}(\sqrt{N_p} \mid x(0) \mid)\hat{H}_{mex,2}D_{ex}^{-1}(\sqrt{N_p} \mid x(0) \mid) =$$
$$= \frac{1}{2}\sum_{\vec{Q}}\Big\{W_{0-0}(\vec{Q})\hat{\rho}(\vec{Q})\hat{\rho}(-\vec{Q}) + W_{a-a}(\vec{Q})\Big[\cos^2(2\nu_p \mid x(0) \mid)\hat{D}(\vec{Q})\hat{D}(-\vec{Q}) +$$
$$+\sin^2(2\nu_p \mid x(0) \mid)N\theta(\vec{Q})\theta(-\vec{Q}) -$$
$$-\cos(2\nu_p \mid x(0) \mid)\sin(2\nu_p \mid x(0) \mid)\sqrt{N}\,(\hat{D}(\vec{Q})\theta(-\vec{Q}) + \theta(\vec{Q})\hat{D}(-\vec{Q}))\Big] + \qquad (113)$$
$$+W_{0-a}(\vec{Q})\Big[\cos(2\nu_p \mid x(0) \mid)\,(\hat{\rho}(\vec{Q})\hat{D}(-\vec{Q}) + \hat{D}(\vec{Q})\hat{\rho}(-\vec{Q})) -$$
$$-\sin(2\nu_p \mid x(0) \mid)\sqrt{N}\,(\hat{\rho}(\vec{Q})\theta(-\vec{Q}) + \theta(\vec{Q})\hat{\rho}(-\vec{Q}))\Big]\Big\}$$

The third transformation concerns the captured photons

$$\hat{\tilde{H}}_{0,ph} = D_{ph}(\sqrt{N_p} \mid y(0) \mid)\hat{H}_{0,ph}D_{ph}^{-1}(\sqrt{N_p} \mid y(0) \mid) =$$
$$= \left(\hbar\omega_{\frac{\pi}{L_c}} - \mu_{ph}\right)N_p \mid y(0) \mid^2 + \sum_{\vec{k}_\parallel}\left(\hbar\omega_{\vec{k}^-} - \mu_{ph}\right)c_{\vec{k},-}^{\dagger}c_{\vec{k},-} -$$
$$-\sqrt{N_p} \mid y(0) \mid\left(\hbar\omega_{\frac{\pi}{L_c}} - \mu_{ph}\right)\left(e^{-i\beta}c_{\frac{\pi}{L_c},-}^{\dagger} + e^{i\beta}c_{\frac{\pi}{L_c},-}\right), \qquad (114)$$
$$\vec{k} = \frac{\pi}{L_c}\vec{a}_3 + \vec{k}_\parallel,\ \vec{k}_\parallel = \vec{a}_1 k_x + \vec{a}_2 k_y$$

The last transformation involves the magnetoexciton and photons operators as follows:

$$\hat{\tilde{H}}_{mex-ph} = D(\sqrt{N_p})\hat{H}_{mex-ph}D^{-1}(\sqrt{N_p}) =$$

$$D_{ex}(\sqrt{N_p} \mid x(0) \mid)\{\hat{H}_{mex-ph} - \sqrt{N_p} \mid y(0) \mid [\varphi(0)e^{-i\beta}(\vec{\sigma}^{+}_{\frac{\pi}{L_c}} \bullet \vec{\sigma}^{*}_{M_h})\hat{\Psi}^{\dagger}_{ex}(0) +$$

$$+\varphi^{*}(0)e^{i\beta}(\vec{\sigma}^{-}_{\frac{\pi}{L_c}} \bullet \vec{\sigma}_{M_h})\hat{\Psi}_{ex}(0)]\}D^{-1}_{ex}(\sqrt{N_p} \mid x(0) \mid) =$$

$$= -\sqrt{N_p} \mid y(0) \mid \{\hat{\Psi}^{\dagger}_{ex}(0)[\frac{1}{2}(\cos(2v_p \mid x(0) \mid)+1)\varphi(0)e^{-i\beta}(\vec{\sigma}^{+}_{\frac{\pi}{L_c}} \bullet \vec{\sigma}^{*}_{M_h}) +$$

$$+\frac{1}{2}(\cos(2v_p \mid x(0) \mid)-1)\varphi^{*}(0)e^{i\beta-2i\alpha}(\vec{\sigma}^{-}_{\frac{\pi}{L_c}} \bullet \vec{\sigma}_{M_h})] +$$

$$+\hat{\Psi}_{ex}(0)[\frac{1}{2}(\cos(2v_p \mid x(0) \mid)+1)\varphi^{*}(0)e^{i\beta}(\vec{\sigma}^{-}_{\frac{\pi}{L_c}} \bullet \vec{\sigma}_{M_h}) +$$

$$+\frac{1}{2}(\cos(2v_p \mid x(0) \mid)-1)\varphi(0)e^{-i\beta+2i\alpha}(\vec{\sigma}^{+}_{\frac{\pi}{L_c}} \bullet \vec{\sigma}^{*}_{M_h})] +$$

$$+\frac{\hat{D}(0)}{2\sqrt{N}}\sin(2v_p \mid x(0) \mid)[\varphi(0)e^{-i\beta+i\alpha}(\vec{\sigma}^{+}_{\frac{\pi}{L_c}} \bullet \vec{\sigma}^{*}_{M_h}) + \varphi^{*}(0)e^{i\beta-i\alpha}(\vec{\sigma}^{-}_{\frac{\pi}{L_c}} \bullet \vec{\sigma}_{M_h})]\} +$$

$$+\frac{1}{2}(\cos(2v_p \mid x(0) \mid)+1)\sum_{\vec{k}_{\parallel}}[\varphi(\vec{k}_{\parallel})(\vec{\sigma}^{+}_{\vec{k}} \bullet \vec{\sigma}^{*}_{M_h})c_{\vec{k},-}\Psi^{\dagger}_{ex}(\vec{k}_{\parallel}) + \varphi^{*}(\vec{k}_{\parallel})(\vec{\sigma}^{-}_{\vec{k}} \bullet \vec{\sigma}_{M_h})c^{\dagger}_{\vec{k},-}\Psi_{ex}(\vec{k}_{\parallel})] +$$

$$+\frac{1}{2}(\cos(2v_p \mid x(0) \mid)-1)\sum_{\vec{k}_{\parallel}}[\varphi(\vec{k}_{\parallel})e^{2i\alpha}(\vec{\sigma}^{+}_{\vec{k}} \bullet \vec{\sigma}^{*}_{M_h})c_{\vec{k},-}\Psi_{ex}(-\vec{k}_{\parallel}) + \tag{115}$$

$$+\varphi^{*}(\vec{k}_{\parallel})e^{-2i\alpha}(\vec{\sigma}^{-}_{\vec{k}} \bullet \vec{\sigma}_{M_h})c^{\dagger}_{\vec{k},-}\Psi^{\dagger}_{ex}(-\vec{k}_{\parallel})] +$$

$$+\frac{1}{2}\sin(2v_p \mid x(0) \mid)\sum_{\vec{k}_{\parallel}}[\varphi(\vec{k}_{\parallel})e^{i\alpha}(\vec{\sigma}^{+}_{\vec{k}} \bullet \vec{\sigma}^{*}_{M_h})c_{\vec{k},-}\frac{\hat{D}(\vec{k}_{\parallel})}{\sqrt{N}} + \varphi^{*}(\vec{k}_{\parallel})e^{-i\alpha}(\vec{\sigma}^{-}_{\vec{k}} \bullet \vec{\sigma}_{M_h})c^{\dagger}_{\vec{k},-}\frac{\hat{D}^{\dagger}(\vec{k}_{\parallel})}{\sqrt{N}}]$$

Taking into account relation (102) between phases α, β and γ and definition (110) of operator $\theta(0)$, one can represent the transformed Hamiltonian with the broken gauge symmetry in the form

$$\hat{\tilde{H}} = N_p \left|y(0)\right|^2 \left(\hbar\omega_{\frac{\pi}{L_c}} - \mu_{ph} \right) - \sqrt{N_p}\left|y(0)\right| \left(\hbar\omega_{\frac{\pi}{L_c}} - \mu_{ph} \right) \left(e^{-i\beta} c^{\dagger}_{\frac{\pi}{L_c},-} + e^{i\beta} c_{\frac{\pi}{L_c},-} \right) -$$

$$-\hat{\theta}(0)\sqrt{N_p}\left[\frac{1}{2}\left(E_{mex}(R_1; M_h, \varepsilon_m^-) - \mu_{ex} \right) \sin(2v_p \left|x(0)\right|) + \right.$$

$$\left. + v_p \left|y(0)\right| \left| \varphi(0) \left(\vec{\sigma}^-_{\frac{\pi}{L_c}} \bullet \vec{\sigma}_{M_h} \right) \right| \cos(2v_p \left|x(0)\right|) \right] +$$

$$+ \frac{\hat{D}(0)}{2} \left[E_{mex}(R_1; M_h, \varepsilon_m^-) - \mu_{ex} - 2v_p \sin(2v_p \left|x(0)\right|) \left|y(0)\right| \left| \varphi(0) \left(\vec{\sigma}^-_{\frac{\pi}{L_c}} \bullet \vec{\sigma}_{M_h} \right) \right| \right] +$$

$$+ \left(G_{e-h}(R_1; M_h, \varepsilon_m^-) - \mu_e + \mu_h \right) \frac{\hat{\rho}(0)}{2} + \sum_{\vec{k}_\parallel} \left(\hbar\omega_{\vec{k}^-} - \mu_{ph} \right) c^{\dagger}_{\vec{k},-} c_{\vec{k},-} +$$

$$+ \frac{1}{2} \sum_{\vec{Q}} \left\{ W_{0-0}(\vec{Q}) \hat{\rho}(\vec{Q}) \hat{\rho}(-\vec{Q}) + W_{a-a}(\vec{Q}) \left[\cos^2(2v_p \left| x(0) \right|) \hat{D}(\vec{Q}) \hat{D}(-\vec{Q}) + \right. \right.$$

$$+ \sin^2(2v_p \left| x(0) \right|) N \hat{\theta}(\vec{Q}) \hat{\theta}(-\vec{Q}) -$$

$$\left. - \frac{1}{2} \sin(4v_p \left| x(0) \right|) \sqrt{N} \left(\hat{D}(\vec{Q}) \hat{\theta}(-\vec{Q}) + \hat{\theta}(\vec{Q}) \hat{D}(-\vec{Q}) \right) \right] +$$

$$+ W_{0-a}(\vec{Q}) \left[\cos(2v_p \left| x(0) \right|) \left(\hat{\rho}(\vec{Q}) \hat{D}(-\vec{Q}) + \hat{D}(\vec{Q}) \hat{\rho}(-\vec{Q}) \right) - \right.$$

$$\left. \left. - \sin(2v_p \left| x(0) \right|) \sqrt{N} \left(\hat{\rho}(\vec{Q}) \hat{\theta}(-\vec{Q}) + \hat{\theta}(\vec{Q}) \hat{\rho}(-\vec{Q}) \right) \right] \right\} +$$

$$+ \frac{1}{2} (\cos(2v_p \left| x(0) \right|) + 1) \sum_{\vec{k}_\parallel} [\varphi(\vec{k}_\parallel) (\vec{\sigma}^+_{\vec{k}} \bullet \vec{\sigma}^*_{M_h}) c_{\vec{k},-} \Psi^{\dagger}_{ex}(\vec{k}_\parallel) + \varphi^*(\vec{k}_\parallel) (\vec{\sigma}^-_{\vec{k}} \bullet \vec{\sigma}_{M_h}) c^{\dagger}_{\vec{k},-} \Psi_{ex}(\vec{k}_\parallel)] + \qquad (116)$$

$$+ \frac{1}{2} (\cos(2v_p \left| x(0) \right|) - 1) \sum_{\vec{k}_\parallel} [\varphi(\vec{k}_\parallel) e^{2i\alpha} (\vec{\sigma}^+_{\vec{k}} \bullet \vec{\sigma}^*_{M_h}) c_{\vec{k},-} \Psi_{ex}(-\vec{k}_\parallel) +$$

$$+ \varphi^*(\vec{k}_\parallel) e^{-2i\alpha} (\vec{\sigma}^-_{\vec{k}} \bullet \vec{\sigma}_{M_h}) c^{\dagger}_{\vec{k},-} \Psi^{\dagger}_{ex}(-\vec{k}_\parallel)] +$$

$$+ \frac{1}{2} \sin(2v_p \left| x(0) \right|) \sum_{\vec{k}_\parallel} [\varphi(\vec{k}_\parallel) e^{i\alpha} (\vec{\sigma}^+_{\vec{k}} \bullet \vec{\sigma}^*_{M_h}) c_{\vec{k},-} \frac{\hat{D}(\vec{k}_\parallel)}{\sqrt{N}} + \varphi^*(\vec{k}_\parallel) e^{-i\alpha} (\vec{\sigma}^-_{\vec{k}} \bullet \vec{\sigma}_{M_h}) c^{\dagger}_{\vec{k},-} \frac{\hat{D}^{\dagger}(\vec{k}_\parallel)}{\sqrt{N}}]$$

Looking at this expression, one may conclude that, side by side with the u-v-type transformation (110) of magnetoexciton superposition-type operator $\hat{\theta}(\vec{Q})$ and acoustical plasmon density operator $\hat{D}(\vec{Q})/\sqrt{N}$, another mixed state of the acoustical plasmon–photon type appeared under the influence of the magnetoexciton–polariton BEC. In addition to them, there are anti-resonant-type terms in the magnetoexciton-photon interaction, even if they were not included in initial Hamiltonian (87). The obtained results permit determining chemical potentials μ_{ex} and μ_{ph} and investigating the energy spectrum of the collective elementary excitations.

7. Conclusions

The influence of the RSOC on the properties of the 2D magnetoexcitons was described taking into account the results concerning the Landau quantization of the 2D electrons and holes with nonparabolic dispersion laws, pseudospin components and chirality terms [18, 19, 22]. The main attention was paid to the study of operators $\hat{\rho}(\vec{Q})$ and $\hat{D}(\vec{Q})$ that, together with magnetoexciton creation and annihilation operators $\hat{\Psi}^{\dagger}_{ex}(\vec{k}_{\|})$ and $\hat{\Psi}_{ex}(\vec{k}_{\|})$, form a set of four two-particle integral operators. It was shown that the Hamiltonians of the electron-radiation and Coulomb electron–electron interactions can be expressed in terms of these four integral two-particle operators. The unitary transformation breaking the gauge symmetry of the deduced Hamiltonian and the BEC of the magnetoexciton–polaritons were introduced in the frame of the Keldysh–Kozlov–Kopaev method using the polariton creation and annihilation operators. They were expressed in terms of the same magnetoexciton and photon operators using the Hopfield coefficients in a simplified form without the anti-resonance terms because the energies of the participant quasiparticles are finite situated near the energy of the cavity mode. The unitary transformation is factorized as a product of two unitary transformations acting independently in two magnetoexciton and photon subsystems. It was realized that the BEC of magnetoexciton polaritons supplementary gives rise to the acoustical plasmon–photon interaction and to a new type plasmon–polariton formation. The antiresonance terms of the magnetoexciton–photon interaction also appeared even if they were neglected in the starting Hamiltonian. The mixed magnetoexciton–acoustical plasmon states in the absence of the RSOC were investigated in [32–34]. The obtained final transformed Hamiltonian will be used to study the collective elementary excitations.

Acknowledgments. E. V. D., I.V.P., and V.M.B. thank the Foundation for Young Scientists of the Academy of Sciences of Moldova for financial support (14.819.02.18F).

References

[1] E. I. Rashba, Fiz. Tverd. Tela, 2, 1224 (1960)
[2] T. Hakioglu and M. Sahin, Phys. Rev. Lett., 98, 166405 (2007)
[3] M. Ali Can and T. Hakioglu, Phys. Rev. Lett., 103, 086404 (2009)
[4] G. Dresselhaus, Phys. Rev., 100, 580 (1955)
[5] Yu. A. Bychkov and E.I. Rashba, Pis. Zh. Eksp. Teor. Fiz., 39, 66 (1984)
[6] R. Winkler, Spin–Orbit Coupling Effects in Two-Dimensional Electron and Hole Systems, Berlin, Springer Tracts in Modern Physics, vol. 191 (2003)
[7] B-f. Zhu and Y-C. Chang, Phys. Rev. B, 50, 11932 (1994)
[8] R. van Gelderen and C.M. Smith, Phys. Rev. B, 81, 125435 (1994)
[9] S. A. Brazovskii, Zh. Eksp. Teor. Fiz., 68, 175 (1975); [S.A.Brazovskii, Sov. Phys.—JETP, 41, 85 (1975) (Engl. transl.)]
[10] R.Winkler, M. Merkler, T. Darnhofer, and U. Rossler, Phys. Rev. B, 53, 10858 (1996)
[11] U. Ekenberg and M.Altarelli, Phys. Rev. B, 32, 3712 (1985)
[12] R. Winkler, Phys. Rev. B, 62, 4245 (2000)
[13] R. Winkler, H. Noh, E. Tutuc, and M. Shayegan, Phys. Rev. B, 65, 155303 (2002)

[14] E. L. Ivchenko and G. E. Pikus, Superlattices and Other Heterostructures. Symmetry and Optical Phenomena, Berlin, Springer Series in Solid-State Sciences, vol. 110 (1997) p. 370
[15] A. H. Castro Neto, F. Guinea, N. M. R. Peres, K. S. Novoselov, and A. K. Geim, Rev. Mod. Phys., 81, 109 (2009)
[16] G. L. Bir and G. E. Pikus, Symmetry and Strain-Induced Effects in Semiconductors, New York: Wiley (1974)
[17] S. A. Moskalenko, M. A. Liberman, and I. V. Podlesny, Phys. Rev. B, 79(12), 125425 (2009)
[18] S. A. Moskalenko, I. V. Podlesny, P. I. Khadzhi, B. V. Novikov, and A.A. Kiselyov, Solid State Commun., 151, 1690 (2011)
[19] T. Hakioglu, M.A. Liberman, S.A. Moskalenko, and I.V. Podlesny, J. Phys.: Cond. Matt., 23, 345405 (2011)
[20] S. A. Moskalenko, M. A. Liberman, P. I. Khadzhi, E. V. Dumanov, I. V. Podlesny, and V. V. Botan, Physica E, 39, 137 (2007)
[21] S. A. Moskalenko, I. V. Podlesny, M. A. Liberman, and B. V. Novikov, J. Nanophotonics, 6, 061806 (2012)
[22] I. V. Podlesny, S. A. Moskalenko, T. Hakioglu, A. A. Kiselyov, and L. Gherciu, Physica E, 49, 44 (2013)
[23] O. L. Berman, R. Y. Kezerashvili, and Yu. E. Lozovik, Phys. Rev. B, 80, 115302 (2009)
[24] E. V. Dumanov, J. Nanoelectron. Optoelectron., 7, 724 (2012)
[25] E. V. Dumanov and L. E. Gherciu, Phys. Status Solidi B, 250(7), 1432 (2013)
[26] S. A. Moskalenko, I. V. Podlesny, E. V. Dumanov, and A. A. Kiselyov, arXiv:1309.1053 (2013); J. Nanoelectron. Optoelectron. (in press)
[27] R. J. Elliott, Phys. Rev., 108, 1384 (1957)
[28] S. A. Moskalenko, Introduction in the theory of high density excitons, Chisinau, Stiinta (1983) (in Russian)
[29] R. S. Knox, Theory of excitons, Academic Press, New York (1963)
[30] A. I. Bobrysheva, S. A. Moskalenko, and S.S. Russu, Physica E, 8, 81 (2000)
[31] P. R. Eastham and P. B. Littlewood, Phys. Rev. B, 64, 235101 (2001)
[32] E. V. Dumanov, M. A. Liberman, S. A. Moskalenko, B. V. Novikov, and S. S. Rusu, Phys. Status Solidi B, 250(1), 115 (2013)
[33] S. A. Moskalenko, M. A. Liberman, D. W. Snoke, E. V. Dumanov, S. S. Rusu, and F. Cerbu, Eur. Phys. J. B, 85: 359 (2012)
[34] S. A. Moskalenko, M. A. Liberman, D. W. Snoke, E. V. Dumanov, S. S. Rusu, and F. Cerbu, Solid State Comm., 155, 57 (2013)

COMPUTATIONAL MATERIALS SCIENCE

M. Nazarov[1] and I. D. Arellano [2]

[1] *Institute of Applied Physics, Academy Sciences of Moldova, Republic of Moldova*
[2] *Department of Physics, Technological University of Pereira, Vereda La Julita, Pereira, Colombia.*
E-mail address: mvnazarov@mail.ru

(Received March 10, 2014)

Abstract

First-principles simulation, meaning density-functional theory calculations with plane waves and pseudopotentials, has become a prized technique in condensed-matter theory. However, it is only in the last 15 years or so that we have been able to compute the properties of condensed matter from first principles. Here we discuss the basics of the subject, give a brief review of the theory, examine the advantages and disadvatnges of its implementation, and illustrate some of the ways simulators approach problems through a small case study. We also discuss why and how modern software design methods can be used in computational materials science.

1. Introduction

The properties of materials are often controlled by defects and impurities. This is particularly true in the case of semiconductors, where the incorporation of impurities in small concentrations determines the electrical conductivity. The fabrication of p-type and n-type doped layers underlies the design of almost all electronic and optoelectronic devices. A similar situation takes place in luminescence of phosphors where the material properties strongly depend on dopants.

To achieve this control of defects and impurities, comprehensive knowledge of the fundamental processes that control doping is required. In recent years, first-principles calculations have made important contributions to this knowledge. Today, the performance of computers is highly advanced, and we have reached the conclusion that the use of first-principles calculation is the most appropriate for highly accurate analysis of problems at the atomic or electronic scale. For the current first-principles calculation, high-speed simulation with high accuracy is necessary.

This paper is written to alleviate the barriers and pains which beginners in computational materials science suffer. Special attention is paid to the fact that experimentalists, rather than specialists, use this package in order to interpret the derived data. The goal of this paper is to provide an overview of the state-of-the-art methodology for performing first principles calculations for defects and impurities. More details can be found in various excellent reviews that are available for that purpose [1–3] and in our future works.

2. Computational, experimental, and theoretical methods

Computational Materials Science aims at enhancing the communication between experimental materials research, theory, and computational work on both existing and new advanced materials and their applications (Fig. 1).

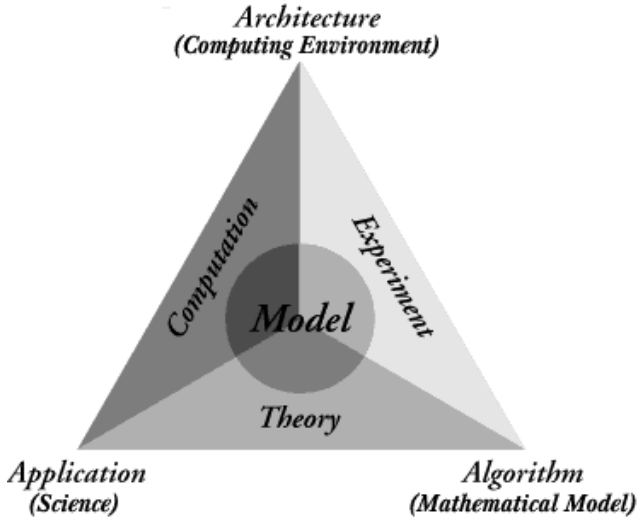

Fig. 1. Unique model combining Experiment, Theory, and Computation.

Computational Materials Science presents the most important approaches in this new interdisciplinary field of materials science and engineering. The reader will learn to assess which numerical method is appropriate for performing simulations at the various microstructural levels and how they can be coupled. Modeling and simulation play an ever increasing role in the development and optimization of materials.

Nevertheless, we have to understand that only very few aspects of chemistry can be computed exactly. However, just as not all spectra are perfectly resolved, often a qualitative or approximate computation can give a useful insight into chemistry if you understand what it tells you and what it does not.

3. First principles or “ab initio” calculations

Big success in the development of computer hardware and software enables now to perform the first principles (ab initio) calculations with accuracy comparable with that obtained in experiment. These approaches also enable predicting the behavior of materials under extreme conditions (for example, at very high pressures inaccessible under laboratory conditions), to study dangerous (radioactive, explosive) materials. They are very useful in predicting new materials with interesting properties that have never been synthesized. Moreover, the first principles calculations enable improving our understanding of physical phenomena occurring in known materials. The Nobel Prizes awarded to Robert S. Mulliken (1966), Walter Kohn and John Pople (1998) can be regarded as an acknowledgment of their significant contribution to the development of first principles methods in physics, chemistry, and materials science.

In physics, a calculation is said to be *from first principles*, or *ab initio*, if it starts directly at the level of established laws of physics and does not make assumptions, such as empirical

model and fitting parameters. For example, calculation of electronic structure using the Schrödinger's equation within a set of approximations that do not include fitting the model to experimental data is an *ab initio* approach.

The term "ab initio" is a Latin term meaning "from the beginning". This name is given to computations which are derived directly from theoretical principles, with no inclusion of experimental data. Most of the time, this is referring to an approximate quantum mechanical calculation. The approximations made are usually mathematical approximations, such as using a simpler functional form for a function or getting an approximate solution to a differential equation.

Scientists mainly use three different methods to make calculations:

- Molecular mechanics uses classical physics to explain and interpret the behavior of atoms and molecules. It relies on force-field with embedded empirical parameters and requires experimental data (or data from *ab initio*) for parameters. This method does not calculate electronic properties. Typically, it is a large system (thousands of atoms).
- Semi-empirical techniques use approximations from empirical (experimental) data to provide the input into the mathematical models. This method uses quantum physics and experimentally derived empirical parameters. It is less demanding computationally than *ab initio* methods and capable of calculating transition states and excited states. At the same time, it is less rigorous than *ab initio* methods and requires experimental data (or data from *ab initio*) for parameters. It is a medium-sized system (hundreds of atoms).
- *ab initio*, a group of methods in which molecular structures can be calculated using nothing but the Schroedinger equation, the values of the fundamental constants and the atomic numbers of the atoms present. This method is useful for a broad range of systems because it does not depend on experimental data. It is capable of calculating transition states and excited states. A disadvantage is that it is computationally expensive. Usually, it is a small system (tens of atoms) requiring rigorous accuracy.

To better understand the computational approaches and simulation packages, we propose the following scheme in Fig. 2.

Some of the most popular computation programs are summarized below:

VASP: Pseudopotential, Ultra-soft, projector augmented-wave (PAW), parallel execution in supercomputer.

SIESTA: localized orbital basis and pseudopotential, parallel execution, very small basis, handle very large system (nano system).

WIEN97: linearized-augmented-plane wave (LAPW) method, parallel execution in supercomputer.

WIEN2K: full potential linear-augmented plane wave (FPLAPW) approach within the framework of DFT. WIEN2K is based on the method which is among the most precise and reliable ways to calculate the electronic structure of solids.

OSAKA-2K: one of the best pseudopotential methods. This package is a set of program codes which calculate electronic structures of materials. It covers a wide range of calculations from optimization of crystal structure to molecular dynamic simulations, in addition to standard self-consistent calculation and band calculations.

CRYSTAL-98 package, which is based on both Density Functional and Hartree–Fock theories. The gradient-corrected correlation functional by Lee, Yang and Parr is used, combined

with the Becke 3 exchange functional (B3LYP).

CRYSTAL-06: linear combination of atomic orbitals (LCAO) formalism. Hybrid Hartree-Fock-DFT Hamiltonians (B3PW and PBE0) is used.

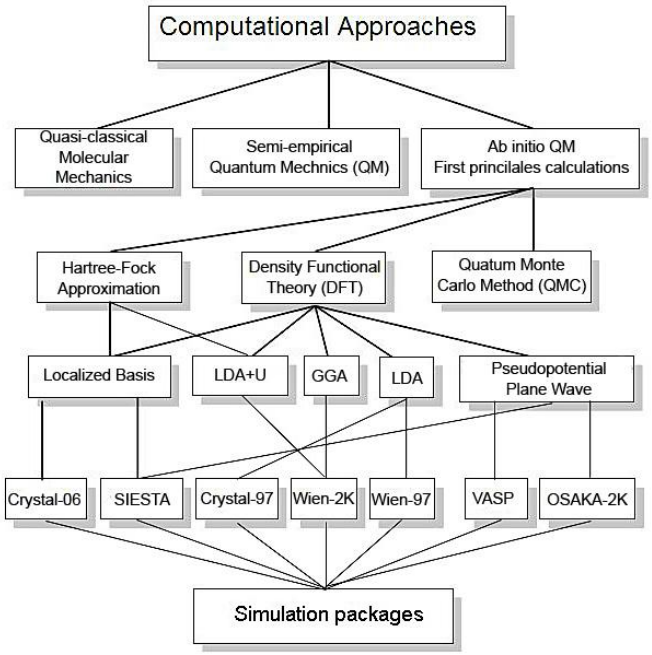

Fig. 2. Scheme of computational approaches and simulation packages.

The most common types of ab initio calculations are referred to as Hartree Fock approximation (abbreviated HF), Density functional theory (DFT), and the quantum Monte Carlo (QMC) method.

We consider here QMC and HF methods very briefly and pay our attention mostly to DFT methods, because they are among the most popular and versatile methods available in condensed-matter physics, computational physics, and computational chemistry.

3.1. Monte Carlo calculations

Quantum Monte Carlo techniques provide a practical method for solving the many-body Schrödinger equation. They are closely related to the well established classical Monte Carlo methods that have been successfully applied to a wide range of problems involving stochastic behavior ranging from scientific problems, engineering problems and modeling the financial markets. A common link between classical and quantum Monte Carlo techniques is the use of random numbers to evaluate multi-dimensional integrals. QMC works with an explicitly correlated wave function and numerically evaluate integrals using a Monte Carlo integration. These calculations can be very time consuming, but they are probably the most accurate methods known today.

There are several flavors of QMC such as variational, diffusion, and Green's functions. The latter two are projection approaches which dispense with quantum chemical basis sets, but they have to deal with the fermion sign problem, and the related fixed-node approximation. In general, all QMC methods have a good scaling with the number of electrons, enabling relatively

large systems to be tackled, but with a computational cost much larger than traditional ab-initio methods based on DFT. The good reviews of Monte Carlo method can be found in Refs, [4-6].

3.2. Hartree–Fock algorithm

The Hartree–Fock method is typically used to solve the time-independent Schrödinger equation for a multi-electron atom or molecule as described in the Born–Oppenheimer approximation. In Hartree-Fock method as a starting point, the wave function is used to describe electronic structure. Since there are no known solutions for many-electron systems, the problem is solved numerically. Due to the nonlinearities introduced by the Hartree–Fock approximation, the equations are solved using a nonlinear method such as iteration, which gives rise to the name "self-consistent field method."

In this method, the primary approximation is referred to as the central field approximation. This means that the Coulombic electron-electron repulsion is not specifically taken into account. However, its net effect is included in the calculation.

The second approximation in HF calculations is that the wave function must be described by some functional form, which is only known exactly for a few one electron systems. The functions used most often are linear combinations of Slater type orbitals or Gaussian type orbitals, abbreviated STO and GTO. The wave function is formed from linear combinations of atomic orbitals or more often from linear combinations of basis functions. Because of this approximation, most HF calculations give a computed energy greater than the Hartree Fock limit.

One of attempts of non-empirical method to obtain the properties of solid is to solve the equation of the many-electron Hamiltonian directly. In practice, this equation is often rewritten through a Slater determinant which is composed of a lot of single-electron wave functions.

In Hartree-Fock approximation only the exchange effect is considered. In many problems, it is known that the exchange term only is not good. Further developments in order to include the correlation effect into account, many methods, such as the configuration interaction by expanding on many Slater determinants and the quantum Monte Carlo method, have been devised [7-10].

Anyway, these approaches are all based upon the wave functions and express the electronic states of solid through the set of wave functions. In the configuration interaction method, the combination of wave functions is very complicated, resulting in a severe limitation of the size of problems. Meanwhile, for the many-electron problems, another and very different approach has been proposed; it is referred to as the density functional theory.

3.3. Density functional theory

Density functional theory is a quantum mechanical modelling method used in physics and chemistry to investigate the electronic structure (principally the ground state) of many-body systems, in particular atoms, molecules, and the condensed phases.

In this approach, the electron density is the quantity, from which the theory is developed. It is much easier to solve one-electron equations derived from the density functional theory than to solve the general equation. With this theory, the properties of a many-electron system can be determined by using functionals, i.e., functions of another function, which in this case is the spatially dependent electron density. Hence, the term density functional theory comes from the use of functionals of the electron density. Electron density is a primary way of describing the system.

DFT has been very popular for calculations in solid state physics since the 1970s. It was impossible to solve many body problems by quantum mechanical methods. It became possible only with the *adiabatic approximation* (Born-Oppenheimer) and *Density Functional Theory*

(Hohenberg and Kohn 1964, Kohn and Sham 1965). Since 1980, this method has established a position as one of the main methods of calculating the properties of solids and molecules from the first principles. However, DFT was not considered accurate enough for calculations in quantum chemistry until the 1990s, when the approximations used in the theory were greatly refined to better model the exchange and correlation interactions. In many cases, the results of DFT calculations for solid-state systems agree quite satisfactorily with experimental data. Computational costs are relatively low compared to traditional methods, such as Hartree-Fock theory based on the complicated many-electron wavefunctions. A price of mathematical simplification of the density functional method, which replaces a many-electronic problem by a one-electron problem, is paid by introducing an unknown functional of exchange and correlation V_{xc} of the charge density. Fortunately, there is an easy approximation for V_{xc}. The most widely used forms of V_{xc} is the so-called Local Density Approximation (LDA) and Generalized Gradient Approximation (GGA) shown in Fig.3.

A generalization of the LDA method for systems with strong Coulomb correlations is proposed as LDA+U [7, 9], which gives a correct description of the Mott insulators. The LDA + U method takes into account orbital dependence of the Coulomb and exchange interactions which is absent in the LDA.

Despite recent improvements, there are still difficulties in using density functional theory to properly describe intermolecular interactions, especially van der Waals forces (dispersion); charge transfer excitations; transition states, global potential energy surfaces, and some other strongly correlated systems; and in calculations of the band gap in semiconductors. The development of new DFT methods designed to overcome this problem, by alterations to the functional or by the inclusion of additive terms, is a current research topic. Some of DFT implementations are summarized and shown in Fig. 3.

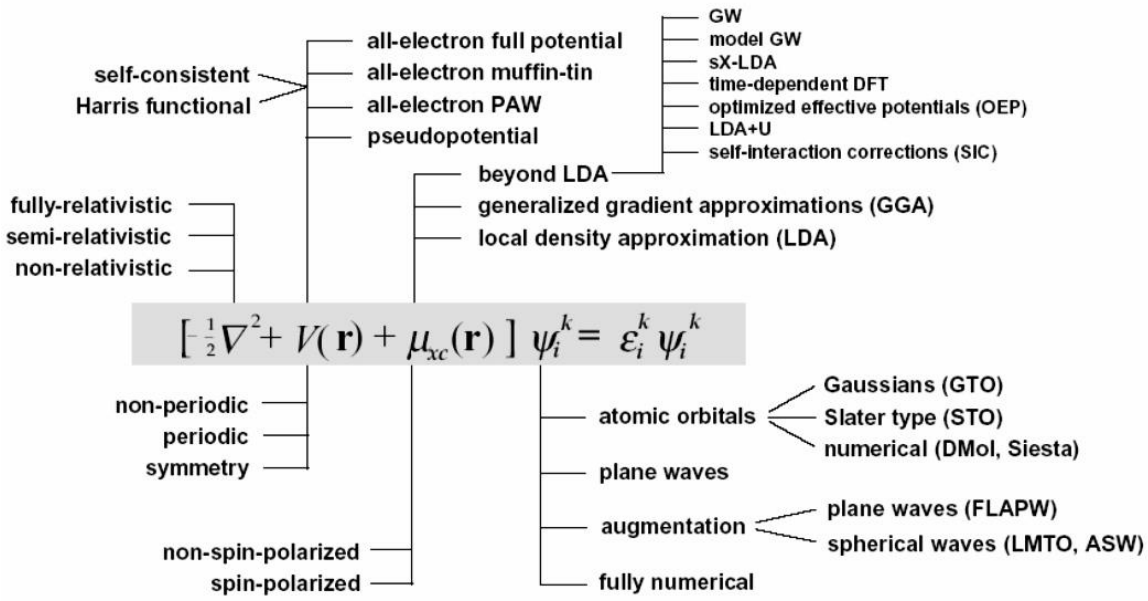

Fig. 3. DFT Implementations.

There are many good reviews about density functional theory [11-14].

Density functional theory is a widely used method to calculate the ground state energy of

a system by mapping a multiple-electron system into a single electron problem. By incorporating exchange-correlation, such as a local (spin) density approximation (L(S)DA) and generalized gradient approximations (GGA), DFT has attained much success in deriving the ground state electronic structure properties. However, when it comes to systems with highly correlated electrons, such as that possessing d- or f-electrons, computations with L(S)DA or GGA reveal their disadvantages. They fail to describe magnetic insulators, such as 3d-transition-metal oxides or a Mott insulator. Despite being able to reproduce the ground state structures for the magnetic NiO and MnO series, the theory wrongly predicted Mott insulators as metal. In addition, the gaps in NiO and MnO are predicted to be too small in magnitude compared to photoemission experiments [15]. Many attempts have been made to improve the L(S)DA and GGA calculations on systems with d- or f-electrons. One of the most successful improvements is the '+*U* ' approach (i.e., L(S)DA+*U* and GGA+*U*). As pointed out by Anisimov et al. [7, 9], the L(S)DA behaves like a weak-coupling mean-field theory. Anisimov et al. generalized the L(S)DA method by proposing the L(S)DA+*U* approach to strongly correlated systems. In this approach effective on-site interactions are introduced to the existing Hamitonian to better account for the orbital dependence of the Coulomb and exchange interactions of the strongly correlated (i.e., d- and f-) electrons. The basic idea of L(S)DA+*U* (which also applies to GGA+*U*) calculation is described as follows [7–9]. For delocalized s- and p-electrons in the atom, only L(S)DA calculations are involved. For localized d- or f-electrons, a on-site d-d column interaction or a Hubbard-like term is used instead of the averaged coulomb energy. The d- or f-electron interactions can be quite accurately calculated via this '+*U* ' approach. Many DFT packages, such as WIEN2k [16], provide computational functionality to conveniently calculate the '+*U* 'effect.

To summarize, computational science is a branch of science that generates data which complements experimental data on the structures, properties, and reactions of substances. The calculations are based primarily on Schroedinger's equation and include:

1. calculation of electron and charge distributions;
2. molecular geometry in ground and excited states;
3. potential energy surfaces;
4. rate constants for elementary reactions;
5. details of the dynamics of molecular collisions.

The good side of ab initio methods is that they eventually converge to the exact solution, once all of the approximations are made sufficiently small in magnitude. However, this convergence is not monotonic. Sometimes, the smallest calculation gives the best result for a given property.

The bad side of ab initio methods is that they are expensive. These methods often take enormous amounts of computer time, memory, and disk space.

In general, ab initio calculations give very good qualitative results and can give increasingly accurate quantitative results in future.

For details readers are referred to Refs. [17-19].

Some examples of application considered computational methods for real luminescent materials will be demonstrated in our future works.

4. Conclusions

In this paper, we reviewed the state of the art in computational approaches for calculating defects and impurities in semiconductors and luminescent materials from first principles. The

methodology is entirely general and can be applied to any material. First-principles theory has played an important role in interpreting and guiding experiments in this rapidly developing field.

Looking toward the future, we can be confident that first-principles computations will continue to play an important role in addressing defects and impurities, especially in luminescence with activator impurities. New developments in methodology could make the approach even more powerful. These first-principles calculations can then form a foundation for realistic simulations of the actual processes.

References

[1] W. E. Pickett, Comput. Phys. Rep. 9, 115, (1989).
[2] M. C. Payne, M. P. Teter, D. C. Allan, T. A. Arias, and J. D. Joannopoulos, Rev. Mod. Phys. 64, 1045, (1992).
[3] M. Bockstedte, A. Kley, J. Neugebauer, and M. Scheffler, Comput. Phys. Commun. 107, 187, (1997).
[4] D. M. Ceperley, B. Alder J. Phys. Rev. Lett., 45(7), 566 (1980).
[5] F. F. Assaad, P. Werner, P. Corboz, E. Gull, and M. Troyer, Phys. Rev. B, 72(22), 224518 (2005).
[6] A. Georges, G. Kotliar, W. Krauth, and M. J. Rozenberg, Rev. Mod. Phys., 68(1), 13 (1996).
[7] V. I. Anisimov, J. Zaanen, and O. K. Andersen, Phys. Rev. B, 44(3), 943 (1991).
[8] A. I. Liechtenstein, V. I. Anisimov, and J. Zaanen, Phys. Rev. B, 52(8), R5467 (1995).
[9] V. Anisimov, F. Aryasetiawan, and A. Lichtenstein, J. Phys.: Condens. Matter, 9(4), 767 (1997).
[10] J. C. Slater, Phys. Rev., 51(10), 846 (1937).
[11] P. Hohenberg and W. Kohn. Phys. Rev., 136(3B), B864 (1964).
[12] W. Kohn and L. J. Sham, Phys. Rev., 140(4A), A1133 (1965).
[13] W. Kohn, Rev. Mod. Phys., 71(5), 1253 (1999).
[14] M. S. Hybertsen and S. G. Louie, Phys. Rev. Lett., 55(13), 1418 (1985).
[15] K. Terakura, T. Oguchi, A. R. Williams, and J. Kubler, Phys. Rev. B 30, 4734 (1984).
[16] P. Blaha, K. Schwarz, G. Madsen, D. Kvasnika, K. Luitz, Wien2k, Technical Universitat Wien, Austria, 2001. ISBN 3-9501031-1-2.
[17] J. Callaway and N. March, Density Functional Methods: Theory and Applications in *Solid State Physics*, H. Ehrenreich F S, and D. Turnbull ed. Academic Press, New York, 1984.
[18] R. O. Jones and O. Gunnarsson, Rev. Mod. Phys. 61(3), 689 (1989).
[19] S. B. Trickey, ed. Density Functional Theory of Many-Fermion Systems, Advances in Quantum Chemistry, Academic Press, San Diego, 1990.

FIRST-PRINCIPLES CALCULATIONS OF YTTRIUM TANTALATE AND NIOBATE CRYSTALS

M. Nazarov[1], L. Th. Leng[2], Y. T. Leong[3], L. L. Chen[2], and I. D. Arellano[4]

[1] Institute of Applied Physics, Academy Sciences of Moldova, Republic of Moldova
[2] Faculty of Engineering and Technology, Multimedia University, Jalan Ayer Keroh Lama, 75450 Melaka, Malaysia
[3] School of Physics, University Sains Malaysia, 11800 USM, Penang, Malaysia
[4] Department of Physics, Technological University of Pereira, Vereda La Julita, Pereira, Colombia.
E-mail address: mvnazarov@mail.ru (Mihail Nazarov)

(Received March 10, 2014)

Abstract

The structural and electronic properties of yttrium tantalate ($YTaO_4$) and yttrium niobate ($YNbO_4$) crystals are studied using experimental and first-principles GGA+*U* total energy calculations. The band gap of the host lattice from absorption and luminescence experiment is measured to be 5.1 eV for $YTaO_4$ and 4.1eV for $YNbO_4$. This is close to 5.14 eV and 4.28 eV, respectively, reproduced by means of GGA+*U* approach. In our calculation, we tune both Hubbard energy *U* and exchange parameter *J* to reproduce the energy gap measured experimentally. It is found that Hubbard energy *U* plays a major role in reproducing the experimentally measured energy gap, but exchange parameter *J* does not. We also calculate the density of states (DOS) using the optimized *U* to interpret the experimentally measured luminescence spectra. Both the experimental and DOS calculations show that the valence band of tantalate (Ta) and niobate (Nb) systems is mainly composed of oxygen (O) 2p states. The lower conduction band is mainly composed of Ta 5d states or Nb 4d states, respectively, while the upper conduction band involves the contribution mainly from yttrium (Y) 4d states, with the middle conduction band mainly a mixture of Ta or Nb and Y states. The calculated partial DOS of each atom in the tantalate and niobate system is then compared with the UV and VUV spectra from photoluminescence excitation (PLE) experiment to explain the nature of the bands observed.

1. Introduction

Undoped $YTaO_4$ and $YNbO_4$ are well known as self-activated phosphors for more than four decades. Even though these materials are well-known self-activated phosphors, their electronic structure, optical absorption mechanism, and optical transitions have not been clearly understood.

Historically, Ferguson [1] in 1957 was the first to describe both natural fergusonite (a yttrium niobium-tantalate) as well as synthetic $YTaO_4$ correctly, where they crystallized in monoclinic symmetry with the space group 15 ($I\,2/a$). $YTaO_4$ exhibits three crystal structures. At high temperature the tetragonal form (T, space group 88) with scheelite structure distorts via a second-order phase transition to monoclinic (M, space group 15) structure having the fergusonite structure. Another monoclinic structure, called M′ (space group 13), can be synthesized directly

at lower temperatures (below 1400°C). M′ transforms to T at approximately 1450°C and then to M upon cooling. $YNbO_4$ has a polymorphism and exhibits two polymorphs: the high temperature T-scheelite and the low temperature M-fergusonite [2-5]. At high-temperature tetragonal form (T) of $YNbO_4$ with scheelite structure distorts via a second-order phase transition to a monoclinic (M) structure having the fergusonite structure. The monoclinic phase transforms into tetragonal phase at 900°C.

$YNbO_4$, together with $YTaO_4$, are commercially valuable and used extensively in X-ray intensifying screens. As we all know, performances of phosphors and luminescence properties strongly depend on their crystal and electronic structures which can be understood via quantum mechanical calculations. Some fundamental questions concerning host lattice emission and charge transfer transitions in $YTaO_4$ and $YNbO_4$ remain to be answered. To better understand the luminescence mechanism, crystallographic structure, and absorption mechanism of these phosphors, first-principles calculations have been carried out.

This paper is dedicated to investigate the electronic properties of yttrium tantalate and niobate systems through the study of its density of states (DOS) and band structure using experimental and first-principles calculations. To the best of our knowledge, there is no offer of any explanation in the literature to the apparent discrepancy between the experimental spectra and calculated DOS [6–9]. The experimental spectra for $YTaO_4$ recorded a 5.1-eV band gap between conduction band and valence band, while the gaps from first-principles calculations are 4.2 eV (without scissor operator) and 4.8 eV (with scissor operator) [6, 10]. Thus, there is a discrepancy of 0.9 eV (without scissor operator) between experiment measurement and first-principles calculation. A scissor operator is applied to include the effects of self-energy and excitonic shift only. Therefore, the band gap issue cannot be resolved even with a scissor operator. Similarly, for $YNbO_4$, from our experimental spectra, we have the band gap between conduction and valence band of 4.1 eV, while the DOS from calculations in [6, 10] infers a band gap of 3.8 eV (value calculated without using the scissor treatment).

Density functional theory (DFT) is a widely used method to calculate the ground state energy of a system by mapping a multiple-electron system into a single electron problem. By incorporating an exchange-correlation, such as a local (spin) density approximation (L(S)DA) and generalized gradient approximations (GGA), DFT has attained much success in deriving the ground state electronic structure properties. However, when it comes to systems with highly correlated electrons, such as that possessing d- or f-electrons, computations with L(S)DA or GGA reveal their disadvantages. They fail to describe magnetic insulators, such as 3d-transition-metal oxides or Mott insulator. Despite being able to reproduce the ground state structures for the magnetic NiO and MnO series, the theory wrongly predicted Mott insulators as metal. In addition, the gaps in NiO and MnO are predicted to be too small in magnitude compared to photoemission experiments [11]. Many attempts have been made to improve the L(S)DA and GGA calculations on systems with d- or f-electrons. One of the most successful improvements is the '+*U*' approach (i.e., L(S)DA+*U* and GGA+*U*). As pointed out by Anisimov et al. [12, 13], the L(S)DA behaves like a weak-coupling mean-field theory. Anisimov et al. generalized the L(S)DA method by proposing the L(S)DA+*U* approach to strongly correlated systems. In this approach, effective on-site interactions are introduced to the existing Hamiltonian to better account for the orbital dependence of the Coulomb and exchange interactions of the strongly correlated (i.e., d- and f-) electrons. The basic idea of L(S)DA+*U* (which also applies to GGA+*U*) calculation is described as follows [12–14]. For delocalized s- and p-electrons in the atom, only L(S)DA calculations are involved. For localized d- or f-electrons, a on-site d-d column

interaction or a Hubbard-like term is used instead of the averaged coulomb energy. The d- or f-electron interactions can be quite accurately calculated via this '+*U* ' approach. Many DFT packages, such as WIEN2k [15], provide computational functionality to conveniently calculate the '+*U* 'effect.

The discrepancy between the published experimental results on the energy band gap of $YTaO_4$ and $YNbO_4$ from luminescence excitation spectra or absorbance data and that calculated from DFT is significant. One of the main goals of this work is to address this issue by reproducing the experimentally measured energy band gap through GGA+*U* calculations using the DFT package WIEN2k [15]. DOS obtained from the GGA+*U* calculation is then used to provide insight into the origin of the features measured in the excitation spectra.

2. Experimental and theoretical methods

2.1. Sample preparation

A few sets of yttrium tantalate and niobate phosphors were prepared by solid state reaction method from a homogeneous mixture consisting of Y_2O_3 (99.9%) and Ta_2O_5 or Nb_2O_5 (Optipur). Different inorganic salts, such as Li_2SO_4, LiCl, and Na_2SO_4, were used as a flux. The mixtures were homogenized with a ball mill, in acetone medium, and dried at 70°C. The phosphor samples were baked at 1200°C for 4 h and slowly cooled to room temperature. Finally, the samples were water washed, dried, and then sieved.

2.2. Characterization techniques

The samples were investigated using X-ray diffraction, UV and VUV excitation luminescence, and first-principles quantum-mechanical calculations in order to study their structural and luminescent properties.

UV measurements were monitored using a Perkin-Elmer LS50B spectrometer with a xenon flash lamp. VUV excitation spectra of samples were measured using a VUV spectrophotometer equipped with a VUV monochromator (ARC, VM 502) and a light source of a 30-W deuterium lamp (ARC, DS775-100).

In XRD measurements, a Cu-Kα radiation (λ = 1.54 Å) source generated from a Rigaku rotating anode generator was used operating at 40 kV and 40 mA. Basically, we measured the powder diffraction profiles (Θ–2Θ scan) in a range of 10° to 80°.

2.3. Ab initio method

Calculations were conducted using the all-electron full potential linearized augmented plane-wave method (FP-LAPW) [16–18] as implemented in WIEN2k [15]. In the FP-LAPW method, the unit cell is divided into non-overlapping atomic spheres, or Muffin-tin spheres that centered at the atomic sites and the interstitial region. In the interstitial region, a plane wave expansion is used, whereas inside the atomic sphere it is a combination of radial functions and spherical harmonics of the solution of the single electron Schrodinger equation. For exchange and correlation effects, the method of generalized gradient approximation (GGA) parameterized by Perdew, Burke, and Ernzerhohf (PBE96) [19] is used. Parameter RK_{max} of 7 is used in the simulation where R is the smallest atomic sphere radius in the unit cell and K_{max} is the magnitude of the largest K vector. RK_{max} will determine the matrix size used in self-consistency iterations. Lattice parameters for the $YTaO_4$ and $YNbO_4$ host lattices are taken from experimental data in Table 1. For integrals over the Brillouin zone, 18 k-points are used, as was implemented in [7].

The quantum effects contributed by strongly correlated d or f-electrons can be properly

treated using the GGA+U approach. There are two types of input parameters in the GGA+U calculation, namely U and J. U is the Hubbard energy or Coulomb parameter, while J refers to the exchange parameter. J is set to zero throughout the simulation. A different value of U will return a different output. The value of U is manually tuned until the resultant band gap from the GGA+U calculation agrees with that obtained by the experiments. The self-interaction corrected (SIC) variant of the GGA+U approach, which was introduced by Anisimov et al. [20], with an approximate correction for the self-interaction is used.

3. Results and discussion

3.1. Crystallographic data

Crystallographic structure of M′ $YTaO_4$ was first described by Wolten [21] with an "R" value of only 0.15. Later on Brixner and Chen [22] were able to reduce the "R" value to 0.034 and confirm the structure. It consists essentially of cube-like 8 coordinated Y polyhedra which can best be described as distorted square antiprisms. The average Y–O distance is 2.355 Å. The tantalum atoms are in a distorted octahedral coordination with four shorter Ta–O bonds at 1.86 and 1.95 Å, and two longer ones at 2.23 Å. The unit cell parameters are a = 5.30, b = 5.45, c = 5.11 Å and β = 96.5°.

The chemistry, as well as the structures of different tantalate's forms, are quite complex and for the purpose of the present article we shall restrict our discussion to the M′ form of $YTaO_4$, as it is the only structure exhibiting superior luminescent properties.

In the $YNbO_4$ host lattice, the niobium atom can be considered tetrahedrally coordinated to the oxygen atoms in a highly distorted site. In M-fergusonite, $YNbO_4$, this is no longer valid, since two of the four next-nearest oxygen ions are at shorter distance, whereas the other two are at longer distance than in the scheelite structure. We have to take into account the interaction between the Nb^{5+}- ion and six oxygen ions, i.e., to consider a Nb^{5+}- ion with a [4+2] coordination. From this point of view, the M-fergusonite structure is in between the scheelite structure with isolated tetrahedral groups and crystal structures of niobates with octahedral niobate groups [2–5, 22].

We took into account the atomic positions and lattice parameters in $YTaO_4$ and $YNbO_4$ mentioned in the cited above references, but the crystallographic data of investigated samples can vary a little from database results due to different sample synthesis and need to be carefully measured for particular samples when comparing crystallographic and luminescent properties. Therefore, we conducted XRD experiments for our samples independently. Our XRD measurements for prepared samples show the monoclinic phases of both phosphors (Fig. 1).

The detailed main peaks of synthesized tantalate phosphors in a range of 15°-50° are shown in Fig. 2b. From this figure it is evident that traditional XRD measurements with Cu-Kα radiation give wide peaks. To correctly determine the crystalline structures of the synthesized phosphors, we carried out XRD measurements on the basis of Synchrotron X-ray Diffraction patterns (Pohang Accelerator Laboratory, Korea). The result is shown in Fig. 2a. Similar results (not shown here) were also registered for niobate crystals.

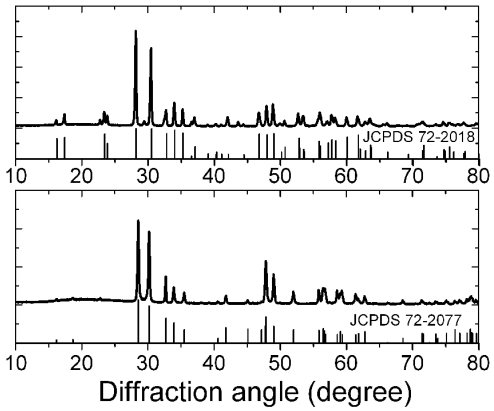

Fig. 1. XRD measurements (Cu-Kα radiation with λ = 1.54 Å source generated from a Rigaku rotating anode generator) of $YTaO_4$ phosphor (top) and $YNbO_4$ (bottom).

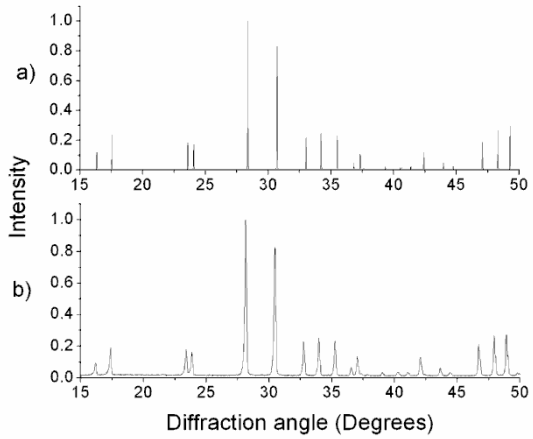

Fig. 2. A comparison of XRD measurements of $YTaO_4$ phosphor on the basis of synchrotron X-ray diffraction patterns (top) and Cu-Kα radiation (λ = 1.54 Å) source generated from a Rigaku rotating anode generator (bottom).

The Rietveld calculation provides the crystallographic information by comparing the model profile with X-ray or neutron curves using the least squares method. The lattice parameters and atomic positions from Rietveld analysis are presented in Table 1.

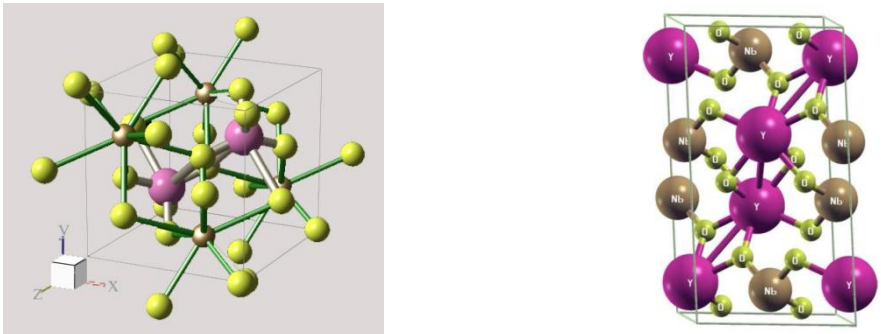

(a) (b)

Fig. 3. Crystal structure of M'- $YTaO_4$ (a) and $YNbO_4$ (b)

Table 1. Atomic positions and lattice parameters in $YTaO_4$ and $YNbO_4$

M'-$YTaO_4$	*Atom*	*x*	*y*	*z*	*F*
a=5.29568Å	Y	0.25	0.76523	0	1
b=5.445447Å	Ta	0.25	0.30632	0.5	1
c=5.10940Å	O(1)	0.49619	0.43402	0.27800	1
β=96.39119	O(2)	0.09912	0.09079	0.24181	1
M-$YNbO_4$	*Atom*	*x*	*y*	*z*	*F*
a=7.61851Å	Y	0	0.37891	0.25	1
b=10.94611Å	Nb	0	0.85620	0.25	1
c=5.29745Å	O(1)	0.20166	0.78039	0.20515	1
β=138.43617	O(2)	0.25050	0.96246	0.65526	1

These results are very close to those cited in Brixner and Chen [22]. One can see that the occupation factor $F = 1$, which means the site is fully occupied by an atom. The crystal structures of M'- $YTaO_4$ and $YNbO_4$ based on Table 1 are presented in Fig. 3.

3.2 Ab initio calculations, DOS and luminescence of $YTaO_4$

Figure 4 shows the DOS and band structure plots for $YTaO_4$ with and without considering *U*.

The coordinates of the special points used in plotting the $YTaO_4$ band structure are listed in Table 2.

Table 2. Coordinates of the special points used in plotting the band structure in Fig. 4

Label	Coordinates
GM	0,0,0
Z	0, 1/2, 0
Y	1/2, 0, 0
A	-1/2, 0, 1/2
B	0, 0, 1/2
D	0, 1/2, 1/2
E	-1/2, 1/2, 1/2

These coordinates can be obtained from standard sources, such as the Bilbao Crystallographic Server [23]. The band gap without Hubbard energy adjustment is 4.225 eV (Fig. 4a), while that with fine-tuned GGA+*U* is 5.15 eV (Fig. 4c). To obtain Fig. 4c and Fig. 4d, we vary the Hubbard energies *U* associated with the d-electrons of the Y and that of the Ta atom, respectively. We observe that when we "switch on" the Hubbard energy terms of either Y or Ta, or both, the band gap widens. While tuning for the best values of *U* for the Y and Ta atoms in a trial-and-error manner, we found that when *U* (Y atom)>*U* (Ta atom), the DOS of the Y atom will *overshadow* that of the Ta atom in the conduction region. Adding the exchange parameter *J* to the system will only make the band gap smaller but the overall DOS profile is almost unperturbed. Putting all these considerations together, the best values to match with the experimental findings are: *U* (Y atom) = 4.08 eV, *U* (Ta atom) = 11.56 eV, *J* (for both Ta and Y) = 0 eV. The band gap obtained with these *U* values is 5.15 eV. The Hubbard energy *U* provides a way to tune the output of the ab initio calculation to match the

energy gap as measured in the experiments. It is to be mentioned that the objective of tuning for the best values of *U* and *J* is not merely to match the band gap between experiment and ab initio calculation. Rather, the best values of *U* and *J* are used in the calculation of density of states (DOS) which are then compared with experiments.

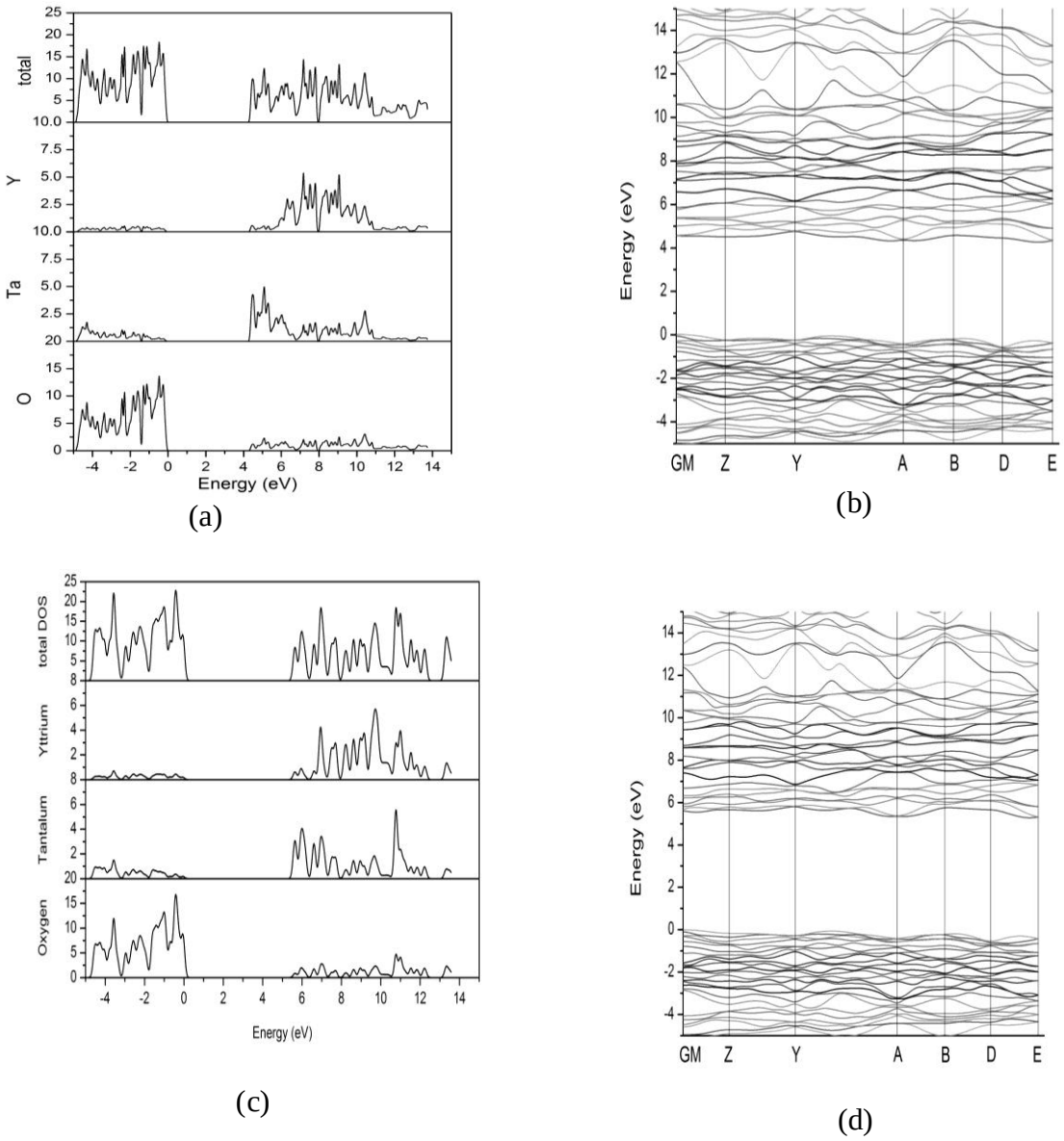

Fig. 4. (a) DOS and (b) band structure plot for $YTaO_4$ without considering Hubbard energy. (c) DOS and (d) band structure obtained with a fine-tuned Hubbard energy.

Although the values of the band gaps calculated by density functional theory are known to be underestimated [24], it is interesting to compare the gaps taken from the luminescence and absorbance experiments with calculated data. The results are compiled in Table 3. Band gap can be directly derived from absorbance spectra, such as that shown in Fig. 5, by determining the absorbance edge. The band gap value of 5.1 eV, as suggested from Fig. 5 (1) for $YTaO_4$, is in

good agreement with other experimental results listed in Table 3.

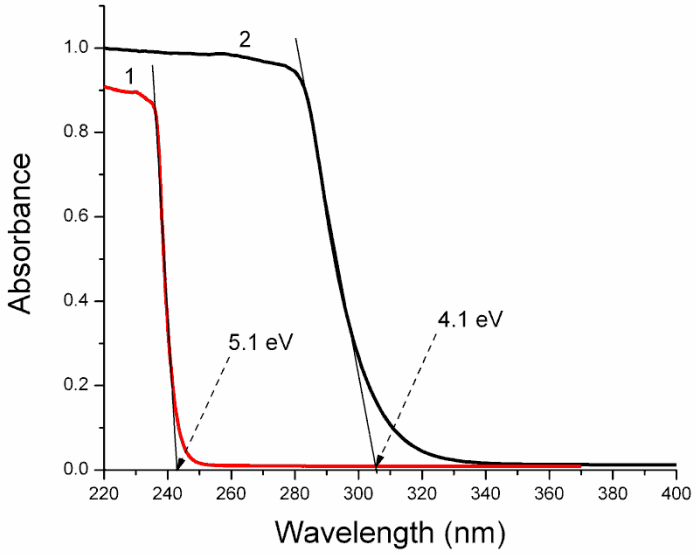

Fig. 5. Experimental absorbance spectra of $YTaO_4$ and $YNbO_4$ as measured in [25]. The band gaps deduced from this spectrum are 5.1 eV and 4.1, respectively.

Table 3. Reported band gap energies of $YTaO_4$

No.	E_{gap} (eV)	Method	Ref.
1	4.8	DFT (GGA method)	[10]
2	3.8	DFT (LDA method)	[7]
	5.0	Excitation spectrum	
3	5.2	DFT (GGA + scissor operator)	[25]
4	5.5	Abstracted from table 4.17 of Ref. [25]	[26]
5	3.8	Diffuse reflectance	[27]
6	5.0	Excitation spectrum	[28]
7	5.0	Excitation spectrum	[29]
8	5.1	Optical absorption spectrum	[30]
9	5.2	Optical absorption spectrum	[31]
10	5.4 5.0	Diffuse reflection spectrum Excitation spectrum	[32]
11	4.2	Calculated from DOS (GGA and LDA) using data from [30]	[33]
12	5.1	From absorption spectrum	This work
13	5.15	DFT (GGA+*U*)	This work

Figure 6 shows the PLE intensity measured experimentally and partial DOS of Y and Ta calculated from GGA+*U*.

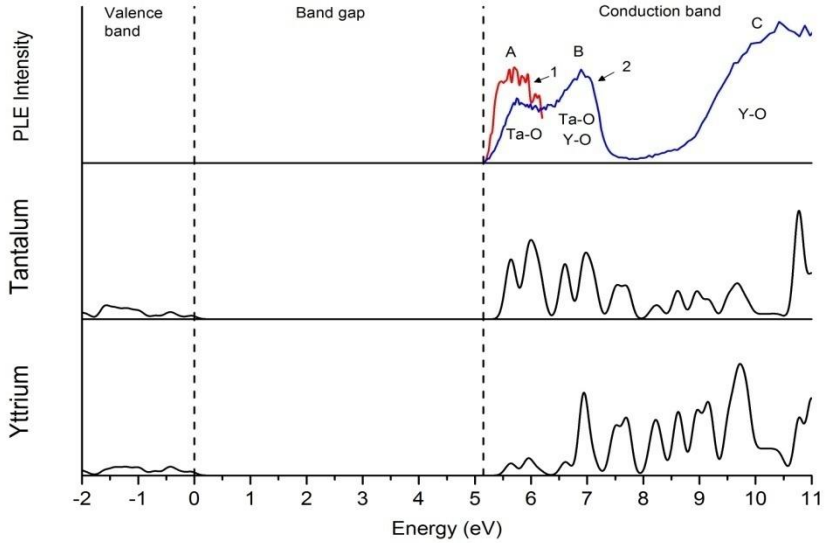

Fig. 6. UV (*1*) and VUV (*2*) excitation spectra of $YTaO_4$ with partial DOS of Y and Ta in the conduction band.

From the luminescence excitation spectra, the band gap in $YTaO_4$ corresponds to 5.15 eV and there are three bands A, B and C peaked around 6, 7, and 10 eV in the conduction band. The calculated partial DOS provides very insightful information to understand the characteristic features of these bands, such as identifying and explaining the nature of excitation bands and determining correctly the band gap in $YTaO_4$. In order to explain the nature of the A, B, and C bands in Fig. 6, we compare the PLE spectra against the calculated DOS. In Fig. 6, the position of the calculated conduction band on the energy scale was aligned with real spectra for the sake of easy comparison. As will be discussed below, the calculated DOS of the tantalum and yttrium provide a basis to understand the nature of bands A, B, and C in the excitation spectra.

Band A in the UV (*1*) and VUV (*2*) PLE around 6 eV in Fig. 6 can be associated with the absorption of the host lattices. The TaO_4^{3-} group can absorb excitation energy through $O^{2-} \rightarrow Ta^{5+}$ host charge transfer transition. This assumption is confirmed clearly by tantalum DOS distribution. The yttrium contribution in this area is negligible.

Band B in the VUV PLE spectra is also associated with the absorption of the host lattice, which involves mostly through $O^{2-} \rightarrow Ta^{5+}$ host charge transfer transition as well as the transitions between 4d-like states of Y and 2p-like states of O or Y^{3+}-O^{2-} (Fig. 6). Band B is a hybrid band, and it is composed from both [Y-O] and [Ta-O] charge transfer transitions.

Band C, peaked around 10 eV, is mostly related to the transitions between 4d-like states and 4s-like states of Y and 2p-like states of O. The Y-O bonds are excited and the energy is transferred to host lattice while the contribution of Ta-O is diminished.

If the high energies X-ray, electron beam, or VUV excitations were applied, it would be quite reasonable to assume that the excitation energy is absorbed first by the host lattice, which involves the transition between 4d-like states of Y and 2p-like states of O. The absorbed energy may then be transferred to TaO_4 groups and last transferred to the activator center, if any.

3.3 Ab initio calculations, DOS and luminescence of $YNbO_4$

As in previous paragraph, we use here the same DFT package WIEN2k to perform the GGA+U calculation for niobate system. Lattice parameters for the host lattice $YNbO_4$ are listed in Table 1. 18 k-points are used for integrals over the Brillouin zone. RK_{max} value is set to 7.

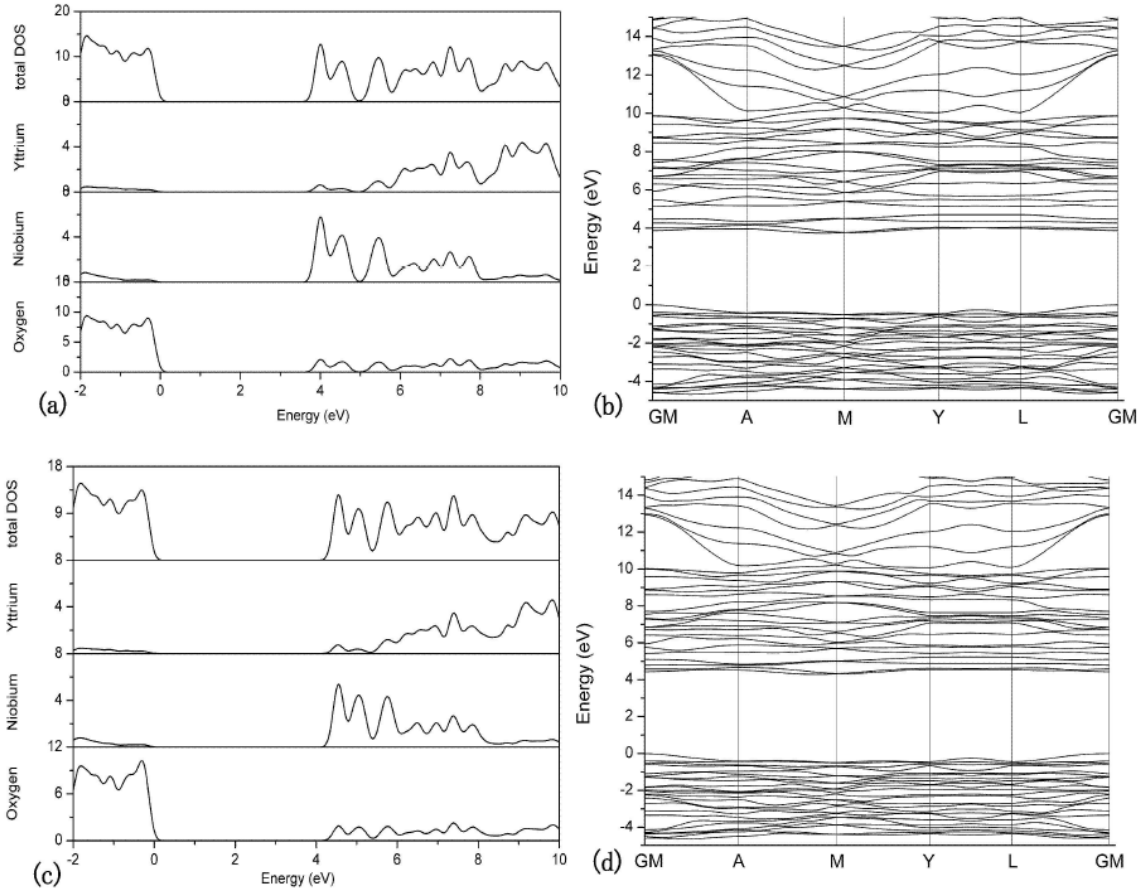

Fig. 7. (a) DOS and (b) band structure plot for $YNbO_4$ without considering Hubbard energy. (c) DOS and (d) band structure obtained with a fine-tuned Hubbard energy.

Figure 7 shows the DOS and band structure plot for $YNbO_4$ with and without considering Hubbard energy U. The band gap without Hubbard energy adjustment is 3.8 eV (Fig. 7a) while that with fine-tuned GGA+U is 4.28 eV (Fig. 7c). To obtain Fig. 7c and Fig. 7d, we vary the Hubbard energies U associated with the d-electrons of the Y and that of the Nb atom, respectively. Once the Hubbard energy U of the atom Y or Nb, or both, is switched on, the band gap widens. In the trial-and-error approach searching for the best values for U for the Y and Nb atoms, the DOS of the Y atom will overshadow that of the Nb atom in the conduction region unless U (Y atom) < U (Nb atom). Considering all the constraints, the best values to match with the experimental findings are: U (Y atom) = 0.68 eV, U (Nb atom) = 6.80 eV and the band gap obtained with these U values is 4.28 eV.

The DOS profile computed with fine-tuned Hubbard energy is almost identical with that computed without, except that the width of the band gap is varied with the strength of U. It thus can be concluded that the main effect of the Hubbard energy U on top of the GGA calculation on

this system is to widen the band gap, which in turn provides a way to tune the output of the ab initio calculations to match the energy gap as measured in the experiments. Band gap can be directly derived from absorbance spectra, such as that shown in Fig. 5, by determining the absorbance edge. The band gap value of 4.1 eV, as suggested from Fig. 5 (2) for $YNbO_4$, is in good agreement with other experimental results listed in the literature, which has a value lying between 4.1–4.4 eV [10, 25, 26, 34–40]. A similar result of ≈ 4.2 eV is estimated from excitation UV and VUV spectra as shown in Fig. 8.

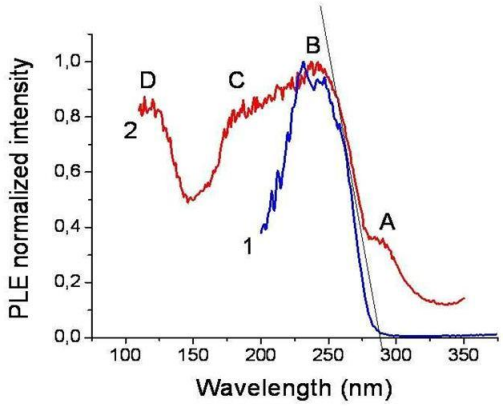

Fig. 8. PLE spectra for $YNbO_4$ under UV (*1*) and VUV (*2*) excitation.

To give a reliable interpretation to the overall feature of the luminescence and structural properties of niobate system, we investigate the excitation spectra of these materials and explain them from DOS theory. Four obvious large bands A, B, C, and D in the VUV PLE (Fig. 8) spectra are observed. We note that band A is only observed in the VUV but not in the UV data. We seek to clarify the nature of these bands with the aid from the DFT results. It is believed that bands B, C, and D in the VUV range in the niobate system are related to the following processes. Band B around 230 nm, which coincides well with the UV data, is associated with the absorption of the host lattices. The NbO_4^{3-} groups can absorb excitation energy through $O^{2-} \rightarrow Nb^{5+}$ host charge transfer transition. Bands C and D, peaking around 170 nm and 125 nm, are probably related to the host absorption. The Y-O bonds are excited and the energy is transferred to the host lattice.

The position of this band C for Y^{3+} ions can be calculated with the help of an empirical formula given by Jorgensen [41]

$$E_{CT} = [(X) - (M)] \times 30,000 \text{ cm}^{-1}.$$

Here, E_{CT} gives the position of the charge transfer band (CTB) in cm^{-1}, (X) the optical electronegativity of the anion, and (M) that of the central metal ion. Using the Pauling scale for electronegativity [42], namely (O)=3.44 and (Y)=1.22, the CTB of Y-O can be estimated near the 67.000 cm^{-1}, or around 150–160 nm.

To check this assumption and to explain the real nature of the bands, we compare the PLE spectra with the DOS calculated from first-principles (see Fig. 9).

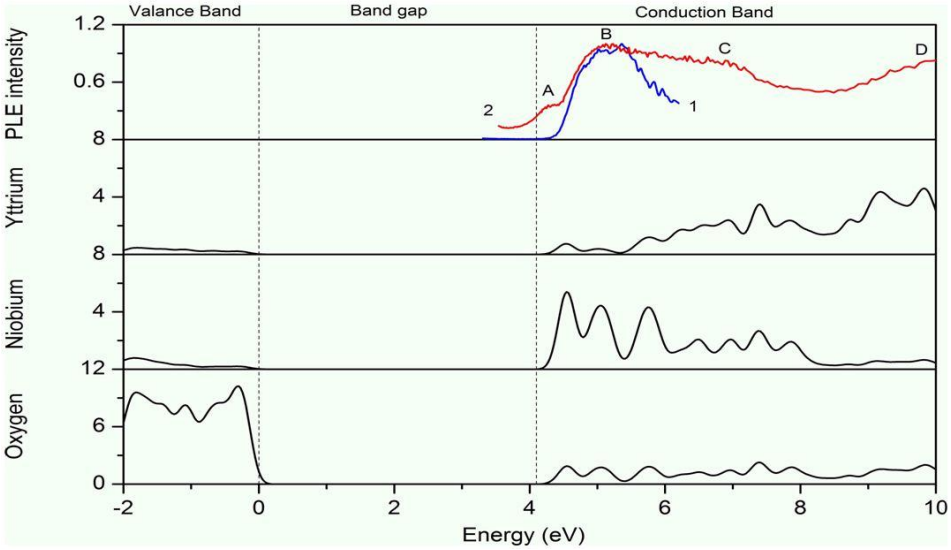

Fig. 9. UV (*1*) and VUV (*2*) excitation spectra of $YNbO_4$ with partial DOS of Y and Nb in the conduction band.

In the energy scale, the position of the calculated conduction band is aligned with real spectra. The contributions of Nb and Y are taken from partial DOS. The partial DOS of Niobium and Yttrium in Fig. 9 provides very insightful information to understand the characteristic features of these bands, such as identifying and explaining the nature of excitation bands and determining correctly the band gap in $YNbO_4$.

The nature of all the bands in excitation spectra can be explained by the Niobium and Yttrium partial DOS. Band A is partially located in the band gap. From DOS calculations for ideal structures, no contribution from Nb, Y, or O is observed in this area. Moreover, this band in UV spectrum for λ_{em} = 400 nm is not observed. It is thus supposed that band A is related to defects that can be excited by other wavelengths, because the excitation spectra in VUV were obtained by observing all emission light. The other possibility may be the calibration function in VUV measurements. The photoluminescence excitation spectra were measured in the VUV range of 100–350 nm using a sodium salicylate powder as a reference and calibrated by that of sodium salicylate, which has constant quantum efficiency in a range of 115–300 nm, and some artifacts can be seen in the ends of this area.

Band B in Fig. 9 is explained through the $O^{2-} \rightarrow Nb^{5+}$ host charge transfer transition. For the niobate system, the filled orbitals are concentrated on the oxygen ions and the empty ones on the niobium ions, so that the lowest optical transitions can be considered as 2p(O)→ 4d(Nb) charge transfer transitions. Thus, the excited state consists of an increased electron density in the vicinity of the metal ion along the tetrahedral bonds.

Band C is a hybrid band, and it is composed from both citation [Y-O] and [Nb-O] charge transfer transitions. Band D in the VUV PLE spectra is associated with the absorption of the host lattice, which involves mostly the transitions between 4d-like states of Y and 2p-like states of O or Y^{3+}- O^{2-} charge transfer transition.

If the high energies X-ray, electron beam or VUV excitations are applied, it would be quite reasonable to assume that the excitation energy is absorbed first by the host lattice, which involves the transition between 4d-like states of Y and 2p-like states of O. The absorbed energy

may then be transferred to NbO_4 groups and last transferred to the activator center, if any.

Using real UV excitation (Fig. 8, curve *1*) and emission spectra of $YNbO_4$ host lattice, as well as DOS interpretation (Fig. 9), the configurational coordinate diagram showing the energy transfer from excited to ground state is presented in Fig. 10.

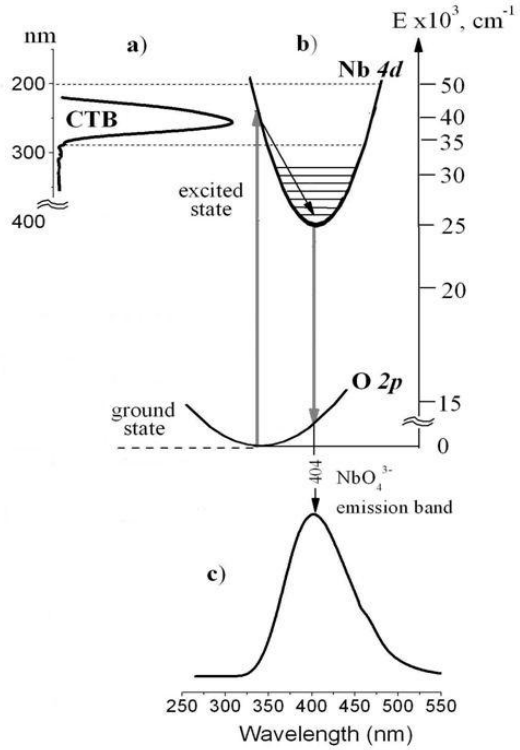

Fig. 10. Excitation (a) and emission (c) spectra of $YNbO_4$ host lattice and configurational coordinate diagram (b) corresponding to real data and showing the energy transfer from excited to ground state.

4. Conclusions

Through the GGA+U method as implemented in WIEN2k, we have addressed the band gap issue and the contribution of d-electrons from Y and Ta or Nb atoms in the conduction band. The band gap of the $YTaO_4$ host lattice is about 5.1 eV based on absorption and luminescence experiments, while the band gap of the $YNbO_4$ host lattice from DOS calculation is 4.28 eV and agrees well with 4.1 eV from absorption and luminescence experimental data. The band gap calculated using GGA+U is tuned to match the value from experiments by varying the Hubbard energies U associated with the Y and Ta or Nb atoms. The Hubbard energy U plays a major role in tuning the energy band gap to the right value. The J parameter, on the other hand, does not affect the calculation. Our GGA+U calculation shows that Ta atoms contribute to the total DOS in the 5–7 eV range for the tantalate system and Nb atoms in the 4–6 eV range for the niobate system, while Y atom dominates from 7eV onwards in the conduction band for both. These results are in good agreement with the luminescence experiment and explain well the three bands as measured in the UV and VUV excitation spectra.

References

[1] R. B. Ferguson, Can. Mineral 6, 72 (1957).
[2] J. M. Jehng and I. E. Wachs, Chem. Mater. 3, 100 (1991).
[3] A. H. Buth and G. Blasse, Phys. Stat. Sol. (a) 64, 669 (1981).
[4] M. J. J. Lammers and G. Blasse, Mater. Res. Bull. 19, 759 (1984).
[5] V. S. Stubican, J. Am. Ceram. Soc. 47, 55 (1964).
[6] M. Nazarov, D. Y. Noh, A. Zhbanov, and Y.-G. Lee, J. Ceram. Process Res. 12, s183 (2011).
[7] D. Xiang, B. Liu, M. Gu, X. Liu, S. Huang, and C. Ni, Acta Optica Sinica. 29, 448 (2009).
[8] I. D. Arellano, M. Nazarov, and D. Y. Noh, Rev. Colomb. Fisica. 41, 123 (2009).
[9] I. Arellano, M. Nazarov, C. C. Byeon, E.-J. Popovici, H. Kim, H. Y. Kang, and D. Y. Noh, Mater. Chem. and Phys. 119, 48 (2010).
[10] M. Nazarov and A. Zhbanov, Mold. J. Phys. Sci. 10, 52 (2011).
[11] K. Terakura, T. Oguchi, A. R. Williams, and J. Kubler, Phys. Rev. B, 30, 4734 (1984).
[12] V. I. Anisimov, J. Zaanen, and O. K. Andersen, Phys. Rev. B, 44, 943 (1991).
[13] V. I. Anisimov, F. Aryasetiawan, and A. I. Lichtenstein, J. Phys: Condens. Matter. 9, 767 (1997).
[14] A. I. Lichtenstein, J. Zaanen, and V. I. Anisimov, Phys. Rev. B, 52, R5467 (1995).
[15] P. Blaha, K. Schwarz, G. Madsen, D. Kvasnika, and K. Luitz, Wien2k, Technical Universitat Wien, Austria, 2001. ISBN 3-9501031-1-2.
[16] D. J. Singh, Plane Waves, Pseudopotential and the LAPW Method, Kluwer-Academic, Boston, 1994.
[17] E. Wimmer, H. Krakauer, M. Weinert, and A. J. Freeman, Phys. Rev. B, 24, 864 (1984).
[18] M. Weinert, E. Wimmer, and A. J. Freeman, Phys. Rev. B, 26, 4571 (1982).
[19] J. P. Perdew, K. Burke, and M. Ernzerhof, Phys. Rev. Lett. 77, 3865 (1996).
[20] V. Anisimov, I. Solovyev, M. Korotin, M. Czyzyk, and G. Sawatzky, Phys. Rev. B, 48, 16929 (1993).
[21] G. M. Wolten, Acta Crystallogr. 23, 939 (1967).
[22] L. H. Brixner and H. Y. Chen, J. Electrochem. Soc. 130, 2435 (1983).
[23] Bilbao crystallographic server, http://www.cryst.ehu.es/cgi-bin/cryst/programs/
[24] M. S. Hybertsen and S. G. Louie, Phys. Rev. B, 34, 5390 (1986).
[25] M. Nazarov and D. Y. Noh, New Generation of Europium and Terbium activated Phosphors, Pan Standford Publishing, 2011.
[26] A. H. Krumpel, P. Boutinaud, E. van der Kolk, and P. Dorenbos, J. Lumin. 130, 1357 (2010).
[27] M. Liu, W. You, Z. Lei, G. Zhou, J. Yang, G. Wu, G. Ma, G. Luan, T. Takata, M. Hara, K. Domen, and C. Li, Chem. Commun. 2192 (2004).
[28] Li Bo, G. Zhen-nan, D. Yi, L. Jian-hua, and S. Mian-zeng, Chem. Res. Chin. Univers. 15, 226 (1999).
[29] Hubin, H. Huangyan, G. Shucai, and Kongli, Chin. J. Lumin. 30, 601 (2009). (in Chinese).
[30] L. Kazakova, A. Dubovsky, G. Semenkovich, and O. Ivanova, Radiat. Meas. 24, 359 (1995).
[31] L. Kazakova, I. Bykov, and A. Dubovsky, J. Lumin. 72–74, 211 (1997).
[32] G. Blasse, A. Bril, J. Lumin. 3, 109 (1970).
[33] H. Hori, T. Kobayashi, R. Miyawaki, S. Matsubara, K. Yokoyama, and M. Shimizu, J. Mineral. Petrolog. Sci. 101, 170 (2006).

[34] G. Blasse and A. Bril, J. Chem. Phys. 48(1), 217 (1968).
[35] S. K. Lee, H. Chang, C. H. Han, H. J. Kim, H. G. Jang, and H. D. Park, J. Solid State Chem. 156(2), 267 (2001).
[36] X. Xiao and B. Yan, J. Alloys and Compd. 421, 252257 (2006).
[37] C. Han, H. Kim, H. Chang, S. K. Lee, and H. D. Park, J. Electrochem. Soc. 147(7), 2800 (2000).
[38] S. H. Shin, D. Y. Jeon, and K. S. Suh, J. Appl. Phys. 90(12), 5986 (2001).
[39] A. Massabni, G. Montandon, and M. C. D. Santos, Mater. Res. 1, 01 (1998).
[40] Y. Zhou, Q. Ma, M. Lu, Z. Qiu, and A. Zhang, J. Phys. Chem. C 112(50), 19901 (2008).
[41] C. K. Jorgensen, Prog. Inorg. Chem. 12, 101 (1970).
[42] L. Pauling, Nature of the Chemical Bond, 3rd ed. (Cornell University Press, 1960).

LET'S FORGET ABOUT THE PAIRING

I. V. Beloussov

Institute of Applied Physics, Academy of Sciences of Moldova,
Academy str.5, Chisinau, 2028 Republic of Moldova
E-mail: igor.beloussov@phys.asm.md

(Received June 04, 2013)

Abstract

The algebraic formulation of a Wick's theorem that allows one to present the vacuum or thermal averages of the chronological product of an arbitrary number of field operators as a determinant (permanent) of the matrix is proposed. Each element of the matrix is the average of the chronological product of only two operators. This formulation is extremely convenient for practical calculations in quantum field theory and statistical physics by the methods of symbolic mathematics using computers.

Wick's theorems are extensively used in quantum field theory [1–4] and statistical physics [5–7]. They allow one to use the Green's functions method and consequently to apply Feynman's diagrams for investigations [1–3]. The first of these, which can be referred to as Wick's Theorem for Ordinary Products, gives us the opportunity to reduce, in an almost automatic mode, the usual product of operators into a unique sum of normal products multiplied by c-numbers. It can be formulated as follows [4]. Let $A_i(x_i)$ $(i=1,2,\ldots,n)$ be "linear operators," i.e., some linear combinations of creation and annihilation operators. Then the ordinary product of linear operators is equal to the sum of all the corresponding normal products with all possible contractions, including the normal product without contractions, i.e.,

$$A_1 \ldots A_n =: A_1 \ldots A_n : + : \underbrace{A_1 A_2} \ldots A_n : + \ldots : \underbrace{A_1 \ldots A_{n-1}} A_n : + : \underbrace{A_1 \ldots A_n} : + : \underbrace{A_1 A_2} \, \underbrace{A_3 A_4} \ldots A_n : + \ldots ,$$

where $\underbrace{A_i A_j} = A_i A_j - : A_i A_j :$ $(i, j = 1,2,\ldots,n)$ is the contraction between the factors A_i and A_j.

Since the vacuum expectation value of the normal ordered product is zero, this theorem provides us a way of expressing the vacuum expectation values of n linear operators in terms of the vacuum expectation values of two operators.

Wick's Theorem for Chronological Products [4] asserts that the T-product of a system of n linear operators is equal to the sum of their normal products with all possible chronological contractions, including the term without contractions. It follows directly from the previous theorem and gives the opportunity to calculate the vacuum expectation values of the chronological products of linear operators.

Finally, from Wick's theorem for chronological products, the Generalized Wick's Theorem [4] can be obtained. It asserts that the vacuum expectation value of the chronological product of $n+1$ linear operators $A, B_1, \ldots, B_n$ can be decomposed into the sum of n vacuum expectation values of the same chronological products with all possible contractions of one of these operators (for example, A) with all others, i.e.,

$$\left\langle T\left(AB_1\ldots B_n\right)\right\rangle_0 = \sum_{1\le i\le n}\left\langle T\left(\overline{AB_1\ldots B_i}\ldots\ldots B_n\right)\right\rangle_0 . \qquad (1)$$

Here $\overline{A_iA_j} = T\left(A_iA_j\right) - :A_iA_j: = \left\langle T\left(A_iA_j\right)\right\rangle_0$ $(i, j = 1,2,\ldots,n)$ is the chronological contraction between factors A_i and A_j. It should be noted that, in contrast to the usual Wick's theorem for chronological products, there are no expressions involving the number of contractions greater than one on the right-hand side of (1).

The Wick's theorem for chronological products or its generalized version is used for the calculation of matrix elements of the scattering matrix in each order of perturbation theory [1–4]. The procedure is reduced to calculation of the vacuum expectation of chronological products of the field operators in the interaction representation. A number of operators ψ_i of the Fermi fields and the same number of their "conjugate" operators $\bar{\psi}_i$, as well as operators of the Bose fields $\varphi_s = \varphi_s^{(+)} + \varphi_s^{(-)}$ may be used as factors in these products**.** Here, all continuous and discrete variables are included in the index. In the interaction, representation operators $\psi_i, \bar{\psi}_i$, and φ_s correspond to free fields and satisfy the commutation relationships of the form $\left[\psi_i, \psi_j\right]_+ = \left[\bar{\psi}_i, \bar{\psi}_j\right]_+ = 0$, $\left[\psi_i, \bar{\psi}_j\right]_+ = D^F_{rsij}$, $\left[\varphi_r^{(+)}, \varphi_s^{(-)}\right]_- = D^B_{rs}$. Therefore, the averaging of the Fermi and Bose fields can be performed independently.

Since we may rearrange the order of the operators inside T-products taking into account the change of the sign, which arises when the order of the Fermi operators is changed, we present our vacuum expectation value of the chronological product of the Fermi operators in the form

$$\pm\left\langle T\left[\left(\psi_{i_1}\bar{\psi}_{j_1}\right)\left(\psi_{i_2}\bar{\psi}_{j_2}\right)\ldots\left(\psi_{i_n}\bar{\psi}_{j_n}\right)\right]\right\rangle_0 . \qquad (2)$$

To calculate (2), we can use Wick's theorem for chronological products. However, while considering the higher-order perturbation theory, the number of pairs $\psi_i\bar{\psi}_j$ of operators ψ_i and $\bar{\psi}_j$ becomes so large that the direct application of this theorem begins to represent certain problems because it is very difficult to sort through all the possible contractions between ψ_i and $\bar{\psi}_j$.

A consistent use of the generalized Wick's theorem would introduce a greater accuracy in our actions. However, in this case, we expect very cumbersome and tedious calculations. Hereinafter, we show that the computation of (2) can be easily performed using a simple formula:

$$\left\langle T\left[\left(\psi_{i_1}\bar{\psi}_{j_1}\right)\left(\psi_{i_2}\bar{\psi}_{j_2}\right)\ldots\left(\psi_{i_n}\bar{\psi}_{j_n}\right)\right]\right\rangle_0 = \det\left(\Delta_{i_\alpha j_\beta}\right), \qquad (3)$$

where

$$\Delta_{i_\alpha j_\beta} = \overline{\psi_{i_\alpha}\bar{\psi}_{j_\beta}} = \left\langle T\left(\psi_{i_\alpha}\bar{\psi}_{j_\beta}\right)\right\rangle_0 \quad (\alpha, \beta = 1,2,\ldots,n) . \qquad (4)$$

The proof of this theorem is provided by induction. Let us assume now that (3) is true for n pairs $\psi_i\bar{\psi}_j$ and consider it for the case of $n+1$. Using the generalized Wick's theorem, we have

$$\left\langle T\left[\left(\psi_{i_1}\bar{\psi}_{j_1}\right)\ldots\left(\psi_{i_{n+1}}\bar{\psi}_{j_{n+1}}\right)\right]\right\rangle_0 = -\Delta_{i_1 j_{n+1}}\left\langle T\left[\left(\psi_{i_{n+1}}\bar{\psi}_{j_1}\right)\left(\psi_{i_2}\bar{\psi}_{j_2}\right)\ldots\left(\psi_{i_n}\bar{\psi}_{j_n}\right)\right]\right\rangle_0$$
$$-\sum_{\gamma=2}^{n-1}\Delta_{i_\gamma j_{n+1}}\left\langle T\left[\left(\psi_{i_1}\bar{\psi}_{j_1}\right)\ldots\left(\psi_{i_{\gamma-1}}\bar{\psi}_{j_{\gamma-1}}\right)\left(\psi_{i_{n+1}}\bar{\psi}_{j_\gamma}\right)\left(\psi_{i_{\gamma+1}}\bar{\psi}_{j_{\gamma+1}}\right)\ldots\left(\psi_{i_n}\bar{\psi}_{j_n}\right)\right]\right\rangle_0$$
$$-\Delta_{i_n j_{n+1}}\left\langle T\left[\left(\psi_{i_1}\bar{\psi}_{j_1}\right)\ldots\left(\psi_{i_{n-1}}\bar{\psi}_{j_{n-1}}\right)\left(\psi_{i_{n+1}}\bar{\psi}_{j_n}\right)\right]\right\rangle_0 + \Delta_{i_{n+1}j_{n+1}}\left\langle T\left[\left(\psi_{i_1}\bar{\psi}_{j_1}\right)\ldots\left(\psi_{i_n}\bar{\psi}_{j_n}\right)\right]\right\rangle_0 .$$

Taking into account (3), we obtain

$$\left\langle T\left[\left(\psi_{i_1}\bar{\psi}_{j_1}\right)\ldots\left(\psi_{i_{n+1}}\bar{\psi}_{j_{n+1}}\right)\right]\right\rangle_0 = -\Delta_{i_1 j_{n+1}}\begin{vmatrix}\Delta_{i_{n+1}j_1} & \Delta_{i_{n+1}j_2} & \cdots & \Delta_{i_{n+1}j_n}\\ \Delta_{i_2 j_1} & \Delta_{i_2 j_2} & \cdots & \Delta_{i_2 j_n}\\ \vdots & \vdots & \ddots & \vdots\\ \Delta_{i_n j_1} & \Delta_{i_n j_2} & \cdots & \Delta_{i_n j_n}\end{vmatrix}$$
$$-\Delta_{i_2 j_{n+1}}\begin{vmatrix}\Delta_{i_1 j_1} & \Delta_{i_1 j_2} & \cdots & \Delta_{i_1 j_n}\\ \Delta_{i_{n+1}j_1} & \Delta_{i_{n+1}j_2} & \cdots & \Delta_{i_{n+1}j_n}\\ \vdots & \vdots & \ddots & \vdots\\ \Delta_{i_n j_1} & \Delta_{i_n j_2} & \cdots & \Delta_{i_n j_n}\end{vmatrix} - \ldots - \Delta_{i_n j_{n+1}}\begin{vmatrix}\Delta_{i_1 j_1} & \Delta_{i_1 j_2} & \cdots & \Delta_{i_1 j_n}\\ \vdots & \vdots & \cdots & \vdots\\ \Delta_{i_{n-1}j_1} & \Delta_{i_{n-1}j_2} & \ddots & \Delta_{i_{n-1}j_n}\\ \Delta_{i_{n+1}j_1} & \Delta_{i_{n+1}j_2} & \cdots & \Delta_{i_{n+1}j_n}\end{vmatrix} \qquad (5)$$
$$+\Delta_{i_{n+1}j_{n+1}}\begin{vmatrix}\Delta_{i_1 j_1} & \Delta_{i_1 j_2} & \cdots & \Delta_{i_1 j_n}\\ \Delta_{i_2 j_1} & \Delta_{i_2 j_2} & \cdots & \Delta_{i_2 j_n}\\ \vdots & \vdots & \ddots & \vdots\\ \Delta_{i_n j_1} & \Delta_{i_n j_2} & \cdots & \Delta_{i_n j_n}\end{vmatrix}.$$

Rearranging the rows in the determinants in (5), it is easy to see that the right hand side is the expansion of the

$$\det\left(\Delta_{i_\alpha j_\beta}\right) = \begin{vmatrix}\Delta_{i_1 j_1} & \Delta_{i_1 j_2} & \cdots & \Delta_{i_1 j_{n+1}}\\ \Delta_{i_2 j_1} & \Delta_{i_2 j_2} & \cdots & \Delta_{i_2 j_{n+1}}\\ \vdots & \vdots & \ddots & \vdots\\ \Delta_{i_{n+1}j_1} & \Delta_{i_{n+1}j_2} & \cdots & \Delta_{i_{n+1}j_{n+1}}\end{vmatrix} \qquad (\alpha,\beta = 1,2,\ldots,n+1)$$

along the last column [8]. The validity of (3) for $n=1$ follows from the definition $\Delta_{i_\alpha j_\beta}$ in (4).

Note that this result does not depend on the way how we divide the operators on the left hand side of (3) into pairs $\psi_{i_\alpha}\bar{\psi}_{j_\beta}$. Indeed, if on the left hand side of (3) we permute, for example, $\bar{\psi}_{j_\beta}$ and $\bar{\psi}_{j_\gamma}$ ($\beta \neq \gamma$), it changes its sign. The same happens on the right hand side of (3) since this change leads to the permutation of two columns in the determinant, and it also changes its sign. Similarly, in the case of a permutation of ψ_{i_α} and ψ_{i_δ} ($\alpha \neq \delta$). Obviously, when the whole pair $\psi_{i_\alpha}\bar{\psi}_{j_\beta}$ is transposed, the left and right hand sides of (3) do not change.

The above theorem has an important consequence. In fact, it establishes a perfect coincidence between the vacuum expectation values of the chronological products of n pairs of field operators and the n-order determinant. If we present this determinant as the sum of the elements and cofactors of one any row or column and thereafter use again the indicated

coincidence for the $(n-1)$-order determinants included in each summand, we will return to the generalized Wick's theorem. Alternatively, in our n-order determinant, we can select arbitrary m rows or columns ($1<m<n$) and use the *Generalized Laplace's Expansion* [8] for its presentation as the sum of the products of all m-rowed minors using these rows (or columns) and their algebraic complements. Then, taking into account our theorem, we obtain a representation of the vacuum expectation values of the chronological products of n pairs of field operators as the sum of the products of vacuum expectation values of the chronological products of m pairs of operators and vacuum expectation values of the chronological products of $n-m$ pairs. The number of terms in this sum is $n!/m!(n-m)!$. This decomposition can be useful for the summation of blocks of diagrams.

Obviously, the formula similar to (3) can be obtained and in the case of Bose fields:

$$\left\langle T\left[\left(\varphi_{i_1}^{(+)}\varphi_{j_1}^{(-)}\right)\left(\varphi_{i_2}^{(+)}\varphi_{j_2}^{(-)}\right)\ldots\left(\varphi_{i_n}^{(+)}\varphi_{j_n}^{(-)}\right)\right]\right\rangle_0 = \mathrm{perm}\left(\overline{\Delta}_{i_\alpha j_\beta}\right),$$
$$\overline{\Delta}_{i_\alpha j_\beta} = \overbrace{\varphi_{i_\alpha}^{(+)}\varphi_{j_\beta}^{(-)}} = \left\langle T\left(\varphi_{i_\alpha}^{(+)}\varphi_{j_\beta}^{(-)}\right)\right\rangle_0 \quad (\alpha,\beta=1,2,\ldots,n)\ . \tag{6}$$

Representations (3) and (6) not only greatly simplify all calculations, but also allow one to perform them using a computer with programs of symbolic mathematics [9].

In quantum statistics the n-body thermal, or imaginary-time, Green's functions in the Grand Canonical Ensemble are defined as the thermal trace of a time-ordered product of the field operators in the imaginary-time Heisenberg representation [5–7]. To calculate them in each order of perturbation theory, the Wick's theorem is also used. Obviously, in this case, the theorem also may be formulated in the form of (3) and (6) convenient for practical calculation.

In order to demonstrate the usability of the proposed formulation of the Wick's theorem, we find the first-order correction to the one- and two-particle thermal Green's functions for the Fermi system described in the interaction representation by the Hamiltonian

$$H_{\mathrm{int}}(\tau) = \frac{1}{2}\int d\mathbf{r}_1 d\mathbf{r}_2\, \bar{\psi}_\alpha(\mathbf{r}_1,\tau)\bar{\psi}_\beta(\mathbf{r}_2,\tau)U(\mathbf{r}_1-\mathbf{r}_2)\psi_\beta(\mathbf{r}_2,\tau)\psi_\alpha(\mathbf{r}_1,\tau),$$

that contains the product of the field operators $\psi_\alpha(\mathbf{r}_1,\tau)$ and $\bar{\psi}_\alpha(\mathbf{r}_1,\tau)$ in this representation (parameter α indicates the spin projections, τ is the imaginary-time). The one-particle Green's function can be represented as [6, 7]

$$\mathcal{G}_I(x_1,x_2) = -\frac{\left\langle T_\tau\left[\psi(x_1)\bar{\psi}(x_2)\mathcal{S}\right]\right\rangle_0}{\left\langle\mathcal{S}\right\rangle_0},$$

where $\langle\ldots\rangle_0$ is the symbol for the Gibbs average over the states of a system of noninteracting particles, $x\equiv(\mathbf{r},\tau,\alpha)$ and

$$\mathcal{S}(\tau) = T_\tau \exp\left\{-\int_0^\tau d\tau' H_{\mathrm{int}}(\tau')\right\}.$$

We obtain

$$\mathcal{G}_I(x_1,x_2) = -\left\langle T_\tau\left[\psi(x_1)\bar{\psi}(x_2)\right]\right\rangle_0 + \frac{1}{2\langle\mathcal{S}\rangle_0}\int dz_1 dz_2\, \mathcal{V}(z_1-z_2)$$
$$\times\left\langle T_\tau\left[\left(\psi(x_1)\bar{\psi}(x_2)\right)\left(\psi(z_1)\bar{\psi}(z_1)\right)\left(\psi(z_2)\bar{\psi}(z_2)\right)\right]\right\rangle_0 \qquad (7)$$
$$= -\Delta(x_1,x_2) + \frac{1}{2\langle\mathcal{S}\rangle_0}\int dz_1 dz_2\, \mathcal{V}(z_1-z_2)\begin{vmatrix}\Delta(x_1,x_2) & \Delta(x_1,z_1) & \Delta(x_1,z_2)\\ \Delta(z_1,x_2) & \Delta(z_1,z_1) & \Delta(z_1,z_2)\\ \Delta(z_2,x_2) & \Delta(z_2,z_1) & \Delta(z_2,z_2)\end{vmatrix},$$

where $\mathcal{V}(x_1-x_2) = U(\mathbf{r}_1-\mathbf{r}_2)\delta(\tau_1-\tau_2)$. We can immediately take into account the reduction of the disconnected diagrams, if we assume in (7) that $\langle\mathcal{S}\rangle_0 = 1$ and $\Delta(x_1,x_2) = 0$ [6]. Then,

$$\mathcal{G}_I(x_1,x_2) = -\Delta(x_1,x_2) + \frac{1}{2}\int dz_1 dz_2\, \mathcal{V}(z_1-z_2)$$
$$\left[\Delta(x_1,z_2)\begin{vmatrix}\Delta(z_1,x_2) & \Delta(z_1,z_1)\\ \Delta(z_2,x_2) & \Delta(z_2,z_1)\end{vmatrix} - \Delta(x_1,z_1)\begin{vmatrix}\Delta(z_1,x_2) & \Delta(z_1,z_2)\\ \Delta(z_2,x_2) & \Delta(z_2,z_2)\end{vmatrix}\right]$$
$$= -\Delta(x_1,x_2) - \int dz_1 dz_2\, \Delta(x_1,z_1)\mathcal{V}(z_1-z_2)\begin{vmatrix}\Delta(z_1,x_2) & \Delta(z_1,z_2)\\ \Delta(z_2,x_2) & \Delta(z_2,z_2)\end{vmatrix}$$
$$= -\Delta(x_1,x_2) + \int dz_1 dz_2\, \Delta(x_1,z_1)\mathcal{V}(z_1-z_2)\Delta(z_1,z_2)\Delta(z_2,x_2)$$
$$-\int dz_1\, \Delta(x_1,z_1)\left[\int dz_2 \mathcal{V}(z_1-z_2)\Delta(z_2,z_2)\right]\Delta(z_1,x_2).$$

Taking into account $\mathcal{G}^{(0)}(x_1,x_2) = -\Delta(x_1,x_2)$, we finally obtain

$$\mathcal{G}_I(x_1,x_2) = \mathcal{G}^{(0)}(x_1,x_2) + \int dz_1 dz_2\, \mathcal{G}^{(0)}(x_1,z_1)\Sigma^{(1)}(z_1,z_2)\mathcal{G}^{(0)}(z_2,x_2)\ ,$$
$$\Sigma^{(1)}(z_1,z_2) = -\mathcal{V}(z_1-z_2)\mathcal{G}^{(0)}(z_1,z_2) + \delta(z_1-z_2)\int dz\, \mathcal{V}(z_1-z)\mathcal{G}^{(0)}(z,z)\ .$$

Similarly, for the two-particle Green's function

$$\mathcal{G}_{II}(x_1,x_2,x_3,x_4) = -\frac{\left\langle T_\tau\left[\psi(x_1)\psi(x_2)\bar{\psi}(x_3)\bar{\psi}(x_4)\mathcal{S}\right]\right\rangle_0}{\langle\mathcal{S}\rangle_0},$$

we have

$$\mathcal{G}_{II}(x_1,x_2,x_3,x_4) = \left\langle T_\tau\left[\left(\psi(x_1)\bar{\psi}(x_3)\right)\left(\psi(x_2)\bar{\psi}(x_4)\right)\right]\right\rangle_0$$
$$-\frac{1}{2\langle\mathcal{S}\rangle_0}\int dz_1 dz_2\, \mathcal{V}(z_1-z_2)\left\langle T_\tau\left[\left(\psi(x_1)\bar{\psi}(x_3)\right)\left(\psi(x_2)\bar{\psi}(x_4)\right)\left(\psi(z_1)\bar{\psi}(z_1)\right)\left(\psi(z_2)\bar{\psi}(z_2)\right)\right]\right\rangle$$

$$= \begin{vmatrix}\Delta(x_1,x_3) & \Delta(x_1,x_4)\\ \Delta(x_2,x_3) & \Delta(x_2,x_4)\end{vmatrix} - \frac{1}{2}\int dz_1 dz_2\, \mathcal{V}(z_1-z_2)\begin{vmatrix}0 & 0 & \Delta(x_1,z_1) & \Delta(x_1,z_2)\\ 0 & 0 & \Delta(x_2,z_1) & \Delta(x_2,z_2)\\ \Delta(z_1,x_3) & \Delta(z_1,x_4) & \Delta(z_1,z_1) & \Delta(z_1,z_2)\\ \Delta(z_2,x_3) & \Delta(z_2,x_4) & \Delta(z_2,z_1) & \Delta(z_2,z_2)\end{vmatrix}$$

$$= \mathcal{G}^{(0)}(x_1, x_3)\mathcal{G}^{(0)}(x_2, x_4) - \mathcal{G}^{(0)}(x_1, x_4)\mathcal{G}^{(0)}(x_2, x_3)$$
$$-\int dz_1 dz_2\, \mathcal{G}^{(0)}(x_1, z_1)\mathcal{G}^{(0)}(x_2, z_2)\mathcal{V}(z_1 - z_2)\Big[\mathcal{G}^{(0)}(z_1, x_3)\mathcal{G}^{(0)}(z_2, x_4) - \mathcal{G}^{(0)}(z_1, x_4)\mathcal{G}^{(0)}(z_2, x_3)\Big]_0 .$$

References

[1] S. Weinberg, The Quantum Theory of Fields: vol. 1, Foundations, Cambridge University Press, Cambridge, 1995.

[2] S. S. Schweber, An Introduction to Relativistic Quantum Field Theory, John Weatherhill, Tokyo, 1961.

[3] M. E. Peskin and D. V. Schroeder, Introduction to Quantum Field Theory, Addison-Wesley, Redwood City, 1995.

[4] N. N. Bogoliubov and D. V. Shirkov, Introduction to the Theory of Quantized Fields, John Willey & Sons, New York, 1980.

[5] J. W. Negele and H. Orland, Quantum Many-Particle Systems, Westview Press, 1998.

[6] A. A. Abrikosov, L. P. Gor'kov, and I. E. Dzyaloshinski, Methods of Quantum Field Theory in Statistical Physics, Dover Publications, Inc., New York, 1963.

[7] A. L. Fetter and J. D. Walecka, Quantum Theory of Many-Particle Systems, McGraw-Hill, New York, 1971.

[8] G. A. Korn and T. M. Korn, Mathematical Handbook for Scientists and Engineers, McGraw-Hill Book Co., New York, 1961.

[9] S. Wolfram, The Mathematica Book, 5th ed., Wolfram Media, Champaign, USA, 2003.